

JOURNAL OF NUCLEAR MATERIALS

A JOURNAL ON METALLURGY, CERAMICS AND SOLID
STATE PHYSICS IN THE NUCLEAR ENERGY INDUSTRY

EDITORS:

R. W. CAHN - BIRMINGHAM, ENGLAND - J. P. HOWE - CANOGA PARK, U.S.A.
P. LACOMBE - PARIS, FRANCE - S. T. KONOBEEVSKI - MOSCOW, U.S.S.R.

CONTENTS

P. A. JACQUET, Etude métallographique des filaments structuraux ("structural stringers") dans le zircaloy-2	1
L. B. GRIFFITHS, The arcing behaviour of metals in contact with a low energy hydrogen plasma	30
W. M. JUSTUSSON, Transformation kinetics of gamma-phase uranium-molybdenum-niobium alloys	37
S. J. GREGG, R. J. HUSSEY and W. B. JEPSON, The high temperature oxidation of beryllium. Part V. In moist carbon dioxide and moist carbon monoxide	46
R. H. JOHNSON and R. W. K. HONEYCOMBE, The solid solubility of zirconium in α -thorium.	59
D. S. EVANS and G. V. RAYNOR, The solubility of zirconium in α -thorium	66
J. A. HEDLEY and D. R. ASHWORTH, Imperfections in natural graphite	70
J. J. LAWRENCE and D. J. O'CONNOR, Some studies of gas evolution from graphite and uraniumoxide/graphite compacts at temperatures up to 1250°C	79
J. F. R. AMBLER and G. F. SLATTERY, New metallographic techniques for the examination of uranium, uranium alloys and uranium dioxide	90
B. R. BUTCHER, D. C. MINTY, K. E. G. MEREDITH and H. STRONG, Grain shapes in quenched uranium	100
<i>Letters to the Editors - Lettres aux Rédacteurs</i>	
J. J. STOBO and B. PAWELSKI, The relationship between irradiation growth and other properties of alpha-uranium	109
A. BROWN and D. HARDIE, The effect of dissolved oxygen on the terminal solubility of hydrogen in alpha-zirconium	110
P. BASTIEN et P. POINTU, A propos de la lettre de A. Moore sur l'amélioration des propriétés mécaniques du béryllium commercial par traitements thermiques	113
Book Reviews	115
Russian abstracts of papers in Vol. 3, No. 3	117



EDITORIAL ADVISORY BOARD — CONSEIL DES REDACTEURS

S. AAS (Kjeller, Norway)
 K. F. ALDER (Lucas Heights, Australia)
 P. ALBERT (Vitry, France)
 G. W. ARDLEY (Whetstone, U.K.)
 D. S. BILLINGTON (Oak Ridge, U.S.A.)
 J. E. BURKE (Schenectady, U.S.A.)
 J. J. CADWELL (Richland, U.S.A.)
 R. CAILLAT (Saclay, France)
 G. CHAUDRON (Vitry, France)
 H. CHISWIK (Argonne, U.S.A.)
 A. T. CHURCHMAN (Bristol, U.K.)
 A. S. COFFINBERRY (Los Alamos, U.S.A.)
 A. H. COTTRELL (Cambridge, U.K.)
 R. L. CUNNINGHAM (Ottawa, Canada)
 C. DECROLY (Bruxelles, Belgium)
 M. D'HONT (Mol, Belgium)
 J. D. FAST (Eindhoven, Netherlands)
 H. M. FINNISTON (Newcastle, U.K.)
 J. FRIEDEL (Paris, France)

E. GEBHARDT (Stuttgart, Germany)
 E. GRISON (Saclay, France)
 R. B. HASIGUTI (Tokyo, Japan)
 J. HERENGUEL (Antony, France)
 L. K. JETTER (Oak Ridge, U.S.A.)
 G. ÖSTBERG (Stockholm, Sweden)
 K. LÜCKE (Aachen, Germany)
 B. LUSTMAN (Pittsburgh, U.S.A.)
 R. MADDIN (Philadelphia, U.S.A.)
 A. MERLINI (Milan, Italy)
 P. MURRAY (Harwell, U.K.)
 B. MYERS (Sydney, Australia)
 E. C. W. PERRYMAN (Culcheth, U.K.)
 J. A. L. ROBERTSON (Chalk River, Canada)
 J. A. SABATO (Buenos Aires, Argentina)
 K. TANGBI (Bombay, India)
 J. TERRAZA (Madrid, Spain)
 P. VACHET (Paris, France)
 J. WILLIAMS (Harwell, U.K.)

Papers or letters should be sent to one of the Editors,

R. W. CAHN (Dept. of Metallurgy, University of Birmingham, Birmingham 15, England).
 J. P. HOWE (Atomics International, P.O. Box 309, Canoga Park, California, U.S.A.).
 P. LACOMBE (Centre de Recherches Métallurgiques de l'Ecole des Mines, Blvd. St. Michel 60, Paris VI, France)
 S. T. KONOBEVSKI (U.S.S.R. Academy of Sciences, Leninsky Prospekt 14, Moscow V-71, U.S.S.R.),

either directly or through a member of the Editorial Advisory Board.

Papers or letters should be written in English, French or German; papers should have a summary in the appropriate language. Translations of the summary into the two other languages and in Russian will be added by the Editors.

Instructions to contributors will be found in Vol. 1, No. 1 (pp. 111-112).

Books for review should be sent to one of the Editors.

The subscription price of a volume of 360 pages is Gld. 68.50 per volume, post-free.

Subscriptions should be sent to the publishers, North-Holland Publishing Company, P.O. Box 103, Amsterdam or to any subscription-agent.

No part of this issue may be reproduced in any form, by print, photoprint, microfilm or any other means without written permission from the publisher. Reprints, photoprints or microfilms are obtainable at cost from the publisher.

Les articles ou les lettres devront être envoyés à un des Rédacteurs-en-chef,

R. W. CAHN (Dept. of Metallurgy, University of Birmingham, Birmingham 15, England).
 J. P. HOWE (Atomics International, P.O. Box 309, Canoga Park, California, U.S.A.).
 P. LACOMBE (Centre de Recherches Métallurgiques de l'Ecole des Mines, 60 Bd. St. Michel, Paris VI, France)
 S. T. KONOBEVSKI (Académie des Sciences de l'U.S.S.R., Leninsky Prospekt 14, Moscow V-71, U.S.S.R.),

ou directement ou par un membre du Conseil des Rédacteurs.

Les articles ou les lettres devront être rédigés en anglais, français ou allemand, les articles avec un résumé dans la langue correspondante. Les traductions du résumé dans les deux autres langues et en russe seront ajoutées par les Rédacteurs-en-chef.

Les instructions aux auteurs se trouvent dans le Vol. 1, No. 2 (pp. 211-212).

Les livres (exemplaires de presse) devront être envoyés à un des Rédacteurs-en-chef.

Prix de souscription par volume d'environ 360 pages: Gld. 68.50, franco.

Les abonnements devront être envoyés aux éditeurs, North-Holland Publishing Company, P.O. Box 103, Amsterdam, ou à votre librairie.

JOURNAL OF NUCLEAR MATERIALS
JOURNAL DES MATERIAUX NUCLEAIRES

EDITORIAL ADVISORY BOARD — CONSEIL DES REDACTEURS

- | | |
|--|--|
| S. AAS (Kjeller, Norway) | E. GEBHARDT (Stuttgart, Germany) |
| P. ALBERT (Vitry, France) | E. GRISON (Saclay, France) |
| K. F. ALDER (Lucas Heights, Australia) | R. R. HASIGUTI (Tokyo, Japan) |
| G. W. ARDLEY (Whetstone, U.K.) | J. HERENGUEL (Antony, France) |
| D. S. BILLINGTON (Oak Ridge, U.S.A.) | L. K. JETTER (Oak Ridge, U.S.A.) |
| J. E. BURKE (Schenectady, U.S.A.) | K. LÜCKE (Aachen, Germany) |
| J. J. CADWELL (Richland, U.S.A.) | B. LUSTMAN (Pittsburgh, U.S.A.) |
| R. CAILLAT (Saclay, France) | R. MADDIN (Philadelphia, U.S.A.) |
| G. CHAUDRON (Vitry, France) | A. MERLINI (Milan, Italy) |
| H. CHISWIK (Argonne, U.S.A.) | P. MURRAY (Harwell, U.K.) |
| A. T. CHURCHMAN (Bristol, U.K.) | R. MYERS (Sydney, Australia) |
| A. S. COFFINBERRY (Los Alamos, U.S.A.) | G. ÖSTBERG (Stockholm, Sweden) |
| A. H. COTTRELL (Cambridge, U.K.) | E. C. W. PERRYMAN (Culcheth, U.K.) |
| R. L. CUNNINGHAM (Ottawa, Canada) | J. A. L. ROBERTSON (Chalk River, Canada) |
| C. DECROLY (Bruxelles, Belgium) | J. A. SABATO (Buenos Aires, Argentina) |
| M. D'HONT (Mol, Belgium) | K. TANGRI (Bombay, India) |
| J. D. FAST (Eindhoven, Netherlands) | J. TERRAZA (Madrid, Spain) |
| H. M. FINNISTON (Newcastle, U.K.) | P. VACHET (Paris, France) |
| J. FRIEDEL (Paris, France) | J. WILLIAMS (Harwell, U.K.) |

JOURNAL OF NUCLEAR MATERIALS

A JOURNAL ON METALLURGY, CERAMICS AND SOLID
STATE PHYSICS IN THE NUCLEAR ENERGY INDUSTRY

Editors :

R. W. CAHN — BIRMINGHAM, ENGLAND

J. P. HOWE — ITHACA, U.S.A.

P. LACOMBE — PARIS, FRANCE

S. T. KONOBEEVSKI — MOSCOW, U.S.S.R.

VOLUME 4

MAY 1961 — SEPTEMBER 1961



NORTH-HOLLAND PUBLISHING COMPANY — AMSTERDAM

DES MATERIAUX NUCLEAIRES

JOURNAL

OF NUCLEAR MATERIALS

DESIGN MATERIALS IN NUCLEAR REACTORS

PRINTED IN THE NETHERLANDS
DRUKKERIJ HOLLAND N.V., AMSTERDAM

ETUDE METALLOGRAPHIQUE DES FILAMENTS STRUCTURAUX ("STRUCTURAL STRINGERS") DANS LE ZIRCALOY-2

PIERRE A. JACQUET †

Reçu le 15 décembre 1960

La nouvelle méthode de polissage électrolytique local "Ellopol" a été appliquée à l'étude des filaments souvent décrits dans les travaux consacrés au Zircaloy-2. Ces défauts ont été ainsi décelés exclusivement dans les billettes forgées et tôles laminées provenant de lingots élaborés au four à électrode consommable avec atmosphère d'argon. Les produits tirés des lingots de fusion sous vide n'en contiennent pas.

L'évolution des aspects micrographiques en fonction des conditions du polissage (nature de l'électrolyte principalement), et l'influence de l'oxydation anodique, tendent à prouver que contrairement à une opinion répandue les filaments structuraux ne sont pas des porosités héritées du lingot de départ. Ils correspondent à des hétérogénéités chimiques (constituant intermétallique non identifié, oxydes) résultant des conditions thermiques de la fusion et des impuretés de l'atmosphère. La confusion entre discontinuités physiques et éléments figurés de la microstructure aurait pour origine l'action corrosive des réactifs sur les surfaces polies mécaniquement.

La comparaison des structure des billettes et tôles, l'analyse aux rayons X et les résultats d'observations indépendantes, permettent d'interpréter les effets du laminage à chaud. L'apparition de défauts macroscopiques résulte du gonflement par oxydation des filaments superficiels. D'autre part, l'insolubilité des oxydes explique le fait connu qu'un traitement prolongé à haute température puisse éliminer les gradients de concentration responsables des "stringers" dits de corrosion, tout en laissant subsister ceux des filaments qui sont précisément formés de ségrégations d'oxydes.

exclusively in forged billets and rolled sheets made from ingots which had been cast from alloy melted in consumable arc furnaces in an argon atmosphere. Products made from ingots produced by vacuum melting do not contain stringers.

The variation of the micrographic appearance with the polishing conditions (primarily the nature of the electrolyte), and the influence of anodic oxidation tend to show that, contrary to a widely held opinion, structural stringers are not a form of porosity inherited from the ingot. They are associated with chemical heterogeneities (an unidentified intermetallic constituent, oxides) resulting from the thermal conditions of melting and from impurities in the atmosphere. A confusion between physical discontinuities and correspondingly shaped features of the microstructure can arise from the corrosive action of the etching reagents on mechanically polished surfaces.

Comparison of the structure of billets and sheets, X-ray analysis and the results of observations by others permit an interpretation of the effects of hot rolling. The appearance of macroscopic defects results from the inflation, by oxygen, of filaments at the surface. Moreover, the insolubility of the relevant oxides accounts for the known fact that a prolonged treatment at high temperature can eliminate the concentration gradients responsible for so-called corrosion-stringers, while leaving unaffected those filaments which are formed by oxide segregation.

The new technique of localised electrolytic polishing, "Ellopol", has been applied to the study of the stringers which have often been described in papers devoted to zircaloy-2. These defects have been detected

Die neue elektrolytische Poliermethode "Ellopol" wurde bei der Untersuchung von Fasenstrukturen angewandt, wie sie des öfteren in Arbeiten über Zircaloy beschrieben wurden. Diese Fehler wurden ausschliesslich in geschmiedeten und längs gewalzten Proben nachgewiesen, welche aus im Lichtbogenofen unter Argonatmosphäre geschmolzenen Barren ent-

† Ingénieur-Contractuel des Constructions et Armes Navales (Marine Nationale), Ingénieur-Conseil à l'Office National d'Etudes et de Recherches Aéronautiques (O.N.E.R.A.) et au Commissariat à l'Energie Atomique (C. E. N. Saclay).

nommen worden sind. Die Schmelzproben, welche im Vakuum hergestellt wurden, zeigen keine Fehler.

Die neuen Ergebnisse der mikroskopischen Untersuchungen in Verbindung mit elektrolytischen Polierbedingungen scheinen zu beweisen, dass im Gegensatz zu einer weitverbreiteten Meinung die Faserstrukturen keine porösen Bestandteile sind, welche aus dem Ausgangsmaterial stammen. Sie entsprechen vielmehr den chemischen Unregelmässigkeiten (Heterogenitäten, noch nicht bestimmte intermetallische Verbindungen, Oxyde), welche aus den thermischen Bedingungen beim Schmelzen und den Unreinheiten der Atmosphäre resultieren. Die Faserstrukturen bestehen daher einmal aus Diskontinuitäten, die (bei der thermischen Behandlung) von den Elementen im

Material gebildet werden, und aus Korrosionserscheinungen auf den mechanisch polierten Oberflächen.

Der Vergleich der Ergebnisse über die Strukturen der gewalzten Bleche aus der Röntgenanalyse mit den Resultaten der mikroskopischen Beobachtung erlaubt eine Erklärung der Effekte aus dem Warmwalzvorgang. Das Auftreten der makroskopischen Fehler resultiert aus der Gasaufnahme durch Oberflächen-Oxydation der Faserstrukturen. Andererseits bestätigt die Unlöslichkeit der Oxyde die bekannte Tatsache, dass eine verlängerte Behandlung bei hohen Temperaturen die Unterscheidung der "Korrosionsfasern" von denen ermöglichte, welche bei Oxydausscheidungen gebildet werden, indem sie letztere durch Ausgleich der Konzentrationsgradienten eliminieren würde.

1. Introduction

La littérature américaine consacrée à l'élaboration, aux propriétés et aux applications du zircaloy-2 et du zircaloy-3 traite fréquemment d'aspects particuliers rencontrés dans ces alliages, et rassemblés sous la dénomination de "stringers", traduisible par le terme filaments.

Les spécialistes s'accordent maintenant à distinguer les "stringers" dits de corrosion, observés sur la surface de tôles exposées à l'eau surchauffée, et les "stringers" dits structuraux déjà présents dans le matériau.

Si une relation directe entre ces deux types de défauts ne semble pas douteuse, en revanche l'origine et la nature des "stringers" appartenant à la microstructure sont encore l'objet de controverses, ainsi qu'en témoignent les plus récentes publications¹⁻³.

Etant donné que les interprétations actuelles reposent toutes sur les résultats d'observations métallographiques, il est permis de se demander si les techniques opératoires utilisées jusqu'ici sont bien adaptées au problème.

C'est afin de tenter de lever ce doute que la nouvelle méthode de polissage électrolytique local au tampon (procédé "Ellopol") a été appliquée à une grande variété de spécimens tirés de billettes et de tôles provenant de lingots de zircaloy-2 élaborés aux fours à atmosphère d'argon et à vide.

Le présent mémoire décrit dans leurs détails les conditions expérimentales et les résultats obtenus. La discussion de ces résultats conduira

à proposer une interprétation assez cohérente de la nature des stringers structuraux, qui ne fait d'ailleurs pas apparaître le rôle fondamental qu'attribuent de nombreux auteurs aux porosités préexistant dans les lingots d'origine.

2. Nature des spécimens étudiés

L'étude métallographique a porté sur une douzaine d'échantillons prélevés soit dans des billettes forgées, soit dans des tôles laminées à partir de certaines de ces billettes †.

Les lingots ayant servi à l'obtention des billettes appartiennent à deux types distincts selon qu'ils ont été fondus au four électrique à électrode consommable, sous atmosphère d'argon à la pression normale, ou au four à vide. Il faut noter aussi que la plupart de ces lingots sont de provenance américaine, trois seulement sont de fabrication française.

Toutes les tôles ont été laminées en France de la façon suivante: Ecrouissage-Forgeage en trois chaudes à 825° C jusqu'à 80 mm-Laminage à chaud entre 825 et 700° C pour amener à l'épaisseur 2,5 mm-Sablage et décapage avec enlèvement de 0,2 mm-Laminage à 550° C jusqu'à 3,2 ou 1,6 mm-Recuit 30 minutes au

† Ces échantillons proviennent du Département Métallurgie du Centre d'Etudes Nucléaires de Saclay. Nous remercions MM. M. Salesse, Directeur de ce Département et M. Jean, Chef de service, d'avoir bien voulu les mettre à notre disposition, et aussi de nous avoir autorisé à faire état de certains renseignements tirés de leurs propres expériences.

four à air à 650° C—Mise en forme à 550° C—Sablage et décapage.

La référence, l'origine et l'état métallurgique de chacun des 12 échantillons sont données au tableau 1.

En ce qui concerne les spécimens provenant des billettes il faut noter que, sauf mention spéciale, ils ont été prélevés après écrouissage, tous à des endroits non définis par rapport à la géométrie du lingot de départ.

3. Techniques métallographiques

D'une manière générale la préparation mécanique des surfaces comporte l'abrasion sur les papiers émeri N° 240 à N° 600 mouillés à l'eau et le polissage avec le papier 00 paraffiné.

Le stade final est un polissage électrolytique par la nouvelle technique du tampon "Ellopol"⁴⁾. Le même appareil est employé pour l'oxydation anodique qui constitue un mode d'attaque intéressant⁵⁾.

Les données relatives à ces deux méthodes déjà publiées seront rappelées ici.

3.1. POLISSAGE AU TAMPON

Dans son principe ce procédé consiste à appliquer sur la surface de l'échantillon un

tampon qui joue le rôle de cathode mobile. Il comporte une tête métallique creuse refroidie par circulation d'un courant d'eau, recouverte d'une coiffe formée de plusieurs couches de tissus synthétiques qui servent d'isolant électrique et de réceptacle à l'électrolyte.

Vis-à-vis de tous les autres procédés de polissage électrolytique, la technique "Ellopol" présente plusieurs avantages. L'opération est réalisée localement à l'endroit voulu, ce qui est très pratique lorsque les spécimens sont volumineux. L'opérateur garde constamment la surface sous les yeux et peut ainsi suivre l'évolution de son aspect. La consommation d'électrolyte est très minime, et celui-ci étant renouvelé n'évolue pas d'une opération à l'autre. En outre, les conditions d'applications du tampon peuvent avoir une certaine influence sur le résultat, d'où la possibilité de réaliser un polissage plus ou moins accompagné d'effets d'attaque.

La technique "Ellopol" utilise des électrolytes spéciaux. Certains d'entre eux sont polyvalents, c'est-à-dire conviennent pour plusieurs types de matériaux. Inversement un métal ou alliage peut être poli avec deux ou trois électrolytes. C'est le cas, par exemple, pour le zirco-

TABLEAU 1
Nature des échantillons de Zircaloy-2 étudiés

Référence	Origine	Etat métallurgique
Z-78 Z-81 Z-82 Z-83 Z-87 Z-90	Américaine	Billetes forgées à partir des lingots fondus sous atmosphère d'argon au four électrique à électrode consommable.
Z-105	Américaine	Billette forgée à partir d'un lingot fondu au four à vide.
Z-127	Française	Billette forgée à partir d'un lingot obtenu par fusion au four à vide des billetes américaines Z-83, Z-87 et Z-90.
A	Française	Billette forgée à partir d'un lingot de fusion sous vide.
Z-82 T Z-105 T Z-A-2 D 127	Française Française Française	Tôle de 1,5 mm, obtenue par laminage de la billette Z-82. Tôle de 1,5 mm, obtenue par laminage de la billette Z-105. Tôle de 3 mm, obtenue par laminage de la billette Z-127.

nium: les solutions dénommées "Buper" et "Peroc" donnent des résultats sensiblement identiques, la seule différence étant une vitesse de dissolution anodique plus grande avec le second. Pour le Zircaloy-2, au contraire, les aspects micrographiques sont parfois très sensibles à la nature de l'électrolyte.

Le tableau 2 résume les conditions opératoires utilisées dans la présente étude.

3.2. OXYDATION ANODIQUE AU TAMPON

L'oxydation anodique préconisée pour la métallographie du zirconium⁶⁾ est réalisée très aisément avec la méthode "Ellopol". L'électrolyte dénommé "Opalu" est la solution d'acide phosphorique en milieu organique mise au point pour l'oxydation anodique de l'aluminium⁵⁾ †.

Le tampon "Ogicol" muni de la coiffe normale fortement imbibée d'électrolyte est appliqué sans pression excessive à l'endroit préalablement poli. L'intensité qui s'établit au premier contact est d'autant plus élevée que la tension aux bornes est elle-même plus grande,

† Une composition un peu différente, dénommée "Opalu B", donne de remarquables résultats pour le polissage de l'uranium et de certains de ses alliages⁷⁾.

mais quelle que soit la valeur de cette dernière, l'intensité décroît très vite pour s'annuler au bout de quelques secondes. Toutefois, elle prend à nouveau une valeur appréciable si la tension est augmentée.

On est donc amené à opérer par paliers de tension, chacun d'une trentaine de secondes. Dans le cas du Zircaloy-2 un film bleuâtre se forme entre 20 et 30 volts, puis disparaît aux tensions plus élevées, la surface devenant alors incolore ou teintée de jaune très clair.

Pour le présent travail le mode opératoire comportait toujours les quatre paliers de tension 10, 20, 30 et 40 volts.

4. Microstructure des billettes forgées

Le polissage "Ellopol" révèle des aspects micrographiques caractéristiques selon qu'il s'agit de l'alliage élaboré au four à vide ou au four à atmosphère d'argon. Il permet également, dans le cas des billettes du premier type (lingot de fusion sous vide), de différencier le produit d'origine américaine (référence Z-105) des deux produits français (références Z-127 et A). Nous considérerons donc successivement ces trois cas.

TABLEAU 2

Conditions de polissage des échantillons de Zircaloy-2

Electrolyte ^a	Modèle ^b	Tampon Mode d'application	Voltage à vide (volts)	Intensité (mA)	Vitesse de dissolution (microns/min)
"BUPER"	"OGIPOL" coiffe normale	Touches à cadence rapide pendant quelques secondes, puis plus lente, c'est-à-dire avec des contacts de 8 à 10 sec.	45 à 50	50 à 100	3 à 4
"BUPER"	"OGIPOL" coiffe normale	Touches à cadence très rapide	45 à 50	150 à 200	
"PEROC"	"SHARPOL" coiffe spéciale	Déplacement rectiligne assez rapide	20	300	15 à 18

^a Les deux électrolytes qui sont des solutions d'acide perchlorique différant par la concentration de cet acide et la nature du solvant.

^b Le tampon "Ogipol" possède une tête à extrémité arrondie et le "Sharpol" une tête à extrémité pointue. Les superficies d'impact sont respectivement de l'ordre de 0,8 et 0,4 cm².

4.1. BILLETES PROVENANT DES LINGOTS DE FUSION SOUS VIDE

Les résultats illustrés par les figures 1 à 3 conduisent aux conclusions suivantes:

(i) Les deux billettes d'origine française se distinguent de la billette d'origine américaine par une distribution plus fine et plus homogène des éléments insolubles.

Dans cette dernière les constituants hors solution, alignés ou rassemblés en amas eutectiques constituent un réseau qui coïncide presque toujours avec les grains équiaxiaux visibles en lumière polarisée (fig. 1).

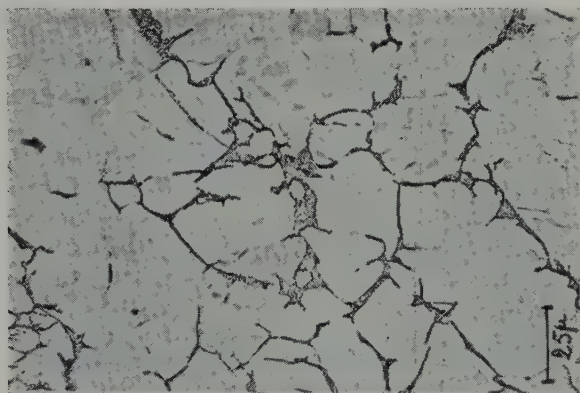
La billette française Z-127 possède, au contraire, une texture fibreuse, en ce qui concerne aussi bien les éléments insolubles que les gros

cristaux maclés dont les contours ne se confondent pas toujours avec ces éléments (fig. 2).

Dans l'autre billette française, référence A, l'aspect fibreux est moins net, ou plutôt les axes de fibres sont orientés selon plusieurs directions (fig. 3).

(ii) La comparaison des micrographies a et b, fig. 1, prouve une certaine influence des conditions du polissage. Les constituants intergranulaires apparaissent mieux définis, c'est-à-dire plus attaqués, avec l'électrolyte "Buper". En revanche, l'électrolyte "Peroc" révèle plus distinctement une sorte de sous-structure à l'intérieur des grains.

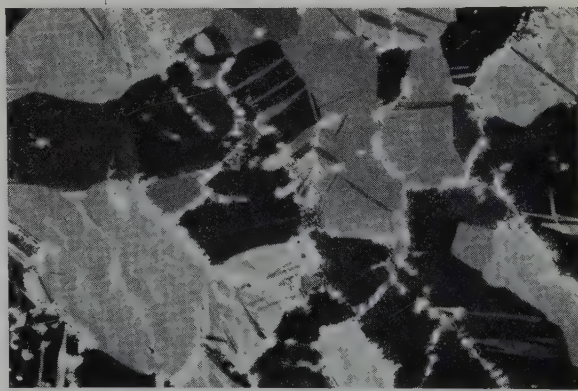
Les effets spécifiques des deux électrolytes se manifestent aussi vis-à-vis des microconstituants dans les billettes françaises (cf. figures 2 et 3),



a

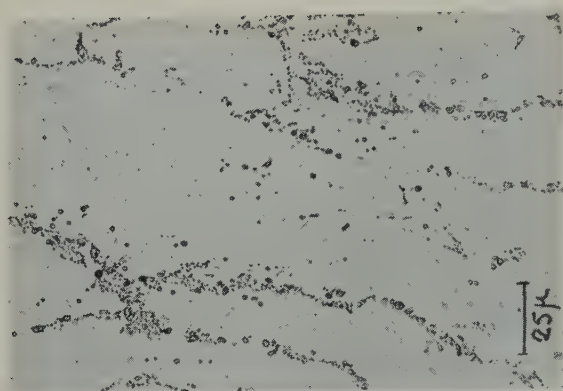


b

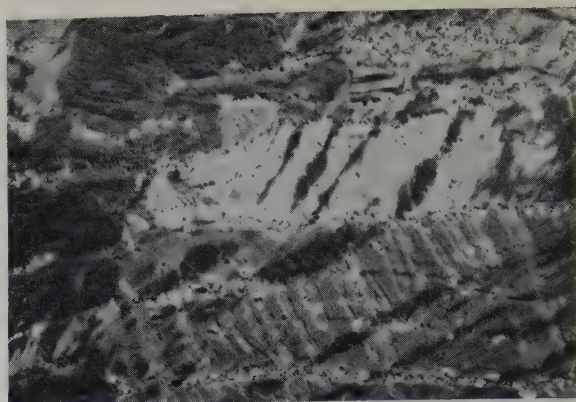


c

Fig. 1. Billette Z-105 de fusion sous vide. (a) Polissage électrolyte "Buper"; (b) Polissage électrolyte "Peroc"; (c) Même champ que (a) en lumière polarisée. $\times 400$.



a



b

Fig. 2. Billette Z-127 de refusion sous vide de trois billettes de fusion en atmosphère d'argon. Polissage électrolyte "Buper". (a) Fond clair; (b) Lumière polarisée. $\times 400$.

mais le "Peroc" ne révèle ici aucun indice de sous-structure de la matrice.

(iii) L'électrolyte "Peroc" ne provoque jamais d'attaque sélective profonde. Cette constatation est très importante, car elle marque, nous allons le prouver, une différence fondamentale entre les billettes de fusion sous vide et les billettes de fusion en atmosphère d'argon.

4.2. BILLETES PROVENANT DES LINGOTS DE FUSION EN ATMOSPHERE D'ARGON

4.2.1. Généralités

Les spécimens prélevés dans les six billettes d'origine américaine, forgées à partir des lingots élaborés au four électrique à électrode con-

sommable sous atmosphère d'argon présentent tous des aspects structuraux rigoureusement identiques.

Par ailleurs, ces aspects comportent des particularités dont la mise en évidence se montre très sensible aux conditions opératoires du polissage, et surtout à la nature de l'électrolyte.

L'influence de la composition de l'électrolyte ressort de la comparaison des figures 4 à 6 relatives à la microstructure des billettes références Z-78 et Z-82.

Les sections polies avec le bain "Peroc" contiennent des domaines en forme de piqures et de segments plus ou moins rectilignes ou incurvés (figs. 5a et 6b). D'abondance variable, ces hétérogénéités ne sont ni des porosités ni des fissures, mais des cuvettes et fossés (fig. 5b) correspondant à une dissolution accélérée, et qui se confondent souvent avec le réseau des microconstituants.

Sur les surfaces polies avec l'électrolyte "Buper", et examinées sous des grossissements, relativement faibles, les domaines d'attaque préférentielle sont beaucoup atténués (fig. 4a) ou bien n'apparaissent plus (fig. 6). Dans le premier cas l'observation à fort grossissement prouve que chacun de ces domaines est en réalité une sorte de filament grisâtre associé au réseau des très petits constituants hors solution (fig. 4b).

Les filaments sont parfois si peu contrastés

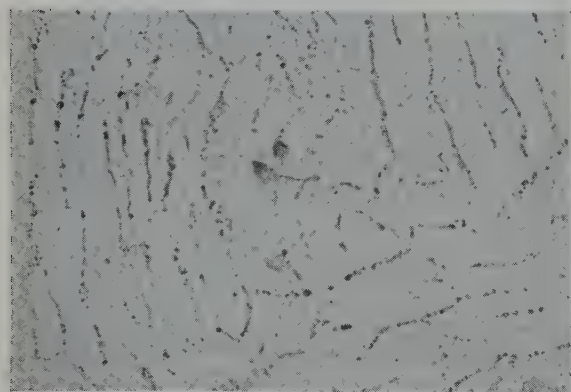


Fig. 3. Billette A de fusion sous vide. Polissage électrolyte "Peroc". $\times 400$.

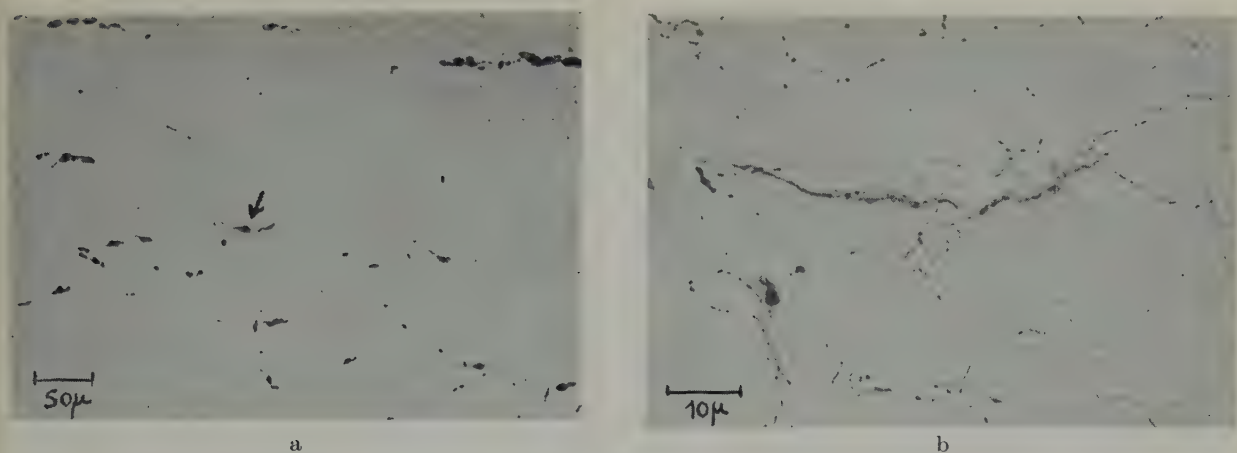


Fig. 4. Billette Z-78 de fusion en atmosphère d'argon. Polissage électrolyte "Buper". (a) $\times 160$; (b) $\times 1000$, filament repéré par la flèche au centre de (a).

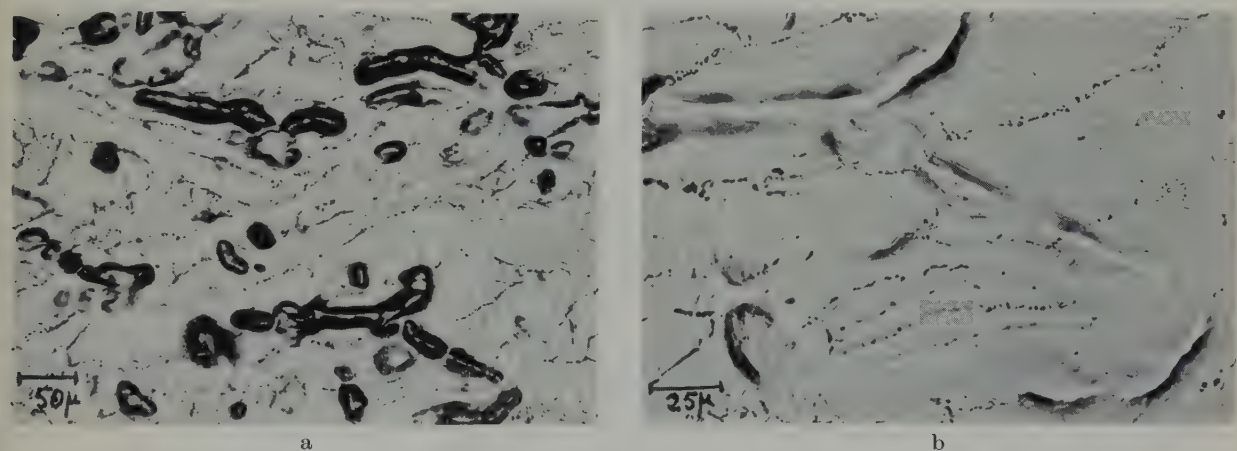


Fig. 5. Même spécimen que figure 4. Polissage 20 sec avec l'électrolyte "Peroc". (a) $\times 160$; (b) $\times 400$, champ de la partie inférieure de (a).

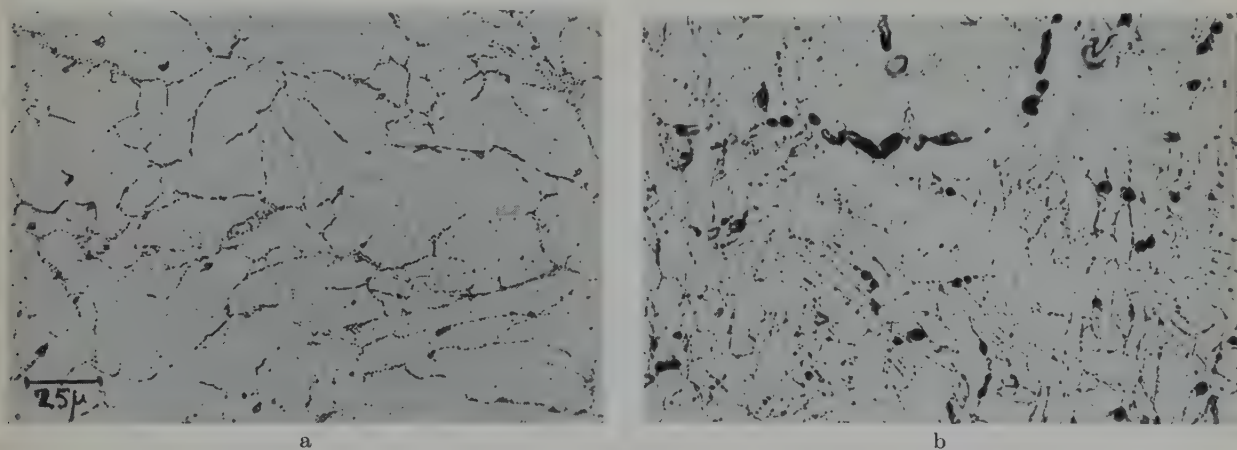


Fig. 6. Billette Z-82 de fusion en atmosphère d'argon. (a) Polissage électrolyte "Buper"; (b) Polissage 35 sec avec l'électrolyte "Peroc".

par rapport à la matrice que seule une observation très minutieuse peut les faire découvrir. Deux moyens permettent alors d'augmenter leur netteté.

Le premier consiste à appliquer le tampon à cadence rapide, de manière à établir des contacts successifs de l'ordre de la demi-seconde. On peut d'ailleurs remarquer que, dans ces conditions, les microconstituants en réseau réagissent à l'inverse des filaments: ils sont moins attaqués que lorsque la durée de chaque contact est de l'ordre de plusieurs secondes. Nous donnerons plus loin un exemple de tels résultats.

Le second moyen est l'oxydation anodique dans les conditions décrites précédemment. La figure 7 montre, par exemple, un filament dont la portion centrale, initialement à peine discernable, acquiert après l'oxydation le même aspect que les extrémités. La figure 8a correspond à un autre échantillon riche en filaments prenant une forte coloration brune à la suite du traitement anodique.

L'attaque oxydante n'est pas uniforme, car sous le grossissement optique maximal on distingue une sorte de sous-structure qui paraît formée de petits éléments submicroscopiques dispersés dans une matrice très sombre (fig. 8b). Il est à remarquer, d'ailleurs, que cette même

sous-structure existe également sur les filaments déjà attaqués au cours du polissage (fig. 9).

Outre les filaments de taille notable, l'oxydation anodique en révèle aussi d'extrême finesse, rectilignes ou sinueux, qui leur sont associés comme une sorte d'appendice (par exemple à droite de la figure 8b), mais existent également à l'état libre. Cette forme correspondrait peut-être à des filaments normaux très minces vus par la tranche.

Nous décrivons maintenant un certain nombre d'observations plus détaillées effectuées sur les deux billettes Z-82 et Z-81. Elles ont principalement pour objet d'illustrer l'extrême sensibilité des structures aux conditions de préparation des sections. De plus, le cas de la billette Z-82 présente un intérêt tout particulier, puisque son laminage a conduit à une tôle très riche en défauts du type "stringers".

4.2.2. Billette Z-82

Les micrographies a, b et c, figure 10, montrent l'évolution d'un même champ à la suite de courts polissages successifs avec l'électrolyte "Buper" le premier de 90 secondes, ayant d'ailleurs laissé subsister des traces de rayures d'abrasion.

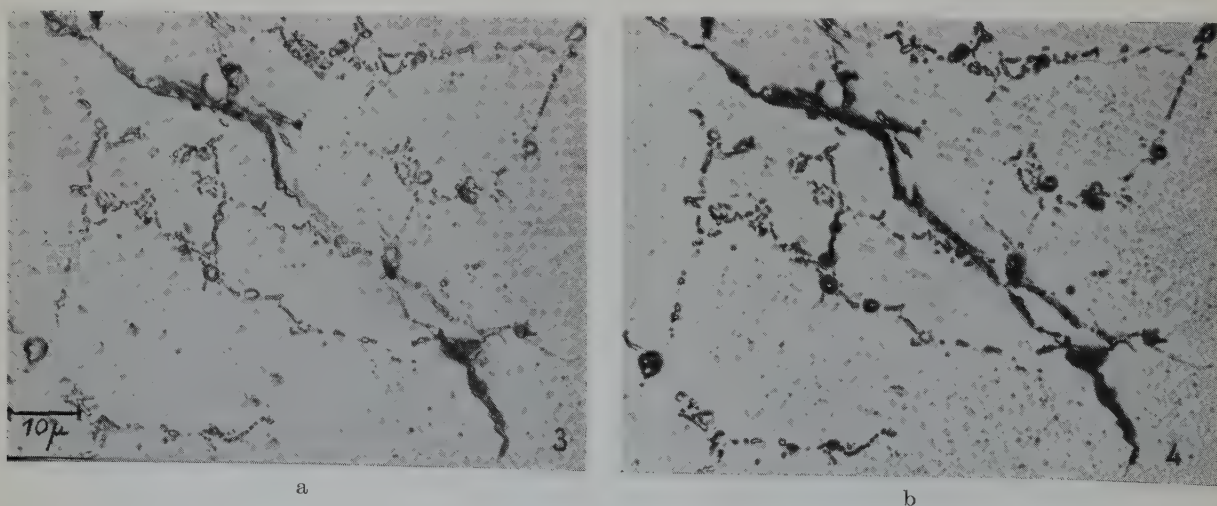
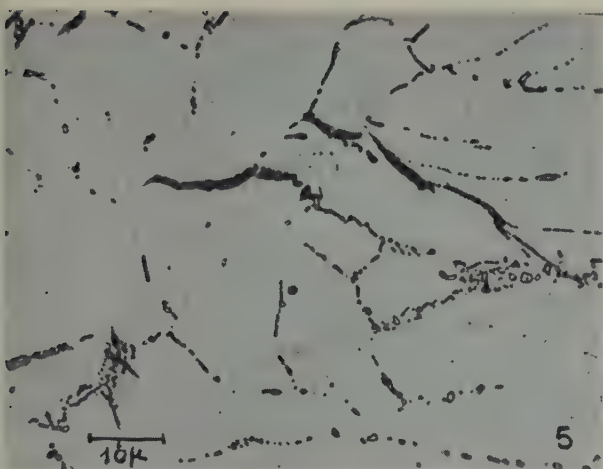
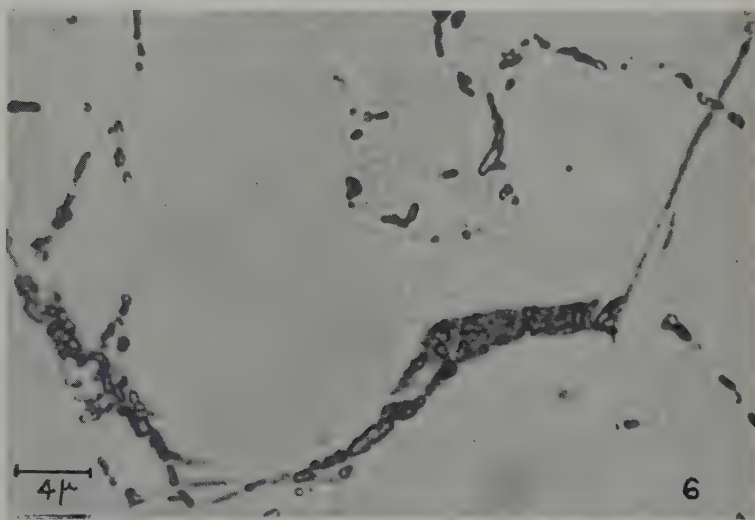


Fig. 7. Billette Z-90 de fusion en atmosphère d'argon. Polissage électrolyte "Buper". (a) Etat poli; (b) Même champ après oxydation anodique. $\times 1000$.



a



b

Fig. 8. Billette Z-81 de fusion en atmosphère d'argon. Polissage électrolyte "Buper" suivi d'oxydation anodique. (a) $\times 1000$; (b) $\times 2500$.

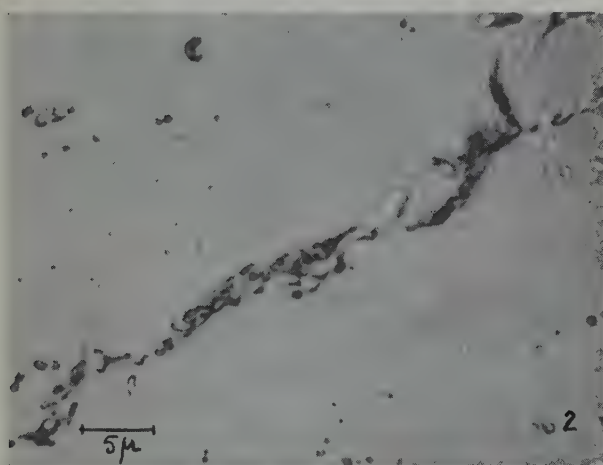


Fig. 9. Billette Z-87 de fusion en atmosphère d'argon. Surface brute de fraisage polie 60 sec avec l'électrolyte "Buper". $\times 2000$.

Tout d'abord, l'on constate que la répartition des alignements d'hétérogénéités les plus contrastées suggère que celles-ci étaient initialement localisées sur les contours des gros grains du lingot qui se sont déformés lors du corroyage, (le même effet est apparent sur la figure 4a).

L'influence du mode d'application du tampon ressort nettement de la comparaison des trois images figure 10. En effet:

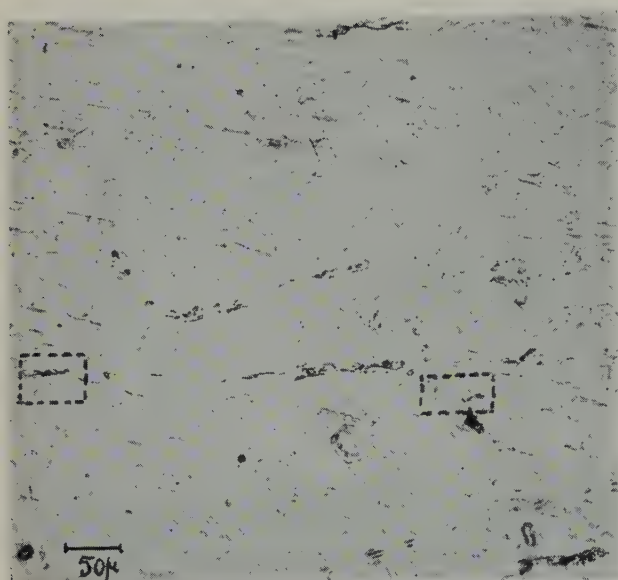
(i) les hétérogénéités s'estompent, alors qu'au contraire le réseau des précipités apparaît beaucoup mieux, quand la surface initialement polie

à cadence rapide est soumise à deux touches de 10 secondes chacune;

(ii) l'aspect initial reparaît après un polissage de même durée (20 secondes) à cadence rapide.

Malgré la très petite épaisseur de matière dissoute, de l'ordre de 2 à 3 microns, on note une évolution des hétérogénéités entre le premier et le dernier polissage. Déjà appréciable sous un faible grossissement (voir les régions encadrées sur a et c figure 10) cette évolution est montrée encore mieux par la comparaison de la figure 11 et de la partie gauche de la figure 12 correspondant au même champ au grossissement 1600.

Outre les alignements assez rares d'hétérogénéités fortement contrastés, il existe de nombreux filaments (indiqués par les flèches sur la figure 12) qui prennent l'intense coloration



a



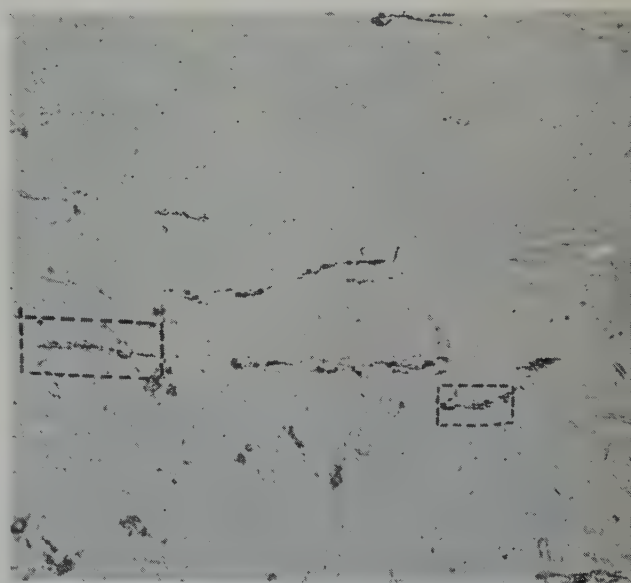
b

brune à l'oxydation anodique. La figure 13 montre que l'attaque oxydante se porte également sur la matrice entourant certains des éléments d'hétérogénéités. De plus, cette micrographie ne laisse subsister aucun doute quant à la localisation des alignements d'hétérogénéités sur les contours des grains primaires de fonderie, déjà soupçonnés à l'examen sous faible grossissement de la section polie.

4.2.3. Billette Z-81

Révlée avec l'électrolyte "Buper" la structure est du type normal montré figure 8 a (abstraction faite, toutefois, du fort contraste provoqué par l'oxydation anodique sur les filaments). Il suffit alors de 30 secondes de polissage avec l'électrolyte "Peroc" pour qu'apparaissent les nombreux défauts de surface déjà mentionnés. Leur relation avec des éléments figurés de la microstructure est démontrée de la façon suivante.

Après que deux de ces défauts aient été repérés (face aux flèches 1 et 2 sur la figure 14) et l'un photographié sous fort grossissement (fig. 15a), la surface est repolie 30 secondes avec le "Buper". La dénivellation s'estompe en même temps qu'apparaissent des microconstituants (fig. 15b), et ces effets se poursuivent lors d'un second polissage de même durée (fig. 15c). A ce



c

Fig. 10. Billette Z-82. Polissage électrolyte "Buper". Aspects successifs du même champ en fonction des conditions d'applications du tampon. (a) Cadence rapide pendant 90 sec; (b) Deux touches de 10 sec chacune; (c) Cadence très rapide pendant 20 sec. $\times 160$.

stade, le domaine initialement sans structure contient, d'une part quelques amas d'aspect eutectique, et d'autre part de très petits segments filiformes (repérés par les flèches). L'oxy-

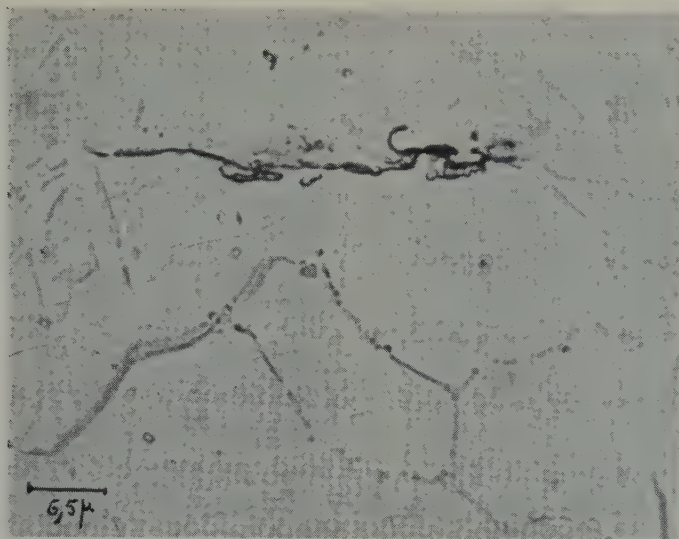


Fig. 11. Champ encadré en bas sur la fig. 10 (a). $\times 1600$.

dation anodique attaque sélectivement ces deux types de microconstituants et l'aspect (fig. 15d) est bien celui des hétérogénéités filamenteuses présentes dans toutes les billettes de fusion sous argon. En outre, la lumière polarisée montre que dans le cas présent cette hétérogénéité marque les contours des grains actuels (fig. 16). Le défaut repéré par la flèche 2 sur la figure 14 correspond, lui aussi, à un filament typique (fig. 17 que l'on comparera à la figure 8b).

5. Microstructures des tôles laminées

Trois des billettes qui viennent d'être étudiées ont été laminées dans les conditions précisées plus haut, de sorte qu'il a été possible de définir les relations structurales existant entre l'état de forge et l'état final de la tôle.

5.1. TOLE REFERENCE Z-82 T

La billette correspondante (Z-82) était tirée d'un lingot de fusion au four à atmosphère d'argon.

Sur toute leur étendue, les deux faces de cette tôle sont couvertes de très nombreux défauts consistant de taches sombres allongées sur 2 à 10 mm dans la direction du laminage et de largeur 1 à 3 mm. Certaines d'entre elles sont accompagnées d'écaillage avec exfoliation du métal (fig. 18).

L'étude micrographique a porté sur la surface et sur une section droite en long, c'est-à-dire parallèle à la direction du laminage.

Tout d'abord il était intéressant de déterminer si la sensibilité de l'alliage à la nature de l'électrolyte de polissage, constatée dans le cas de la billette, existait encore pour la tôle.

A cet effet la surface est abrasée aux papiers d'émeri jusqu'à disparition complète des accidents. Un polissage de 80 secondes, en deux stades, avec l'électrolyte "Buper", fait apparaître des hétérogénéités qui reproduisent assez bien l'aspect initial (fig. 19a). Les microconstituants sont dispersés d'une manière homogène dans la matrice, mais on ne retrouve aucune trace des filaments peu contrastés. Le même échantillon est poli mécaniquement sur le papier 00 paraffiné puis soumis à un nouveau polissage, cette fois avec l'électrolyte "Peroc", en deux stades de 45 secondes chacun. Le résultat (fig. 19B) est pratiquement identique au précédent. En aucun cas n'apparaissent les fossés et les piqures d'attaque sélective que produisaient les mêmes conditions de polissage sur la section de la billette (fig. 6b).

Les résultats des examens de la section de tôle peuvent se résumer comme suit.

(i) Les couches superficielles, jusqu'à une profondeur de l'ordre de 0,15 à 0,20 mm con-

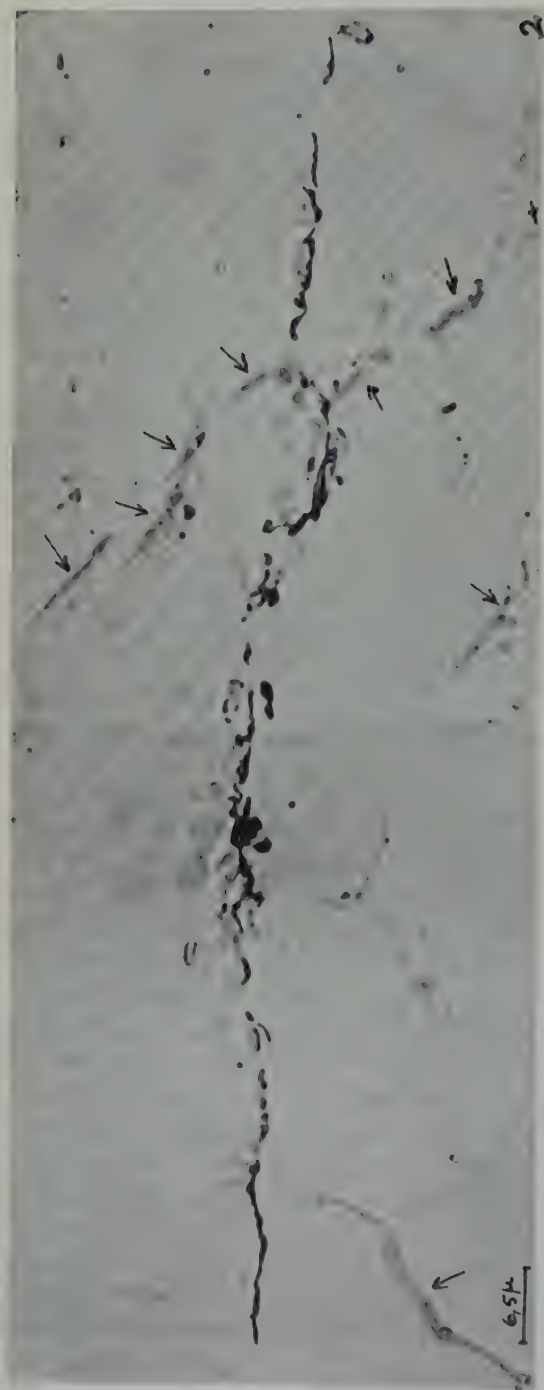


Fig. 12. Champ encadré en bas sur la fig. 10 (c). $\times 1600$.

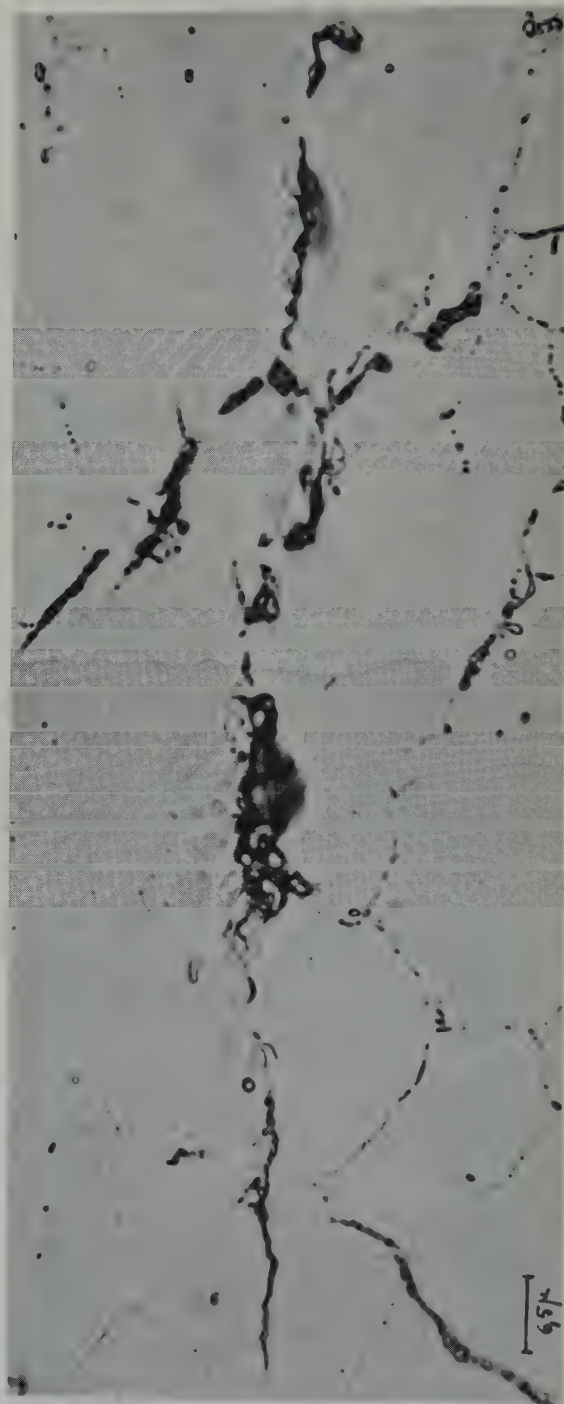


Fig. 13. Champ de la fig. 12 après oxydation anodique. $\times 1600$.

Fig. 14. Billette Z-81 de fusion en atmosphère d'argon. Polissage électrolyte "Buper", puis 30 sec avec l'électrolyte "Peroc". $\times 160$.

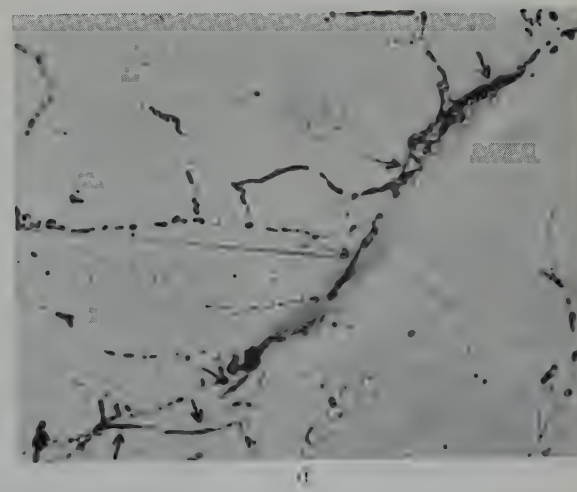
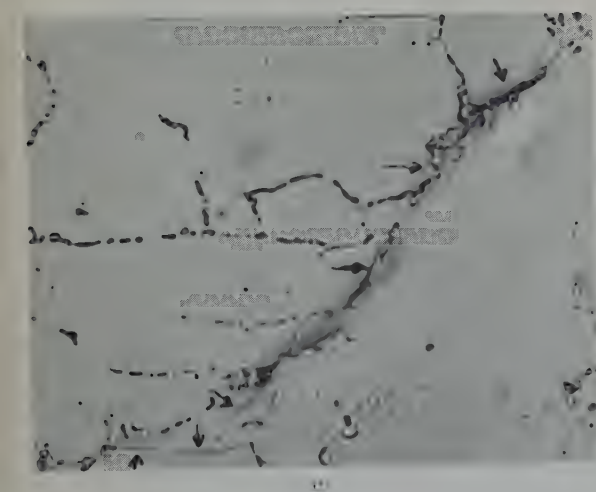
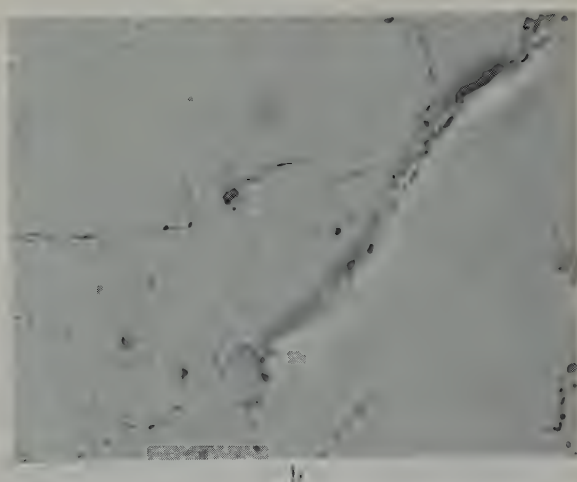
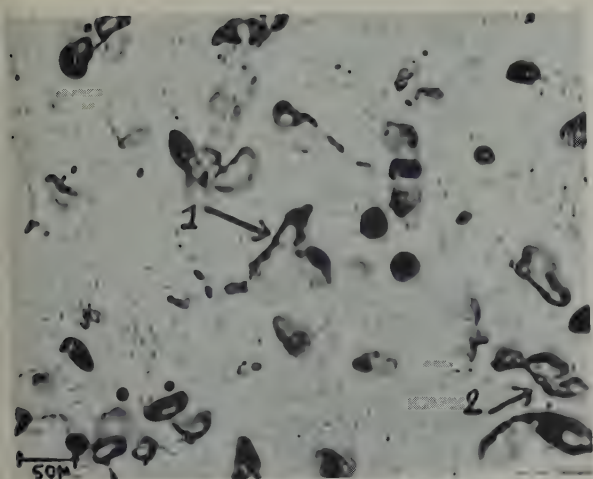
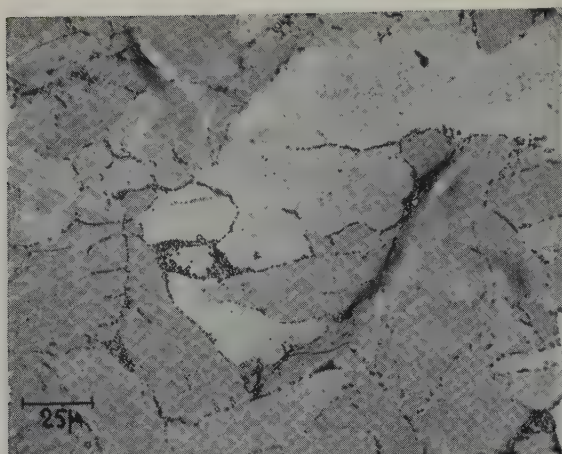
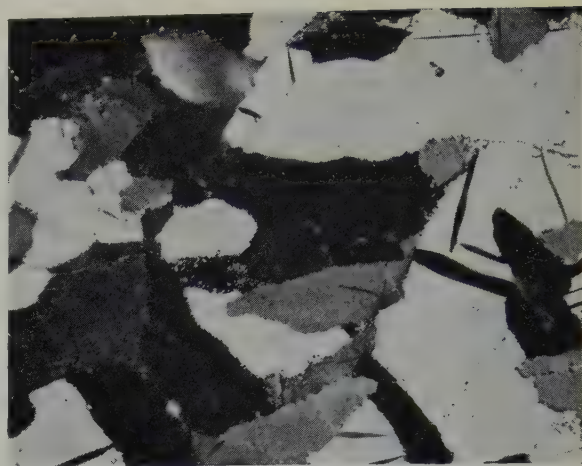


Fig. 15. Endroit repéré par la flèche 1 sur la fig. 14. (a) Même état que fig. 14; (b) Polissage supplémentaire 30 sec avec l'électrolyte "Buper"; (c) Polissage supplémentaire 30 sec avec l'électrolyte "Buper"; (d) Oxydation anodique. $\times 900$.



a



b

Fig. 16. Même surface et même région que fig. 15 (d). (a) Fond clair; (b) Lumière polarisée. $\times 400$.

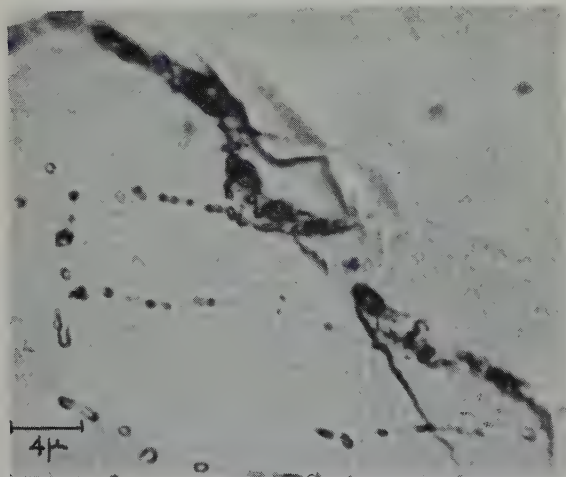


Fig. 17. Même surface que fig. 15 (d). Endroit repéré par la flèche 2 sur la fig. 14. $\times 2500$.

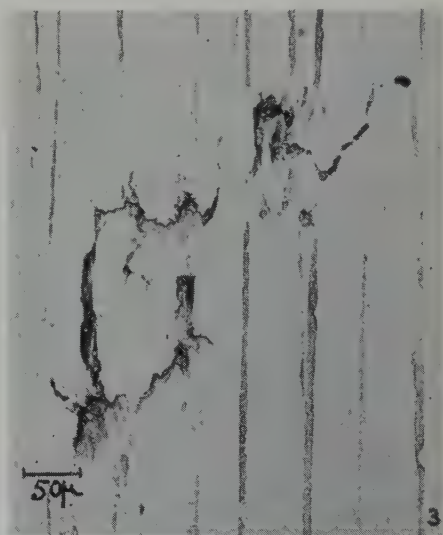


Fig. 18. Tôle Z-82 T brute de laminage. Réplique au vernis prise sur l'une des faces (Direction du laminage parallèle au grand côté). $\times 160$.

tiennent de longs et larges filaments noirs, plus ou moins sinueux, parallèles à la direction de laminage (fig. 20).

(ii) Des filaments de même orientation générale existent dans toute l'épaisseur de la tôle. Ils se distinguent des précédents par leur grande finesse et par un morcellement fréquent en tronçons distincts (fig. 21a).

(iii) Les forts grossissements optiques prouvent que ces fins éléments étirés ne peuvent être assimilés à des fissures ou décohésions, mais

bien à des constituants de la microstructure. D'ailleurs, ils sont toujours étroitement associés à des stries ou bandes dont ils constituent, en quelque sorte, des exagérations locales (figs. 22 et 23).

(iv) Les volumineux filaments localisés dans les couches superficielles ne correspondent pas non plus à des solutions de continuité franches. En effet, des fissures seraient ouvertes par le polissage et apparaîtraient aux forts grossissements comme des fossés uniformément noirs.

Or, une mise au point correcte, qui coïncide d'ailleurs avec la meilleure netteté des détails de la matrice, laisse entrevoir des contrastes internes, malheureusement mal reproduits sur les photographies. De plus, ces larges filaments comportent souvent de fines ramifications et ils se développent toujours au sein d'une matrice striée (fig. 24).

(v) Les microconstituants ponctuels sont moins nombreux et distribués autrement que dans la billette. Ils s'alignent parallèlement à la direction du laminage et la majorité d'entre eux se situent sur les bords sombres des bandes

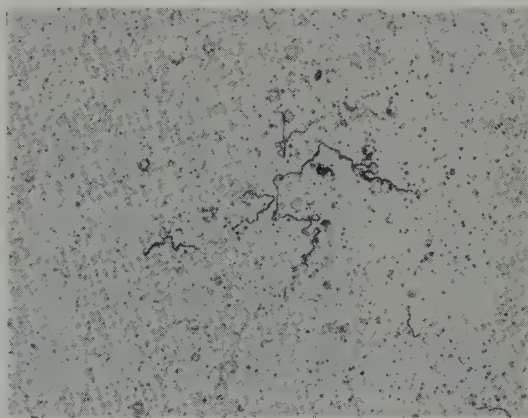
de la matrice dont ils suivent ainsi toutes les sinuosités (figs. 22 et 24).

(vi) La comparaison des figures 22, 23 et 24 confirme que les électrolytes "Buper" et "Peroc" sont pratiquement équivalents du point de vue des aspects micrographiques révélés. La seule différence pourrait être une légère tendance du second à extraire de la matrice certains microconstituants ponctuels (cf. figs. 22 et 23).

(vii) Les contours des grains discernables aux observations en fond clair dessinent une cristallisation équiaxiale qui apparaît encore mieux sous la lumière polarisée. Ce mode



a



b

Fig. 19. Tôle Z-82 T. Même face que fig. 18; (a) Abrasion et polissage 80 sec avec l'électrolyte "Buper"; (b) Abrasion et polissage 80 sec avec l'électrolyte "Peroc". $\times 160$.

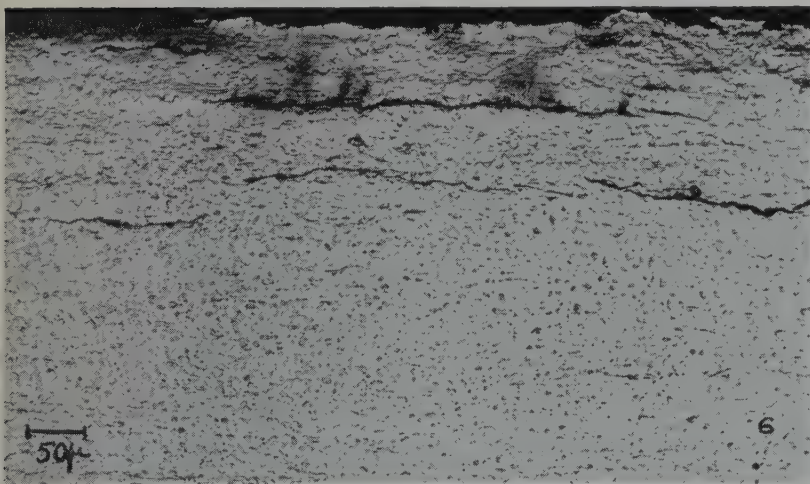


Fig. 20. Tôle Z-82 T. Section droite en long polie 20 sec avec l'électrolyte "Peroc". (Direction du laminage parallèle au grand côté.) $\times 160$.

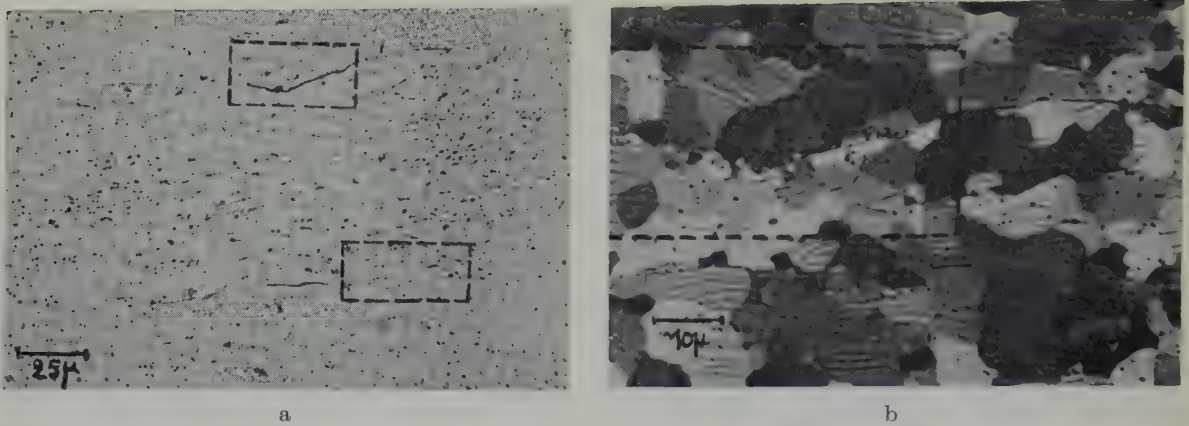


Fig. 21. Spécimen de la fig. 20 après polissage supplémentaire de 15 sec avec l'électrolyte "Buper". Région vers la raie-épaisseur de la tôle. (a) $\times 400$, fond clair; (b) $\times 1000$, lumière polarisée, encadré à gauche le champ encadré vers le haut sur (a). (Direction de laminage parallèle au grand côté).

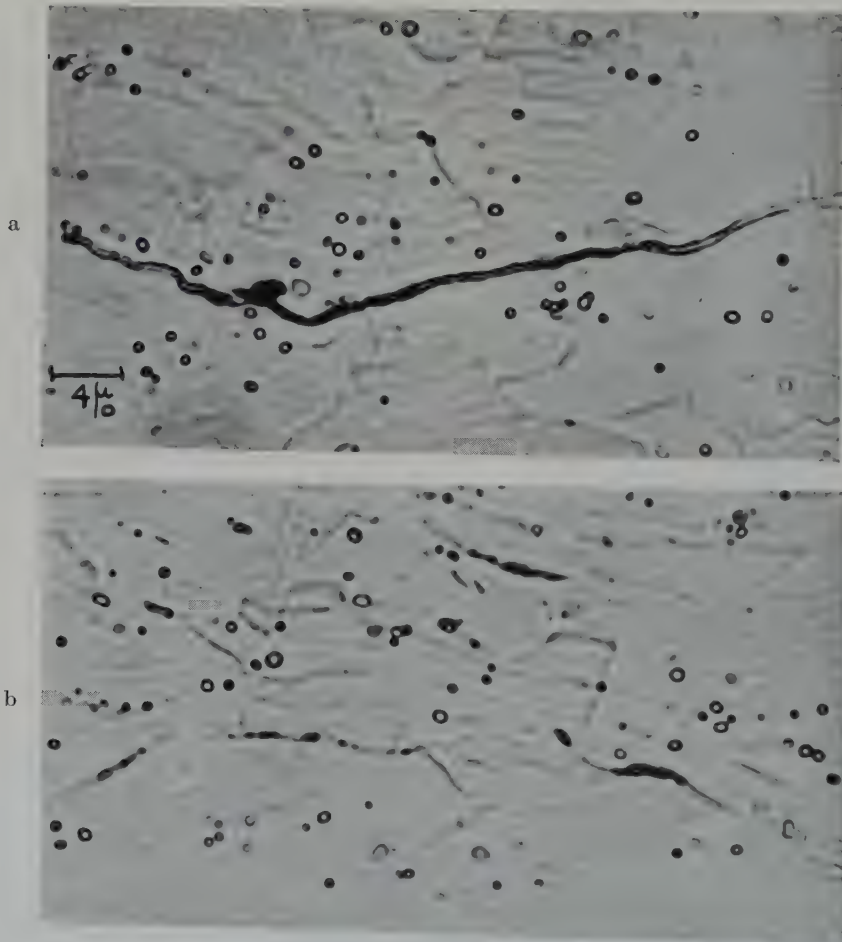


Fig. 22. Même spécimen que fig. 21. (a) et (b) correspondent respectivement aux champs encadrés vers le haut et vers le bas sur la fig. 21 (a). (Direction de laminage parallèle au grand côté). $\times 2500$.

d'illumination fait également bien ressortir les stries dans la matrice, et elle permet de reconnaître la nature intergranulaire de la plupart des fins filaments (fig. 21b).

5.2. TOLE REFERENCE Z-105-T

Provenant de la billette américaine Z-105 forgée à partir d'un lingot de fusion sous vide et laminée à la même épaisseur et dans les mêmes conditions que Z-82-T, cette tôle ne présente aucune trace de défauts superficiels macroscopiques.

Sa microstructure sur section en long est bien du type attendu du corroyage de la structure de forge (cf. figs. 25a et 1). Comme pour cette dernière, on note les effets respectifs des deux

électrolytes, à savoir: dans le cas du polissage avec le "Peroc" une moins bonne définition des microconstituants précipités et une certaine attaque de la matrice (fig. 25b). Il n'existe, d'autre part, aucun indice d'éléments filamenteux.

L'examen en lumière polarisée montre une texture assez confuse de fibres allongées dans la direction du laminage (fig. 25c).

5.3. TOLE REFERENCE Z-A 2 D-127

Ainsi que l'indique le tableau 1 elle provient de la transformation d'un lingot élaboré par refusion sous vide, en France, de trois billettes américaines d'origine fusion sous argon. Comme la précédente cette tôle est macroscopiquement

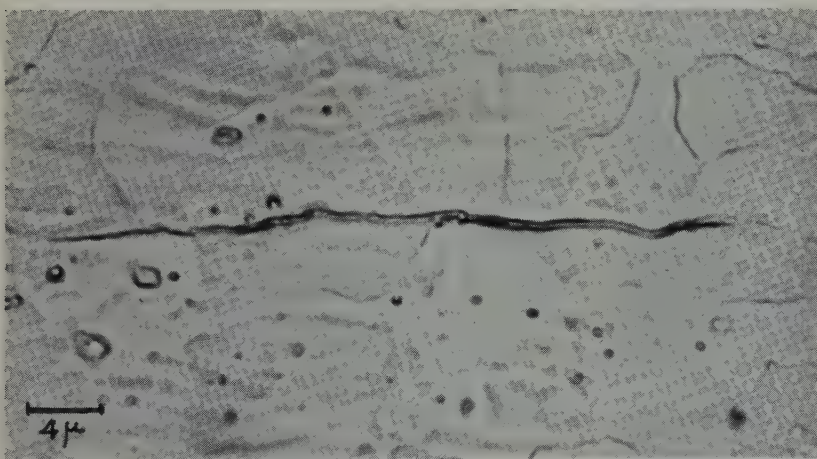


Fig. 23. Même spécimen que fig. 20 vers la mi-épaisseur de la tôle. (Direction de laminage parallèle au grand côté). $\times 2500$.

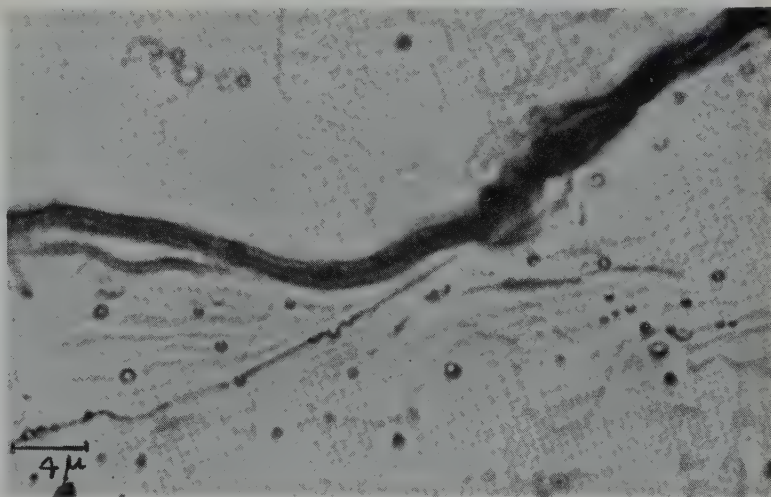
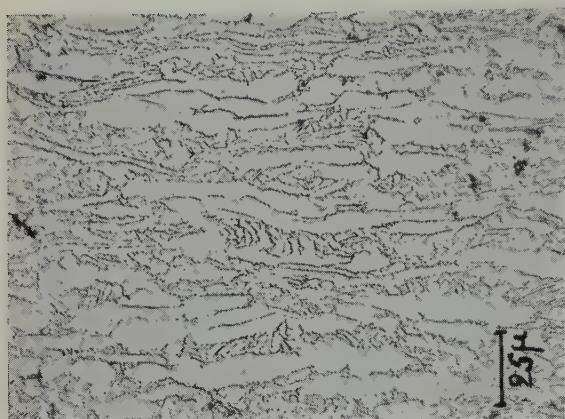
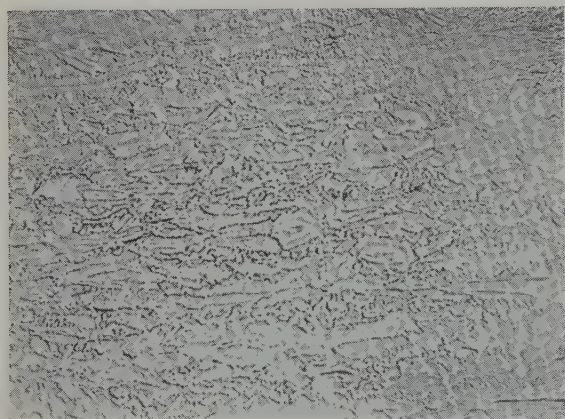


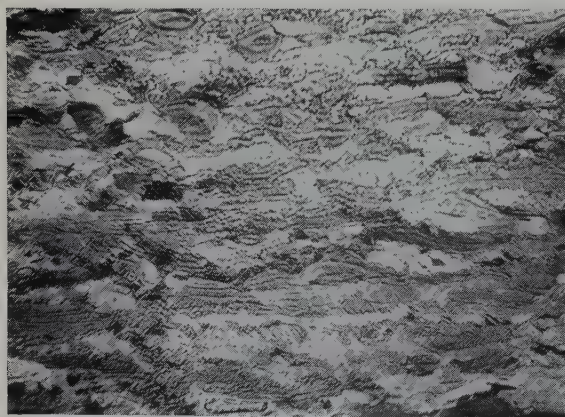
Fig. 24. Même spécimen que fig. 21 et fig. 22. A 0,02 mm environ sous la surface de la tôle. (Direction de laminage parallèle au grand côté). $\times 2500$



a



b



c

Fig. 25. Tôle Z-105 T. Section droite en long (direction du laminage parallèle au grand côté). (a) Polissage électrolyte "Buper"; (b) et (c) Polissage électrolyte "Peroc", fond clair et lumière polarisée. (Direction de laminage parallèle au grand côté). $\times 400$.

parfaitement saine, mais étant donné que, du point de vue structural, les deux billettes correspondantes ne sont pas identiques (cf. figs. 1a et 2a) nous devons retrouver quelque différence entre leurs produits de laminage respectifs.

La figure 26a, obtenue à partir de la section en long polie avec l'électrolyte "Peroc" montre effectivement une proportion plus faible et une meilleure dispersion des microconstituants, d'une part, l'absence d'attaque sur la matrice, d'autre part. Corrélativement la cristallisation, bien qu'encore de type fibreux, est mieux définie (fig. 26b).

6. Discussion

Les faits essentiels qui se dégagent de l'étude métallographique des billettes et de certaines des tôles correspondantes se résument comme suit:

(i) Les six billettes forgées à partir des lingots élaborés au four électrique à électrode consommable sous atmosphère d'argon à la pression normale, possèdent des caractéristiques structurales identiques qui n'existent dans aucune des trois billettes provenant des lingots de fusion au four à vide.

(ii) Ces caractéristiques concernent l'existence de deux types d'hétérogénéités qui ont en commun leur forme générale filamenteuse ainsi qu'une remarquable sensibilité vis-à-vis des conditions de polissage électrolytique et de l'oxydation anodique.

(iii) La surface de la tôle tirée de l'une des billettes de fusion sous argon est riche en défauts superficiels connus sous le nom générique de "stringers". Ces défauts ne sont qu'un aspect particulier d'hétérogénéités, également filamenteuses, mais beaucoup plus discrètes, présentes dans toute l'épaisseur de la tôle.

(iv) Aucun indice de tels défauts superficiels et hétérogénéités internes n'apparaît dans les deux tôles provenant de billettes de fusion sous vide.

Ces résultats prouvent une relation univoque entre la microstructure typique de chacune des deux catégories de billettes et les caractéristiques

du laminé résultant. En d'autres termes les "stringers" dérivent directement des hétérogénéités structurales spécifiques de l'alliage élaboré en atmosphère d'argon. Il est important, d'ailleurs, de souligner que toute intervention d'un facteur accidentel doit être exclue, car la refusion sous vide de trois billettes d'origine fusion sous argon a fourni un produit de forge et une tôle sans hétérogénéités anormales.

Le problème se pose donc maintenant d'essayer de préciser la nature des hétérogénéités en cause et d'expliquer leur disparition dans l'alliage élaboré au four à vide.

6.1. NOTIONS ACTUELLES SUR LA NATURE DES STRINGERS

Depuis quelques années la littérature américaine contient une abondante bibliographie relative aux défauts rencontrés dans les produits de transformation des alliages Zircaloy-2 et Zircaloy-3 †, et désignés sous le nom de "stringers", c'est-à-dire filaments.

Cette désignation s'appliquait tout d'abord aux taches de corrosion brunâtres ou grisâtres

† Ces deux alliages diffèrent par leurs teneurs en étain et en fer qui sont respectivement égales à 0,25 % et 0,25 % pour le Zircaloy-3, à 1,45 % et 0,125 % pour le Zircaloy-2. Ce dernier renferme en outre 0,10 % de chrome et 0,05 % de nickel.

de forme allongée, apparaissant sur la surface couverte uniformément d'oxyde noir des tôles après plusieurs centaines d'heures d'exposition à l'eau surchauffée à 400° C.

Lorsque fut reconnu, par la suite, que ces produits d'attaque sont associés à la présence d'hétérogénéités dans le matériau, celles-ci reçurent également le nom de "stringers", et pour les distinguer des premiers, le qualificatif "structuraux" leur est maintenant généralement ajouté.

La nature exacte des "stringers" présents dans la structure des produits tirés des lingots de fusion sous atmosphère d'argon a été, et demeure d'ailleurs encore, controversée. Considérés initialement comme des composés intermétalliques⁸), l'opinion actuelle la plus répandue admet qu'il s'agit de porosités gazeuses ("gas voids") préexistantes dans le lingot de départ et dont les parois sont tapissées de précipités ou inclusions formés au refroidissement, ou pendant les transformations ultérieures²). De forme plus ou moins arrondie dans le lingot, ces porosités acquièrent l'aspect de filaments lors du travail mécanique de forge et de laminage. Le fait que leur cicatrisation ne se fait pas est attribué à la fragilité des précipités inclus et aussi à la pression des gaz.

Plusieurs constatations ont été avancées à



a



b

Fig. 26. Tôle Z-A 2 D 127. Section droite en long (direction du laminage parallèle au grand côté). Polissage électrolyte "Peroc". (a) fond clair; (b) même champ en lumière polarisée. (Direction du laminage parallèle au grand côté). $\times 400$.

l'appui de cette interprétation. Par exemple, les "stringers structuraux" dans une tôle laminée à 92 % ne sont pas éliminés par un traitement de plusieurs heures vers 1000° C suivi de trempe à l'air. En revanche, les précipités disposés initialement sur les contours des grains primaires se redistribuent aux joints des cristaux actuels²⁾.

On insiste aussi sur le fait qu'un tel traitement peut réussir à empêcher l'apparition des "stringers de corrosion", probablement "parce que les gradients de concentration existant sur les parois ou autour des vides pendant le travail à chaud disparaissent par homogénéisation"²⁾.

En définitive, les "stringers structuraux" ne seraient pas de simples impuretés réparties sur les contours des gros grains dendritiques du lingot et alignées lors des transformations, mais ils traduiraient une association porosités-micro-constituants. De cette association seuls les microconstituants interviendraient d'une manière plus ou moins directe dans l'apparition ultérieure des stringers de corrosion.

Une autre preuve avancée par J. D. Grozier *et al.*²⁾ en faveur du rôle déterminant des porosités gazeuses en tant que piège à micro-constituants est le fait que "le problème des stringers de corrosion ne se pose pas avec les produits tirés des lingots de Zircaloy-2 fondus sous vide qui ne renferment, précisément, aucune porosité". Or, disent en substance les auteurs "si des constituants indépendants étaient responsables, ils seraient observés dans l'alliage élaboré sous vide, ce qui n'est pas le cas". Nous verrons plus loin (§ 6.5) qu'une telle interprétation néglige certains facteurs propres aux deux techniques de fusion.

Il faut bien dire, enfin, que tous les métallographes n'adoptent pas sans critique les conclusions exposées ci-dessus. Ainsi Picklesimer estime toujours que le rôle fondamental attribué aux "gas voids" reste à démontrer³⁾.

6.2. IMPORTANCE DE LA NATURE DES SPECIMENS ET DES CONDITIONS DE PREPARATION DE LEUR SURFACE

Les données relatives à la définition, à l'origine et à la nature des "stringers" dits

structuraux reposent toutes sur des observations micrographiques. La confiance que l'on doit leur accorder tient à la fois à la nature des échantillons étudiés et aux méthodes de préparation des surfaces.

Du point de vue de l'interprétation des anomalies structurales décelées dans les tôles finales, la structure des billettes est sans doute plus intéressante à connaître que celle des lingots de départ. En effet, le forgeage modifie vraisemblablement les formes des défauts éventuels de nature purement physique (porosités, soufflures). Par conséquent, toute relation entre les caractéristiques de la tôle d'une part, et de l'état de fonderie, d'autre part, apparaîtra plus clairement si l'on considère l'étape intermédiaire que constitue la billette forgée.

Or, la grande majorité, pour ne pas dire la totalité, des travaux publiés sont relatifs aux tôles définitives, ou à des stades intermédiaires assez avancés du laminage à chaud correspondant, par exemple, aux épaisseurs de 19, 13 et 7 millimètres. Plutôt rares sont les observations sur les lingots et les produits bruts de forge ne sont jamais mentionnés.

Dans ces conditions une corrélation univoque entre l'état de fonderie et les anomalies des laminés paraît difficile à établir. Ceci vaut tout particulièrement pour les "stringers", car la conception selon laquelle il s'agit d'un simple allongement des porosités gazeuses du lingot néglige les effets probables de la déformation mécanique, de la température et même du milieu ambiant oxydant sur les microconstituants de la structure.

En ce qui concerne les conditions de préparation des surfaces soumises aux examens, il est assez surprenant de constater que les plus récents mémoires consacrés à la métallographie générale du zirconium et de ses alliages ignorent l'électropolissage et décrivent l'emploi exclusif du polissage mécanique et de l'attaque fluonitrique^{9,10)}. Ce sont, effectivement, ces procédés "traditionnels" qui figurent dans les études sur les "stringers", tout au moins quand les auteurs précisent les modes opératoires, ce qui n'est pas toujours le cas.

C'est à peine si nous devons souligner les sérieuses réserves que suscite, d'une manière générale, l'interprétation des aspects obtenus avec le polissage mécanique suivi d'attaque chimique lorsqu'il s'agit d'établir une distinction entre des cavités réelles et des microconstituants, et *a fortiori*, d'affirmer leur association. L'abrasion a des effets multiples (arrachement et morcellement des éléments fragiles, camouflage plus ou moins complet des vides, etc. . . .). De leur côté, des réactifs agressifs — et les mélanges fluonitriques le sont à coup sûr vis-à-vis du Zircaloy — provoquent de véritables corrosions.

S'il est admissible que des conditions de polissage électrolytique incorrectes puissent conduire au même genre de difficultés, nous sommes en mesure d'affirmer que le processus anodique est toujours adaptable à tel ou tel cas particulier. A ce propos la technique et les électrolytes "Ellopol" se sont avérés d'une remarquable souplesse †.

6.3. ORIGINE STRUCTURALE DES "STRINGERS"

Nos expériences apportent de sérieux arguments aux critiques que soulèvent les études métallographiques publiées jusqu'à présent.

Tout d'abord, les défauts macroscopiques observés dans les couches superficielles de la tôle Z-82 T sont manifestement un aspect particulier des "stringers" typiques présents dans toute l'épaisseur. Or, leur grand nombre est en désaccord avec l'hypothèse d'une hérédité remontant aux porosités de fonderie, hypothèse qui exigerait que le lingot initial eût été une véritable éponge. En fait, l'observation des sections de toutes les billettes d'origine fusion sous argon, polies sous les conditions optimales avec l'électrolyte "Buper", ne révèle qu'une quantité infime de défauts assimilables à de vraies porosités: ce sont de très petites cavités de forme arrondie, aspect très différent des filaments qui, eux, sont toujours très nombreux.

L'origine structurale de ces filaments n'est donc pas douteuse. Si l'on suppose que les hétérogénéités chimiques qu'ils représentent se

trouvaient dans le lingot, associées aux porosités gazeuses, il faut admettre aussi que ces dernières n'existent plus en quantité appréciable après le travail de forge.

Nous avons vu que dans les billettes la micrographie révèle deux types d'hétérogénéités dont l'aspect filamenteux les différencie des microconstituants normaux précipités sur les contours des grains.

Le type le plus apparent, grâce à son fort contraste sur la matrice, forme soit des alignements plus ou moins morcelés dessinant un réseau orienté par le corroyage (figs. 10 et 12), soit des domaines relativement volumineux et continus (fig. 7). Il s'agirait de ségrégations d'impuretés insolubles intergranulaires et interdendritiques héritées directement du lingot initial.

Les filaments du second type sont plus nombreux et moins orientés que les précédents, tout en leur étant, cependant, parfois associés (figs. 7 et 12). Très souvent localisés sur les contours des grains actuels (figs. 12 et 15), nous supposons qu'ils représentent des constituants partiellement miscibles séparés au cours du refroidissement du lingot et de la billette forgée. Une caractéristique très importante du gradient de concentration résultant est son extrême sensibilité aux conditions du polissage et au processus d'oxydation anodique. En effet, l'électrolyte "Peroc" provoque la dissolution sélective du constituant et de la matrice environnante, tandis qu'après formation du film d'oxyde les différences d'aspect entre les deux types d'hétérogénéités tendent à s'estomper (voir par exemple fig. 7). Néanmoins, à l'état oxydé, le premier se distingue du second par des indices de sous-structure, d'ailleurs non résolue sous les grossissements optiques maximaux. L'effet sélectif de l'oxydation anodique peut aussi se porter sur la matrice entourant les hétérogénéités du premier type (fig. 13), ce qui traduit à nouveau l'existence de gradients de concentration. Ce genre de phénomène est instructif du point de vue de la nature chimique des filaments discutée plus loin.

Si nous considérons maintenant la tôle obtenue

† Un exemple récent est celui de la détection des microporosités dans l'aluminium et ses alliages ¹¹⁾.

à partir d'une billette dont la structure vient d'être décrite et interprétée, trois faits fondamentaux se dégagent:

(i) Les filaments encore présents sont à la fois plus abondants et plus volumineux dans les zones s'étendant jusqu'à 0,15–0,20 mm environ sous la surface (fig. 20).

(ii) La microstructure a perdu toute sensibilité aux conditions du polissage et à l'oxydation anodique.

(iii) Les microconstituants normaux, dont le nombre a d'ailleurs considérablement diminué, ne sont pas séparés aux contours des grains actuels, mais s'alignent sur les stries ou bandes sinueuses qui ont envahi toute la matrice (fig. 22).

Ces trois faits sont les conséquences logiques attendues des effets mécaniques et thermiques du laminage, auxquels s'ajoute un facteur chimique pour ce qui est des couches superficielles.

Nous admettons, la preuve en sera apportée plus loin, que les gros et longs "stringers" localisés près de la surface résultent de la déformation et de la corrosion sèche simultanées des filaments existant dans la billette de départ, et peut-être aussi des portions environnantes de la matrice sensibilisées à l'oxydation.

Dans toute l'épaisseur comprise entre les deux couches superficielles, les fins filaments continus ou morcelés (figs. 22 et 23) résulteraient de l'allongement, de l'écrasement et de la fragmentation des plages plus ou moins volumineuses d'hétérogénéités dites du premier type, c'est-à-dire formées principalement d'impuretés insolubles. Cependant, les caractères rappelés ci-dessus en (i) et (ii) traduisent une nette homogénéisation vis-à-vis de l'état antérieur. C'est ainsi que les hétérogénéités dites du second type tendraient à passer en solution.

Néanmoins la présence des bandes ou stries sinueuses au sein de la matrice, et surtout leur relation incontestable avec les filaments et microprécipités normaux suggèrent la persistance de certains gradients de concentration. La nature exacte de ces bandes n'est pourtant pas claire. Si leur allongement global selon la

direction du laminage est bien la preuve du rôle de la déformation plastique, le fait qu'elles changent fréquemment d'orientation et d'intensité en passant d'un grain à l'autre de la cristallisation actuelle reste assez troublant. Une explication pourrait faire intervenir l'influence de la concentration en éléments bêta-gènes (Fe, Ni, Cr) sur la cinétique de la transformation $\alpha \rightleftharpoons \beta$.

Le degré de finesse des aspects typiques révélés à l'intérieur de la tôle justifierait l'observation sous les grossissements du microscope électronique. La technique de la double empreinte vernis nitrocellulosique-carbone¹²⁾ a donc été appliquée à la section polie ayant fourni les images optiques (fig. 22). Encore qu'incomplets, les premiers résultats confirment d'une manière indiscutable que les minces et longs filaments (fig. 27a) ne sont pas des discontinuités de la matière, mais appartiennent bien à la microstructure. La figure 27b donne une idée de l'extrême petitesse des éléments constitutifs. Certaines régions contiennent des détails encore plus ténus (fig. 27c, d) qui correspondent probablement à des aspects optiques du genre de ceux visibles sur la figure 22b. On devine également des alignements diffus dans la matrice ponctuée qui pourraient peut-être indiquer des segments de bandes. Un autre fait intéressant est la fragmentation des microconstituants normaux que le microscope optique montrait sous forme de points à contour fermé.

D'un point de vue général, ces micrographies électroniques démontrent la qualité du polissage. La preuve qu'une attaque chimique fausse complètement les aspects a été apportée par une récente observation indépendante de N. Azam¹³⁾ sur la section longitudinale d'une tôle de même origine que Z-82 T. Après polissage électrolytique (électrolyte "Buper"), une partie est attaquée par le réactif fluonitrique et une autre soumise au bombardement ionique (atmosphère d'argon 10^{-1} mm Hg, 4000 V, 3 mA, 10 min, incidence normale). La figure 28a indique une intense corrosion du filament et d'une large portion de la matrice environnante, confirmant ainsi les critiques émises plus haut

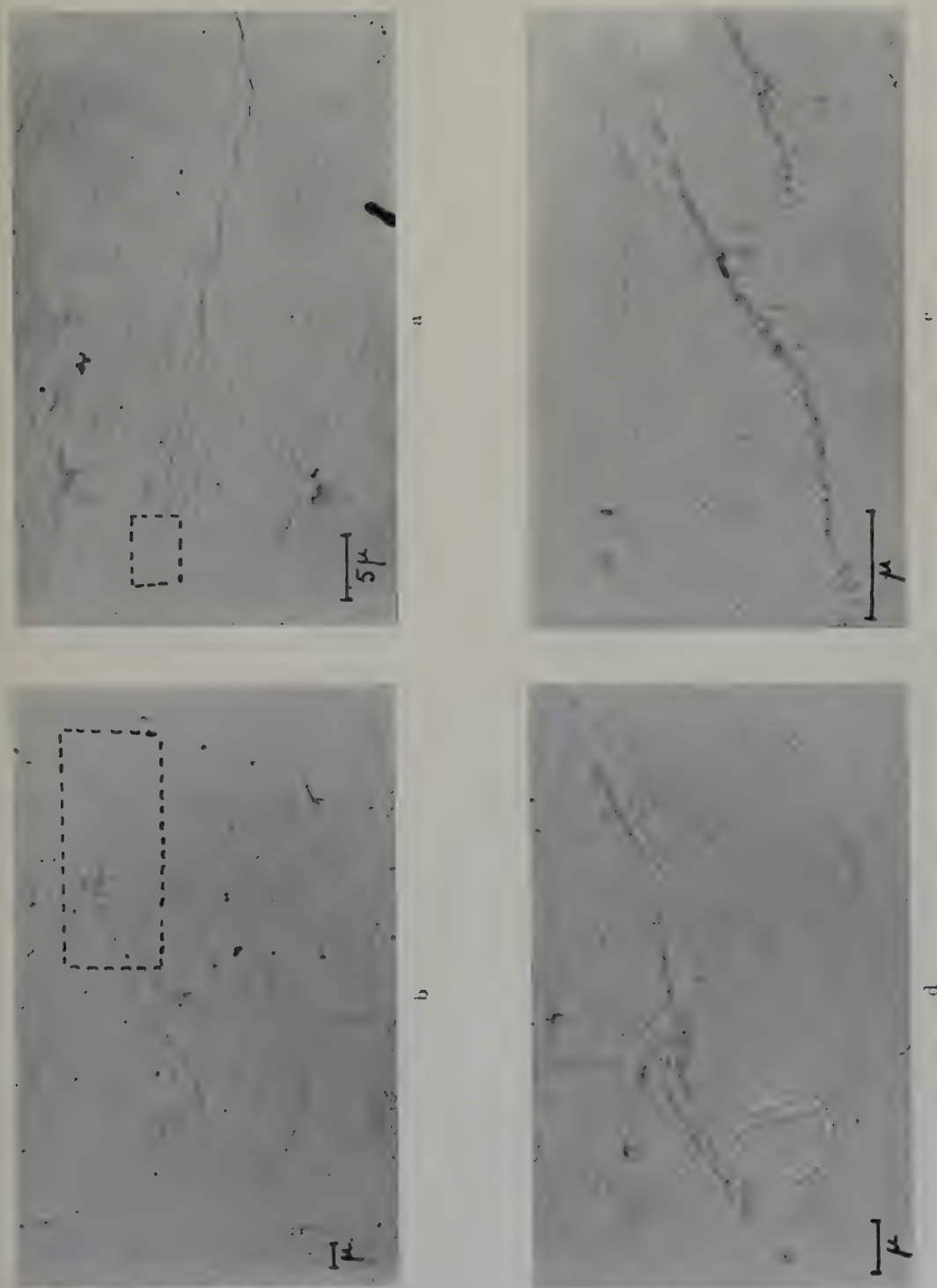


Fig. 27. Micrographes électroniques vers la mi-épaisseur de la section de la tôle Z 82 T (fig. 20). (a) $\times 2000$; (b) $\times 16\ 000$, champ encadré sur (a); (c) $\times 8000$, champ encadré sur (c). (Direction du laminage parallèle au grand côté).

à propos de la métallographie "traditionnelle" des alliages de zirconium (voir § 6.2). Au contraire, l'attaque par bombardement respecte la géométrie de l'hétérogénéité, mais ne fait pas apparaître les fins détails révélés par le polissage électrolytique.

6.4. NATURE CHIMIQUE DES STRINGERS

Les seules constatations d'ordre métallographique sont évidemment impuissantes à préciser la composition des divers genres d'hétérogénéités filamenteuses présentes dans les billettes et les tôles d'origine fusion en atmosphère argon.

Certains renseignements ont été apportés par l'analyse de fragments détachés à la microfraise¹⁴) et par des diagrammes de rayons X exécutés dans notre laboratoire par Mme. A. R. Weill, mais ils concernent exclusivement les couches superficielles de la tôle Z-82 T renfermant les filaments volumineux.

Nous rappelons tout d'abord que dans la doctrine qui attribue les "stringers" à des porosités gazeuses tapissées d'un constituant intermétallique, celui-ci est généralement considéré comme étant la phase θ SnZr_4 qui peut dissoudre jusqu'à 10 % de fer. La microsonde électronique aurait effectivement décelé 8 à 10 % de fer dans les inclusions filamenteuses¹⁵).

M. Jean a soumis à des microdosages colorimétriques les copeaux prélevés, d'une part dans les "stringers" superficiels de la tôle Z-82 T, et, d'autre part, dans les régions saines à cœur du même échantillon.

Le tableau 3, qui contient aussi les résultats de l'analyse de la billette Z-82, fait ressortir un enrichissement appréciable en fer des zones contaminées, sans que les autres éléments, l'étain en particulier, ne montrent de variation vraiment significative.

Le même auteur a également dosé les gaz dans un large "stringer". Par rapport aux teneurs dans la billette d'origine, l'oxygène présente une nette augmentation (2000 ppm contre 100 à 1144 ppm), tandis que l'hydrogène et l'azote ne changent pas.

TABLEAU 3¹⁴)

Concentration de quelques éléments dans les produits Z-82 et Z-82 T

Elément	Billette Z-82	Tôle Z-82 T	
		"Stringers" superficiels	A cœur
Sn	1,36 %	1,30 %	1,25 %
Fe	1220 ppm	2680 ppm	1600 ppm
Cr	1000 ppm	1110 ppm	1100 ppm
Ni	555 ppm	670 ppm	500 ppm

Afin d'essayer de pousser plus loin l'identification de la nature chimique des volumineux filaments localisés jusqu'à 0,15–0,20 mm environ sous la surface de la tôle Z-82 T (fig. 20) des analyses ont été effectuées par Mme A. R. Weill avec un diffractomètre à compteur (rayonnement monochromatique du cuivre¹⁷). Quatre séries d'enregistrements correspondent respectivement à la surface brute de laminage et après élimination (par abrasion douce sur les papiers d'émeri mouillés à l'eau) d'épaisseurs égales à 0,05–0,10 et 0,15 mm. A titre de contrôle, la surface à l'état brut de la tôle Z-105 T (de provenance fusion sous vide) est examinée dans les mêmes conditions.

Par rapport à ce témoin les diagrammes de la première série contiennent une réflexion supplémentaire très visible, située à $14^\circ 5'$, qui, d'après les références de l'Index A.S.T.M., appartient au diagramme de l'oxyde ZrO_2 dont c'est la raie la plus forte. Cette réflexion anormale diminue d'intensité dans les enregistrements des deux séries suivantes, c'est-à-dire après élimination de 0,05 et 0,10 mm, et elle disparaît complètement sur la dernière série prise à 0,15 mm de profondeur sous la surface.

On a pu également reconnaître sur les diagrammes de la surface non abrasée des indices d'autres raies de ZrO_2 , telles que les réflexions à 12° et à $15^\circ 85'$.

Ces résultats confirment l'impression suggérée par la micrographie, à savoir que les volumineux filaments étirés dans les couches superficielles ne sont pas des discontinuités. Ils apportent, de plus, une précision quant à la nature du

composé inclus : c'est l'oxyde ZrO_2 . Les réflexions déduites de la structure cristallographique connue de la phase SnZr_4 ¹⁶⁾ n'ont été repérées sur aucun diagramme.

6.5. RELATION ENTRE LES CONDITIONS D'ELABORATION ET LA MICROSTRUCTURE DU ZIRCALOY-2

L'étude métallographique a prouvé que les hétérogénéités de forme générale filamenteuses, ou "stringers" selon la terminologie américaine, sont toujours présents dans les produits de transformation des lingots élaborés par fusion de l'alliage au four à électrode consommable en atmosphère d'argon. Puisqu'elles n'existent pas dans les billettes et tôles tirées des lingots de fusion sous vide, et que, d'autre part, les éléments constitutifs de l'alliage dans l'un et l'autre cas ne peuvent être mis en cause (la refusion au four à vide de billettes à "stringers" a donné des produits normaux), les facteurs responsables de l'apparition de ces hétérogénéités sont inhérents à la technique de la fusion en atmosphère.

Sans entrer dans les détails, il est sûr que les conditions d'un tel mode d'élaboration favorisent la pollution et contrarient l'homogénéisation.

(i) Non seulement l'alliage sera mal dégazé mais il subira une contamination par l'azote et l'oxygène d'un argon imparfaitement purifié.

(ii) Le refroidissement relativement rapide du bain fondu entraîne de grandes variations de concentration des éléments d'alliage et peut-être même une mise en solution incomplète de certains d'entre eux.

La fusion sous vide, au contraire, réalise un dégazage efficace et réduit les risques de pollution. A cet égard, de récentes analyses des gaz sur un grand nombre de billettes des deux origines sont assez probantes : les valeurs moyennes des teneurs en oxygène et azote passent respectivement de 1300 et 85 ppm pour la fusion en atmosphère à 582 et 37 ppm pour la fusion sous vide ¹⁴⁾. De son côté, un refroidissement moins rapide favorise la mise en solution complète et une bonne homogénéisation du bain.

Ces considérations technologiques paraissent

bien rendre compte des structures respectives des deux sortes de billettes et des anomalies structurales spécifiques de celles provenant des lingots élaborés au four en atmosphère d'argon.

Il est évident que les microconstituants normaux sont plus abondants et se séparent sous une forme eutectique beaucoup plus nette dans le cas de la fusion sous vide (cf. par exemple, figs. 1a et 6a), ce qui démontre à la fois une meilleure homogénéité du bain liquide et un refroidissement moins rapide.

En ce qui concerne les constituants anormaux d'aspect général filamenteux, nous admettons que les hétérogénéités à fort contraste sont pour la majeure partie des ségrégations de produits oxydés, tandis que les plages peu contrastées représentent plutôt le constituant intermétallique, conséquence de la mauvaise homogénéisation et du refroidissement rapide.

Une telle distinction, basée sur les caractères morphologiques observables sur la section polie, peut sembler assez subtile, étant donné l'extrême sensibilité à l'oxydation du constituant dit intermétallique et l'association assez fréquente des deux types. En tout cas l'un et l'autre préexistent à coup sûr dans le lingot d'origine. L'intervention de l'oxygène au cours du travail de forge est très vraisemblable mais ne doit intéresser que les couches superficielles. La preuve a été fournie par l'examen d'un spécimen prélevé avec la peau de forgeage dans la billette Z-83 : le polissage électrolytique révèle de nombreux filaments noirs, volumineux à leur départ de la peau et s'amenuisant à mesure qu'ils s'en éloignent. L'écroûtage qui précède la suite des transformations doit, en principe, retirer ces zones contaminées.

Pour des raisons évidentes, le processus d'oxydation sélective de l'hétérogénéité intermétallique va prendre une importance considérable pendant les trois chaudes de forgeage à 825° C et la première passe de laminage entre 825 et 700° C. A ce stade la tôle de 2,5 mm d'épaisseur subit cependant un sablage et un décapage destinés à éliminer 0,1 mm de chaque côté. Ces derniers traitements sont sans doute insuffisants, et en tout cas, la micrographie et

les rayons X révèlent qu'après le dernier laminage à 550° C et le recuit de 30 minutes à 650° C, suivis de sablage et de décapage, les filaments oxydés pénètrent jusqu'à 0,2 mm de profondeur sous chacune des deux faces.

Le rôle déterminant de l'oxygène atmosphérique, au point de vue de la naissance des filaments d'oxyde à partir des stringers structuraux, est prouvé par le fait que le filage direct d'une billette fournit un produit beaucoup moins riche en défauts superficiels que la tôle laminée¹⁴). Or, le filage s'effectue à une température moins élevée et à une plus grande vitesse que le laminage, le refroidissement étant, d'autre part, très rapide. De plus, et ce facteur est capital, l'alliage se trouve protégé du milieu ambiant par une gaine de verre ou de cuivre.

Si nous considérons maintenant les portions internes de la tôle non polluées par l'oxygène, la micrographie indique une évolution très nette par rapport à l'état initial billette. Les filaments sinueux à fort contraste qui persistent correspondent sans doute aux ségrégations insolubles (oxydes). L'absence de réactivité vis-à-vis de

l'électrolyte "Peroc" traduirait une certaine mise en solution des hétérogénéités du type constituant intermétallique. Toutefois, des gradients de concentration existent encore, puisque le réactif fluonitrique attaque la matrice autour des filaments (fig. 28a) qui sont eux-mêmes en relation évidente avec les stries ou bandes sinueuses attribuées à des variations de composition de la solution solide (figs. 22 et 23).

La diminution très sensible du nombre des microconstituants normaux et leur alignement parallèlement à la direction du laminage sont aussi des conséquences du travail à chaud. Ces effets se manifestent également dans les tôles tirées des billettes de fusion sous vide, mais les stries étant alors beaucoup moins marquées, nous pouvons supposer que leur intense développement dans la tôle à "stringers" est liée à la déformation et à la dissolution partielle des très nombreuses plages du constituant intermétallique anormal.

Pour résumer ces discussions des aspects micrographiques comparés, nous dirons que les "stringers" rencontrés exclusivement dans les

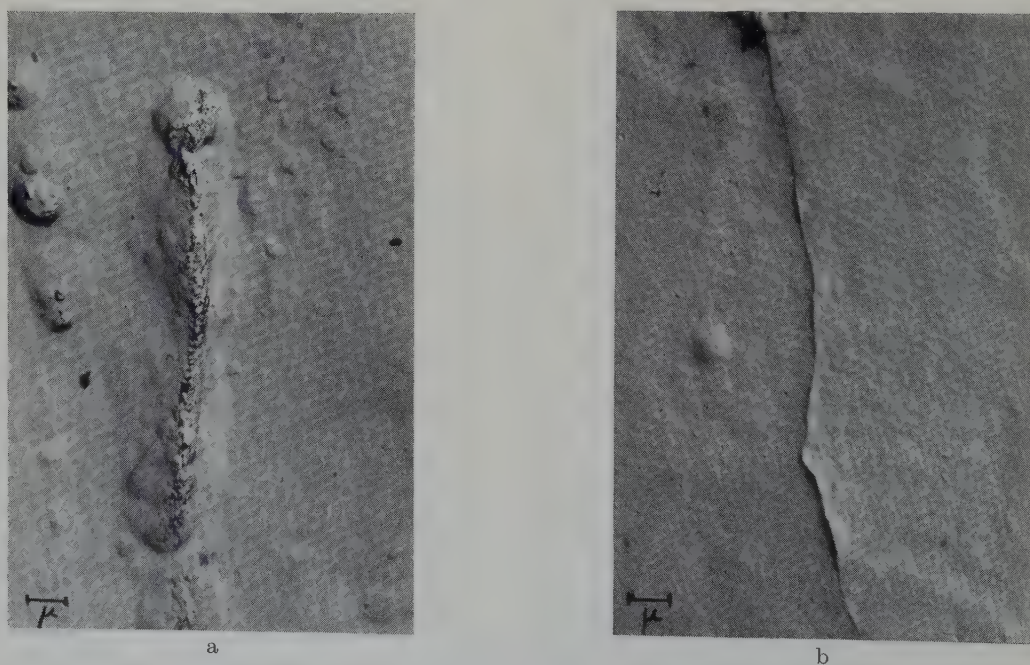


Fig. 28. Micrographies électroniques vers la mi-épaisseur d'une section droite, en long, de tôle de même origine que Z-82 T. Polissage électrolyte "Buper". (a) Attaque au réactif fluonitrique; (b) Attaque ionique. (Direction du laminage parallèle au grand côté). $\times 5000$. [D'après N. Azam¹³).]

produits de transformation de l'alliage élaboré en atmosphère d'argon dérivent d'hétérogénéités structurales préexistant dans les lingots de départ. Ces hétérogénéités évoluent sous l'action des facteurs de nature mécanique et thermique, auxquels s'ajoute un phénomène chimique d'oxydation sélective limité aux couches superficielles. La micrographie démontre, d'autre part, que le rôle généralement attribué aux porosités gazeuses des lingots ne peut être retenu, car il repose sur les résultats de techniques métallographiques non adaptées au problème.

Pour terminer nous rappellerons que du point de vue de la cristallisation, la tôle à stringers (Z-82 T) contient des grains équiaxiaux, alors que les tôles de fusion sous vide (Z-105 T et Z-A-2 D 127) sont à grains nettement allongés dans la direction du laminage.

Des examens sommaires aux rayons X (diffractographe à compteur) permettant d'établir les relations d'intensité entre les diverses réflexions ont fourni les résultats suivants¹⁷).

(i) Pour les trois tôles la réflexion la plus intense est celle d'ordre (0002) et non (10 $\bar{1}$ 1) comme le veut la structure cristallographique, et qui a d'ailleurs été effectivement trouvée sur les échantillons des trois billettes correspondantes.

(ii) La texture de laminage se présente avec la même allure pour les deux tôles sans anomalies structurales. Elles est, au contraire, beaucoup plus accentuée sur le diagramme de la tôle Z-82 T où la réflexion majeure domine de très loin toutes les autres.

Les conditions de transformation à partir des billettes étant identiques pour les trois tôles, il semblerait que les hétérogénéités filamenteuses perturbent le développement normal de la cristallisation. Le mécanisme responsable reste obscur; on peut seulement remarquer que l'anomalie est associée à la localisation quasi générale des "stringers" sur les limites intergranulaires, et aux variations d'intensité de grain à grain des bandes sinueuses typiques de la matrice de cette tôle.

6.6. RELATION ENTRE "STRINGERS STRUCTURAUX" ET "STRINGERS DE CORROSION"

Malgré que cette question sorte du cadre de la présente étude, et n'ait pas fait l'objet d'expériences spéciales, quelques remarques méritent d'être mentionnées.

La sensibilité à l'oxydation anodique, aux conditions du polissage électrolytique, au réactif oxydant fluonitrique et à la corrosion sèche des constituants filamenteux anormaux, et aussi de certaines portions de la matrice environnante, laissent prévoir une attaque préférentielle de ces hétérogénéités lorsqu'elles se trouveront exposées à la vapeur d'eau surchauffée.

Nous devons, cependant, supposer que les "stringers de corrosion" décrits dans la littérature sont apparus sur des tôles apparemment saines, c'est-à-dire n'ayant pas donné lieu à des défauts superficiels aussi flagrants que sur le produit laminé Z-82 T, ou, en tout cas, débarrassées par un moyen mécanique de la couche renfermant de tels défauts. Dans ces conditions, la structure exposée au milieu corrodant sera comparable à celle observée à partir de 0,20 mm environ sous la surface. Or nous avons dit au précédent paragraphe que l'évolution structurale du stade billette au stade final tôle se manifestait dans le sens d'une homogénéisation partielle, déduite précisément d'une diminution considérable des domaines de haute réactivité. Néanmoins, la sensibilité au réactif fluonitrique des submicroéléments rassemblés sur les "stringers" internes et de la matrice qui les entoure (cf. figs. 27a, 28a, b) laisse prévoir que le degré d'hétérogénéité est encore suffisant pour entraîner la corrosion sélective à l'eau surchauffée.

S'il en est bien ainsi, ces "stringers" doivent subir aussi le gonflement par corrosion sèche dans l'air, de la même façon que pendant le travail à chaud des couches superficielles. J. D. Grozier *et al.* ont effectivement trouvé que le chauffage à l'air vers 500° C pendant plusieurs heures fait apparaître sur la tôle des "stringers de corrosion" analogues à ceux produits au bout d'une vingtaine de jours dans l'eau à 400° C¹).

D'autre part, il est permis de penser qu'un recuit ultérieur pourra parfaire l'homogénéisation amorcée lors du laminage. Ce traitement affectera les plus petits microconstituants et les gradients de concentration dans la matrice, en particulier autour des filaments. Cependant ces derniers resteront pratiquement inchangés, puisque formés d'oxydes insolubles. Par un tel mécanisme on obtiendrait donc un matériau renfermant encore des "stringers structuraux", mais moins apte à la corrosion du fait de la disparition plus ou moins complète des domaines sensibilisés.

Les résultats expérimentaux de M. L. Pickles⁸⁾, ceux plus récents de J. D. Grozier *et al.*²⁾, sont conformes à notre interprétation. En revanche, ces derniers auteurs considèrent que la persistance de nombreux "stringers structuraux" après recuit de 8 heures à 1010° C prouve bien qu'ils représentent des porosités gazeuses, le traitement thermique n'affectant que les précipités séparés sur leurs parois, et responsables des "stringers de corrosion". Ici encore, ce sont des aspects micrographiques mis en évidence par des techniques non adéquates qui conduisent à confondre les ségrégations avec des vides de la matière.

7. Conclusions générales

La méthode de polissage électrolytique au tampon qui permet de réduire au minimum, ou au contraire d'exagérer, l'attaque sélective des constituants de la microstructure du Zircaloy-2, s'est avérée convenir remarquablement à l'étude des hétérogénéités rencontrées parfois dans cet alliage et connus sous le nom de "stringers structuraux". Elle a donc été appliquée à des spécimens provenant de billettes forgées d'origines diverses et de certaines tôles laminées correspondantes.

Les aspects micrographiques conduisent à classer les billettes en deux catégories selon que les lingots de départ ont été élaborés au four à électrode consommable en atmosphère d'argon, ou au four à vide.

Les six billettes de la première catégorie renferment des hétérogénéités de forme générale

filamenteuse dont sont privées les billettes de la seconde.

Le comportement de ces hétérogénéités, vis-à-vis des conditions de polissage et d'une oxydation anodique subséquente, permet d'en distinguer deux types, de fréquences inégales et plus ou moins associés. Tous deux représentent un constituant intermétallique préexistant dans le lingot à l'état libre et partiellement ou totalement transformé en oxydes sous l'action de l'oxygène de l'atmosphère de fusion. La séparation de ce constituant est la conséquence de l'homogénéisation incomplète et du refroidissement rapide du bain, sans relation avec des porosités vraies qui sont extrêmement rares dans toutes les billettes.

La transformation en oxydes des filaments du constituant, déjà amorcée dans les couches superficielles lors du forgeage, prend une grande importance pendant le laminage à chaud. Le phénomène d'oxydation se traduit par le gonflement des filaments localisés jusqu'à 0,2 mm environ sous la surface, celle-ci se trouvant, de ce fait, couverte de très nombreux défauts macroscopiques.

Malgré que les portions internes d'une telle tôle renferment des filaments intergranulaires d'épaisseur infime, continus et morcelés, leur microstructure traduit une certaine mise en solution des éléments du constituant intermétallique et des précipités normaux. Toutefois, la matrice est encore le siège de gradients de concentration, ainsi qu'en témoignent les stries sinueuses transgranulaires et les attaques sélectives avec le réactif fluonitrique révélées par la micrographie électronique.

On conçoit qu'un recuit approprié puisse éliminer les gradients de concentration, tout en laissant subsister les filaments d'oxydes insolubles. Ainsi s'explique que des "stringers" de cette nature soient présents dans les tôles peu ou pas sensibilisées aux "stringers de corrosion".

En définitive, deux facteurs dominent le problème des "stringers". D'une part, la présence d'hétérogénéités structurales spécifiques des conditions thermiques de la fusion sous argon. D'autre part, l'extrême sensibilité de ces

hétérogénéités à l'oxygène, qui se manifeste à la fois pendant l'élaboration et pendant le travail à chaud. De plus, ce même phénomène rend compte de la formation des "stringers" de corrosion.

Enfin, une sensibilité analogue aux réactifs chimiques acides intervient sans doute pendant les décapages intermédiaires, et, du point de vue métallographique, elle est incontestablement responsable de la confusion entre porosités vraies et éléments figurés de la microstructure, que l'on relève dans la grande majorité des études antérieures.

Bibliographie

- 1) J. G. Goodwin, L. S. Rubenstein, J. D. Grozier et F. L. Shubert, Westinghouse Atomic Power Division (USA) Report, WAPD-212-TID-4500 (1959)
- 2) J. D. Grozier, L. S. Rubenstein et J. G. Goodwin, Trans. Amer. Soc. Metals 52 (1960) 812
- 3) M. L. Picklesimer, Discussion du mémoire réf. 2)
- 4) P. A. Jacquet, Comptes Rendus Acad. Sc. Paris 243 (1956) 2068; Note Technique ONERA No. 40 (1957); Rev. Métall. 55 (1958) 531
- 5) P. A. Jacquet, La Recherche Aéronautique, No. 60 (Sept.-Oct. 1957) p. 57
- 6) M. L. Picklesimer, ONRN-2296 (1957)
- 7) P. A. Jacquet, non publié
- 8) M. L. Picklesimer et G. M. Adamson, Oak Ridge (USA) Report ORNL-56-11-115 (1956)
- 9) E. L. Richards et E. A. Wrigh, Bettis Techn. Rev. (Genève, 1958) p. 90
- 10) E. Mandel et J. Intrater, Westinghouse Electric (USA) Report, WEC-No. 73, 14-3633 (1958)
- 11) Mme C. Renon et J. Calvet, Journées Métallurgiques de la Soc. franç. Métall., Paris, Oct. 1960, à paraître dans Mém. Scient. Rev. Métall.
- 12) P. A. Jacquet et E. Mencarelli, Mém. Scient. Rev. Métall. 57 (1960) 241
- 13) N. Azam, Mém. Scient. Rev. Métall. 57 (1960) 41
- 14) M. Jean, Communication personnelle (Déc. 1959)
- 15) D. J. McPherson et M. Hansen, Trans. Amer. Soc. Metals 45 (1953) 915
- 16) D. J. McPherson et M. Hansen, Trans. Amer. Soc. Metals 45 (1953) 915
- 17) Mme A. R. Weill, non publié

THE ARCING BEHAVIOUR OF METALS IN CONTACT WITH A LOW ENERGY HYDROGEN PLASMA

L. B. GRIFFITHS

UKAEA, Metallurgy Division, Atomic Energy Research Establishment, Harwell, Didcot, Berks, UK

Received 28 November 1960

Previous work has been extended under highly reproducible conditions in an attempt to ascertain the mechanism of arc initiation. Results show that only quite small potential differences, of the order of 10 volts, need exist between parent metal and inclusions therein in order to initiate arcing. The proposed mechanism leads to the production of a vapour of impurity atoms above the cathode surface and is based upon the electrical properties of the interface between metal and inclusions which are viewed as being semi-conducting in character.

Un travail préliminaire a été poursuivi dans des conditions hautement reproductibles dans le but de se rendre compte du mécanisme d'amorçage de l'arc. Les résultats montrent que seules de toutes petites différences de potentiel de l'ordre de 10 volts doivent exister entre le métal de base et les inclusions qui s'y trouvent pour amorcer l'arc. Un mécanisme est

proposé qui conduit à la production d'une vapeur d'atomes d'impuretés à la surface de la cathode. Les propriétés électriques de l'interface entre le métal et les inclusions sont considérées comme analogues à celles des semi-conducteurs.

Frühere Arbeiten wurden unter sehr genau reproduzierbaren Bedingungen weitergeführt, um den Mechanismus der Lichtbogenzündung sicherzustellen. Die Ergebnisse zeigen, dass nur sehr kleine Potentialdifferenzen von den Grössenordnung 10 V zwischen der Metallmatrix und vorhandenen Einschlüssen zu existieren brauchen, um eine Zündung des Lichtbogens zu bewirken. Es wird ein Mechanismus vorgeschlagen, durch welchen über der Kathodenoberfläche ein im wesentlichen aus den Verunreinigungsatomen bestehender Dampf entsteht. Berücksichtigt sind dabei die elektrischen Eigenschaften der Grenzfläche zwischen Metall und Einschlüssen, welche als halbleitend angesehen werden.

1. Introduction

Previous work¹⁾ demonstrated a connection between non-metallic inclusions and the initiation of arcs on a metal surface in contact with a low energy plasma. Confirmation of this connection^{2,3)} was also obtained under more energetic plasma conditions. In a review of metallic materials for use in thermonuclear assemblies, Pfeil and Griffiths⁴⁾ discussed briefly further aspects of arcing including the so-called "conditioning" phenomenon. The work discussed in this paper was undertaken to extend the earlier work and, if possible, to ascertain the mechanism of arc initiation on metals. The theories concerned with the "cold cathode arc", as it is called, in the main commence with the

assumption that there exists a vapour of comparatively heavy atoms above the surface of the cathode⁵⁾. It is the stage leading up to the production of this vapour with which we are concerned here.

2. Experimental Arrangement

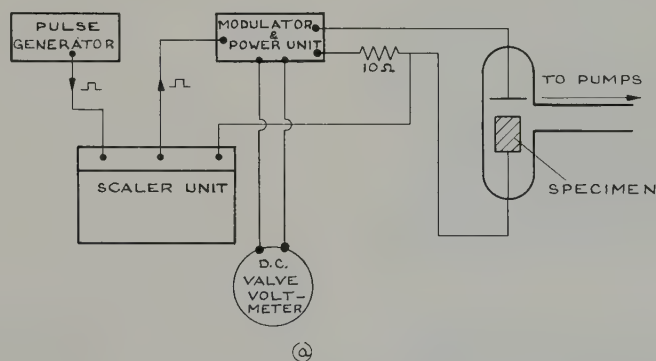
The apparatus consisted of a small discharge tube containing two electrodes, one of which was the specimen. The spacing between electrodes was about 3 mm. The discharge tube formed part of a vacuum system (built as a multi-purpose apparatus) which could be evacuated to a pressure of about 10^{-10} mm Hg, using techniques of a now conventional nature. The object of pumping to such a low pressure

was to obtain clean, reproducible conditions. After evacuation, the discharge tube was isolated from the vacuum system by means of an all-metal high vacuum valve of the Alpert pattern and "spec-pure" hydrogen was then admitted to the tube, via a second isolation valve, to a pressure of 50μ Hg. The gas was ionized by means of a small high frequency coil outside the experimental tube.

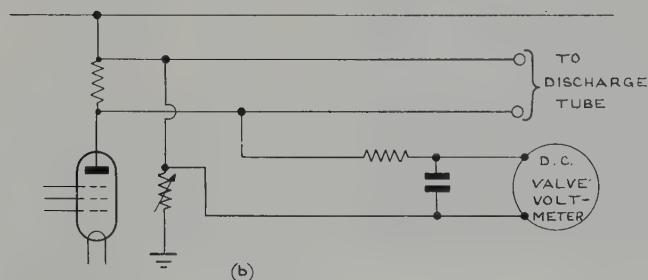
The potential applied to the discharge tube was made up of two parts, these being a square-wave pulse superimposed upon a normal d.c. potential. The specimen formed the negative electrode of the discharge tube. Pulses were counted on a scaler unit which stopped counting automatically when an arc was initiated. The pulse amplitude was variable up to 500 volts and the width from 1–250 microseconds. The d.c. potential was also variable and was measured by means of a d.c. valve voltmeter. In these

experiments an attempt was made to measure the potential (inclusion arcing potential) to which a low conductivity inclusion would charge under positive ion bombardment, relative to the metal in which it was embedded, before an arc occurred. Measurement of the "inclusion arcing potential" using only a variable d.c. potential on the discharge tube would be difficult, since the charging rate of an inclusion would rapidly decrease as its potential approached that of the plasma. The pulse technique was therefore adopted in an attempt to maintain a linear charging rate. Fig. 1 illustrates the general experimental arrangement.

The experiment consisted in measuring the d.c. potential necessary to initiate an arc under pre-set pulse conditions. Under the conditions outlined above, the current to the specimens was of the order of 300 micro amps/cm² during the duration of the pulse.



GENERAL EXPERIMENTAL ARRANGEMENT



MODULATOR OUTPUT STAGE WITH ARRANGEMENT FOR PRODUCING BIAS POTENTIAL

Fig. 1. Experimental arrangement.

3. Specimen Preparation

A master alloy of composition 18 wt % Cr, 12 wt % Ni, balance Fe was prepared in the laboratory by arc-melting together materials of a very high purity. Microscopical examination subsequent to manufacture showed that the alloy was virtually inclusion-free. Small samples were then re-melted together with quantities of aluminium oxide, magnesium oxide, titanium dioxide and vanadium oxide. Fig. 2 shows photomicrographs of the alloy both before and after the addition of these oxides. By this method, specimens were obtained in which the inclusion types were known with a reasonable degree of certainty. Specimens were used in the as-polished condition and took the form of

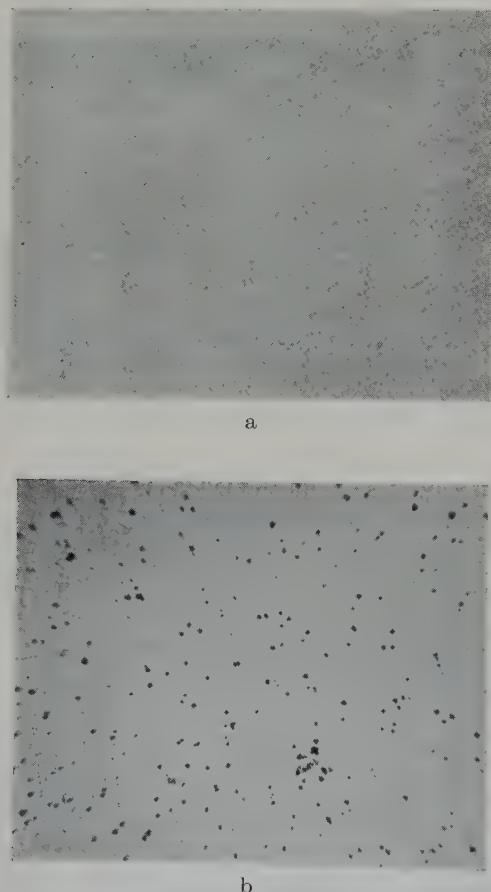


Fig. 2. (a) Photomicrograph of master alloy. Unetched. $\times 120$. (b) Master alloy after addition of magnesium oxide particles. Unetched. $\times 120$.

cylinders 0.6 mm ($\frac{1}{4}$ in.) and 0.3 mm ($\frac{1}{8}$ in.) diameter.

4.1. RESULTS AND DISCUSSION

As had previously been found¹⁻⁴, arc damage was associated with inclusions in the metals, and in addition the so-called "conditioning" phenomenon⁴) was again observed. Specimens containing vanadium oxide inclusions did not give rise to arcing, thus confirming an earlier finding under similar conditions. The specimen containing titanium dioxide, although initially arcing, very quickly became completely "conditioned". This is discussed in more detail below.

Figs. 3 and 4 show respectively the results obtained for specimens containing magnesium oxide and aluminium oxide inclusions. Pulse width is plotted against d.c. potential for various pulse amplitudes. The intercept with the ordinate is identified as the potential which an

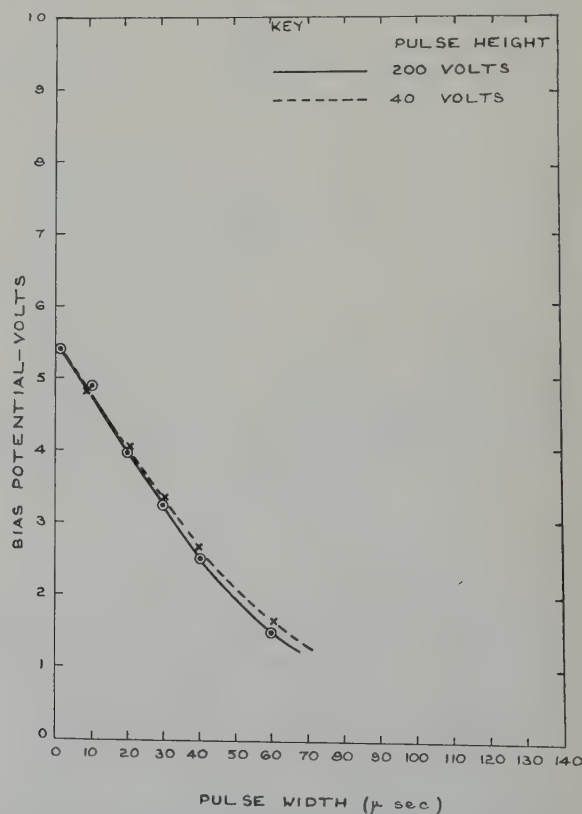


Fig. 3. Arcing potentials: — magnesia particles in stainless steel.

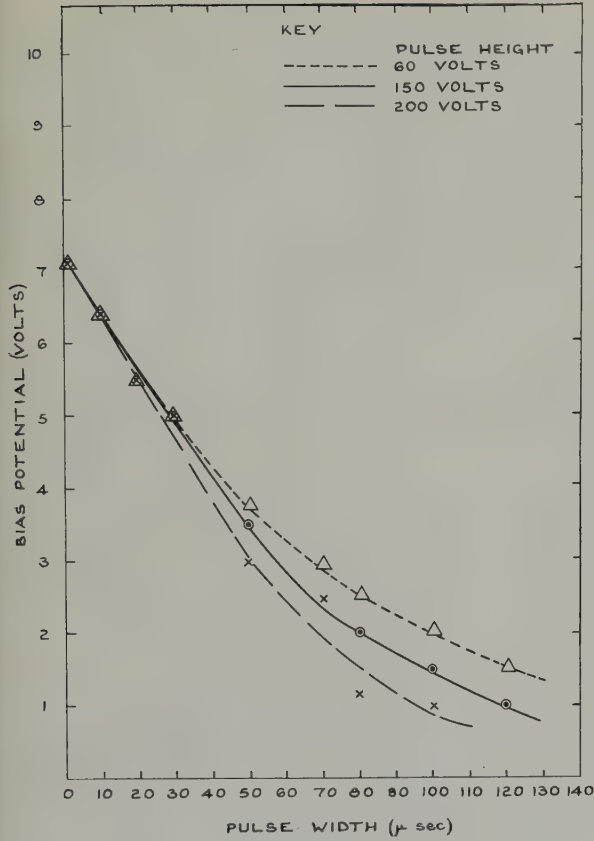


Fig. 4. Arcing potentials:—alumina particles in stainless steel.

inclusion has to attain for arcing to be initiated and the results demonstrate the relative independence of this potential of pulse amplitude. It is clear that an inclusion need only be charged to a relatively small positive potential with respect to the metal in which it is embedded, in order to initiate an arc. Figs. 5 and 6 demonstrate the effect of hydrogen ion bombardment (200 volts and 300 $\mu\text{amp}/\text{cm}^2$) upon the "inclusion arcing potential" for specimens containing magnesium oxide and aluminium oxide inclusions respectively. The falling-off of this potential, culminating in the complete cessation of arcing, is believed to be one cause of the "conditioning" phenomenon, and is what was expected from recent work⁶) on the effects of ion bombardment on the electrical properties of magnesium oxide and aluminium oxide

under similar conditions to those pertaining to experiments described in this paper.

4.2. ARCING

The proposed mechanism of arc initiation, under the present experimental conditions, is based upon metal/semiconductor contact theory. Fig. 7 illustrates the usually accepted picture of the relative positions of the energy levels of a semiconductor with respect to those of the metal when in contact and at equilibrium. As is well known, the tops of the Fermi distribution in metal and semiconductor must be coincident at equilibrium. In the most general case where the Fermi level of the semiconductor lies above that of the metal, coincidence is achieved by electrons leaving a region of semiconductor (impurity centres) near to the metal, and entering the metal. This sets up a positive space charge region (barrier layer) in the semiconductor. As a result, the potential energy system of the semiconductor will be pushed down as in shown in fig. 7a. Deposition of positive charge upon the semiconductor surface, as is the case in the experiments outlined above, will result in a further depression of the energy levels and an increase of the width of the barrier layer, thus tending towards the state of affairs shown in fig. 7b. As the potential of the semiconductor surface rises, as a result of positive ion bombardment, a finite current will flow from the metal to the semiconductor, tending to reduce the field across the barrier layer. This arises as a direct result of the Fermi distribution of electrons in a metal at a temperature above absolute zero. However, this current will be small with respect to the ion current from the plasma until a field of about 10^5 volt/cm exists across the barrier layer. Measuring x from B (fig. 7b) the potential variation over the barrier layer is

$$\frac{\partial^2 \phi}{\partial x^2} = \frac{4\pi Ne}{\epsilon} \quad (1)$$

where N is the number of ionized donors present, ϵ is the dielectric constant, and e is the electronic

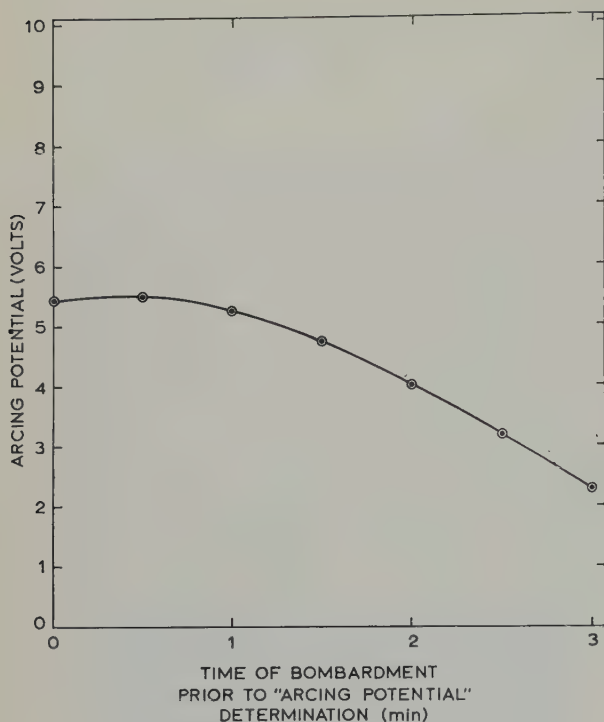


Fig. 5. Variation of arcing potential with bombardment time for MgO inclusions in stainless steel. (Bombardment conditions: 200 volts, 300 amp/cm².)

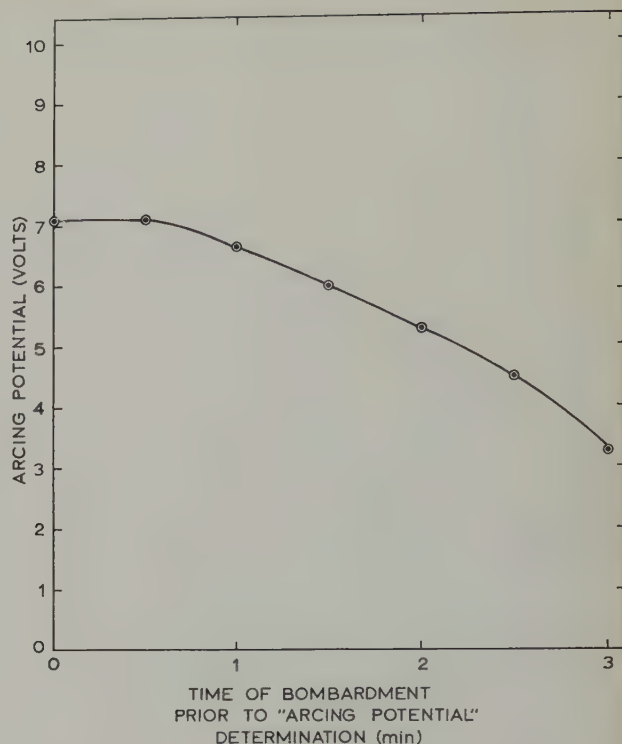


Fig. 6. Variation of arcing potential with bombardment time for Al₂O₃ inclusions in stainless steel. (Bombardment conditions: 200 volts; 300 amp/cm².)

charge. Solution of (1) gives:

$$\varphi = \frac{2\pi Ne}{\epsilon} x^2 \quad (2)$$

from which the width, AB, of the barrier layer is:

$$AB = \frac{(\varphi_0 \epsilon)^{\frac{1}{2}}}{(2\pi Ne)} \text{ cm} \quad (3)$$

where φ_0 is the height of the top of the barrier above the bottom of the conduction band.

The width of the barrier layer will tend to increase when a field is applied across it, as is the case in these experiments, and (3) does not take this into account since it is for equilibrium conditions. However, the theory for the metal/semiconductor contact outlined above completely ignores the screening of the semiconductor electron system by surface states †

† The theory of surface states may be found in any modern text on semiconductors, ref. ⁹ for example.

and the modifying influence of the image force. These effects tend to limit the width and height of the barrier layer respectively. Therefore, (3) appears to be a reasonable approximation for the barrier layer width.

Putting $\varphi_0 \sim 1$ volt, $\epsilon \sim 10$ and $N \sim 10^{16}$, which are fairly reasonable figures for the particular cases in question, AB is about 10^{-5} cms. From the experimentally determined "inclusion arcing potential" i.e. about 10 volts, a field of about 10^6 V/cm would exist across the barrier. Under the action of the field existing across the barrier it is suggested that electrons are accelerated from the metal into the inclusion. It is further suggested that the accelerated electrons gain sufficient kinetic energy to excite further electrons into the conduction band of the semiconductor. The process is pictured, therefore, as an avalanche of electrons leading to breakdown of the inclusion surface. In this manner the required catastrophic

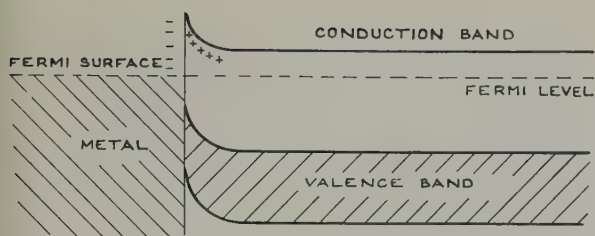


Fig. 7a. Semiconductor energy levels depressed after contact with metal.

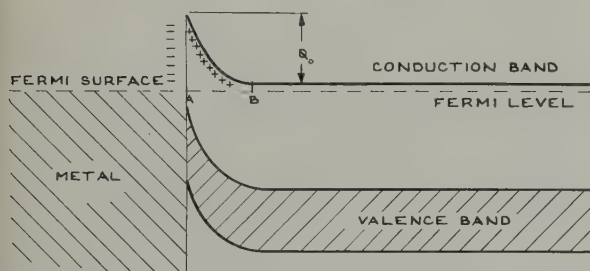


Fig. 7b. Further depression of energy levels after positive ion bombardment.

release of energy is obtained. The current flow will result in ohmic heating of the surface of the inclusion which may conceivably lead to evaporation of a small quantity of the inclusion. From the comparatively small amount of energy stored, however, it is estimated, from thermodynamic data, that only a few hundred atoms could be evaporated from aluminium oxide and magnesium oxide inclusions.

An alternative explanation, based upon certain experimental observations, by Dugdale and McVickers⁷⁾ is that the evaporated atoms are not material of the inclusions themselves, but are of adsorbed foreign atoms (oxygen for example). The binding energy of an adsorbed species on the surfaces of the relatively stable inclusion-materials under discussion here would presumably be quite small. Under these conditions, dissipation of the stored energy residing on an inclusion surface could evaporate 10^3 – 10^4 atoms from a monolayer of adsorbed gas.

4.3. "CONDITIONING"

Eq. (3) shows the dependence of barrier layer width upon N , the number of ionized donors present in the semiconductor. Hence any agency which causes N to vary will also give rise to

variation in barrier width. In this work, N was varied by bombarding the specimen surface with hydrogen ions of fairly low energy. Measurements of electrical resistivity⁶⁾ of magnesium oxide and aluminium oxide showed a decrease in resistivity upon bombardment which in turn reflects, among other things, an increase in carrier concentration. From (3), therefore AB will decrease and there should be a corresponding decrease in the potential to which an inclusion should require to rise before initiating an arc. Figs. 5 and 6 show the variation of the "inclusion arcing potential", with bombardment, for magnesium oxide and aluminium oxide inclusions respectively, and, as can be seen, the expected decrease is obtained. On this simple model, arcing ceases when the breakdown voltage becomes so small that the stored energy is insufficient to evaporate the required number of atoms from the inclusion surface. The fall in "inclusion arcing potential" was recoverable at room temperature if bombardment was stopped for several minutes⁶⁾. However, under more energetic and higher current plasma conditions, the "conditioning" effect appears to be rather more permanent⁸⁾, suggesting that bombardment damage had occurred in the semi-conducting inclusion and in this way changed the electrical properties. If this is the case then annealing of the damage should occur at some particular temperature level. Direct experimental examination of this point is therefore possible.

An additional method by which specimens may become "conditioned" is by the loss of one of the constituents of the inclusion material. Titanium dioxide is a case in point. As was briefly mentioned above, specimens containing titanium dioxide inclusions very rapidly become "conditioned". It is well known that titanium dioxide is reduced when the partial pressure of oxygen above it is decreased, with the result that the electrical resistivity is markedly reduced. Titanium dioxide in fact behaves as a metal-excess semiconductor. The application of high vacuum in the experiments obviously aided this process. Under the reducing condi-

tions of a partially ionized hydrogen plasma, further reduction probably occurred which, in addition to the bombardment effect discussed above, could account for the very rapid "conditioning" observed. Confirmation of the above was obtained in an experiment in which a specimen, after "conditioning", was subjected to a low pressure (50μ Hg) oxygen atmosphere for a period of two minutes. Subsequent to this procedure arcing was again obtained with a specimen containing titanium dioxide inclusions. The effect was not observed with the other inclusions used in these experiments.

The mechanism of arc initiation described in the foregoing suggests several interesting points. Firstly, for any type of inclusion there should exist a threshold ion current (to the specimen) below which arcing will not occur. Secondly, there should be a temperature dependence of both the threshold ion current and the charging rate above the threshold since both φ_0 and N in eq. (3) are temperature dependent. This latter effect may, however, be quite small for certain inclusions and therefore difficult to observe experimentally.

5. Conclusions

Earlier findings concerned with the effect of low conductivity inclusions upon the arcing behaviour of metals in contact with a plasma have been confirmed. Only quite small potential differences need exist between inclusions and metal to initiate arcs.

The mechanism of arc initiation may be based upon the properties of the "barrier layer"

existing at the junction between metal and inclusion which is looked on as being semi-conducting in character. The conditioning process is a direct result of the effects of ion bombardment from the plasma, and in some cases partial dissociation, upon the properties of inclusions.

Acknowledgments

I wish to thank Mr. C. H. Thomas for preparation of specimens, Mr. D. R. Arkell for the photomicrographs in fig. 2 and Mr. R. A. Dugdale, Mr. R. C. McVickers and Mr. J. T. Maskrey for many helpful discussions. Finally, I wish to express my appreciation to Dr. P. C. L. Pfeil for his continued interest and advice during the whole course of this work. All the above colleagues are members of the Metallurgy Division, AERE, Harwell.

References

- ¹) P. C. L. Pfeil and L. B. Griffiths, *J. Nucl. Mat.* **1** (1959) 244
- ²) R. Hancox and C. H. Walker, Harwell (UK) Report, AERE-R 3254 (1960)
- ³) R. Barnfield and J. T. Maskrey, Harwell (UK) Report, AERE-R 3161 (1959)
- ⁴) P. C. L. Pfeil and L. B. Griffiths, Harwell (UK) Report, AERE-R 3207 (1959)
- ⁵) For example, A. von Engel and A. E. Robson, *Proc. Roy. Soc. A* **243** (1957) 217
- ⁶) L. B. Griffiths, *Nature (Lond.)* **188** (1960) 4744
- ⁷) R. A. Dugdale and R. C. McVickers, private communication
- ⁸) R. A. Dugdale *et al.*, private communication
- ⁹) R. A. Smith, *Semiconductors* (Cambridge, University Press, 1959)

TRANSFORMATION KINETICS OF GAMMA-PHASE URANIUM-MOLYBDENUM-NIOBIUM ALLOYS

W. M. JUSTUSSON

Ford Motor Company, Scientific Laboratory, P.O. Box 2053, Dearborn, Michigan, USA

Received 24 October 1960

Some properties of gamma phase uranium-base molybdenum-niobium ternary alloys are described. Transformation kinetics of the gamma phase at 550, 500, and 450° C were followed primarily by resistometric techniques. Molybdenum-rich alloys with small additions of niobium were found to have the most sluggish transformation kinetics. Duplex gamma phase alloys had lower thermal stability than single phase alloys.

Densities and electrical resistivities of alloys quenched from 1000° C were measured. Duplex phase alloys were determined by resistometric measurements and metallographic examination.

On décrit quelques propriétés des alliages ternaires uranium-molybdène-niobium en phase γ . Les cinétiques de transformation de la phase γ à 550, 500 et 450° C ont été d'abord suivies par des mesures de résistance. On a remarqué que les alliages riches en molybdène avec de petites additions de niobium présentent les cinétiques de transformation les plus lentes. Les alliages présentant une phase γ en même

temps qu'une deuxième phase ont une stabilité thermique plus faible que les alliages présentant une phase γ unique.

Les densités et résistivités électriques des alliages trempés à partir de 1000° C ont été mesurées. Les alliages à deux phases ont été décelés par mesures de résistivité et examen métallographique.

Es werden einige Eigenschaften ternärer γ -Legierungen auf Uranbasis mit Molybdän- und Niobzusatz beschrieben. Die Umwandlung der γ -Phase wurde bei 550, 500 und 450° C zunächst durch Widerstandsmessungen verfolgt. Dabei hatten molybdänreiche Legierungen mit kleinen Niobzusätzen die trügste Umwandlung aufzuweisen. Zweiphasige Legierungen mit γ -Phase waren thermisch instabiler als einphasige Legierungen.

Es wurde die Dichte und der elektrische Widerstand von Proben gemessen, die von 1000° C abgeschreckt waren. Zweiphasige Legierungen wurden resistometrischen Messungen und einer metallographischen Untersuchung unterzogen.

1. Introduction

The body-centered cubic phase (γ) of uranium-rich alloys has received considerable attention over the past few years as a potential nuclear fuel. Pure uranium has an orthorhombic crystal structure at low temperatures which is characterized by poor radiation stability and corrosion resistance and by dimensional growth under thermal cycling. However, the high temperature γ phase can be retained by suitable alloying additions in a metastable condition at low temperatures. The metastable gamma phase has much better corrosion resistance and radiation stability, and being isotropic, does not

undergo dimensional growth with thermal cycling.

Extensive solubilities of Mo, Nb, Ti and Zr in gamma uranium have been reported¹). Of these elements, Mo and Nb are the most effective in promoting metastable gamma phase retention. The U-Mo and U-Nb binary systems are shown in figs. 1 and 2¹). The gamma phase can be retained at room temperature in each of the binary systems when more than 7 wt % alloy is present. In alloys containing 2 to 7 wt % Mo, the quenched gamma phase undergoes a diffusionless phase change to a base-centered orthorhombic structure (α'). The

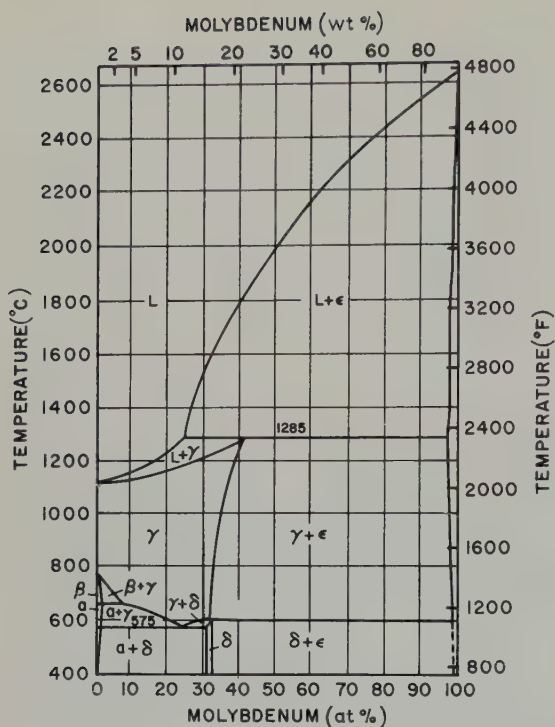


Fig. 1. Uranium-molybdenum binary system.

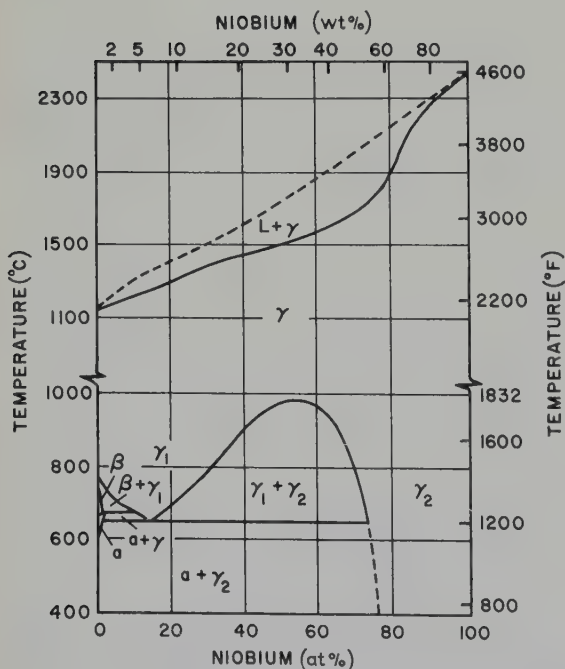


Fig. 2. Uranium-niobium binary system.

gamma phase with alloy additions up to 15 wt % in the U-Mo system decomposes eutectoidally to α -uranium and an ordered tetragonal phase (γ') (δ) † 2). The gamma phase in uranium-rich niobium alloys undergoes a monotectoid transformation to α -uranium and γ -uranium of higher Nb content.

The decomposition of the metastable gamma phase is extremely sluggish. Transformation kinetics of gamma phase U-Mo alloys have been studied by Van Thyne and McPherson ³⁾ and Saller *et al.* ⁴⁾. The transformation kinetics of binary U-Nb alloys and, to a limited extent, ternary U-Mo-Nb alloys have been investigated by Van Thyne and McPherson ⁵⁾ and Storhok *et al.* ⁶⁾. Transformation kinetics of the metastable gamma phase reported by the investigators cited were often measured in hours and even days in some cases. This work was undertaken in an attempt to determine the most stable gamma phase composition in the uranium-rich U-Mo-Nb system.

2. Experimental Procedure

The alloys were prepared from the metals listed in table 1. The U was pickled in a nitric acid solution prior to melting. The Mo and Nb pellets were clean as received; however, the Mo pellets were crushed to small pieces to hasten solution during melting.

The 2200-gram charges were induction-melted in bottom-pour stabilized zirconia crucibles under a pressure of less than 10^{-3} mm Hg and poured into a flame-sprayed alumina-coated cast iron mold. Chemical analyses of the tops and bottoms of all 2.5 cm (1") diameter by 15 cm (6") length ingots differed by less than 0.2 % alloy additions. Molybdenum entered into solution quite readily, but the niobium was difficult to dissolve in the liquid uranium, requiring up to 30 minutes at 1600° C depending on alloy content. Zirconium contamination from

† Note by Editor: The new nomenclature given by Lehman and Hills has been inserted here. In fig. 1 the nomenclature of the ref. ¹⁾ is preserved. Please see Mme J. Lehman and R. F. Hills, *J. Nucl. Mat.* 2 (1960) 261, for new symbols.

TABLE 1
Composition of materials

Metal	Form	Purity	Major impurities	Supplier
Natural uranium	3.15 cm ($1\frac{1}{4}$ ") dia bar	99.9	0.08 % C	AEC
Molybdenum	3.78 cm ($1\frac{1}{2}$ ") dia \times 1.26 cm ($\frac{1}{2}$ ") pellet	99.9	0.05 % O ₂	Fansteel Metallurgical Corporation
Niobium	0.63 cm ($\frac{1}{4}$ ") dia \times 0.32 cm ($\frac{1}{8}$ ") pellet	99.5	0.10 % Ta 0.30 % O ₂	Kawecki Chemical Corporation

the crucible was less than 0.01 %. The carbon level of the alloys varied from 0.06 to 0.08 %.

The ingots were hot rolled from 800 to 1050° C, depending on alloy content, to 1.3 cm (0.5") diameter rod. Resistivity samples, 0.63 cm (0.25") dia. by 5.08 cm (2.00") long, were machined from the rolled rod. The alloys were cleaned with an organic solvent, wrapped in molybdenum foil, sealed in vycor tubing with a purified argon atmosphere, homogenized at 1000° C for 24 hours and water quenched by breaking the tube under water. Density measurements were made on the resistivity samples by the water displacement method; the accuracy of the measurement was estimated to be ± 0.02 g/cc. The resistance of each specimen was measured over a length of 1.900 cm by a double Kelvin bridge method employing a Rubicon instrument. The instrument was standardized with known resistances. The reported resistivities are accurate to ± 0.7 micro-ohm-centimeters.

Van Thyne and McPherson⁵⁾ comparing metallographic, X-ray, resistometric, and hardness measurements for determining TTT diagrams of U-Mo alloys observed that electrical resistivity data represents an accurate method for determining initiation of transformation in these alloys. Thus, transformation kinetics were followed primarily with resistivity measurements by a quench-age heat treatment. However, metallographic examination was employed to confirm transformation. The aging treatments were done in a lead bath with a carbon powder cover at temperatures of 450, 500, and 550° C.

3. Experimental Results

The alloy compositions, densities, and resistivities are given in table 2, and on a triangular coordinate plot in fig. 3. The partially shaded

TABLE 2
Resistivities and densities of alloys homogenized 24 hours at 1000° C, and water quenched

Alloy No.	wt % Mo	wt % Nb	Resistivity	Density (g/cc)
1	3.48	—	65.4	18.15
2	6.43	—	64.3	17.68
3	9.37	—	69.2	17.26
4	—	3.42	57.6	18.00
5	—	5.32	66.8	17.53
6	—	8.65	65.7	16.63
7	—	11.69	68.5	16.09
8	3.30	3.50	65.3	17.45
9	2.89	6.57	68.0	16.68
10	2.91	8.93	70.4	16.25
11	3.02	13.05	74.8	15.55
12	4.62	5.23	69.3	16.75
13	4.23	10.78	71.1	16.08
14	6.13	2.35	67.6	17.22
15	6.07	3.71	68.4	17.00
16	6.06	5.45	68.8	16.58
17	5.74	7.05	67.6	16.31
18	5.81	10.08	67.4	15.84
19	8.63	1.76	69.9	17.00
20	8.51	2.85	70.2	16.77
21	8.37	3.88	71.4	16.65
22	8.48	4.75	67.9	16.50
23	8.34	6.94	61.9	16.03
24	8.31	8.97	62.9	15.72
25	10.50	1.61	72.8	16.75
26	11.10	3.06	66.0	16.42
27	11.05	4.17	65.3	16.25
28	10.84	6.82	58.8	15.69
29	10.53	10.39	57.5	15.22

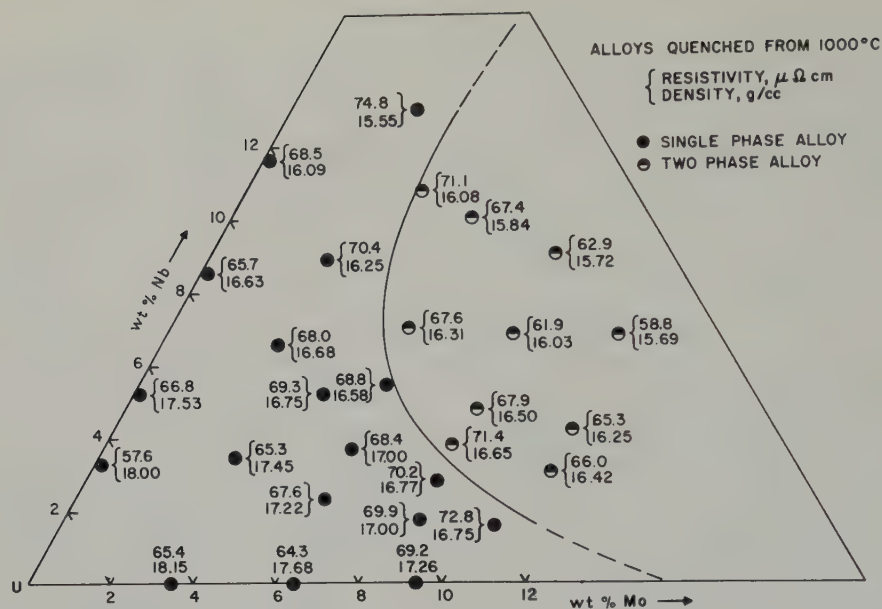


Fig. 3. Resistivities and densities of gamma phase uranium-molybdenum-niobium alloys.

circle represents two-phase alloys as determined by metallographic examination. Fig. 4 shows a large amount of a second phase in a U-10.5 % Mo-10.4 % Nb alloy which was identified by X-ray diffraction as a body-centered-cubic phase rich in niobium and molybdenum. The microstructures of quenched U-5.8 % Mo-10.1 % Nb and U-2.9 % Mo-8.9 % Nb are shown in figs. 5

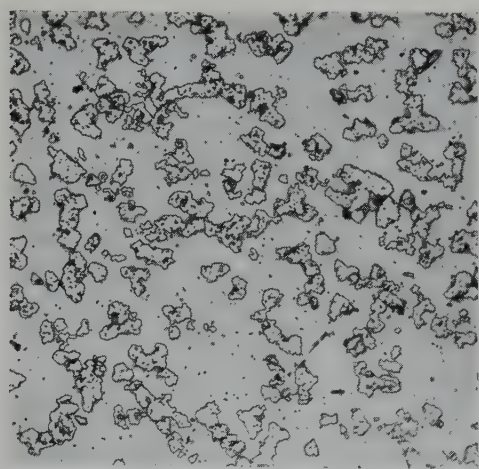


Fig. 4. Uranium - 70.5 % molybdenum - 10.4 % niobium alloy. Structure is γ_2 in γ_1 matrix. Solution heat treated at 1000° C for 24 hours and H₂O quenched. As polished with 1 % HF solution. 250 \times .

and 6. A small amount of the second phase is evident in fig. 5 while none is present in fig. 6.

The change in resistivity versus time during aging at 500° C for several alloys is illustrated in fig. 7. Since the resistivity measurements were accurate to approximately ± 1 %, a drop of 1 % in the resistivity was regarded as the beginning of transformation. A triangular coordinate plot for the beginning of transformation, as determined by electrical resistivity measurements at 550, 500, and 450° C, is shown by fig. 8. In all cases, metallographic examination confirmed the beginning of transformation.

The transformation characteristics of alloys containing more than 8 % Mo and less than 4 % Nb behaved in a peculiar manner as compared to other ternary alloys. Whereas lower molybdenum and higher niobium alloys showed precipitous decreases in resistivity with the beginning of transformation, these alloys exhibited an increase followed by a decrease in resistivity, as shown in fig. 9. The beginning of transformation was taken at the point of initial increase in resistivity since transformation products were observed metallographically during the increase. Initial transformation products appeared as a pearlitic structure in alloys con-

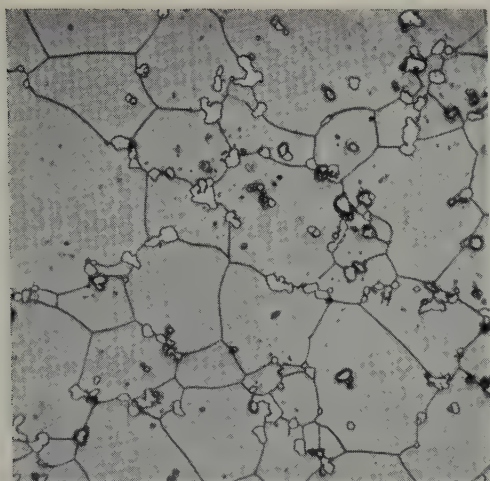


Fig. 5. Uranium — 5.8 % molybdenum — 10.1 % niobium alloy. Small amounts of γ_2 in γ_1 matrix. Same heat treatment as above. Etched in 5 % HF and 5 % P_2O_5 solution. 500 \times .

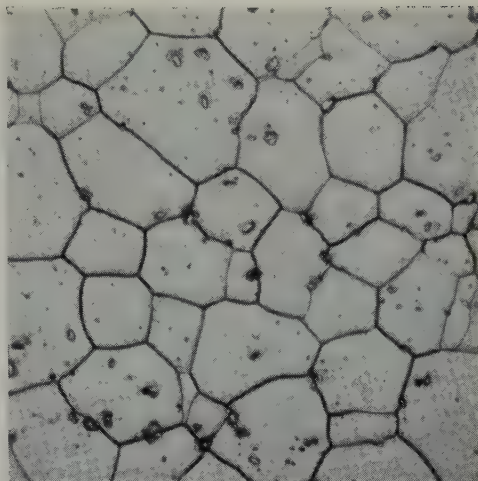


Fig. 6. Uranium — 2.9 % molybdenum — 8.9 % niobium alloy. Structure is γ_1 plus impurities. Same heat treatment as above. Heavily etched with 5 % HF and 5 % P_2O_5 solution. 500 \times .

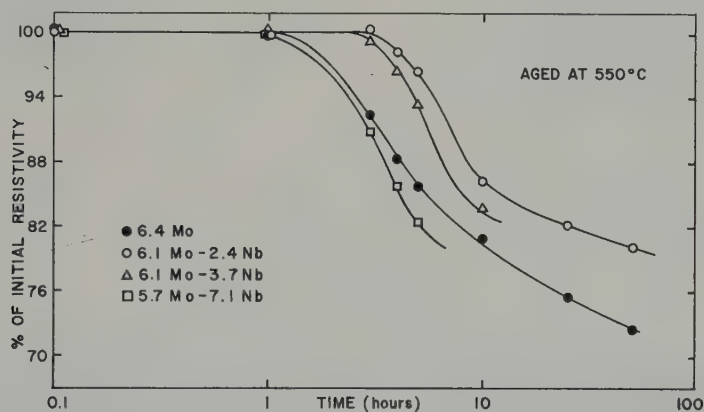


Fig. 7. Resistivity change with start of transformation.

taining more than 8 % Mo except in the U-10.5 % Mo-1.6 % Nb. The pearlitic structure was much finer at 500° C than at 550° C, as shown in figs. 10 and 11.

The U-10.5 % Mo-1.5 % Nb alloy also transformed in an unusual manner characteristic of high Mo and low Nb contents. The resistivity increased gradually with aging time at all temperatures and no discrete transformation products were observed in the microstructure at the time of the most rapid increase in resistivity. However, areas which appeared to be twinned were present in the microstructure, as shown in fig. 12. This microstructure was also

present in the U-11.1 % Mo-3.1 % Nb alloy. The microstructure after prolonged aging is illustrated by fig. 13. The outline of what appear to be coarse angular particles in fig. 13 were present as solid particles in the as-cast structure, as shown in fig. 14; they were nearly completely dissolved during the homogenization treatment.

4. Discussion of Experimental Results

The resistivities and densities of retained gamma alloys behave as expected; that is, the density decreases and the resistivity increases with alloy content in solution. The resistivity

reaches a maximum at the boundary of the two phase region of uranium-rich (γ_1) and molybdenum-niobium-rich (γ_2) body-centered cubic phases and then decreases with increasing amounts of (γ_2). Metallographic examination confirmed the presence of a second phase. The decrease in resistivity at the phase boundary is probably the result of the appearance in the (γ_1) matrix of the (γ_2) phase which has a lower resistance. Storhok *et al.*⁶ indicate in their work on ternary alloys with 7.5 and 10 % Mo that the phase boundary in this region is approxi-

mately as shown in fig. 3. Resistivity increases with an increasing amount of solute element. However, as noted from fig. 3, the resistivity drops in quenched alloys as the alloying elements exceed 5.3 % Nb and 3.5 % Mo and then increases with further alloy additions. This behavior of the 3.4 and 5.3 % Nb and 3.5 % Mo alloys is the result of a diffusionless phase transformation to a base-centered orthorhombic structure; that is, the gamma phase cannot be retained by quenching to room temperature. The metallographic appearance of these alloys

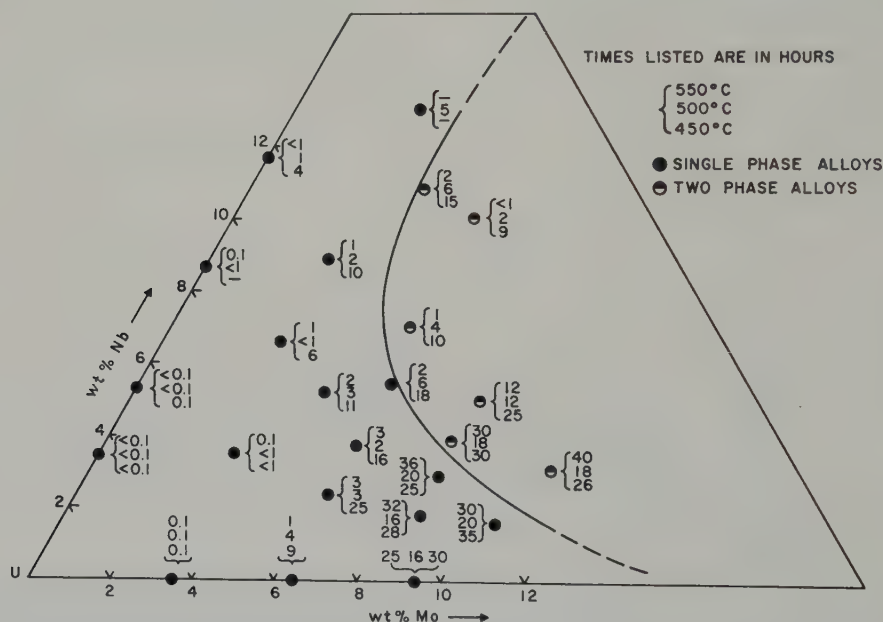


Fig. 8. Beginning of transformation as determined by resistivity measurements.

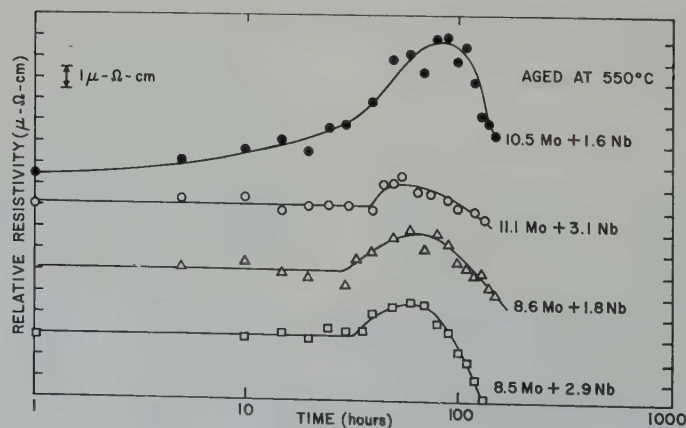


Fig. 9. Resistivity change with transformation of molybdenum-rich alloys.

under polarized light is illustrated in fig. 15.

Generally, the niobium-rich ternary alloys were much less stable than the molybdenum-rich alloys. The most stable gamma phase alloys contained more than 8 % Mo with niobium content limited to soluble niobium in the gamma

phase. With transformation, the alloys corrode extremely rapidly in high temperature water. McGeary ⁷⁾ reported that alloys with more than 8 % Mo and 1 to 3 % Nb were the most corrosion resistant alloys in the U-Mo-Nb ternary system, suggesting that these alloys have the greatest

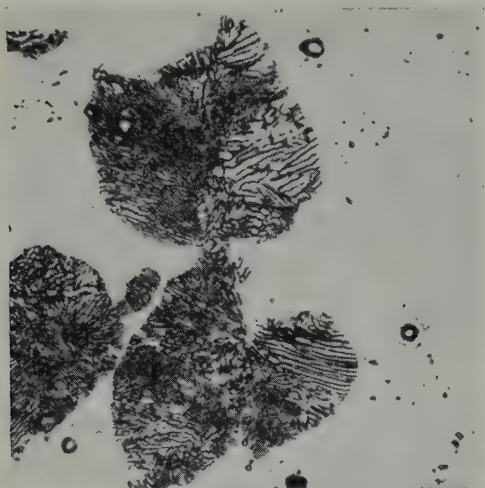


Fig. 10. Uranium — 8.6 % molybdenum — 1.8 % niobium alloy. Initial pearlitic transformation products of α and γ' in a white matrix. Solution heat treated at 1000° C for 24 hours, H₂O quenched, and aged at 500° C for 20 hours. As polished with 1 % HF solution. 1000 \times .

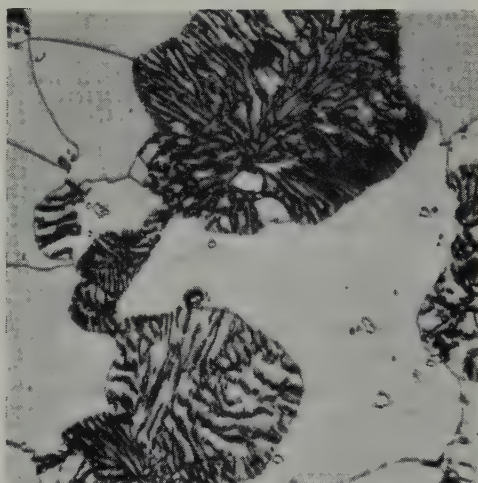


Fig. 11. Uranium — 8.5 % molybdenum — 2.9 % niobium alloy. Same structure as in fig. 10. Solution heat treated at 1000° C for 24 hours. H₂O quenched and aged at 550° C for 125 hours. Etched with 5 % HF and 5 % P₂O₅ solution. 750 \times .



Fig. 12. Uranium — 10.5 % molybdenum — 1.6 % niobium alloy. Partially ordered γ_1 phase. Solution heat treated at 1000° C for 24 hours, H₂O quenched, and aged at 500° C for 25 hours. Etched with 5 % HF and 5 % P₂O₅ solution. 250 \times .

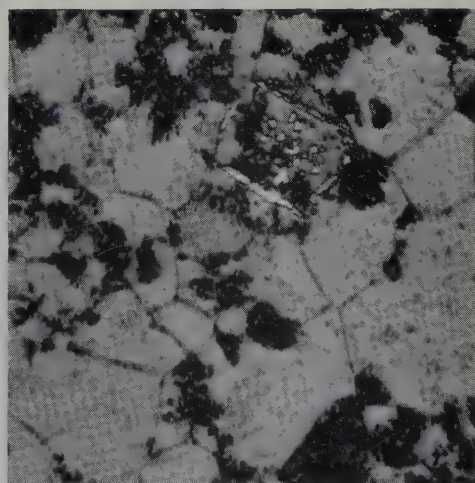


Fig. 13. Uranium — 10.5 % molybdenum — 1.6 % niobium alloy. Fine pearlite in ordered γ_1 matrix. Solution heat treated at 1000° C for 24 hours, H₂O quenched, and aged at 450° C for 450 hours. Etched with 5 % HF and 5 % P₂O₅ solution. 750 \times .

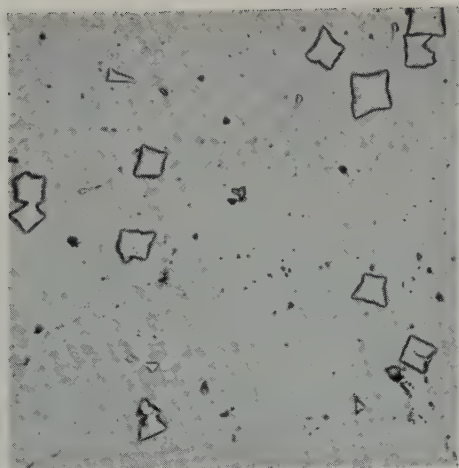


Fig. 14. Uranium — 10.5 % molybdenum — 1.6 % niobium alloy. As-cast structure with angular particles of complex carbides, nitrides and oxides. As polished with 1 % HF solution. 250 \times .

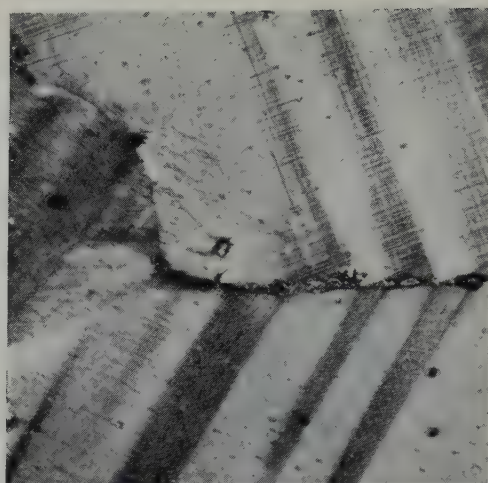


Fig. 15. Uranium — 3.5 % molybdenum alloy. Structure is α' . Solution heat treated at 1000° C for 24 hours and H₂O quenched. As polished. Polarized light. 250 \times .

thermal stability. The reaction kinetics for niobium-rich alloys were most rapid at 550° C while molybdenum-rich alloys transformed more rapidly at 500° C.

In most cases, additions of niobium increased the stability of the gamma phase at any base Mo content; this has been observed by previous investigators ^{5,6}). However, in two phase alloys consisting of uranium-rich and molybdenum-niobium-rich body-centered cubic phases, the stability is sharply decreased, as shown in fig. 8. Since the uranium-rich matrix in these alloys represents alloys of a composition somewhere along the phase boundary, the transformation kinetics indicated are actually of alloys of different compositions. The decrease in stability appears to indicate that the composition of the matrix is depleted of molybdenum and enriched in niobium according to the phase boundary shown in the figure. However, metallographic examination of the duplex alloys shows that nucleation of the transformation products takes place preferentially along the interface of the two body-centered cubic phases, as shown in fig. 16. It is suggested that both depletion of Mo in the matrix and favorable nucleation sites at the two-phase interfaces contribute to the decreased stability of duplex phase alloys.

Attempts to dissolve the molybdenum-niobium-rich phase by higher solution of the specimens was observed metallographically in the form of platelets which resembled a hydride precipitate. It was anticipated that more complete solution of the two phase molybdenum-rich alloys would result in alloys of greater stability.

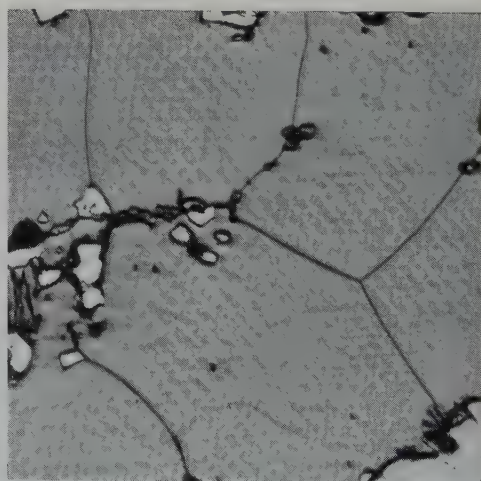


Fig. 16. Uranium — 11.1 % molybdenum — 4.2 % niobium alloy. Matrix is γ_1 and ordered γ_1 . White phase is γ_2 . Note pearlitic transformation products starting at edge of γ_2 . Solution treated at 1000° C for 24 hours, H₂O quenched and aged at 550° C. Etched in 5 % HF and 5 % P₂O₅ solution. 750 \times .

The resistivity-aging time curves show a sudden decrease with transformation in alloys of low thermal stability and an increase followed by a decrease in alloys of high thermal stability (figs. 7 and 9). Van Thyne and McPherson³⁾ suggest the increase in resistivity of U-Mo binary alloys is the result of a pre-precipitation phenomenon. Since the increase in resistivity is observed only in alloys with high molybdenum contents, it is believed that the increase is the result of the formation of ordered transformation product (δ). Bostrom and Halteman²⁾ report that the ordered structure is a tetragonal unit cell composed of three pseudo cubes; the axial ratio of each pseudo cube is 0.957 permitting easy twinning along 103 planes. Their photomicrographs of a U-16.2 % Mo ordered structure were heavily striated. During the rise in resistivity, the microstructures showed striated regions indicating transformation to an ordered structure had begun as shown in fig. 12. Evidently strains associated with the ordering process are responsible for the rise in resistivity.

The coarse angular particles present in the as-cast microstructure of the U-10.5 % Mo-1.6 % Nb alloy (fig. 14) are believed to be a complex compound of U-Mo-Nb with carbon and/or nitrogen. Microhardness readings proved the particles to be quite hard; the approximate hardness was V.H.N. 750. Upon solution treatment the particles dissolve leaving the remaining residual impurities outlining the former particle.

5. Summary and Conclusions

Uranium-rich molybdenum-niobium alloys were prepared by induction melting in zirconia crucibles. Metallographic and resistometric techniques and density measurements were employed to study the properties of these alloys after homogenizing at 1000° C for 24 hours and water quenching. Density of the quenched alloys decreased with alloy content. Resistivity measurements increased until a two phase region of uranium-rich gamma (γ_1) and niobium-

molybdenum-rich gamma (γ_2) was encountered, whereupon the resistivities decreased. The two phase region was confirmed metallographically.

Transformation of the metastable gamma at 550, 500, and 450° C was followed primarily by resistometric techniques. Niobium-rich and molybdenum-rich alloys transformed the most rapidly at 550° C and 500° C, respectively, with the most sluggish transformation kinetics overall displayed by the molybdenum-rich alloys with molybdenum content greater than 8 % and niobium limited to that in solid solution (less than 4 %). Ternary alloys with greater than 8 % Mo and less than 4 % Nb showed an initial increase in resistivity upon transformation which is ascribed to strain associated with the ordering process. The thermal stability of two phase alloys decreased with increasing amounts of the molybdenum-niobium rich second phase. The lower stability is attributed to niobium enrichment of the matrix and/or increased nucleation of the transformation products at the two phase interface.

Acknowledgments

The author wishes to thank Mr. K. Bush, who prepared the alloys and obtained many of the experimental results, and Ford Motor Company for permission to pursue this study and publish the results.

References

- 1) F. A. Rough and A. A. Bauer, Battelle Memorial Institute (USA), Report BMI-1300 (1958)
- 2) W. A. Bostrom and E. K. Halteman, NESC paper 57-NESC-12 (1957)
- 3) R. J. van Thyne and D. J. McPherson, Amer. Soc. Metals Transactions **50** (1957) 598-619
- 4) H. A. Saller, F. A. Rough and A. A. Bauer, Battelle Memorial Institute (USA), Report BMI-957 (1954)
- 5) R. J. van Thyne and D. J. McPherson, Amer. Soc. Metals Transactions **50** (1957) 576-591
- 6) V. W. Storhak, A. A. Bauer and R. F. Dickerson, Battelle Memorial Institute (USA), Report BMI-1278 (1958)
- 7) R. K. McGeary, Westinghouse Atomic Power Division (USA), Report WAPD-127 (1955)

THE HIGH TEMPERATURE OXIDATION OF BERYLLIUM

PART V

IN MOIST CARBON DIOXIDE AND MOIST CARBON MONOXIDE

S. J. GREGG, R. J. HUSSEY and W. B. JEPSON

Department of Chemistry, University of Exeter, Exeter, UK

Received 2 January 1961

The chemistry and the kinetics of the oxidation of electrolytic flake beryllium in moist carbon dioxide and in moist carbon monoxide (either gas, total pressure 10 cm of mercury; partial pressure of water, 1.2 cm) have been investigated at temperatures in the ranges 500° to 750° C and 600° to 700° C respectively. In moist carbon dioxide, the reaction with water vapour predominates over that with carbon dioxide in the proportions of approximately 4:1; the reactions are: $\text{Be} + \text{H}_2\text{O} = \text{BeO} + \text{H}_2$; $\text{Be} + \text{CO}_2 = \text{BeO} + \text{CO}$ and $2\text{Be} + \text{CO}_2 = 2\text{BeO} + \text{Be}_2\text{C}$. The oxidation is protective up to 600° C and non-protective at 650° C and above; the reaction after breakaway takes place at the particle boundaries giving rise to an interpenetrating region of oxide and unattacked metal. In moist carbon monoxide, the principal reaction is with water vapour and the reaction $\text{Be} + \text{CO} = \text{BeO} + \text{C}$ only contributes about 3 % to the total weight gain. An investigation of the oxidation in a moist carbon monoxide-carbon dioxide mixture (partial pressures: water, 1.2 cm; carbon monoxide, 0.5 cm; carbon dioxide, 8.3 cm) at 700° C shows that the kinetics are the same as in moist carbon dioxide, the reaction with carbon monoxide only contributing 0.2 % to the total weight gain.

La cinétique et la chimie de l'oxydation de paillettes de béryllium d'origine électrolytique ont été étudiées respectivement:

- sous atmosphère de CO_2 humide dans un domaine de températures allant de 500° C à 750° C.
- sous atmosphère de CO humide dans un domaine de températures allant de 600° C à 700° C.

(Dans les deux cas la pression totale était de 10 cm de mercure et la pression partielle de vapeur d'eau 1,2 cm.) En atmosphère de CO_2 humide, la réaction avec la vapeur d'eau est sensiblement 4 fois plus importante qu'avec le CO_2 . Les réactions sont les

suivantes: $\text{Be} + \text{H}_2\text{O} = \text{BeO} + \text{H}_2$; $\text{Be} + \text{CO}_2 = \text{BeO} + \text{CO}$ et $2\text{Be} + \text{CO}_2 = 2\text{BeO} + \text{Be}_2\text{C}$. L'oxydation crée un film protecteur jusqu'à 600° C; à 650° C et au-delà la couche oxydée cesse d'être protectrice. Après rupture du film (breakaway) la réaction a lieu aux contours des particules en formant ainsi une région où l'oxyde et le métal inattaqué sont intimement mêlés.

En atmosphère de CO humide, la réaction principale a lieu avec la vapeur d'eau et la réaction $\text{Be} + \text{CO} = \text{BeO} + \text{C}$ contribue seulement pour environ 3 % du gain de poids total. Une étude de l'oxydation à 700° C dans un mélange oxyde de carbone-gaz carbonique humide (pression partielle de l'eau 1,2 cm, pression partielle de l'oxyde de carbone 0,5 cm, pression partielle du gaz carbonique; 8,3 cm) montre que la cinétique est du même type que celle observée avec le gaz carbonique humide, la réaction avec l'oxyde de carbone contribuant seulement pour 0,2 % du gain de poids total.

Die Chemie und Kinetik der Oxydation von elektrolytischem Flocken-Beryllium in feuchtem Kohlendioxyd und feuchtem Kohlenmonoxyd (Gas, Totaldruck von 10 cm Hg; Teildruck des Wassers 1,2 cm) wurde untersucht bei Temperaturen von 500–750° C und 600–700° C. In feuchtem Kohlendioxyd überwog die Reaktion mit Wasserdampf über die Reaktion mit Kohlendioxyd in dem Verhältnis von annähernd 4:1. Die Reaktionen sind: $\text{Be} + \text{H}_2\text{O} = \text{BeO} + \text{H}_2$; $\text{Be} + \text{CO}_2 = \text{BeO} + \text{CO}$ und $2\text{Be} + \text{CO}_2 = 2\text{BeO} + \text{Be}_2\text{C}$. Die Oxydation wirkt schützend bis 600° C und nicht schützend ab 650° C und darüber. Die Reaktion nach dem Zerbrechen findet an den Korngrenzen statt und ergibt einen Abschnitt, in dem sich Oxyd und unangegriffenes Metall gegenseitig durchsetzen. In feuchtem Kohlenmonoxyd spielt sich die prinzi-

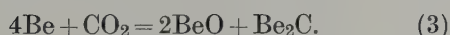
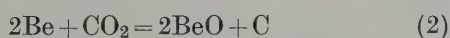
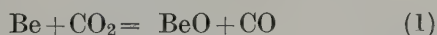
pielle Reaktion mit Wasserdampf ab, während die Reaktion $\text{Be} + \text{CO} = \text{BeO} + \text{C}$ nur einen Anteil von 3 % an dem Gesamtgewichtsgewinn hat. Eine Untersuchung der Oxydation in einem feuchten Kohlenmonoxyd-Kohlendioxyd-Gemisch (Partialdrücke:

Wasser 1,2 cm; Kohlenmonoxyd 0,5 cm; Kohlendioxyd 8,3 cm) bei 700° C zeigt, dass die Kinetik der in feuchtem Kohlendioxyd entspricht. Die Reaktion mit Kohlenmonoxyd liefert nur einen Beitrag von 0,2 % zum Gesamtgewichtsgewinn.

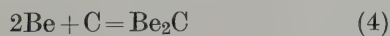
1. Introduction

In Parts II ¹⁾ and III ²⁾ of this series, the chemistry and the kinetics of the oxidation of electrolytic flake beryllium in dry carbon dioxide and in dry carbon monoxide between 500° and 750° C were described. In the present Part, the studies have been extended to the oxidation in moist carbon dioxide and in moist carbon monoxide. The only published work on the oxidation of beryllium in moist carbon dioxide appears to be that of Munro and Williams ³⁾ covering the temperature range 500° to 700° C; there appears to be no published work on the oxidation of beryllium in moist carbon monoxide.

The chemistry of the reaction in either of the moist gases is in principle more complicated than in the corresponding dry gas because the beryllium may react with either one or both of the components. In carbon dioxide the following reactions are thermodynamically possible at the temperatures (500°–750° C) and pressures (10 cm of mercury) of the present work ¹⁾.



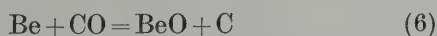
There is the possibility that carbon deposited in reaction (2) may react with beryllium according to



and with carbon dioxide according to



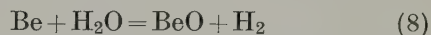
In carbon monoxide the chemistry is simpler and is confined to the reactions



with the possibility of the carbon deposited in (6) reacting with beryllium as in (4). Finally the carbon monoxide may equilibrate on the sample surface according to (5).

In Part II ¹⁾, reactions (1), (2) and (6) were shown to occur in the dry gases and in Part III ²⁾ it was argued on kinetic grounds that the beryllium carbide, whose presence was demonstrated, was formed indirectly by reaction (4) rather than directly by reactions (3) and (7).

Water vapour can only react with beryllium according to



since beryllium hydroxide is unstable at the temperatures and partial pressure of water vapour (1.2 cm) of the present work ⁴⁾.

The present investigation shows that when beryllium is oxidised in either moist carbon dioxide or moist carbon monoxide, both components react although in moist carbon monoxide the reaction is predominantly one with water vapour. The reactions which occur in the dry gases also occur in the presence of water vapour. The kinetics at a given temperature bear more resemblance to those in water vapour than to those in either of the dry gases.

2. Experimental

The electrolytic flake beryllium was of the same batch as that used for the oxidation studies in dry carbon dioxide and the analysis is given in Part I ⁵⁾. As in all the previous studies, each sample was chemically polished before use for 30 sec at 100° C in an aqueous solution of chromic, phosphoric and sulphuric acids. The carbon dioxide and carbon monoxide, which were isotopically labelled with C¹⁴, were prepared in the same manner as described in Part II ¹⁾.

The course of the oxidation was followed by measuring the total weight gain (deposited

carbon and combined oxygen) on a vacuum microbalance¹⁾ capable of detecting a weight gain of $1.7 \mu\text{g}$. The runs in both moist carbon dioxide and carbon monoxide were carried out with a total pressure of gas of 10 cm containing a partial pressure of water of 1.2 cm, equivalent to the saturation vapour pressure at 15°C .

Now during the oxidation of beryllium in dry carbon dioxide and carbon monoxide²⁾, a troublesome feature of the results was the rapid initial weight gain which occurred when the gas was admitted to the pre-heated sample and which amounted to as much as 50 % of the total weight gain registered after 300 h in carbon dioxide at 750°C . It was found that this initial weight gain could be avoided if the

sample were heated from room to reaction temperature in the gas and accordingly this procedure was adopted in the present work. Usually, about one hour elapsed before the sample had reached the temperature of the run so that no data are available over this initial period.

3. Results

3.1. IN MOIST CARBON DIOXIDE

3.1.1. Kinetics

The course of the oxidation of electrolytic flake beryllium in moist carbon dioxide at a total pressure of 10 cm (partial pressure of water of 1.2 cm) was followed on the micro-

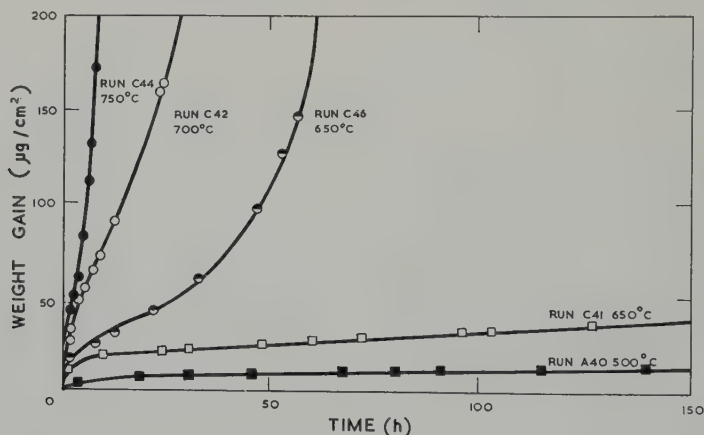


Fig. 1. Oxidation of beryllium at 500° , 650° , 700° and 750°C in moist carbon dioxide at a total pressure of 10 cm with 1.2 cm partial pressure of water.

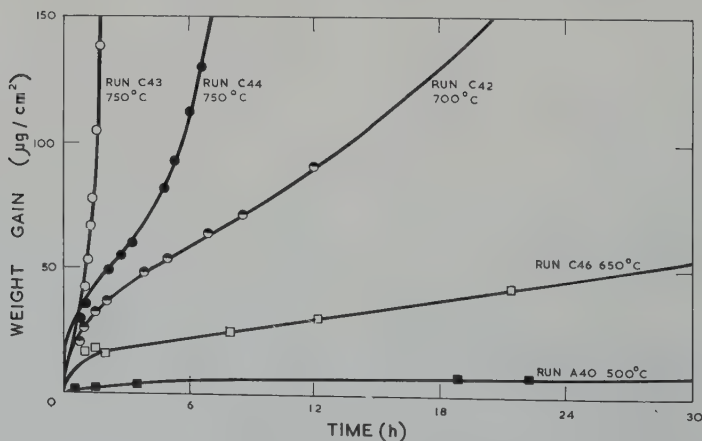


Fig. 2. Oxidation of beryllium at 500° , 650° , 700° and 750°C in moist carbon dioxide at a total pressure of 10 cm with 1.2 cm partial pressure of water. Showing the first 30 h.

balance at temperatures of 500°, 650°, 700° and 750° C; in supplementary test runs carried out at 500°, 550°, 600° and 650° C, the course of the oxidation was not followed, the samples being weighed before and after oxidation only.

The results are summarised in figs. 1 and 2 where the *total* weight gain is plotted against time whilst table 1 gives the weight of deposited carbon (w_c) and of combined oxygen (w_o) on the samples at the end of each run.

It is clear that the kinetics fall into two groups corresponding to the temperature ranges 500°–600° C and 700°–750° C respectively. Thus in the range 500°–600° C, the oxidation is protective at any rate within the first 300 h:

TABLE 1
Oxidation of beryllium in moist carbon dioxide

Run No. ^{b, c, d}	Length of run (h)	Temp. (°C)	w_c ^a ($\mu\text{g}/\text{cm}^2$)	w_o ^a ($\mu\text{g}/\text{cm}^2$)	w_c/w_o %
A40	151	500	0.1	13.1	0.8
A52	296		0.1	11.0	0.9
A53	168		0.1	13.2	0.8
A54	301	550	0.2	9.0	2.2
A55	152		0.1	10.2	1.0
A56	300	600	2.9	50.2	5.8
A57	152		0.4	23.0	1.7
C41*	240	650	1.6	43.2	3.7
C46	57		10.9	135.9	8.0
A49	100		41.1	658.9	6.2
A50	299		69.4	3365.4	2.1
A51	50		8.1	78.9	10.3
C42*	24	700	8.9	155.4	5.7
C43*	2		9.4	169.2	5.6
C44	8	750	4.2	168.2	2.5
C45	1		2.7	34.4	7.9

^a w_c is the weight of deposited carbon and w_o the weight of oxygen taken up as beryllium oxide;

^b the letters A and C before the run number indicate sample sizes of 4×1.5 cm and 3×1.5 cm respectively;

^c Runs 40–46 were carried out on the vacuum microbalance;

^d* the asterisk denotes those samples which were sectioned and examined metallographically.

the run at 500° C on the microbalance (fig. 1) shows that the rate of oxidation continually decreases with time to reach the negligibly small value of $0.03 \mu\text{g}/\text{cm}^2 \cdot \text{h}$ after about 70 h whilst the total weight gain of $13 \mu\text{g}/\text{cm}^2$ corresponds to an increase in film thickness above the "room-temperature" value of only 650 Å. This result was confirmed by the two test runs at 500° C (A52 and A53, table 1) and the weight gains are in good agreement with that obtained in the microbalance run. The test runs at 550° and 600° C (table 1) show that the weight gain on oxidation is again small, being comparable with that at 500° C, so that presumably the oxidation curves at these temperatures are similar to the one shown in fig. 1 for 500° C.

The oxidation curves at 700° and 750° C (figs. 1 and 2) are distinguished from that at 500° C (fig. 1) by the fact that breakaway occurs, the rate of oxidation first decreasing and then increasing with time. Reference to fig. 2 will show that breakaway occurs after a shorter time at 750° than at 700° C (2 h compared with 8 h). The rate after breakaway is considerable, that at 750° C (run C43) being $200 \mu\text{g}/\text{cm}^2 \cdot \text{h}$.

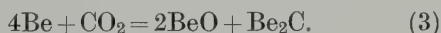
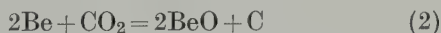
The temperature 650° C appears to represent a transition between the protective oxidation at 600° C and below and the non-protective oxidation at 700° C and above. Thus of the two runs on the microbalance at 650° C, one conformed to the low temperature pattern (run C41, fig. 1) in that the rate of oxidation continuously decreased with time and the weight gain after 240 h was only $45 \mu\text{g}/\text{cm}^2$, whilst with the other (Run C46, fig. 1) breakaway occurred (but after a longer time than at 700° C) and the weight gain after only 57 h was $147 \mu\text{g}/\text{cm}^2$. Judging by the total weight gain, breakaway occurred in two of the three test runs at 650° C (A49 and A50, table 1) and in one of them, the weight gain was $3400 \mu\text{g}/\text{cm}^2$ after 300 h.

3.1.2. Chemistry

The presence of (C^{14} -labelled) carbon on the oxidised beryllium samples was revealed by placing them below a 2.4 cm diameter end-

window Geiger-Müller tube, and by successively counting over the two faces of each specimen²⁾ it was possible to estimate the amount of deposited carbon (w_c). The results are shown in table 1 together with the amount of combined oxygen (w_o); it will be seen that the values of w_c follow the same general trend as w_o , the more heavily oxidised samples showing a greater amount of carbon deposition. The trend is less marked when the results are expressed as the ratio w_c/w_o , although higher temperatures again favour a higher value of this ratio.

It may be concluded that carbon is deposited at all temperatures by one or both of the possible carbon deposition reactions:

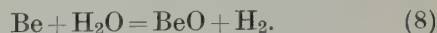


Evidence for the reaction



was provided by experiments at 550° and 650° C (Runs A55 and A50) in which, when the unreacted carbon dioxide and water vapour were condensed out at the end of the run, a radioactive gas remained which was presumably carbon monoxide. In the run at 650° C (A50), for which the weight gain was considerable, it was possible to estimate from the values of w_c , w_o and the amount of carbon monoxide

which was formed, the relative contributions of the three reactions (1), (2) (or (3)) and (8) to the total weight gain. This calculation shows that reaction (1) contributes 14.9 %, reaction (2) (or (3)) contributes 7.4 % so that the remaining 77.7 % is due to reaction with water vapour:



Stated in other terms, 29 molecules of water react for every 7 molecules of carbon dioxide and of the latter, 6 molecules react according to (1) and 1 molecule reacts according to (2) (or (3)).

The rate of carbon deposition during oxidation in moist carbon dioxide at a total pressure of 2 cm (including a partial pressure of 0.46 cm of water) was measured at 650°–750° C on the volumetric apparatus¹⁾ which was modified to include a bulb containing liquid water surrounded by melting ice at 0° C. Unfortunately, because of the necessarily small volume of the apparatus and therefore of the narrow inter-connecting tubes, replenishment of the oxidised gases in the reaction chamber was probably slow; this was evidenced by the fact that after condensing out the carbon dioxide and water vapour at the end of one run at 700° C (C60), there was a residual pressure of a non-radioactive gas which disappeared on leaving overnight in contact with the heated cupric oxide.

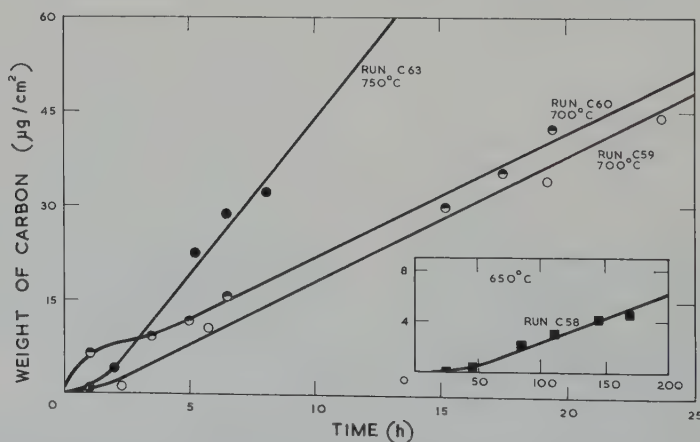


Fig. 3. Oxidation of beryllium at 650°, 700° and 750° C showing the rate of carbon deposition in moist carbon dioxide at an initial pressure of 2 cm with a partial pressure of water of 0.46 cm.

This gas was presumably hydrogen (formed in (8)) which had not been converted back to water vapour during the run. Since the composition of the oxidising gas was not well defined, the results can only be regarded as semi-quantitative; they do show however (fig. 3) that carbon deposition occurs throughout the run; further, since as judged by the total weight gain (table 2), breakaway had occurred in all the runs, the curves show that carbon dioxide continues to react with beryllium after breakaway. As a check, the amount of carbon deposited on the samples in the experiments of fig. 3 and table 2 was determined by a direct count at the end of each run, and satisfactory agreement with the calculated values of table 2 was found.

Finally, as with oxidation in dry carbon dioxide, there is the possibility of beryllium carbide being formed directly (by (3)) or indirectly (by (4)); the kinetic measurements do not distinguish between these possibilities. Evidence for the presence of beryllium carbide in the oxide layer was however provided by an experiment (C63) at 750° C on the volumetric apparatus when a sample was first oxidised in moist carbon dioxide for 8 h by which time 32 $\mu\text{g}/\text{cm}^2$ of carbon had been deposited on the sample; the carbon dioxide was then pumped out of the apparatus and the sample then exposed to water vapour at 750° C. A radioactive gas built up in the apparatus and in the 3 h period of

the test, carbon equivalent to 1.3 $\mu\text{g}/\text{cm}^2$ of sample was returned to the gas phase, presumably as methane resulting from the hydrolysis

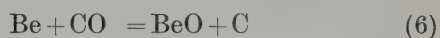


The occurrence of (5), $\text{C} + \text{CO}_2 = 2\text{CO}$, was not investigated and it is assumed that, as for oxidation in dry carbon dioxide, it does not occur.

3.2. IN MOIST CARBON MONOXIDE

The study of the kinetics of the oxidation of beryllium in moist carbon monoxide at a total pressure of 10 cm (partial pressure of water, 1.2 cm) was confined to the three temperatures 600°, 650° and 700° C; the results are shown in figs. 4 and 5 where the total weight gain is plotted against the time. It will be seen (fig. 4) that at 600° and 650° C, the rate of oxidation decreases with time to reach values of 0.1 and 1.0 $\mu\text{g}/\text{cm}^2$ at 150 and 100 h respectively whilst at 700° C (fig. 5) the rate of oxidation was increasing when the run was stopped after 5 hours' oxidation.

The amount of carbon (w_c) deposited on the sample at the end of each run was measured and the results are shown in table 3 together with the amount of combined oxygen (w_o); since there are no gaseous oxidation products when carbon monoxide reacts with beryllium, it is possible to compare the relative proportions of the two reactions



and



(No distinction is made here between (6) and (7)). This comparison is made in table 3 where the weight of carbon monoxide reacted is expressed as a percentage of the total weight gain, and it is evident that reaction (8) predominates over reaction (6) at all temperatures; the oxidation is predominantly due to water vapour.

3.3. IN A MOIST 5 % CARBON MONOXIDE-CARBON DIOXIDE MIXTURE

The oxidation of beryllium in a moist carbon monoxide-carbon dioxide mixture (10 cm total

TABLE 2

Oxidation of beryllium in moist carbon dioxide (volumetric method)

Run No.	Length of run (h)	Temp. (°C)	w_c ($\mu\text{g}/\text{cm}^2$)	w_o ($\mu\text{g}/\text{cm}^2$)	w_c/w_o (%)
C58	243	650	5.5	750	0.73
C59	30	700	51.7	spalled	—
C60	20		42.5	3097	1.37
C61	2	750	4.1	154	2.7
C63	8		31.6	not determined	—

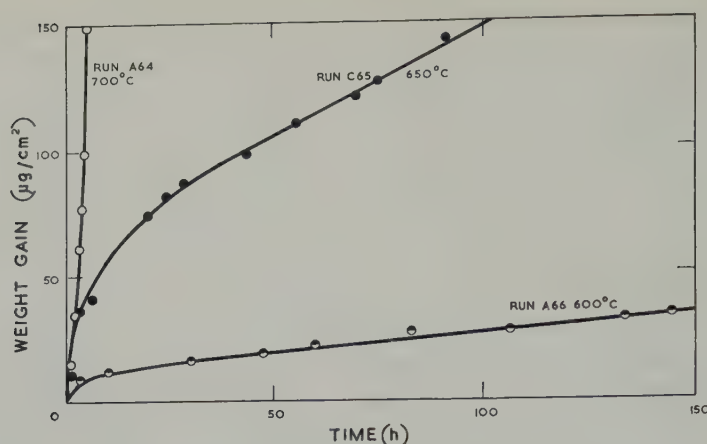


Fig. 4. Oxidation of beryllium at 600°, 650° and 700° C in moist carbon monoxide at a total pressure of 10 cm with 1.2 cm partial pressure of water.

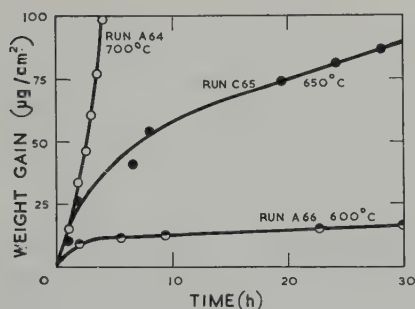


Fig. 5. Oxidation of beryllium at 600°, 650° and 700° C in moist carbon monoxide at a total pressure of 10 cm with 1.2 cm partial pressure of water. Showing the first 30 h.

pressure; partial pressure of water, 1.2 cm; partial pressure of carbon monoxide, 0.5 cm) was investigated at 700° C; of the four experiments which were carried out, the first was on the microbalance and the remainder were test runs, in which the sample was weighed on an

analytical balance at the start and at the end of the exposure. The oxidation curve is shown in fig. 6 together with comparison curves for the oxidation in moist carbon dioxide, moist carbon monoxide and water vapour.

The numerical data are summarised in table 4 as the total weight gain w and the amounts of carbon w_c' and w_c'' deposited as the result of reaction with carbon dioxide and with carbon monoxide respectively; it was possible to make this distinction experimentally by only labelling one of the reactants in each run. That the ratio w_c''/w is considerably less than the ratio w_c'/w (table 4) shows that there is little reaction between beryllium and carbon monoxide under these conditions. On the other hand, the values of w_c'/w are in relatively good agreement with the values of w_c/w_0 obtained for oxidation in moist carbon dioxide (table 1), suggesting that the reaction in the moist carbon monoxide-

TABLE 3
Oxidation of beryllium in moist carbon monoxide

Run No.	Length of run (h)	Temp. (°C)	Wt. of carbon monoxide reacted (μg/cm²) (A)	Total weight gain (μg/cm²) (B)	Ratio A/B per cent
A 66	145	600	1.9	33.3	5.7
A 65	91	650	3.0	143.2	2.1
A 64	5	700	4.0	149.5	2.7

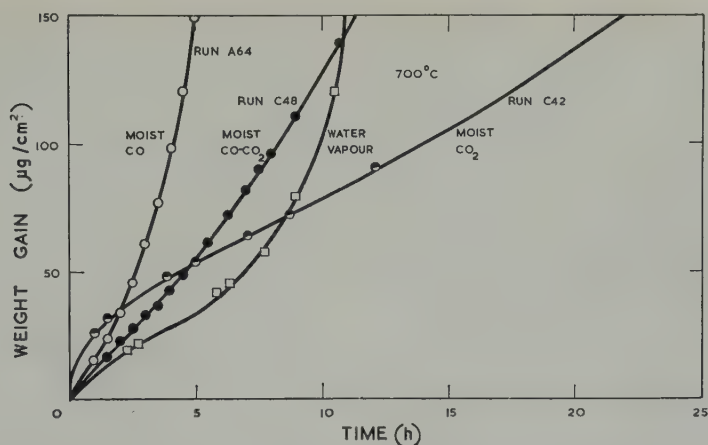


Fig. 6. Oxidation of beryllium at 700° C in moist carbon monoxide-carbon dioxide (10 cm total pressure; partial pressure of water, 1.2 cm; partial pressure of carbon monoxide, 0.5 cm). The oxidation is compared with that in moist carbon dioxide, moist carbon monoxide and water vapour (1.2 cm).

TABLE 4
Oxidation of beryllium in moist carbon monoxide-carbon dioxide at 700° C

Run No.	Length of run (h)	w'_c ^a (μg/cm ²)	w''_c ^a (μg/cm ²)	w ^a (μg/cm ²)	w'_c or w''_c/w (%)
C 47	24	33.4	—	876	3.8
C 48	11	9.7	—	139	7.0
C 67	51	—	2.2	3073	0.07
C 68	28	—	1.8	1065	0.2

^a w'_c and w''_c are the weights of carbon deposited as the result of reaction with carbon dioxide and with carbon monoxide respectively; w is the total weight gain.

^b Run C 48 was carried out on the microbalance.

carbon dioxide mixture is essentially the same as in moist carbon dioxide. This is borne out by the reasonable agreement (fig. 6) between the curve for oxidation in the moist carbon monoxide-carbon dioxide mixture with that for oxidation in moist carbon dioxide.

3.4. RADIOGRAPHIC AND METALLOGRAPHIC EXAMINATION OF OXIDISED SAMPLES

with R. T. PEPPER

Atomic Energy Division, GEC Erith, Kent, UK

Autoradiographs were taken of a number of the samples which had been oxidised in moist carbon dioxide and, as with oxidation in the dry gas²), the distribution of deposited carbon over the sample surface was by no means uniform (fig. 7). This was particularly the case

with those samples which had undergone break-away.

Those samples which had been oxidised in moist carbon dioxide at temperatures up to 650° C and for which breakaway had not occurred showed interference colours which varied from place to place over their surface. On the samples which had been oxidised in moist carbon dioxide at 700° and 750° C and which had undergone breakaway, interference colours were absent and the surface was grey in colour with raised blisters.

A number of the oxidised samples (table 1) were examined metallographically. For this purpose, each sample was sectioned and one half of it was mounted in "Araldite" resin and the cut surface was polished and examined. Coarse polishing was carried out on 180, 320

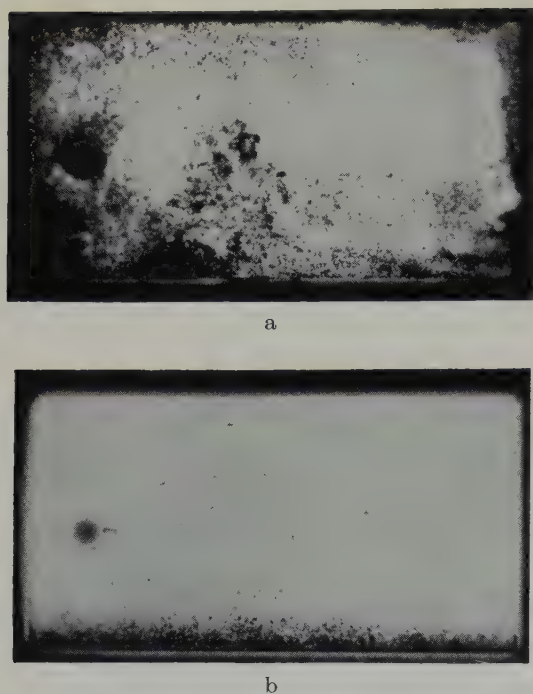


Fig. 7. Autoradiographs showing the variation in the distribution of carbon (elementary and combined) over the specimen surface. (a), the sample of Run C46; (b), the sample of Run C43. Magnification $\times 4$ before reduction for publication.

and 600 grade silicon carbide papers using water as lubricant, and fine polishing on diamond

polishing wheels of $6\ \mu$ and $0.25\ \mu$ grades. Each specimen was finally etched for 2 min in a 2 % solution of hydrofluoric acid in glycol.

The micrograph of the sample which had been oxidised at 750°C for 2 h (C43, table 1) is shown in fig. 8 and it is evident that penetration of the metal has occurred at the grain boundaries during oxidation. The sample oxidised at 700°C for 24 h (C42), which had also undergone breakaway gave a similar micrograph but the depth of penetration was less despite the fact that the weight gain was approximately the same as that of the 750° sample. Since no penetration could be detected on the sample oxidised at 650°C (C41) which had not undergone breakaway, it is evident that (as for oxidation in water vapour and in moist oxygen⁶) breakaway takes the form of attack down the particle boundaries with a corresponding increase in the geometrical area of metal available for oxidation.

Metallographic examination of a single "as-received" sample showed a zone of high inclusion content near the surface of one of the faces and that the inclusions were located at the grain boundaries (fig. 9). This zone of high inclusion content was about $100\ \mu$ thick and would therefore have not been removed if the sample

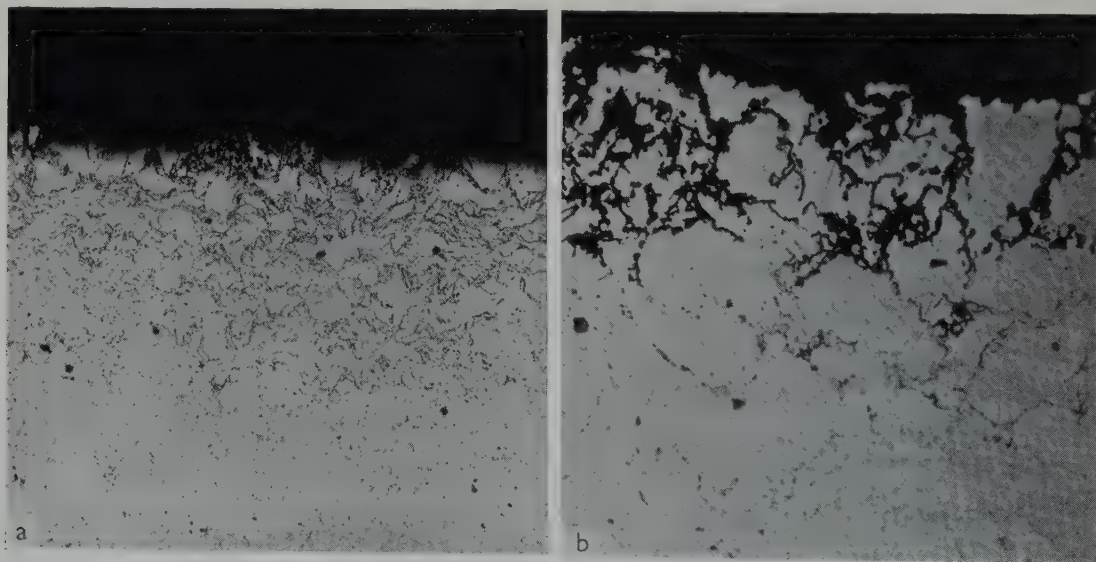


Fig. 8. Micrograph of a sample oxidised in moist carbon dioxide (C43) showing the intergranular penetration of oxide into the metal. Taper section of 3:1. Magnifications (a) $\times 100$; (b) $\times 500$.

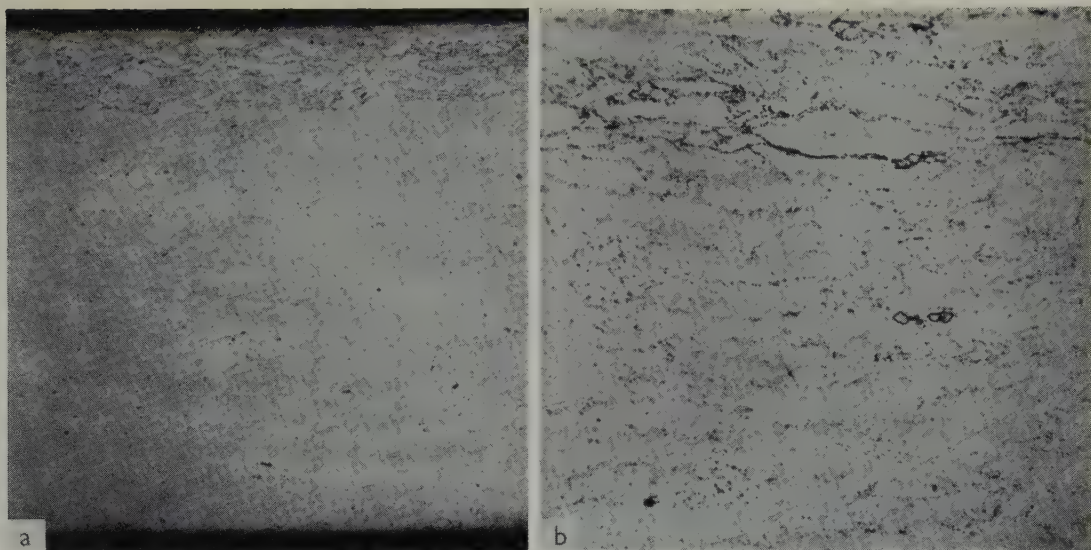


Fig. 9. Micrograph of an as received beryllium specimen showing the zone of high inclusion content at one face. (a) $\times 100$; (b) $\times 500$.

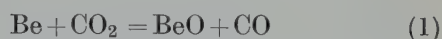
had been chemically polished (thickness removed is $7\ \mu$) according to the normal procedure of surface preparation prior to oxidation. Clearly, this particular sample was not homogeneous and it seems very reasonable to suppose that this may also have been true of some of the

other samples; this may be the key to the poor reproducibility between repeat runs which was a feature of the oxidation studies described in previous Parts. There is some evidence that regions of high inclusion content have a higher corrosion resistance (to water vapour) than regions of normal inclusion content; this fact is based on an examination of a sample (fig. 10) oxidised in moist carbon monoxide in the volumetric apparatus at 650°C where, as for oxidation in moist carbon dioxide (Sect. 3.1), the conditions were not well defined.

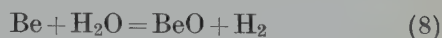
4. Discussion

4.1. OXIDATION IN MOIST CARBON DIOXIDE

The experimental results show that when electrolytic flake beryllium is oxidised in moist carbon dioxide (10 cm total pressure, 1.2 cm partial pressure of water) at temperatures between 500° and 750°C , both components react. The reactions



and



certainly occur, whilst the deposition of carbon on the sample surface which occurs at 550°C

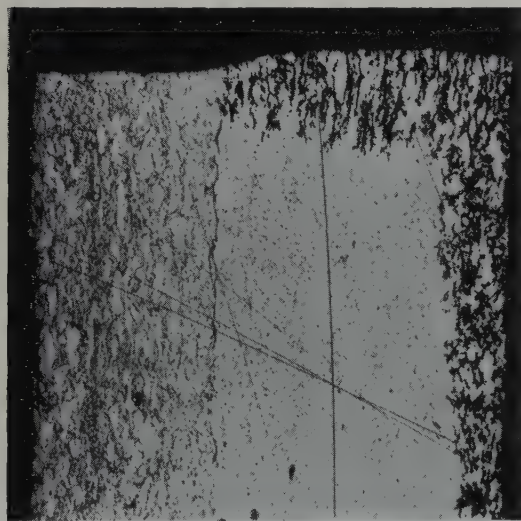
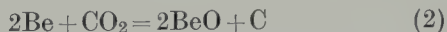
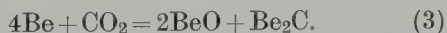


Fig. 10. Micrograph of a sample oxidised in moist carbon monoxide (2 cm total pressure, partial pressure of water 0.46 cm) on the volumetric apparatus at 650°C for 104 h. The oxidation conditions were not well defined (compare Sect. 3.1) but it is clear that the zone of high inclusion content shows a higher corrosion resistance. Magnification $\times 100$.

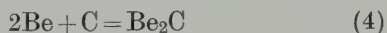
and above (deposition at 500° C is uncertain, table 1) must result from either one or both of the reactions



and



It is not possible to distinguish between reactions (2) and (3) from the kinetic measurements but it is believed that the beryllium carbide, whose presence was demonstrated on a sample which had been oxidised at 750° C, is formed indirectly by reaction of beryllium with deposited carbon



rather than directly by reaction (3). It can be argued along the lines developed in Part III ²⁾ that reaction (3), which would involve a transition state on the oxide surface between 4Be⁺⁺ ions and a carbon dioxide molecule, is less likely to occur than reaction (2) for which the transition state would involve only 2Be⁺⁺ ions.

Turning now to the quantitative aspects of the oxidation, it has only been possible to assess the relative contributions of reactions (1), (2) and (8) at 650° C; at this temperature reaction (8) predominates, contributing almost 78 % to the total weight gain, with reaction (1) contributing 15 % so that the contribution from the carbon deposition reaction (2) is only 7 %. These values refer of course to the total weight gain and it is possible that in the protective region of oxidation where the weight gains are much smaller (at 600° C and below, and up to the time at which breakaway occurs at the higher temperatures), the relative proportions of the reactions may change as the oxide layer thickens. Further, after breakaway, the metal/oxide interface is no longer distinct but consists of an interpenetrating network of oxide and unattacked metal and as for oxidation in moist oxygen the oxide is presumably porous (this was demonstrated in Part IV ⁶⁾); it follows that the carbon dioxide and water molecules must diffuse inwards against the outward diffusion of the reaction products, carbon monoxide and hydrogen. It is conceivable that the com-

position of the gas in the immediate vicinity of the metal may be significantly different from that in the bulk gas although judging from the results for oxidation in moist carbon monoxide, the effect of a local build up in the concentration of carbon monoxide might not be serious.

The relative contributions of the various reactions will be determined by two factors:

- (a) the relative number of sites which the carbon dioxide and water molecules occupy at the gas/oxide interface;
- (b) the relative rates of reaction of Be⁺⁺ ions with the respective adsorbed species.

A third possible factor, the rate of adsorption from the gas phase, can probably be discounted in view of the relatively high temperatures of the present work. No predictions can be made with regard to (b); but the fact that the water reaction predominates over the carbon dioxide reaction (in the proportion of about 4:1) is what would be expected from (a), in that water is probably more strongly chemisorbed than carbon dioxide (as evidenced by the fact that a temperature of 500° C is required to remove the last 10 % of moisture from beryllium hydroxide ³⁾ while ordinary beryllium carbonate is unknown).

At temperatures up to and including 600° C, the oxidation kinetics in dry carbon dioxide, moist carbon dioxide and water vapour are similar although a strict comparison is not possible because of the different starting procedures in the runs. At 650° C and above, on the other hand, breakaway occurs during oxidation in moist carbon dioxide and in water vapour whilst in the dry gas, the oxidation is protective at 700° C and even at 750° C, breakaway only occurred after oxidation for 150 h. Judging from fig. 11, the curves for beryllium in moist carbon dioxide are surprisingly similar to those for water vapour.

4.2. OXIDATION IN MOIST CARBON MONOXIDE

When electrolytic flake beryllium is oxidised in moist carbon monoxide (10 cm total pressure, 1.2 cm partial pressure of water) at temperatures

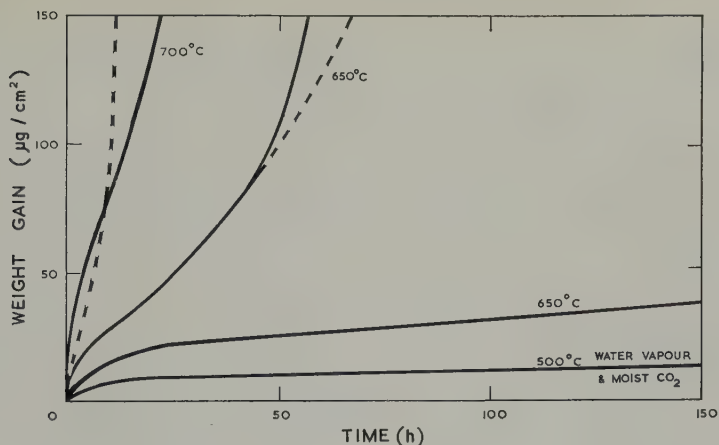


Fig. 11. Comparison of the oxidation of beryllium at 500°, 650° and 700° C in moist carbon dioxide (full line) with that in water vapour (1.2 cm, broken line). The experimental points are omitted for clarity.

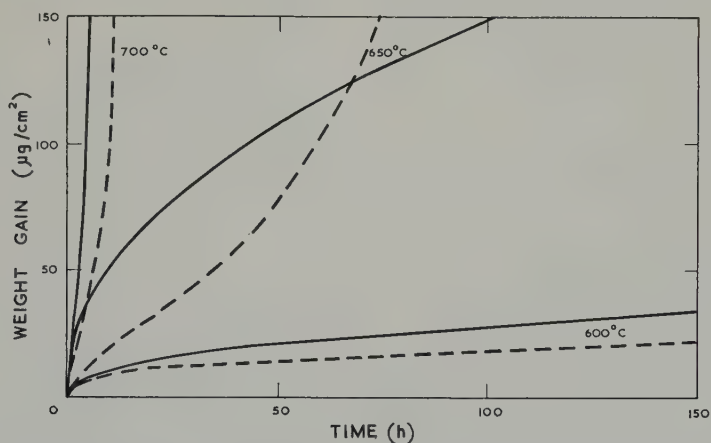
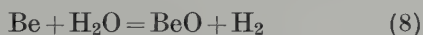


Fig. 12. Comparison of the oxidation of beryllium at 600°, 650° and 700° C in moist carbon monoxide (full line) with that in water vapour (1.2 cm, broken line). The experimental points are omitted for clarity.

of 600°, 650° and 700° C, the reaction with water vapour



predominates and the contribution of the reaction



to the total weight gain is only a few per cent. This would be expected in the light of the results for oxidation in moist carbon dioxide because of the much weaker chemisorption of carbon monoxide. (This point is also brought out by the results²) for the oxidation of beryllium in dry carbon monoxide-carbon dioxide mixtures at 650° C; here there exists a minimal

concentration of carbon monoxide (about 90 %) below which the reaction is essentially one with carbon dioxide alone).

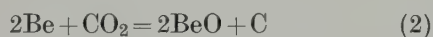
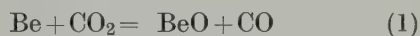
A novel feature of the results is that whereas the oxidation of beryllium in carbon monoxide is non-protective at 550° C and above, the oxidation even at 600° C in moist carbon monoxide is still protective (fig. 4) just as it is in water vapour; this is clearly because reaction (8) predominates. As judged from fig. 12, which compares the oxidation of beryllium in moist carbon monoxide with that in water vapour, there appears to be a significant difference between the two gases although further work is needed to confirm this point.

4.3. OXIDATION IN MOIST CARBON MONOXIDE-CARBON DIOXIDE

As is to be expected in the light of the results for oxidation in moist carbon dioxide and moist carbon monoxide, when beryllium is oxidised in a moist carbon monoxide-carbon dioxide mixture, the reaction is essentially the same as in moist carbon dioxide (fig. 6). The carbon monoxide plays a negligible part in the reaction, the contribution to the total weight gain being only about 0.2 % (table 4).

5. Conclusions

When electrolytic flake beryllium is oxidised in moist carbon dioxide (10 cm total pressure, 1.2 cm partial pressure of water) between 500° and 750° C, both the water and the carbon dioxide react with the metal. The reactions with carbon dioxide



are the same as in the dry gas and it is believed that the beryllium carbide, which is found in the oxide layer, is formed indirectly



rather than directly. At 650° C, 29 molecules of water react for every 7 molecules of carbon dioxide and of the latter, 6 molecules react according to (1) and 1 molecule reacts according to (2). At temperatures up to 600° C, the rate of oxidation continuously decreases with time and the oxidation is protective; at 650° C and above, the oxidation is non-protective and the

reaction after breakaway takes the form of penetration between the grains of the metal. The kinetics are remarkably similar to those in water vapour.

In moist carbon monoxide (10 cm total pressure, 1.2 cm partial pressure of water) at 600° to 700° C, the reaction is essentially one with water vapour, the reaction with carbon monoxide only contributing a few per cent to the total weight gain. Similarly the oxidation in a moist carbon monoxide-carbon dioxide mixture (10 cm total pressure, 1.2 cm partial pressure of water, 0.5 cm partial pressure of carbon monoxide) at 700° C is similar to that in moist carbon dioxide; here the reaction with carbon monoxide only contributes 0.2 % to the total weight gain.

Acknowledgements

It is a pleasure to thank Mr. R. T. Pepper for carrying out the metallographic work, and Dr. J. E. Antill for his continued interest. We are also grateful to the U.K. Atomic Energy Authority for their support of this work.

References

- ¹) S. J. Gregg, R. J. Hussey and W. B. Jepson, *J. Nucl. Mat.* **2** (1960) 225
- ²) S. J. Gregg, R. J. Hussey and W. B. Jepson, *J. Nucl. Mat.* **3** (1961) 175
- ³) W. Munro and J. Williams, Harwell (UK), Report AERE M/M 108 (1956)
- ⁴) P. Murray and R. W. Thackray, Harwell (UK), Report AERE M/R 1410 (1954)
- ⁵) D. W. Aylmore, S. J. Gregg and W. B. Jepson, *J. Nucl. Mat.* **2** (1960) 169
- ⁶) D. W. Aylmore, S. J. Gregg and W. B. Jepson, *J. Nucl. Mat.* **3** (1961) 190

THE SOLID SOLUBILITY OF ZIRCONIUM IN α -THORIUM

R. H. JOHNSON † and R. W. K. HONEYCOMBE

Department of Metallurgy, Sheffield University, Sheffield 1, UK

Received 5 January 1961

Metallographic and X-ray diffraction methods have been used to determine the solid solubility of zirconium in α -thorium. The solubility changes from 5.0 at % at 650° C to 9.9 at % at 920° C and reaches a maximum of 10.2 at % in the range 940° C–1000° C. Data for both iodide and electrolytic thorium are given.

Les méthodes d'examen métallographique et de diffraction par rayons X ont été utilisées pour déterminer la solubilité à l'état solide du Zr dans le thorium α . La solubilité varie de 5 at % à 650° C à 9,9 at % à 920° C et atteint un maximum de 10,2 at % dans

le domaine de températures compris entre 940°–1000° C. Les résultats obtenus soit avec le thorium d'origine électrolytique, soit avec le thorium ex-iodure sont mentionnés successivement.

Metallographische und Röntgenbeugungsmethoden werden zur Bestimmung der Löslichkeit in festem Zustand von Zirkon in α -Thorium benutzt. Die Löslichkeit wechselt von 5,0 At % bei 650° C zu 9,9 At % bei 920° C und erreicht ein Maximum von 10,2 At % in dem Temperaturintervall von 940° bis 1000° C. Ausserdem sind Daten von Iodid und elektrolytischem Thorium angegeben.

1. Introduction

The present study of the solubility of zirconium in α -thorium was carried out to provide essential basic information prior to an investigation on the age-hardening behaviour of thorium-zirconium alloys. A previous study of the thorium-zirconium binary system was carried out by Carlson in 1950¹). However, owing to the low purity of the alloys in this early work the results, particularly the metallographic interpretations, were of doubtful validity. This probably accounts for the modifications to the diagram which appeared later in a compilation of thorium phase diagrams²). Further work on the thorium-rich end was reported to have been carried out, but no details were given and the α -thorium solid solution boundary was again represented by a dotted line. Additional work on the thorium-zirconium system³) using materials of higher purity was published when this research was in progress, but the need for an accurate survey of the α -thorium solid solution boundary remained.

2. Experimental Techniques

2.1. MATERIALS

Two grades of material were employed. The basic raw material was electrolytically prepared thorium dendrites containing at least 1 wt % oxide. Hand-picking of the non-metallics (ceramic fragments in the form of blue-grey plates and grey masses suspected to be chiefly thoria) was carried out after washing with 5 % nitric acid. To eliminate further the impurities associated with the thorium, the coarse fraction from sieving with a 50 mesh sieve was taken for melting. This preliminary preparation gave figures of 99.8 wt % thorium, 0.19 wt % oxygen as oxide, and 50–63 VPN hardness after consolidation by argon arc melting. The full analysis of an average arc melted button is given in table 1. A small amount of iodide thorium was available to make critical alloys; a typical (not actual) analysis of the iodide thorium is also shown in table 1, together with an analysis of the iodide zirconium used in alloying.

† Now at the Berkeley Nuclear Laboratories of the Central Electricity Generating Board.

TABLE I
Analyses of starting materials

	Thorium		Zirconium
	arc-melted sample	iodide bar †	iodide bar †
Total thorium	99.8 wt %	—	—
Oxygen	0.15, 0.22, 0.21 wt %	not available ††	0.004–0.022 wt %
Carbon	50–170 ppm	—	—
Nitrogen	—	60 ppm	20–50 ppm
Hydrogen	—	—	30 ppm
Calcium	270 ppm	200 ppm	—
Iron	170 ppm	20 ppm	—

† typical, not actual analyses. †† hardness 19–38 VPN.

2.2. PREPARATION OF ALLOYS

The weight losses on arc-melting in a zirconium-gettered argon atmosphere were negligible and as a result of the agreement between the nominal composition and the analysis of a number of alloys made at the start of the work, later alloys were not analysed. All ingots were reduced by cold work together with many intermediate anneals. This not only ensured sufficient, suitably-sized, specimens for heat-treatment but also assisted greatly in obtaining homogeneous material. The alloy ingots were reduced to 6 mm square bar to provide specimens for the microscopic work and to 1.5 mm square rod for the X-ray work. For heat-treatment, the specimens were tightly wrapped in tantalum foil and sealed in silica tubes under vacuum or a reduced pressure of gettered argon calculated to produce a slight positive pressure inside the capsule at the temperature of treatment.

2.3. METALLOGRAPHY

The micro-examination of thorium and its alloys presents certain difficulties, consequently after using the conventional methods to obtain a polished and scratch-free surface, several techniques were employed to assist in the interpretation of the microstructures. Specimens often had to be examined by each of the following methods in turn before satisfactory conclusions could be reached.

Diamond-polished specimens, on standing in

the atmosphere, exhibit preferential tarnishing of the α -thorium solid solution phase which provides a sufficiently high degree of contrast to distinguish it from a second phase. Untarnished surfaces could be obtained by attack-polishing after diamond polishing, using a suspension of gamma-alumina in various solutions, usually a chromic oxide-nitric acid mixture⁴). Such specimens were usually etched by argon ion bombardment following the procedure described by Armstrong *et al.*⁵).

Very satisfactory electrolytically-prepared surfaces were obtained using the Shandon electrolytic cell⁶). The basic conditions were an etch, after diamond polishing, of 7–10 seconds at 8–20 V (0.25 A/cm²) in a solution containing 10 parts by volume of glacial acetic acid and 1 part by volume of perchloric acid at room temperature.

2.4. LATTICE PARAMETER MEASUREMENT

Due to the difficulties associated with the heat-treatment of the filings of a metal which is both reactive and radioactive, thin rod specimens were used (1.5 mm square). After heat-treatment, the rods were thinned by etching. A 9 cm Debye–Scherrer camera was used and gave sharp X-ray diffraction patterns from the rods which were relatively fine-grained because of the restraining influence of oxide inclusions on grain-growth⁷). Unfiltered radiation from a copper target under standard conditions gave at least five high angle lines

with θ values in the range 84 – 72° . The wavelengths⁸⁾ used were $\lambda_{\alpha_1} = 1.53740$ kX; $\lambda_{\alpha_2} = 1.54122$ kX; $\lambda_{\beta} = 1.38936$ kX (Cauchois and Hulubei, 1947). Film measurements were made to 0.05 mm and after calculation of the parameters the values were plotted against the Nelson–Riley function from which an extrapolation was made to give the lattice constant at $\theta = 90^\circ$. Accuracy to ± 0.0002 kX was usually obtained but in films where the maximum θ value was less than 80° , or where the points in the Nelson–Riley extrapolation graph showed more variance than usual, the error was appropriately larger.

3. Results

3.1. MICROSTRUCTURES

Results of the microscopic examination of alloys up to 16 at % zirconium, heat-treated in the range 600 – 1360°C , are presented in fig. 1. The majority of the specimens used were made from electrolytic thorium.

The second phase in the microstructures was tarnish resistant, as expected from the higher zirconium content. Typical structures are shown in figs. 2 and 3. The matrix is tarnished α -thorium solid solution and the grey-black particles are thorium oxide, ThO_2 . There are differences in the appearance of the zirconium-rich phase after etching. Above the monotectoid horizontal, β is present which transforms on quenching and can appear partly acicular (fig. 4) or as a weave pattern (fig. 5).

When attempting to bracket the phase boundary, it was difficult to decide whether an alloy was single or two phase due to the presence of inclusions. However, an estimation of the position of the phase boundary for two series of quenches (900°C and 1000°C) using alloys made entirely from iodide materials was carried out by quantitative metallography on the untarnished β phase in diamond-polished specimens. These metallographic methods could only be considered as a guide to the location of the boundary and therefore the lattice parameter method was applied to obtain the phase boundary precisely.

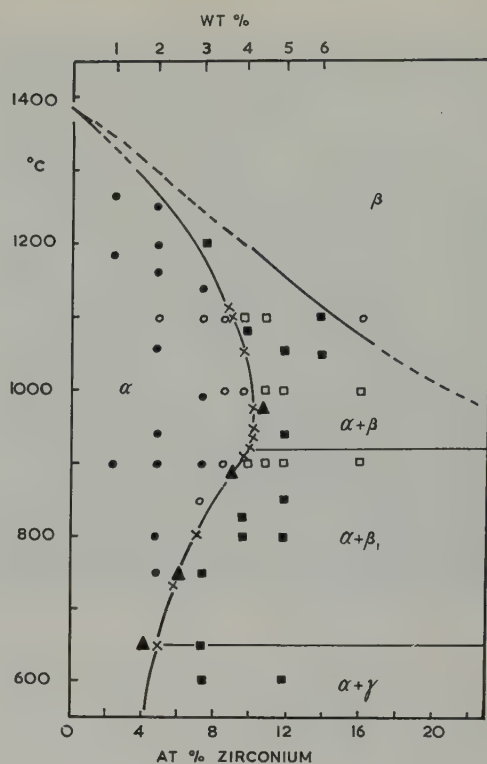


Fig. 1. Phase diagram of thorium-zirconium alloys containing 0–16 at % zirconium.

Key \times lattice parameter work on *iodide* thorium alloys
 \blacktriangle lattice parameter work on *electrolytic* thorium alloys
 \circ single phase microstructure, *iodide* thorium alloys
 \bullet single phase microstructure, *electrolytic* thorium alloys
 \square two phase microstructure, *iodide* thorium alloys
 \blacksquare two phase microstructure, *electrolytic* thorium alloys.

3.2. LATTICE PARAMETERS

The actual phase boundary line drawn in fig. 1 is the result of X-ray work on iodide thorium-zirconium alloys. The lattice spacing values for the solid solution alloys taken from table 2 are represented graphically in fig. 6 and were obtained by averaging the parameters of several specimens of the same composition after different heat-treatments in the α -solid solution region. The good agreement of these lattice spacing values meant that the error for each alloy was sufficiently low to

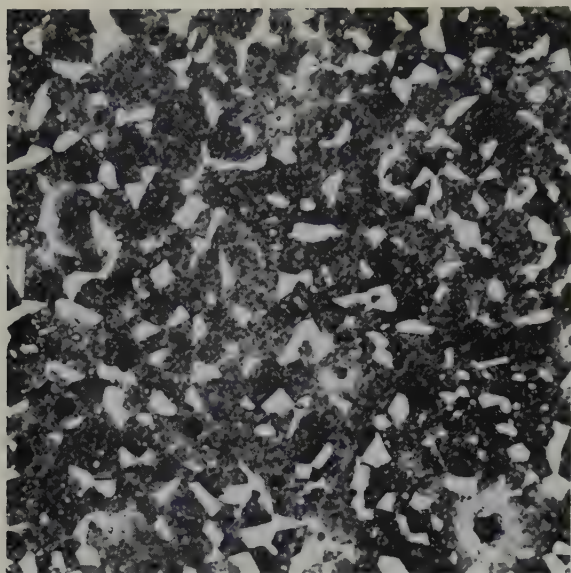


Fig. 2. 11.8 at % zirconium alloy. Annealed at 1000° C, for 7 days and water-quenched. Matrix is tarnished α , white phase is β . Black particles with halos are thoria. Diamond polished. $\times 150$.

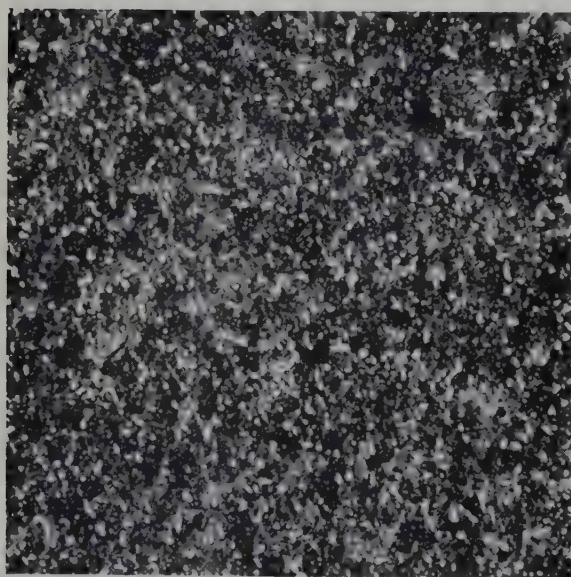


Fig. 3. 11.8 at % zirconium alloy. Annealed at 900° C for 21 days and water-quenched. Matrix is tarnished α , white phase is β_1 . Diamond polished. $\times 150$.



Fig. 4. 10.8 at % zirconium alloy. Annealed at 1100° C for 7 days and water-quenched. The transformed β phase is heavily outlined and possesses grains, some with acicular markings. The α phase is pitted. Electrolytic polish. $\times 750$.

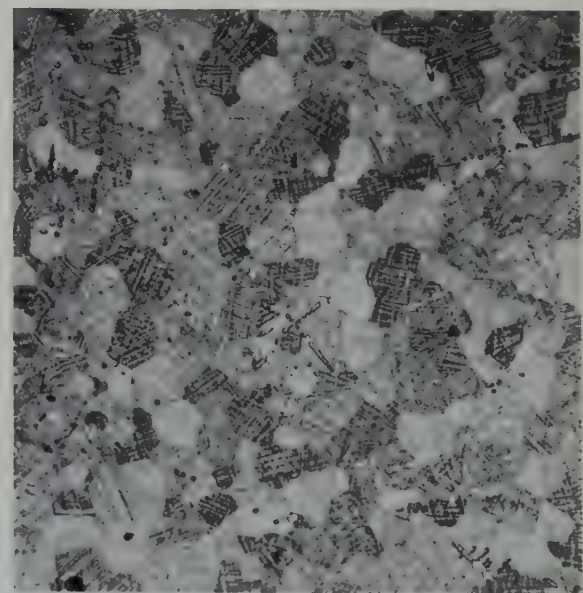


Fig. 5. 39 at % zirconium alloy. Annealed at 1050° C for 1 hour and water quenched. Weave-type banded structure of transformed β . Small white particles are zirconium carbide; oxide (grey) is in partially dendritic form. Cathodically etched. $\times 150$.

TABLE 2

The lattice parameters of thorium-zirconium alloys (Results in kX units, corrected to 18° C)

Temp. °C	at % Zr	Lattice parameter	Temp. °C	at % Zr	Lattice parameter
1300	4.9	5.0528 \pm 0.0004	893	0	5.0749 \pm 0.0002
	7.3	5.0378 \pm 0.0002		2.4	5.0645 "
	11.8	5.0161 \pm 0.0004		4.9	5.0535 "
1200	2.4	5.0639 \pm 0.0002		7.3	5.0389 "
	4.9	5.0530 "	850	9.6	5.0362 \pm 0.0003
1119	7.3	5.0382 "		11.8	5.0363 "
	9.6	5.0337 "		13.8	5.0362 "
	11.8	5.0342 "	800	7.3	5.0419 \pm 0.0002
1100	9.6	5.0317 "		9.6	5.0419 "
	11.8	5.0320 \pm 0.0003		11.8	5.0421 "
	13.8	5.0322 "		13.8	5.0420 \pm 0.0003
1050	9.6	5.0286 \pm 0.0002	734	2.4	5.0648 \pm 0.0002
	11.8	5.0285 "		4.9	5.0534 "
	13.8	5.0281 \pm 0.0003		7.3	5.0481 "
				9.6	5.0484 "
975	7.3	5.0383 \pm 0.0002		11.8	5.0488 "
	9.6	5.0289 "		13.8	5.0484 "
	11.8	5.0241 "	650	2.4	5.0651 "
	13.8	5.0242 "		7.3	5.0528 "
949	9.6	5.0290 "		11.8	5.0533 \pm 0.0004
	11.8	5.0248 "		13.8	5.0532 "
	13.8	5.0246 "	slow	0	5.0748 \pm 0.0002
935	9.6	5.0288 "	cool	2.4	5.0643 "
	11.8	5.0251 "		7.3	5.0515 "
	13.8	5.0253 "		9.6	5.0535 \pm 0.0003
933	11.8	5.0263 \pm 0.0002	<i>Electrolytic thorium</i>		
	13.8	5.0261 "	974	7.3	5.0421 \pm 0.0004
920	7.3	5.0387 "		9.6	5.0306 "
	9.6	5.0289 "		11.8	5.0256 \pm 0.0002
	11.8	5.0266 "		13.8	5.0256 "
	13.8	5.0268 "	887	0	5.0750 "
910	9.6	5.0289 "		2.4	5.0647 "
	11.8	5.0274 "		4.9	5.0539 \pm 0.0003
	13.8	5.0273 "		7.3	5.0423 \pm 0.0002
900	2.4	5.0650 "		11.8	5.0340 \pm 0.0004
	4.9	5.0533 "		13.8	5.0341 "
	7.3	5.0382 "	658	4.9	5.0573 \pm 0.0003
	9.6	5.0296 "		7.3	5.0574 \pm 0.0004
	11.8	5.0288 "		9.6	5.0571 \pm 0.0002
	13.8	5.0289 "			

permit a curve to be drawn through the points, rather than the mean, straight line. There is a positive deviation from Vegard's Law. The constant lattice parameter of the α -thorium solid solution in the two-phase mixtures was

extrapolated back to the lattice constant-composition curves for the solid solution to give the intercepts shown in table 3. The results from alloys made with electrolytic thorium are given in fig. 7 and are included in tables 2 and 3.

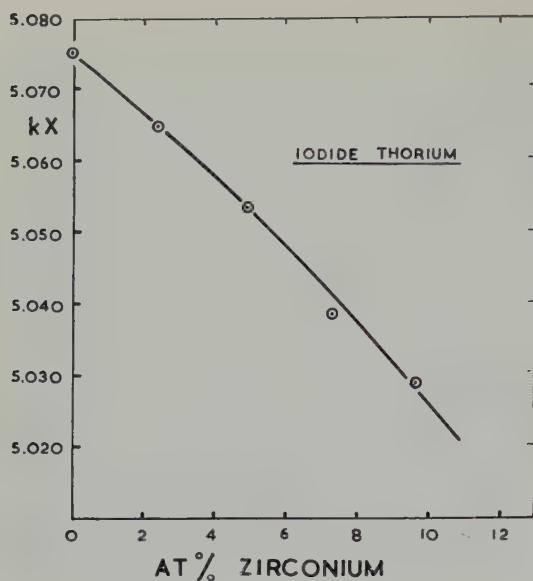


Fig. 6. Effect of zirconium concentration on α -thorium lattice parameter in quenched *iodide* thorium-rich alloys.

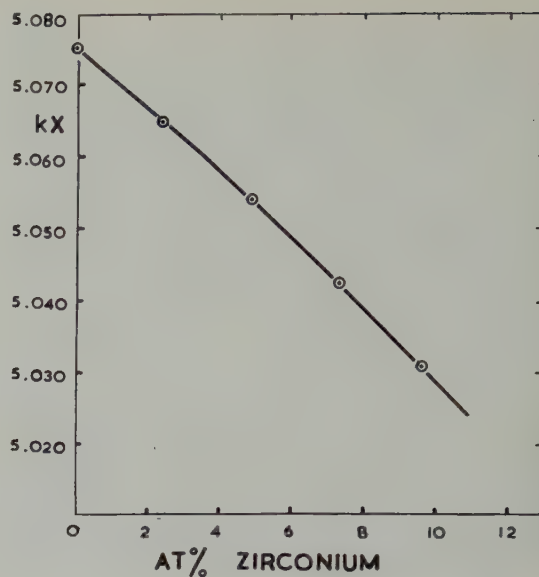


Fig. 7. Effect of zirconium concentration on α -thorium lattice parameter in quenched *electrolytic* thorium-rich alloys.

TABLE 3

Values of constant lattice parameter of two-phase alloys and intercept on composition-lattice parameter curve

(lattice parameters in kX units)

Temp. (°C)	Lattice parameter (iodide thorium base)	Intercept (at % Zr)	Lattice parameter (electrolytic thorium base)
1100	5.0320	8.9	—
1050	5.0284	9.6	—
975	5.0241	10.3	5.0256 †
949	5.0247	10.2	—
935	5.0252	10.1	—
933	5.0262	10.0	—
920	5.0267	9.9	—
910	5.0273	9.7	—
900	5.0291	9.4	—
887	—	8.9	5.0340
850	5.0362	8.2	—
800	5.0420	7.1	—
750	—	6.0	5.0483
734	5.0484	5.9	—
658	—	4.1	5.0573
650	5.0531	5.0	—

† intercept = 10.5 at %.

The logarithm of the solubility of zirconium in thorium, when plotted against $1/T$ °K for values of T in the range 734–920° C, fall on a straight line †.

4. Discussion

The proposed limit of the α -thorium solid solution (fig. 1) has been determined basically by the parametric method with support from the examination of microstructures. Although the microstructural evidence was not as precise as the X-ray results, there is substantial agreement between the two methods. Furthermore, the results from the two grades of thorium used are closely comparable.

The maximum solubility is less than that reported by Gibson, Loomis and Carlson ³), who used sponge thorium (0.037 wt % carbon, 0.015 wt % nitrogen). The carbon content of the thorium in this work is lower (50–170 ppm) but a discrepancy still exists after allowance is made for the formation of insoluble zirconium carbide in the American alloys.

† The value of this relationship is more fully utilized and illustrated in the accompanying paper by Evans and Raynor ¹²).

In the present investigation the lattice parameters of both iodide and electrolytic thorium fall within the range 5.0749 ± 0.0001 kX (table 2). As the experimental error on each result is ± 0.0002 kX, no difference in parameter between the two qualities could be detected. The good agreement illustrates the effect of the precautions taken in the selection and preparation of the dendrites prior to melting.

Evans and Raynor⁹) recently obtained values of the lattice parameter for electrolytic thorium, 5.0778 kX (99.5 wt % thorium) and iodide thorium, 5.0741 ± 0.0001 kX, the latter value confirming the earlier result of James and Straumanis¹⁰). Evans and Raynor demonstrated the ease of contamination of thorium specimens for X-ray work and it appears therefore that the somewhat higher value obtained in the present work is due partly to adsorbed gas. However, batch-to-batch compositional variations are possible with iodide materials and could account, in part, for the observed discrepancy.

The result for the 7.3 at % zirconium alloy in fig. 6 appears to be slightly low. This did not occur with electrolytic thorium and therefore an error in composition of the iodide thorium alloy may be responsible.

The values of the lattice parameters of the alloys with 4.9, 7.3 and 11.8 at % zirconium quenched from 1300° C were found to lie on the lattice parameter-composition curve for the α -thorium solid solution. However, the diffraction lines from these specimens were slightly diffuse, indicating a strained lattice. This is a characteristic of the transformed β solid solution¹¹). In cases where specimens had been quenched from the $(\alpha + \beta)$ field, the sharply defined α -thorium lines are "shadowed" with the slightly diffuse lines of the transformed β solid solution.

The most satisfactory microscopic evidence

was obtained from specimens prepared by diamond polishing. The location of the phase-boundary by metallography alone is difficult because of the similarity in appearance of inclusions to the zirconium-rich phase. Similar difficulties with the detection of small amounts of second phase in alloys made from both iodide and electrolytic thorium have been reported in investigations on other thorium systems.

Acknowledgements

The work was financed by an extra-mural research contract with the United Kingdom Atomic Energy Authority, to whom R.H.J. is indebted for a maintenance grant. The gift of the iodide thorium from Associated Electrical Industries (Manchester) Limited is gratefully acknowledged.

References

- 1) O. N. Carlson, U.S. Atomic Energy Commission, Publication AECD 3206 (1950)
- 2) H. A. Saller and R. A. Rough, U.S. Atomic Energy Commission, Publication BMI-1000 (1955)
- 3) E. D. Gibson, B. A. Loomis and O. N. Carlson, Trans. A.S.M., **50** (1958) 348
- 4) V. J. Hadrell, E. C. Sykes and B. W. Mott, J. Inst. Metals **84** (1955) 112
- 5) D. Armstrong, P. E. Madsen and E. C. Sykes, J. Nucl. Mat. **1** (1959) 127
- 6) W. J. McG. Tegart, The Electrolytic and Chemical Polishing of Metals in research and industry (London 1959) 46
- 7) M. D. Smith and R. W. K. Honeycombe, J. Nucl. Mat. **1** (1959) 345
- 8) X-ray Diffraction of Polycrystalline Materials, Inst. of Physics, (London, 1955) Appendix p. 653
- 9) D. S. Evans and G. V. Raynor, J. Nucl. Mat. **1** (1959) 281
- 10) W. J. James and M. E. Straumanis, Acta Cryst. **9** (1956) 376
- 11) R. H. Johnson; Ph. D. Dissertation, University of Sheffield (1960)
- 12) D. S. Evans and G. V. Raynor, J. Nucl. Mat. **4** (1961) 66

THE SOLUBILITY OF ZIRCONIUM IN α -THORIUM

D. S. EVANS and G. V. RAYNOR

Department of Physical Metallurgy, University of Birmingham, Birmingham 15, UK

Received 5 January 1961

The lattice spacings of seven thorium-rich thorium-zirconium alloys have been measured after quenching from 900°, 750°, 675° and 550° C. The results, and the solid solubility values derived from them, are in very good agreement with those reported by Johnson and Honeycombe²⁾, but do not confirm those of Gibson, Loomis and Carlson¹⁾. The solid solubility of zirconium falls from 9.4 atomic per cent at 900° C to 2.9 at % at 550° C. From the linear relationship between $\log_{10} S$ and $1/T$ °K where S is the solubility in atomic per cent, the solubilities at 920° and 25° C may be calculated as 9.84 and about 0.002 at % respectively.

Les paramètres cristallins de sept alliages thorium-zirconium riches en thorium ont été mesurés après trempe à partir de 900°, 750°, 675° et 550° C. Les résultats et les valeurs de la solubilité à l'état solide qui en sont déduits sont en très bon accord avec les données de Johnson et Honeycombe, mais ne confirment pas celles de Gibson, Loomis et Carlson¹⁾. La solubilité à l'état solide du zirconium dans le

thorium tombe de 9,4 at % à 900° C à 2,9 at % à 550° C. A partir de la relation linéaire existant entre $\log_{10} S$ et $1/T$ °K, dans laquelle S est la solubilité en atomes %, on peut calculer les valeurs de solubilité à 920° et 25° C; elles sont respectivement de 9,84 at % et, 0,002 at % environ.

Die Gitterkonstanten von 7 thoriumreichen Thorium-Zirkon-Legierungen wurden gemessen, nachdem sie von 900°, 750°, 675° und 550° C abgeschreckt worden waren. Die Ergebnisse und die Werte der Löslichkeit im festen Zustand, die aus diesen abgeleitet wurden, sind in sehr guter Übereinstimmung mit Ergebnissen, die von Johnson und Honeycombe²⁾ veröffentlicht wurden. Dagegen stimmen sie nicht überein mit den Werten von Gibson, Loomis und Carlson¹⁾. Die Löslichkeit im festen Zustand von Zirkon fällt von 9,4 At % bei 900° C auf 2,9 At % bei 550° C. Aus der linearen Beziehung zwischen $\log_{10} S$ und $1/T$ °K, wo S die Löslichkeit in At % bedeutet, lassen sich die Löslichkeiten bei 920° und 25° C zu 9,84 bzw. 0,002 At % berechnen.

1. Introduction

Above temperatures of 1360° and 865° C respectively, thorium and zirconium exist in body-centred cubic forms. In view of the similarity of crystal structure and group valency, and size-factor values which lie within the range permitting extensive solid solution formation, the formation of a complete series of solid solutions between the two body-centred cubic forms is not surprising. Below 1360° C however the crystal structure of thorium is face-centred cubic, so that a miscibility gap must exist between the face-centred cubic solid solution of zirconium in thorium (α) and β -zirconium (>865° C) or α -zirconium (<865° C) which is close-packed hexagonal in crystal structure.

According to Gibson, Loomis and Carlson¹⁾ the solubility of zirconium in α -thorium reaches 14.4 at % at 910° C, while that of α -thorium in zirconium is less than 1 at %.

In connection with a general programme on the alloying properties of thorium in progress in the authors' laboratory, it became desirable to determine the lattice spacings of thorium-rich thorium-zirconium alloys, which provided an opportunity of redetermining the solid solubility curve for zirconium in α -thorium. When this work, which is reported in this paper, had been completed, the results of a similar study by Johnson and Honeycombe²⁾ became available, which also indicated that the solubility of zirconium in α -thorium was more restricted than

that proposed by Gibson, Loomis and Carlson ¹⁾. The present work and that of Johnson and Honeycombe ²⁾ are in good agreement, and fix the solubility limit at 9.4 at % at 900° C; the comparison of the two researches is of interest as indicating the degree of consistency now obtainable in work on reactive materials.

2. Materials and Experimental Methods

Alloys were prepared by arc-melting iodide thorium and hafnium-free zirconium, both kindly supplied by the Atomic Energy Research Establishment, Harwell. Seven alloys with compositions up to 19 at % zirconium were examined, and, in view of the large difference in atomic weight between the components, were made up from a master-alloy containing 19 at % zirconium by dilution with iodide thorium. Weight losses during preparation and subsequent homogenization of the ingots were negligible, and compositions are therefore estimated to lie within ± 0.1 at % of those intended. Homogenization was carried out for eight days at 1000° C, and this treatment was followed by several days at 750° C. The specimens were then quenched in water.

The technique used for preparing and annealing filings of thorium-rich alloys out of contact with air so as to minimise the risk of contamination has been fully described in previous publications ^{3,4)}. In the present work, similar methods were employed, except that, since annealing treatments to establish equilibrium in filings at temperatures other than that of the homogenization anneal were prolonged relative to the time required merely for stress relief, the annealing operations were carried out in highly evacuated silica capsules. In general, samples of filings were annealed for various times at 900°, 750°, 675°, and 550° C, and quenched into silicone oil. Specimens were exposed to copper K α radiation in a Philips Debye-Scherrer camera (radius 11.483 cm), and systematic errors were eliminated from the lattice spacings derived from the resulting diffraction patterns by the use of the Nelson-Riley extrapolation function ⁵⁾.

3. Results

Using the techniques outlined, the lattice spacings of the zirconium metal after annealing for two hours at 750° C were:

$$a = 3.2272 \text{ kX}; c = 5.1393 \text{ kX}.$$

These values are in reasonable agreement with those of Treco ⁶⁾ ($a = 3.2256$; $c = 5.1371$ kX) and of Russell ⁷⁾ ($a = 3.2247$; $c = 5.1373$ kX) for material of similar purity. The lattice spacing of thorium, following annealing of the filings at 675° C for four hours, was $a = 5.0745$ kX, in good agreement with values previously obtained in the authors' laboratory ^{3,4)}. The lattice spacings obtained for the alloys, examined as a function of temperature of heat treatment, are given in table 1, and plotted in fig. 1, in which, for clarity, the spacings of filings annealed at 750°, 675°, and 550° C have been displaced downwards successively by 0.01 kX.

TABLE 1
Lattice spacings in the thorium-zirconium system

Composition (at % Zr)	Lattice spacings (kX at 25° C) after annealing for:			
	10 h 550° C	4 h 675° C	2 h 750° C	2 h 900° C
0	5.0745	5.0745	5.0750	5.0750
2.14	5.0645	5.0646	5.0654	5.0657
4.12	5.0610	5.0554	5.0558	5.0555
9.00	5.0609	5.0522	—	5.0323
9.20	—	5.0523	—	5.0300
9.34	—	5.0523	5.0464	5.0290
15.47	—	5.0523	—	5.0287
19.00	—	5.0523	5.0464	5.0292

The results obtained by Johnson and Honeycombe ²⁾ are in good agreement with the present work, in which the consistency of the results is high, both for single phase alloys annealed at different temperatures and for two-phase alloys of different compositions. The solid solubility values deduced from these measurements are shown in fig. 2; again agreement with the results of Johnson and Honeycombe ²⁾ is very good, and the higher solid solubility limits suggested by Gibson, Loomis and Carlson ¹⁾ are not confirmed.

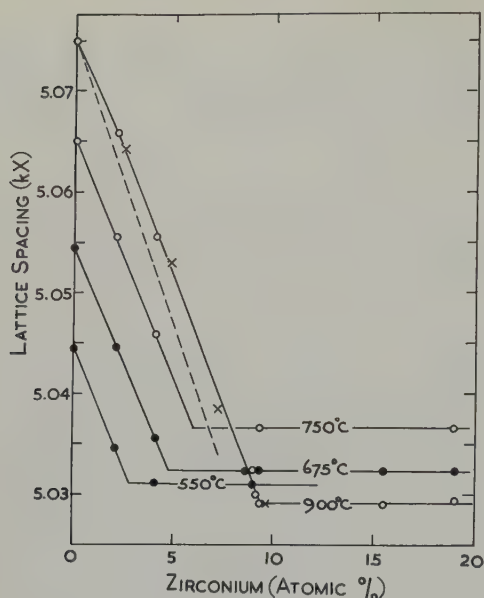


Fig. 1. Lattice spacings in the thorium-zirconium system. Spacings corresponding to annealing temperatures below 900° C have been displaced successively by 0.01 kX. For explanation of broken line, see text. ○ ● present work X results due to Johnson and Honeycombe²⁾.

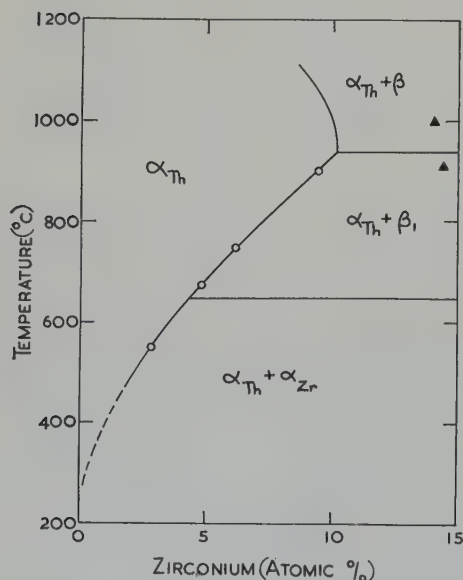


Fig. 2. Solid solubility of zirconium in α -thorium. ○ present work. ▲ Gibson *et al.*¹⁾. The solubility curve is calculated from the relationship

$$\log_{10} S = 2.2026 - \frac{1442}{T^{\circ}K}$$

4. Discussion

When the logarithm of the solubility of zirconium in thorium is plotted against $1/T^{\circ}K$ the experimental points fall on a straight line as pointed out by Johnson and Honeycombe²⁾. The present results confirm this, except for that at 500° C, which may correspond to incomplete equilibration in spite of the relatively long heat-treatment or may indicate that the slope of the graph changes slightly below the eutectoid horizontal at 645° C. From the three remaining values, the relationships between solubility S in atomic per cent and temperature takes the form:

$$\log_{10} S = 2.2026 - \frac{1442}{T^{\circ}K}$$

This equation has been used in calculating the solid solubility curve shown in fig. 2, and adequately describes the experimental results. Extrapolation to lower temperatures is also possible, assuming no marked change of slope below 645° C, and gives rise to the broken curve in fig. 2. In table 2, interpolated and extrapolated solid solubility values are given as a function of temperature. The comparatively rapid decrease in solid solubility with decrease in temperature is consistent with the large negative size-factor (-11%) of α -zirconium with respect to α -thorium.

TABLE 2
Solid solubility of zirconium in α -thorium

Temp. (°C)	Solubility in at % Zr		Gibson <i>et al.</i> ¹⁾
	Present work calculated	observed	
920	9.84		14.4
910	9.63		
900	9.40	↔ 9.4	
800	7.22		
750	6.20	↔ 6.1	
700	5.25		approx. 5
675	4.80	↔ 4.8	
550	(2.82)	2.9	
300	(0.21)		
25	(0.002)		

The lattice spacing curves in fig. 1 are virtually linear. An assessment of the lattice

contraction to be expected from atomic size considerations alone may be made on the assumption that the mean interatomic distance d in the alloy varies according to the expression:

$$d = nd_{\text{Zr}} + (n-1)d_{\text{Th}}$$

where n is the atomic fraction of zirconium, d_{Th} is the closest distance of approach of atoms in face-centred cubic thorium, and d_{Zr} is the average of the two close distances of approach of atoms in close-packed hexagonal zirconium. This assessment is represented as the broken line in fig. 1, and the measured spacing curve shows a small positive deviation only. This behaviour is consistent with the general assumption that both thorium and zirconium have the same valency of 4 in the solid state.

Acknowledgements

Grateful acknowledgement is made to the United Kingdom Atomic Energy Authority for the general support given to this work, and to the General Electric Company, Limited, UK, for the award of a research scholarship to one of us (D.S.E.).

References

- 1) E. D. Gibson, B. A. Loomis and O. N. Carlson, Trans. Amer. Soc. Metals **50** (1958) Preprint 24
- 2) R. H. Johnson and R. W. K. Honeycombe, J. Nucl. Mat. **4** (1961) 59
- 3) D. S. Evans and G. V. Raynor, J. Nucl. Mat. **1** (1959) 281
- 4) D. S. Evans, G. V. Raynor and R. T. Weiner, J. Nucl. Mat. **2** (1960) 121
- 5) J. P. Nelson and D. P. Riley, Proc. Phys. Soc. **57** (1945) 160
- 6) R. M. Treco, Trans. Amer. Inst. Min. Metall. Engrs. **101** (1953) 344
- 7) R. B. Russell, J. Appl. Phys. **24** (1953) 232

IMPERFECTIONS IN NATURAL GRAPHITE

J. A. HEDLEY and D. R. ASHWORTH †

C. A. Parsons & Co. Ltd., Nuclear Research Centre, Fossaway, Newcastle-upon-Tyne, 6, UK

Received 17 January 1961

Lattice or surface imperfections in graphite may play an important role as active sites in its oxidation. Thin films of a natural graphite, Madagascar flake, examined by electron microscopy revealed the presence of flat graphite sheets whose basal planes were predominantly normal to the electron beam. Dislocations lying in the basal planes were frequently observed, the estimated mean density being $10^9/\text{cm}^2$.

Graphite has a high incidence of stacking faults. Basal plane dislocations frequently split into partials which bound ribbons of stacking fault, 650–1000 Å wide. If these ribbons of stacking fault occur at the same level in the film they often interact to form stable networks. From measurements of the radius of curvature of dislocation nodes, the stacking fault energy has been estimated to be approximately 0.25 erg/cm^2 .

Because of the fortuitous relative rotation of graphite sheets, Moiré patterns have been observed with dislocations imaged as extra inserted fringes.

Les imperfections réticulaires ou superficielles du graphite peuvent jouer un rôle important comme sites actifs au cours de son oxydation. Des films minces de graphite naturel, (paillettes de Madagascar) examinés au microscope électronique ont révélé la présence de feuillets plats de graphite dont le plan basal était pour la plupart des feuillets normal au faisceau électronique. On observait fréquemment des dislocations dans les plans de base, dont la densité moyenne était estimée à $10^9/\text{cm}^2$.

Le graphite comporte un grand nombre de fautes d'empilement. Les dislocations du plan de base se divisent fréquemment en dislocations partielles qui

relient des rubans de fautes d'empilement de 650 à 1000 Å de large. Si ces rubans de défauts d'empilement se trouvent au même niveau dans le film, il y a souvent interaction pour former des réseaux stables. D'après les mesures du rayon de courbure des noeuds de dislocations, l'énergie des fautes d'empilement est à peu près de 0.25 erg/cm^2 .

A cause de la rotation relative fortuite des feuillets de graphite, des figures de Moiré ont été observées avec des dislocations représentées sous forme de franges insérées supplémentaires.

Gitter- oder Oberflächenunvollkommenheiten in Graphit spielen eine wichtige Rolle für die Oxydationsaktivität. Dünne Filme von natürlichem Graphit, sog. Madagaskar-Flake, wurden im Elektronen-Mikroskop untersucht. Es zeigten sich flache Graphitblätter, deren Grundflächen vorwiegend normal zum Elektronenstrahl orientiert waren. In den Grundflächen wurden häufig Versetzungen beobachtet. Ihre mittlere Dichte konnte auf 10^9 pro cm^2 geschätzt werden.

Graphit hat einen hohen Stossfehleranteil. Die Grundflächenversetzungen sind häufig geteilt durch Grenzstreifen von Stapelfehlern, 650–1000 Å breit. Wenn mehrere solcher Stapelfehler in der-selben Ebene liegen, bilden sie ein stabiles Netzwerk. Messungen an dem Radius von Versetzungsknoten haben ergeben, dass die Stapelfehlerenergie auf etwa 0.25 erg/cm^2 geschätzt werden kann.

Durch eine zufällige Drehung der Graphitschichten konnten sog. Moire-Muster mit Versetzungen festgestellt werden, die wie besonders eingesetzte Fransen erscheinen.

1. Introduction

1.1. STRUCTURE OF GRAPHITE

Recent work by Franklin ¹⁾ and Bacon ²⁾ has shown that the normally accepted hexagonal layered structure of graphite proposed by

Bernal ³⁾ has to be modified to take into account anomalies in the X-ray diffraction pattern. It has been found that diffraction anomalies may be due to:

(a) variations in the crystallite size between

† Now at Hawker Siddeley Nuclear Power Plant Co. Ltd. Sutton Lawe, Langley Bucks.

non-graphitisable carbon ($\sim 10 \text{ \AA}$) and fully graphitised material ($\sim 2000 \text{ \AA}$);

- (b) stacking faults in which the normal AB stacking changes to ABC rhombohedral stacking owing to thermal and mechanical stresses or to a growth mechanism;
- (c) turbostratic (two dimensional) packing in which packets of lamellae are grouped together without any definite relation to each other: and
- (d) holes, pores or buckling in the hexagonal nets where the lamellae meet, resulting in unsaturated valency bonds.

In addition to internal structural defects, surface imperfections may play an important role during oxidation and Tsuzuku ⁴⁾ has observed the following topographical features in synthetic graphite:

- (a) pyramidal layer growth of hexagonal monocrystals;
- (b) formation of conical crystal habit by a spiral growth mechanism;
- (c) laminar cleavage of spiralled crystals along the basal plane: and
- (d) occurrence of polygonisation.

These lattice or surface imperfections may play an important role, as "active" sites, in the oxidation of graphite. A detailed study of such imperfections could lead to information regarding the types which are important in the oxidation process. The inherent limitations of the X-ray diffraction method prevents a detailed picture being obtained of the nature and distribution of the lattice imperfections which are present while the examination of replicated surfaces in the electron microscope lacks sufficient resolution to study the oxidation sites. Examination by transmission electron microscopy, however, enables a direct study of crystal imperfections in both natural and synthetic graphite and, with new methods of specimen preparation, more reliable results are being obtained.

1.2. PREVIOUS ELECTRON MICROSCOPE WORK ON GRAPHITE

Few electron microscope studies have been carried out on graphite but the results indicate the complexity of its microstructure.

Tsuzuku ⁴⁾ synthesised graphite by heating carbon black powder at 2500°C and subsequently dusted or rubbed the graphite so formed on to a collodion film. Examination showed that hexagonal monocrystals were formed by pyramidal layer growth as proposed by Frank ⁵⁾ in his spiral dislocation growth mechanism. These crystals cleaved by twisting or breaking along the basal planes to form semicircular plates. The cleavages were explained by the interaction of a screw and an edge dislocation.

Grenall ⁶⁾ rubbed natural graphite crystals between glass slides and mounted thin sections on to a copper grid for examination. Single dislocations were seen to line up in individual grains to form square and hexagonal sub-grain boundaries.

Dawson and Follet ⁷⁾ prepared samples from nuclear grade graphite by microtoming. Individual grains and pores, at the junction of grain boundaries, were observed and the presence of dislocations inferred from the extra lines seen in the Moiré fringe pattern.

Bollman *et al.* ⁸⁾ studied specimens thinned by ionic bombardment and also samples of fine graphite powders. In this case dislocations were seen directly and also inferred by means of extra planes in the Moiré pattern.

Williamson ⁹⁾ examined natural graphite flakes and observed partial dislocations which interacted to form nodes and networks.

Except for slight orientation effects due to extrusion, nuclear grade graphite is random in its microstructure. This complicates both the preparation of suitable specimens and the interpretation of results. To record and understand the types of defects associated with the graphite structure this study has been carried out on a well-oriented natural graphite, Madagascar flake in which the basal planes lie parallel to the surface of the flake.

2. Experimental Techniques

2.1. SPECIMEN PREPARATION

Grenall's method of rubbing flakes between glass microscope slides was tried initially, but was found to produce excessive debris on the surface of the thin graphite film. Eventually, the most satisfactory method was found to be

rubbing electron microscope specimen grids directly over the flakes at a pressure which was found, by experience, to remove the correct thickness of film free from debris.

2.2. ELECTRON MICROSCOPE AND DIFFRACTION

The specimens were examined by transmission in an EM 6 electron microscope. An intense fine



Fig. 1. Typical graphite flake produced by smearing. $\times 4600$.



Fig. 3. Typical dislocation distribution. $\times 14\,000$.

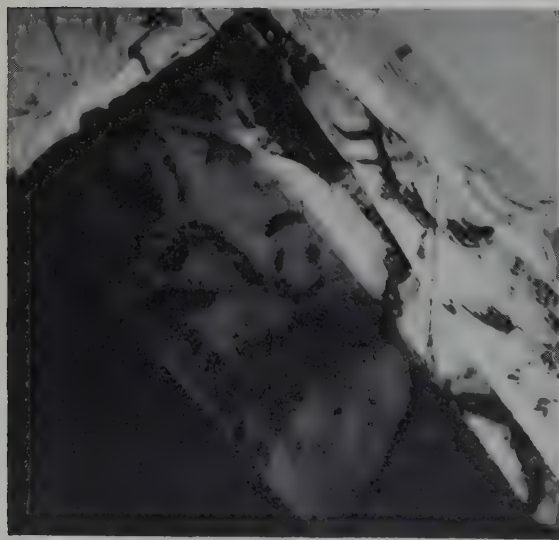


Fig. 2. Sheared graphite layers producing a stepped effect. $\times 5000$.

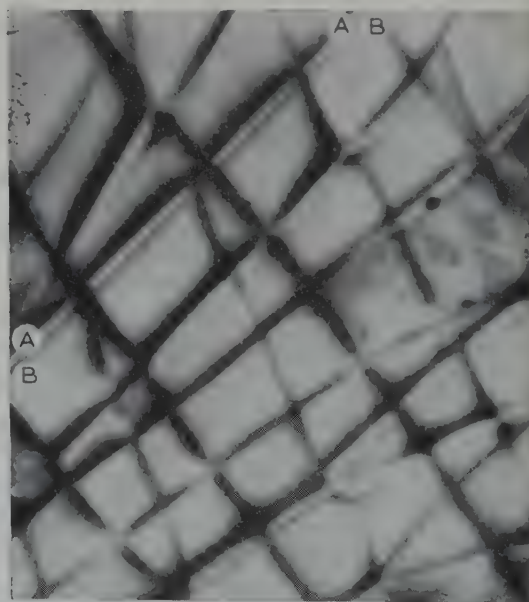


Fig. 4. Dissociated dislocations. $\times 20\,000$.

spot on the specimen was achieved by correcting for beam astigmatism before the beam entered the double condenser lens system. Image astigmatism was compensated for by an electrostatic field placed after the objective stage.

Selective area diffraction was used to determine the orientation of thin sections and to record the effects of double diffraction. The method given by Agar¹⁰) was employed to ensure that the diffraction pattern was from the area being examined.

3. Results

3.1. GENERAL MORPHOLOGY

Examination of the specimens in the electron microscope at relatively low magnifications ($\times 2000$ – $20\,000$) shows the presence of flat graphite sheets. These are predominantly normal to the direction of the electron beam. In places, the sheets are buckled and twisted creating areas of thicker, but distorted graphite, as shown in fig. 1. Graphite shears most easily along the basal planes and, owing to the mode of preparation, sheets are often found to be overlapped and displaced from one another, giving a stepped effect (fig. 2).

In contrast to the bulk material, thin films can bend in the basal planes, producing scroll shaped whiskers which have been noticed both projecting from and inside crystals. Crystals containing 120° angles are a common feature and very small hexagonal crystals have been noted.

Except for the occurrence of small hexagonal crystals in natural graphite none of the features observed by Tsuzuku⁴) in synthetic graphite have been noted. These seem to be the main topographical differences between natural and synthetic graphite.

3.2. DIRECT OBSERVATION OF DISLOCATIONS

Fig. 3 shows a typical section of natural graphite containing dislocations, the estimated density of which is between 10^8 and $10^{10}/\text{cm}^2$ (i.e. the number of dislocations cutting unit

area of a plane perpendicular to the surface and passing through the specimen). The actual values vary considerably from area to area, some regions being free from dislocations while others are so profusely tangled that no reliable estimate can be made.

The majority of dislocations observed are very long and occasionally they can be seen to end on cleavage steps or crystal edges. Selective area diffraction shows that the basal planes are parallel to the surface of the graphite film and therefore the dislocations lie in the basal planes. The large number of dislocations in some areas give the appearance of square or hexagonal networks. A more careful analysis, however, shows that the majority of dislocations are at different levels throughout the thickness of the material.

As shown in fig. 4, dislocations split into partials with a separation of 650 – 1000 Å bounding areas of stacking faults. The interaction of partials produces nodes as shown in fig. 5 and instances of large networks have been observed which appear either triangular or hexagonal depending on the angle of tilt of the specimen, figs. 6 and 7. Specimen tilting has the effect of taking one of the partials out of diffraction conditions and causing it to disappear. It may be that, because of this, all apparently single dislocations are in fact partials, but areas containing single dislocations have frequently been tilted without any more appearing.

Under the heat of the electron beam, thermal stresses are set up and the dislocations are observed to move. A series of micrographs has been taken showing the sequential position of these dislocations and the following observations made:

- (a) jerky motion of the dislocations which indicates that their movement is impeded by inclusions or other obstacles;
- (b) bowing of dislocation lines due to pinning of the dislocations at their ends. This is caused by pinning between cleavage steps rather than inclusions;
- (c) piling up of dislocations against ob-

stacles, as shown by comparison of figs. 8 and 9. Dislocations of the same sign repel each other and normally the spacing of piled up dislocations gradually increases with distance from the obstacle. In this case, however, no such relationship is observed and so it is inferred that the majority of dislocations are at different levels in the film and therefore do not interact; and

(d) short dislocation lines, stretched between cleavage steps, moved in a direction perpendicular to the dislocation line. No types of dislocations have been noted other than those which lie in the basal plane.

Several examples of dislocation sources have been observed. The majority of dislocations



Fig. 5. Interaction of partials to form extended and contracted nodes. $\times 230\,000$.

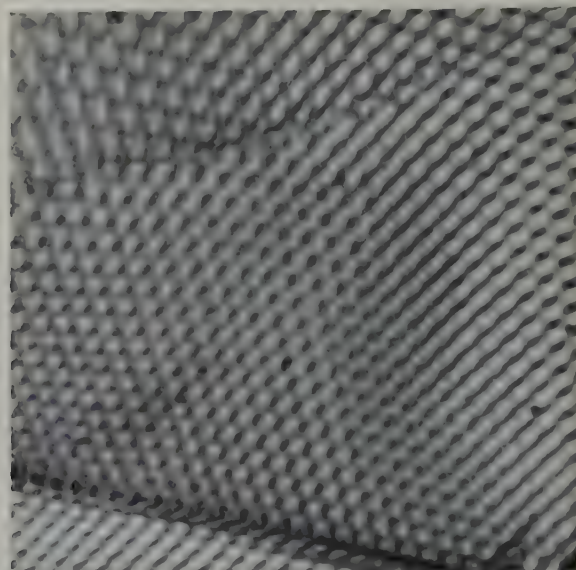


Fig. 7. Dislocation network shown in fig. 6, tilted to form a hexagonal network. $\times 42\,000$.

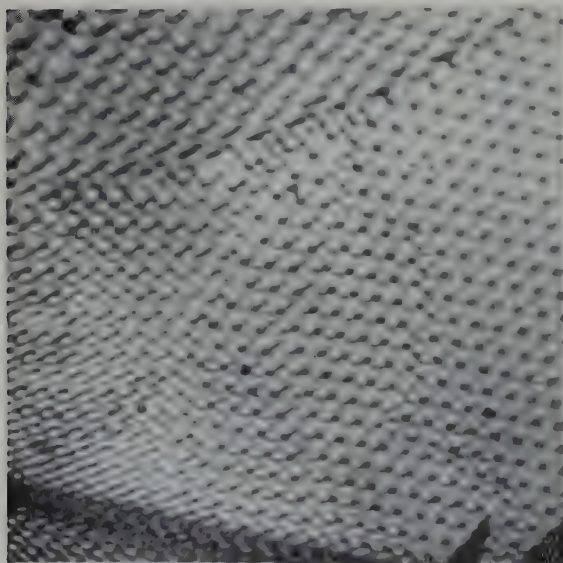


Fig. 6. Triangular network of partial dislocations. $\times 42\,000$.

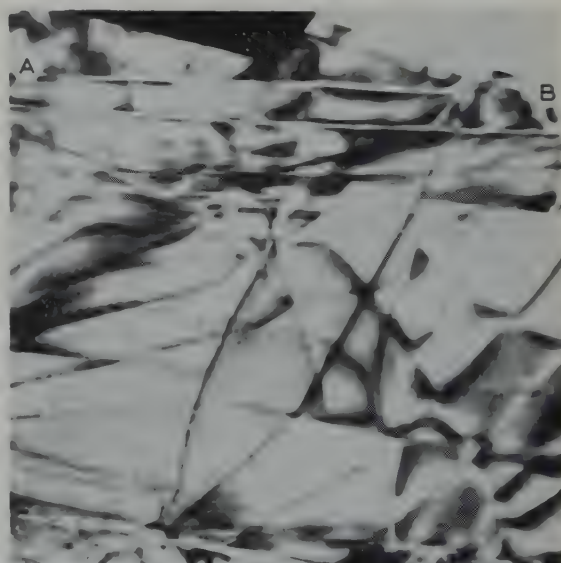


Fig. 8. Probable cleavage step AB from which many dislocations originated. $\times 21\,000$.

seem to originate from cleavage steps and an example of this is shown in figs. 8 and 9.

3.3. OBSERVATIONS ON MOIRÉ FRINGES

The most common feature in all specimens examined was the presence of a series of equally

spaced fringes, spread over large areas, the periodicity of which varied between 40 and 300 Å (fig. 10). Various explanations for the formation of these Moiré fringes have been given, but the work of Dowell⁽¹¹⁾, Bassett *et al.*⁽¹²⁾ and Agar⁽¹³⁾ has conclusively demonstrated that

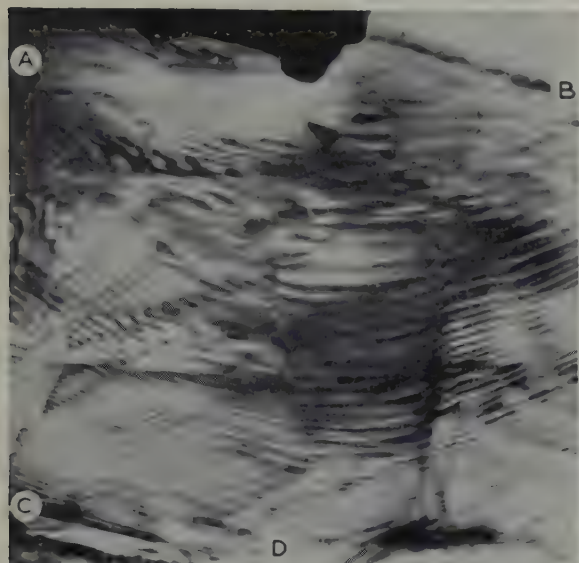


Fig. 9. Dislocations originating from AB region and pilling against barrier at CD. $\times 21\,000$.

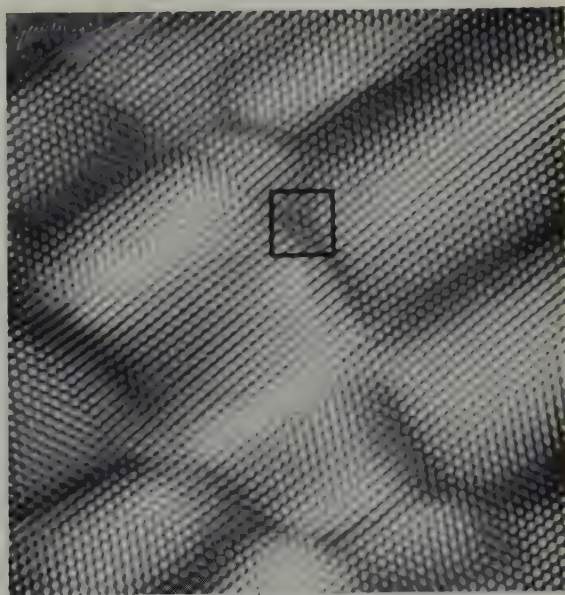


Fig. 11. Hexagonal Moiré pattern with extra fringe indicated. $\times 80\,000$.



Fig. 10. Moiré fringes. $\times 120\,000$.

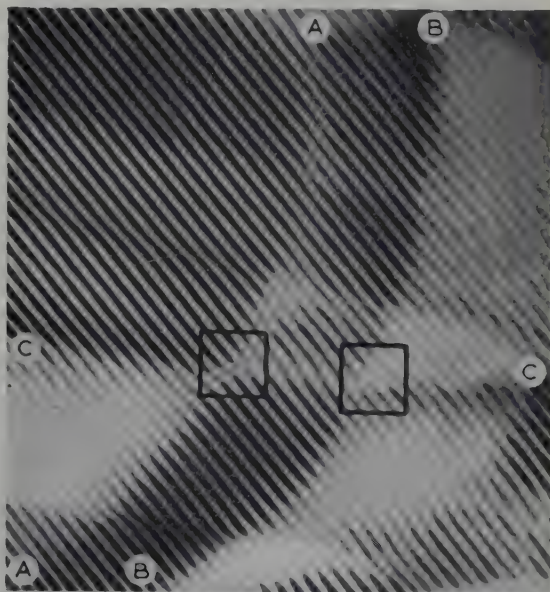


Fig. 12. Extra fringes in the Moiré pattern where dislocations AA and BB intersect with CC. $\times 210\,000$.

double diffraction of the electron beam from specific crystallographic planes is responsible.

By using the $(10\bar{1}0)$ and $(11\bar{2}0)$ diffraction spots to produce dark field illumination the Moiré pattern is intensified considerably, indicating that these planes are responsible for the double diffraction effect. This is confirmed by the observation that sets of Moiré fringes form at 120° ; three sets forming a hexagonal network are shown in fig. 11.

It has been shown by Bassett *et al.*¹²⁾ that dislocations at an angle to the thin film surface in face centred cubic metals are imaged in the Moiré pattern and frequent examples of this effect have been observed in graphite (fig. 12).

Any imperfection in the lattice which distorts the atomic planes giving rise to double diffraction will be imaged in the Moiré pattern. Many examples of distorted Moiré fringes have been observed (fig. 13). The nature of these types of imperfections is not yet clear although dimples in the film may be a contributory factor.

4. Discussion

Graphite has a hexagonal layer structure which is shown looking down the c direction in fig. 15. Observations on dislocations in

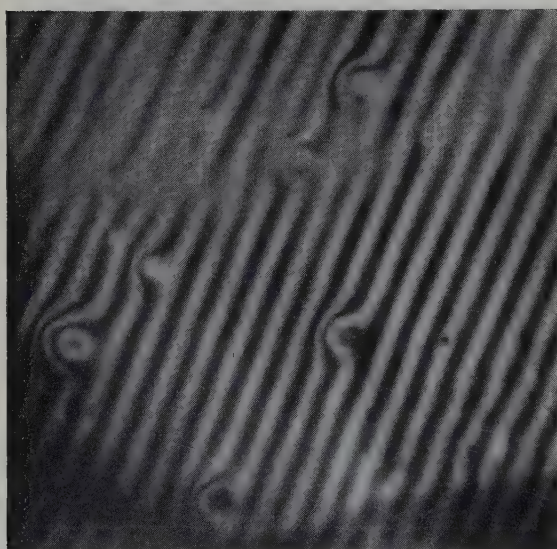


Fig. 13. Imperfections in a Moiré pattern. $\times 100\,000$.

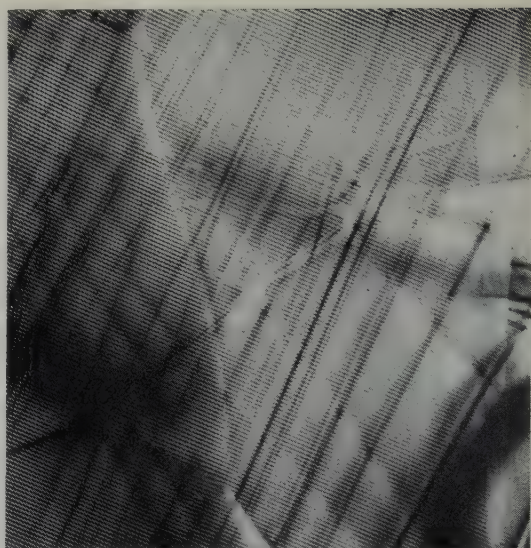


Fig. 14. Moiré pattern superimposed on basal plane dislocations. $\times 16\,000$.

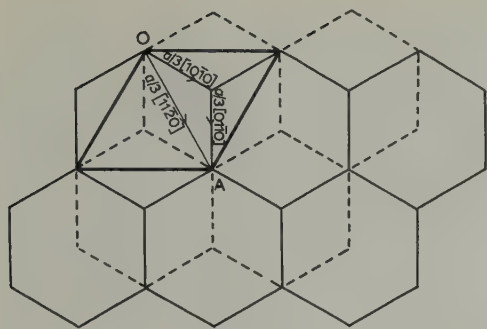
graphite have shown that they lie in the basal planes and under the heat of the electron beam are mobile. Williamson⁹⁾ analysed this type of dislocation and has shown that it has a Burgers vector of $a/3 [11\bar{2}0]$ which splits into partials or extended dislocations with Burgers vectors of $a/3 [10\bar{1}0]$ and $a/3 [01\bar{1}0]$. As the angle between the Burgers vectors of the partials is 60° they will repel each other¹³⁾. As they separate, a sheet of stacking fault is formed between them and the energy of the fault limits their separation according to

$$E = \frac{\mu b_2 b_3}{2\pi D} \text{ erg/cm}^2 \quad (1)$$

where E is the energy per unit area of stacking fault, μ is the shear modulus along the basal plane, D is the distance of separation of the partials, and b_2 and b_3 are the moduli of the Burgers vectors of the partial dislocations. It is also possible to calculate the stacking fault energy from the radius of curvature of dislocation lines which form a three point node. In this case

$$E = \frac{\mu b_2 b_3}{2R} \text{ erg/cm}^2 \quad (2)$$

where R is the radius of curvature of the partial.



A Layer ———, B Layer - - - - -, Unit cell ———

Fig. 15. The normal graphite lattice viewed along the c direction. A dislocation with Burgers vector OA dissociates into partials OB and BA . A movement from O to B corresponds to an A layer moving into a C layer position and hence creating the rhombohedral modification of graphite with an ABC stacking.

The only value obtainable for the shear modulus of graphite was a bulk value of 5×10^{10} dynes/cm² (ref.¹⁴). This will be higher than the shear modulus along the basal planes and hence the calculated stacking fault energy of 0.25 ergs/cm² will be too high. On substituting this value in (1) the separation of partials D is found to be 650 Å which is in good agreement with the experimental values of 650–1000 Å. These values must be considered as approximations since only elastic forces have been considered in the calculations.

From analysis of extra planes observed in Moiré patterns, Dawson and Follet⁷) suggest the presence of dislocations passing through the basal planes. Williamson⁹) observed no interaction between basal plane dislocations and non-basal plane dislocations and suggests that the extra planes found in the Moiré pattern are due to the basal plane dislocations. Our observations have shown that when basal dislocation and Moiré patterns occur in the same area three types of interaction or non-interaction occur.

a) Extra inserted fringes are observed without any sign of basal plane dislocations, as in Dawson's micrographs.

b) Extra inserted fringes are observed when two indistinct basal plane dislocations intersect at the point where the extra fringe terminates (see figs. 11 and 12). When the specimen is

tilted, either the basal plane dislocations appear with much greater contrast and the Moiré pattern disappears, or the basal plane dislocation disappears and the extra plane in the Moiré pattern is left.

When dislocations in case (b) move owing to the heat of the electron beam, the extra fringe in the Moiré pattern moves to retain the same position relative to the intersection point of the dislocations.

c) Basal plane dislocations and Moiré patterns are clearly observed with no obvious interaction, apart from a slight increase in density of the Moiré fringes at the point of intersection (see fig. 14).

These observations would suggest that the "Moiré dislocations" are caused by some interaction between basal plane dislocations in different layers. Case (a) will then be a particular diffraction condition of (b) and in case (c) basal plane dislocations must be in widely separated layers as no interaction occurs.

5. Future Work

The purpose of this work is to find possible active sites for the initial oxidation of graphite. Preliminary work on oxidation of graphite flakes outside the microscope has already been published¹⁵) and oxidation of specimens inside the microscope has been started.

Acknowledgements

The authors wish to thank the directors of C. A. Parsons for permission to publish this report and Drs. I. M. Dawson, G. K. Williamson and A. Sutton for valuable discussions.

References

- 1) R. E. Franklin, *Acta. Cryst.* **4** (1951) 253
- 2) G. E. Bacon, UKAEA (Harwell) Report, AERE M/R-2702 (1958)
- 3) J. D. Bernal, *Proc. Roy. Soc.* **106 A** (1924) 749
- 4) T. Tsuzuku, *Proceedings of the Third Conference on Carbon*, Buffalo (Pergamon, 1958) p. 422
- 5) F. C. Frank, *Discussions of the Faraday Society*, No. 5 (1948) p. 48
- 6) A. Grenall, *Nature* **182** (1958) 448

- ⁷⁾ I. M. Dawson and E. A. C. Follett, Proc. Roy. Soc. **253 A** (1959) 390
- ⁸⁾ W. Bollman *et al.*, Battelle Progress Report No. 1 for Agip Nucleare (Italy), (April 1959)
- ⁹⁾ G. K. Williamson, Proc. Roy. Soc. **257 A** (1960) 457
- ¹⁰⁾ A. W. Agar, Brit. J. Appl. Phys. **11** (1960) 185
- ¹¹⁾ W. C. T. Dowell *et al.*, Proc. Reg. Conf. Electron Microscopy, Tokyo (Electrotechnical Laboratory, Nagata-cho, Chiyoda-Ku, Tokyo, 1956) p. 320
- ¹²⁾ G. A. Bassett *et al.*, Proc. Roy. Soc. **246 A** (1958) 345
- ¹³⁾ P. B. Hirsch, Metallurgical Reviews **4** (1959) 101
- ¹⁴⁾ W. G. O'Driscoll and J. C. Bell, Nuclear Engineering **3** (1958) 480
- ¹⁵⁾ J. A. Hedley, Nature **188** (1960) 44

SOME STUDIES OF GAS EVOLUTION FROM GRAPHITE AND URANIUMOXIDE/GRAPHITE COMPACTS AT TEMPERATURES UP TO 1250° C

J. J. LAWRENCE and D. J. O'CONNOR

Chemistry Section, Australian Atomic Energy Commission, Lucas Heights, NSW, Australia

Received 7 January 1961

The quantities and compositions of gases evolved from uranium oxide/graphite compacts have been measured at temperatures up to 1250° C after prior degassing for 17 hours at 200° C. Similar studies have been made on graphite and four uranium oxides, viz. $\text{UO}_{2.008}$, $\text{UO}_{2.014}$, $\text{UO}_{2.33}$ and U_3O_8 . In agreement with thermodynamic data, reduction stopped at the $\text{UO}_{2.0}$ stage for all four oxides and all oxide/graphite ratios used (1:1–1:70 M). The quantity of gas ($\text{CO}_2 + \text{CO}$) evolved from the oxide/graphite compacts was dependent on the oxygen content of the uranium oxide in excess of the ratio $\text{O/U} = 2.00$.

Les quantités et la composition des gaz dégagés par des compacts de graphite-oxyde d'uranium ont été mesurées aux températures allant jusqu'à 1250° C après dégazage préalable de 17 heures à 200° C. Des études analogues ont été effectuées sur du graphite et quatre oxydes d'uranium, à savoir $\text{UO}_{2.008}$, $\text{UO}_{2.014}$, $\text{UO}_{2.33}$ et U_3O_8 . En accord avec les données thermodynamiques, la réduction ne dépassait pas le stade

$\text{UO}_{2.0}$ pour les 4 oxydes et pour toutes les proportions oxyde/graphite utilisées (1:1 à 1:70 M). La quantité de gaz $\text{CO} + \text{CO}_2$ dégagée à partir de compacts oxyde/graphite dépendait de la teneur en oxygène de l'oxyde d'uranium dépassant le rapport $\text{O/U} = 2.00$.

Die Mengen und Zusammensetzungen von Gasen, die aus Uran-Oxyd/Graphit-Mischungen frei wurden, sind bei Temperaturen bis 1250° C nach einer ersten Entgasung von 17 Stunden bei 200° C gemessen worden. Ähnliche Studien wurden an Graphit und 4 Uran-Oxyden unternommen. Die Oxyde hatten die Zusammensetzungen: $\text{UO}_{2.008}$, $\text{UO}_{2.014}$, $\text{UO}_{2.33}$ und U_3O_8 . In Übereinstimmung mit thermodynamischen Daten geht die Reduktion nicht unter die $\text{UO}_{2.0}$ -Stufe bei allen 4 Oxyden und allen Mischungsverhältnissen Oxyd/Graphit, die verwendet wurden (1:1–1:70). Die Mengen des CO_2 und CO -Gases, die von den Oxyd/Graphit-Mischungen freigegeben wurden, sind abhängig vom Sauerstoffgehalt des Uran-Oxydes, insbesondere vom Überschuss in dem Verhältnis $\text{O/U} = 2.00$.

1. Introduction

Uranium dioxide is being currently used as a fuel element material for high temperature and pressurised water reactors. The advantages of this material over metallic uranium have been reported in many publications. The use of uranium carbide and uranium-uranium carbide cermet as reactor fuels for high temperature use instead of fuels based on UO_2 is also now receiving considerable attention. However, the possibility of using UO_2 canned in low permeability graphite as a reactor fuel does not seem to have been seriously investigated. The thermal and the radiation induced reaction between UO_2 and graphite at operative fuel temperatures

could possibly produce sufficient gases to distort or rupture the graphite can.

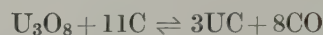
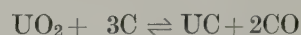
The studies reported herein were made to obtain some assessment of the potential of uranium dioxide dispersed and/or canned in graphite for use as a H.T.G.C. fuel. The quantities and compositions of gases evolved from graphite, uranium oxides, and uranium oxide/graphite compacts have been measured at temperatures to 1250° C. These studies were performed, not to verify the equilibrium constants for the reduction of uranium oxides by graphite, but to investigate the rate at which known equilibria are approached at a given temperature and which depend largely on the

degree of contact between the two components. In an attempt to obtain extreme conditions, compacts prepared from powdered uranium oxide and graphite were used, and oxides of O/U ratios 2.008, 2.014, 2.33, 2.67 were employed. Also, the oxide/graphite molar ratios were varied between 1:1–1:70 M.

Most of the work reported in the literature on the reaction between uranium oxides and graphite has been concerned with the preparation of uranium carbides and at temperatures generally greater than 1800° C (refs. ¹⁻⁸). Wilhelm *et al.* ²) found that reaction of a near-stoichiometric mixture of finely divided UO₂ and graphite above 2400° C produced UC₂. Barnes *et al.* ⁸) prepared uranium monocarbide by the carbon reduction of the dioxide at 1900° C. Greenwood ⁹) reported that the reaction between UO₂ and carbon in vacuum commenced at 1490° C, and that the gas evolved reached atmospheric pressure at 1800° C. Heusler ¹⁰) measured the equilibrium pressure of CO over a UO₂/C mixture and found this pressure was 20 mm at 1500° C, and one atmosphere at 1800° C. Craven ¹¹) studied the reaction between UO_{2.079} and Acheson graphite by heating separate pellets in contact and examining the product layer microscopically. At 1500° C a product of layer thickness only 0.075 mm was

formed after 76 hours heating. Sangster and Wright ¹²) investigated the reaction between uranium dioxide and graphite in a thermal flux of 1.8×10^{11} n/cm² sec, but found that evidence for a radiation induced reaction at 75° C was not conclusive because of gas evolution from the Acheson colloidal graphite used.

The equilibrium pressure of CO for the reactions



and



have been calculated in the present work, using selected free energy data due to Glassner ¹³), Coughlin ¹⁴) and Krikorian ¹⁵). The results are shown in table 1. The reduction of UO₂ and U₃O₈ by carbon to form UC should not occur to any appreciable extent in the equilibrium systems below 1500° K. Reduction beyond UC to U₂C₃ and UC₂ is less favourable thermodynamically.

However, the reduction of U₃O₈ by carbon to form UO₂ is more favourable at temperatures of 1000–1500° K. The pressure of CO in equilibrium with U₃O₈, UO₂ and C is one atmosphere at 1060° C.

TABLE 1

Calculated equilibrium pressure of CO for uranium oxide/graphite reactions at various temperatures

Reaction	Temp. (°K)	<i>p</i> _{CO} (atm)
UO ₂ + 3C \rightleftharpoons UC + 2CO	500	1.0×10^{-30}
	1000	2.9×10^{-11}
	1500	7.6×10^{-5}
	2000	1.6×10^{-1}
	2500	1.2×10^1
U ₃ O ₈ + 11C \rightleftharpoons 3UC + 8CO	500	8.7×10^{-26}
	1000	2.2×10^{-9}
	1500	5.8×10^{-2}
U ₃ O ₈ + 2C \rightleftharpoons 3UO ₂ + 2CO	500	1.3×10^{-12}
	1000	1.1×10^{-3}
	1500	1.8×10^7

2. Materials and Experimental

The four oxides studied ($\text{UO}_{2.008}$, $\text{UO}_{2.014}$, $\text{UO}_{2.33}$ and U_3O_8) were prepared by controlled oxidation and/or reduction of uranium dioxide ($\text{UO}_{2.15}$). The graphite powder was prepared by crushing and grinding off-cuts of pile grade A graphite; its surface area being $23.2 \text{ m}^2/\text{g}$. A micromerograph analysis of particle diameters showed that 7 % were less than 0.6μ , 58 % less than 10μ and 100 % less than 100μ . Particle size analysis of the $\text{UO}_{2.008}$ showed that 7 % were less than 0.8μ , 60 % less than 12μ and 100 % less than 80μ . The particle size distributions of the other three oxides were not measured, but appeared to be similar to that of the $\text{UO}_{2.008}$.

Compacts of the uranium oxide and graphite were prepared by compacting the mixed powders in 1 cm diameter hardened steel dies at $3.5 \times 10^5 \text{ kg/cm}^2$ at room temperature, the powders having previously been weighed separately into a 100 ml sample bottle and hand shaken for 30 min. The compacts were reacted in a silica reaction tube connected to a vacuum system which could attain better than $1 \times 10^{-5} \text{ mm Hg}$. An automatically controlled Heraeus rhodium tube furnace was used and temperatures were measured with an Ir/Ir, Rh thermocouple.

The quantities of evolved gases were measured volumetrically after cooling the reaction tube to room temperature. The volumetric system consisted of the reaction tube, gas burette and constant volume type mercury manometer. Quantities of gases could be measured to an accuracy of $5 \times 10^{-7} \text{ mole}$. No allowance was made for re-adsorption of gases by the sample on cooling to room temperature.

The evolved gases were analysed with a Metropolitan Vickers MS3-type mass spectrometer. The quantities of gases evolved from graphite, uranium dioxide, and uranium oxide/graphite compacts were measured separately for various temperatures and reaction times. The quantities of gases attributed to the uranium oxide/graphite reaction were then obtained by difference.

3. Results

3.1. GAS EVOLUTION FROM GRAPHITE

Fig. 1 shows the quantities of gas (mole of gas/g graphite) evolved from graphite compacts (0.356–3 g) on heating at temperatures of 1250°C for periods up to 300 min. These compacts had been previously degassed for 17 hours at 200°C . A separate compact was used for the measurements at any one temperature. Duplicate experiments at 1250°C were reproducible to within 5.4 %. The results for a compact which was heated to 1250°C without prior degassing are also shown.

Most of the gas (in all cases more than 75 %) is evolved in the first 5 minutes of heating. This applies for heating times up to 240 minutes. The initial rapid evolution of gas suggests that the surface film of gas is rapidly desorbed at temperatures as low as 700°C , but that diffusion from the pores is the controlling process after heating periods of 5–10 minutes. The quantity of gas evolved also increases with temperature; the ratios of quantities evolved at 700, 800, 900, 1000 and 1250°C after heating for 200 minutes were 1:1.9, 2.2, 2.4, 2.8. The ratios of the quantities of gas evolved at 1250°C after 240 minutes heating without prior degassing and with degassing for 17 hours at 200°C were 1.7:1.

The composition of the gases evolved on heating graphite compacts at 700 – 1250°C are shown in table 2; the figures quoted are expressed in molecular per cent. Generally, the results show that the gases which are adsorbed are the components of air (N_2 , O_2 , CO_2 , A). This air is largely desorbed by degassing at 200°C for 17 h or is continuously eliminated by heating at 700 – 1000°C . After initial degassing, the evolved gas consists mainly of CO_2 and CO. The CO_2/CO ratio decreases as the temperature increases and at 1250°C the evolved gas is almost entirely CO. The measured CO_2/CO ratios at temperatures of 700 – 1250°C are of the same order as the ratios which can be calculated on the basis of thermodynamic considerations for the system $\text{C} + \text{CO}_2 \rightleftharpoons 2\text{CO}$ (ref. ¹⁶). Generally,

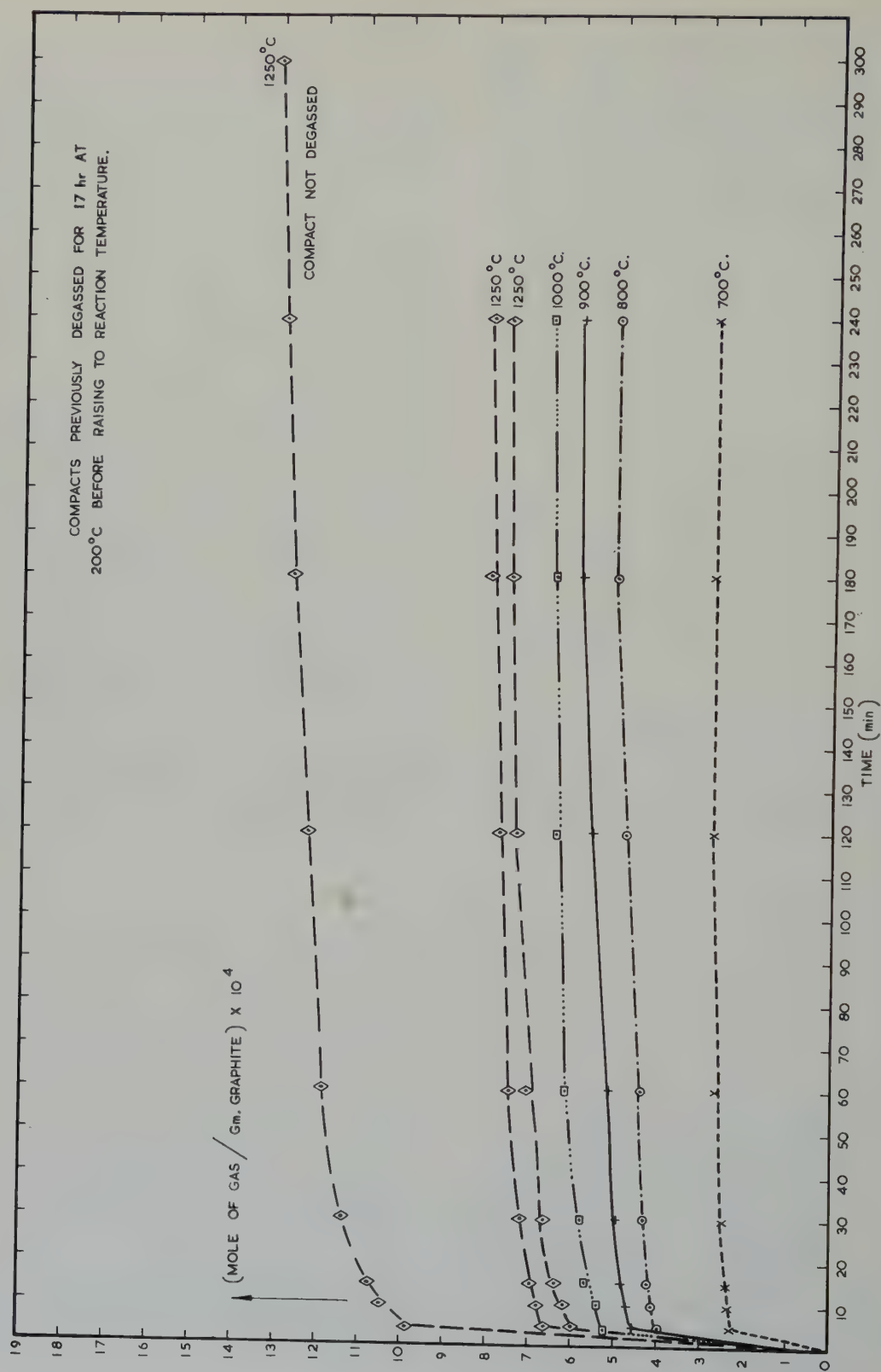


Fig. 1. Quantities of gas evolved on heating graphite compacts at various temperatures.

TABLE 2
Compositions of gases evolved on heating graphite compacts †

Temp. (°C)	Time (min)	Pre-treatment	Gas composition (mol %)
700	60	de-gassed	CO ₂ = 67, CO = 32,
1200	60	de-gassed	CO > 99, CO ₂ < 1 %
700	240	de-gassed	CO ₂ = 54, CO = 45, CH ₄ = 1.0, O ₂ = 0.7
1250	240	de-gassed	CO ₂ = 2.5, CO = 95, Air = 2.5
1250	240	de-gassed	CO ₂ = 3.0, CO = 97
700	60	not de-gassed	N ₂ = 79, O ₂ = 19, CO ₂ = 1, A = 1
800	60	not de-gassed	N ₂ = 77, O ₂ = 22, CO ₂ < 1, A < 1
900	60	not de-gassed	N ₂ = 35, O ₂ = 11, CO = 53, CO ₂ = 0.5, A = 0.5
1000	60	not de-gassed	N ₂ = 1.7, O ₂ = 0.6, A = 0.1, CO ₂ = 0.4, CO = 97.2

† Separate compact used for each extraction.

the results shown in fig. 1 and table 2 are in agreement with previous studies on the degassing of graphite ^{11,17}).

3.2. GAS EVOLUTION FROM URANIUM OXIDES

The quantities of gases evolved from compacts of three uranium oxides (UO_{2.008}, UO_{2.33}, U₃O₈) were measured at temperatures up to 1250° C and found to be small compared with those from graphite compacts under equivalent heating conditions. In all cases the quantity of gas evolved from uranium oxide compacts was less than 8 % of the quantities evolved from graphite compacts under the same heating conditions: e.g., heating of UO_{2.33} at 1250° C for 600 min produced only 0.46×10^{-4} mole of gas per gram of oxide, compared with 7.2×10^{-4} mole of gas per gram of graphite when this was heated at 1250° C for 240 min.

3.3. GAS EVOLUTION FROM URANIUM OXIDE/GRAPHITE COMPACTS

Fig. 2 shows a series of curves for the measured quantities of gas evolved from U₃O₈/graphite compacts heated at temperatures to 1250° C. Similar curves have been obtained for UO_{2.008} and UO_{2.014}/graphite compacts for oxide/graphite ratios of 1:1 (fig. 3), 1:4 and 1:22.5 M. Figs. 2 and 3 show that there is an

increase in the quantity of evolved gas with increase in temperature from 700–1250° C. The variations of molar ratio of UO_{2.008} and UO_{2.014}/C from 1:4 to 1:22.5 did not have a significant effect on total gas evolution. The general shapes of the curves shown in figs. 2 and 3 are of a parabolic nature (suggesting a diffusion-controlled process) and are different from those obtained for the outgassing of graphite (fig. 1).

The variations of the quantities of gases evolved from UO_{2.33}/C compacts (1:4.08 M–1:22.9 M) with temperature when heated at 750–1250° C for periods up to 270 minutes were similar to those shown in fig. 2, but the quantities evolved were less by a factor of two. The quantities of gas evolved were independent of the molar ratio of oxide to graphite used.

The compositions of gases evolved on reaction of UO_{2.008}, UO_{2.33} and U₃O₈ with graphite in various molar ratios from 700–1250° C are shown in table 3. These analyses were made on gas samples taken from the system after the furnace tube had cooled to room temperature. The gas mixture consisted mainly of CO₂ and CO and the measured CO₂/CO ratios decrease sharply with increase in temperature above 700–800° C and follow the pattern for the CO₂/CO ratios determined by the equilibrium $\text{CO}_2 + \text{C} \rightleftharpoons 2\text{CO}$ (ref. ¹⁶)). It would appear that

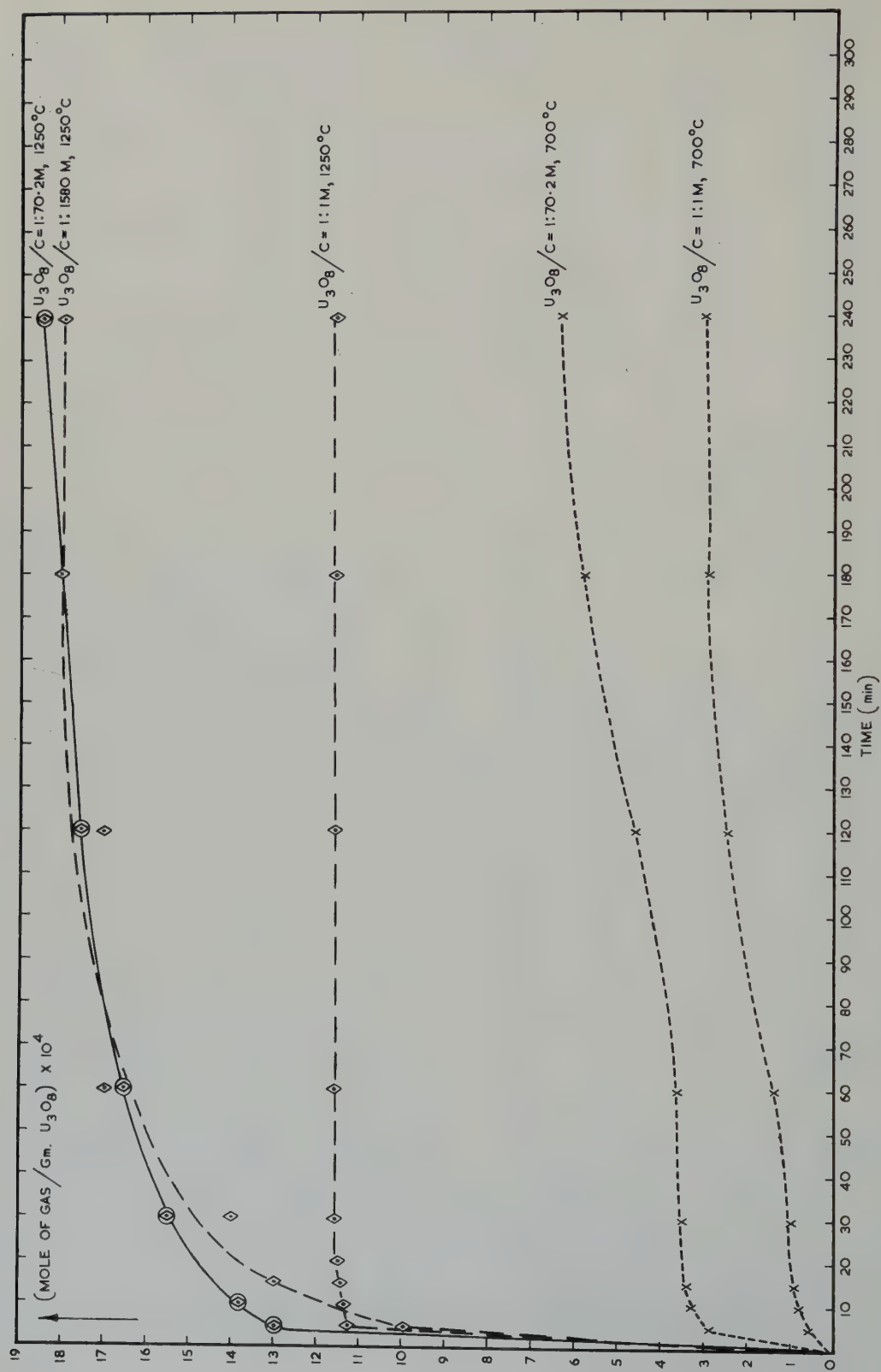


Fig. 2. Quantities of gas evolved from reaction of U_3O_8 and graphite at temperatures to $1250^\circ C$ (These quantities have been corrected for gas evolution from the components separately.)

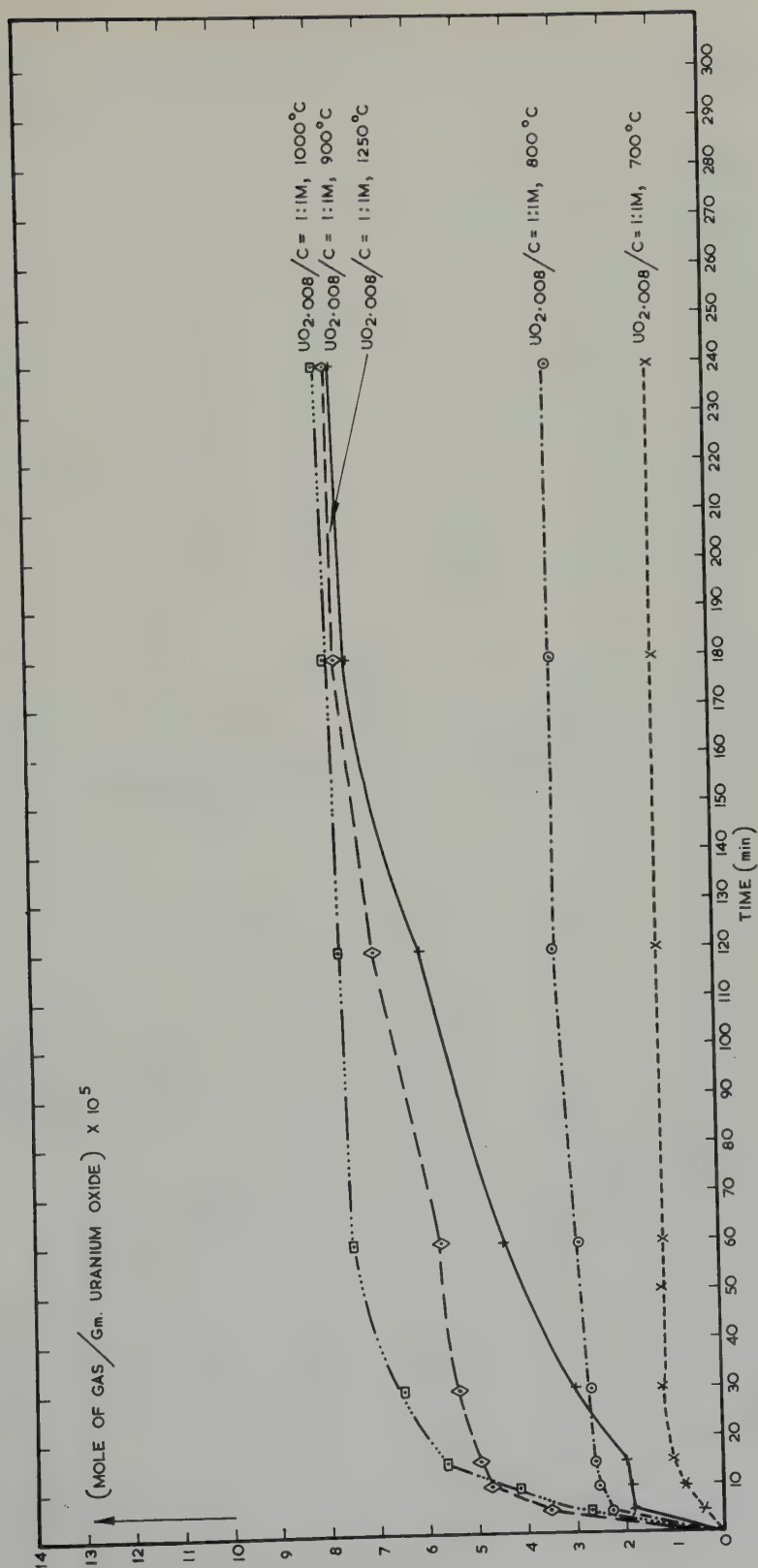


Fig. 3. Quantities of gas evolved from reaction of $\text{UO}_{2.008}$ and graphite at temperatures to 1250°C (These quantities have been corrected for gas evolution from the components separately.)

TABLE 3

Compositions of gases evolved on reaction of uranium oxide-graphite compacts at various temperatures

Oxide	Oxide/C ratio (M)	Reaction		Composition of evolved gas (mol %)				CO ₂ /CO ratio
		Temp (°C)	Time (min)	CO ₂	CO	O ₂	N ₂	
UO _{2.008}	1:1	1000	240	1.9	97.7	0.1	0.3	0.0175
		1250	240	1.3	97.4	0.3	1.0	0.0133
	1:22.52	700	240	90	10			9.0
		800	240	3.2	96.4	0.1	0.3	0.332
		1000	240	1.9	97.7	0.1	0.3	0.0175
		1250	240	1.3	97.4	0.3	1	0.133
UO _{2.33}	1:4.08	1250	225	10	90			0.0111
	1:4.64	1250	150	3	97			0.0309
	1:6.12	1250	150	13	87			0.149
	1:22.9	750	345	90	10			9.0
		1000	690	3	97			0.0309
		1250	600	3	97			0.0309
U ₃ O ₈	1:70.2	1250	240	6.5	92.6		Air=0.9	0.0702

For the equilibrium $C + CO_2 \rightleftharpoons 2CO$ at 1 atm pressure the CO₂/CO ratios at 700 and 800° C are 0.73 and 0.11 respectively. At temperatures higher than 800° C, the CO₂/CO ratio decreases sharply.

TABLE 4

Ratio of quantity of gas evolved to oxygen in excess of 2.00 for reaction of various uranium oxide/graphite compacts

1	2	3	4	5	6	7	8	9	10
Oxide	Oxide/C ratio(M)	Reaction		Theoretical quantity of CO evolved on basis of reduction of 1 g oxide to UO _{2.00} (mole)	Measured amount of gas from reaction of 1 g of uranium oxide (mole)	Amount of gas evolved from quantity of graphite corresponding to 1 g oxide (mole)	Amount of gas/g uranium oxide (mole)	Corrected quantity of gas evolved/g oxide (mole) = [(6)-(7)-(8)]	Mole of gas/unit of oxygen-uranium ratio in excess of 2.00
		Temp. (°C)	Time (min)						
UO _{2.008}	1:4.02	1250	240	2.94×10^{-5}	2.33×10^{-4}	1.43×10^{-4}	2.50×10^{-5}	6.50×10^{-5}	8.06×10^{-3}
	1:1	1250	240	2.94×10^{-5}	1.37×10^{-4}	3.57×10^{-5}	2.50×10^{-5}	7.63×10^{-5}	9.54×10^{-3}
UO _{2.014}	1:22.5	1250	240	5.13×10^{-5}	9.0×10^{-4}	8.05×10^{-4}	2.50×10^{-5}	7.00×10^{-5}	5.00×10^{-3}
UO _{2.33}	1:4.08	1250	225	1.20×10^{-3}	1.14×10^{-3}	1.44×10^{-4}	4.60×10^{-5}	9.50×10^{-4}	2.85×10^{-3}
	1:4.64	1250	150	1.20×10^{-3}	1.20×10^{-3}	1.54×10^{-4}	4.60×10^{-5}	10.00×10^{-4}	3.00×10^{-3}
	1:6.12	1250	150	1.20×10^{-3}	1.24×10^{-3}	2.04×10^{-4}	4.60×10^{-5}	9.90×10^{-4}	2.97×10^{-3}
	1:22.9	1250	600	1.20×10^{-3}	1.65×10^{-3}	7.64×10^{-4}	4.60×10^{-5}	8.40×10^{-4}	2.52×10^{-3}
U ₃ O ₈	1:1	1250	240	2.33×10^{-3}	1.20×10^{-3}	1.15×10^{-5}	4.20×10^{-5}	11.47×10^{-4}	1.71×10^{-3}
	1:70.2	1250	240	2.33×10^{-3}	2.69×10^{-3}	8.05×10^{-4}	4.20×10^{-5}	18.43×10^{-4}	2.76×10^{-3}
	1:1580	1250	240	2.33×10^{-3}	19.84×10^{-3}	18.0×10^{-3}	4.20×10^{-5}	17.98×10^{-4}	2.68×10^{-3}

the gases evolved from the reaction between uranium oxide and graphite are in equilibrium with the excess graphite in the compact at reaction temperature. This suggests that there is very little re-oxidation of the product by CO_2 and/or CO during the time that the furnace is allowed to cool from reaction to room temperature; the temperature of the reaction tube fell from 1250°C to less than 200°C within 5 minutes after removal from the furnace.

The experimentally measured quantities of gas produced by reaction of the four oxides with graphite at 1250°C for reaction times of 150–600 minutes are shown in table 4 (column 6). Also shown are the theoretical quantities of CO produced by reduction of $\text{UO}_{2.008}$, $\text{UO}_{2.014}$, $\text{UO}_{2.33}$ and U_3O_8 to $\text{UO}_{2.00}$ (column 5). The

right hand column of table 4 gives the quantities of gas evolved per unit of oxygen/uranium ratio of the oxide in excess of 2.00.

Slightly more than the theoretical quantity of gas is evolved from the $\text{UO}_{2.008}$ and $\text{UO}_{2.014}/\text{C}$ compacts (column 9; this is the measured value, corrected for gas evolved from the constituents separately). It cannot be stated unequivocally that this represents reduction below $\text{UO}_{2.00}$, because the quantities of gas evolved are small (of the order of 10^{-5} mole/g oxide) and they are obtained from the difference of two quantities of similar magnitude. For both the $\text{UO}_{2.33}$ and $\text{U}_3\text{O}_8/\text{C}$ compacts the quantities of gas evolved are only slightly less than the quantities calculated on the basis of reduction to $\text{UO}_{2.00}$. The ratios of moles of gas evolved to the

TABLE 5
Lattice constants of uranium oxides before and after various treatments

Oxide	Reaction			a_0 (Å)
	Compact	Temp. ($^\circ\text{C}$)	Time (h)	
$\text{UO}_{2.15}$ (Stock material)	—	—	—	5.4686 ± 0.0010
$\text{UO}_{2.15}$ H_2 reduction, 3 h at 800°C , then oxidation in air	—	—	—	5.4697 ± 0.0010
$\text{UO}_{2.15}$ H_2 reduction, 3 h at 800°C	—	—	—	5.4691 ± 0.0010 5.4682 ± 0.0010
$\text{UO}_{2.014}$	$\text{UO}_{2.014}/\text{C}$ (1:1 M)	1500	4	5.4702 ± 0.0015
$\text{UO}_{2.33}$	$\text{UO}_{2.33}/\text{C}$ (1:1 w/w)	750	5.75	5.4690 ± 0.0015
$\text{UO}_{2.33}$	$\text{UO}_{2.33}/\text{C}$ (1:1 M)	1000	11.5	5.4700 ± 0.0010
$\text{UO}_{2.33}$	$\text{UO}_{2.33}/\text{C}$ (1:4.5 M)	1250	2.75	5.4703 ± 0.0010
U_3O_8	$\text{U}_3\text{O}_8/\text{C}$ (1:1 M)	1250	4	5.4702 ± 0.0015
U_3O_8	$\text{U}_3\text{O}_8/\text{C}$ (1:1 M)	1250	30	5.4717 ± 0.0015

oxygen/uranium ratio of the oxide in excess of $O/U = 2.00$ are of the same order of magnitude for all oxides studied. These ratios are approximately the same for $UO_{2.33}$ and U_3O_8 .

For all four oxides, irrespective of the oxide/graphite ratio and the temperature of reaction, the reaction product as analysed by X-ray diffraction showed only UO_2 and graphite. Table 5 shows lattice parameters (a_0) of several uranium oxides before and after hydrogen reduction or reaction with graphite. X-ray studies¹⁸) have shown that there is a decrease in the lattice spacing of uranium oxides with increase in the O/U ratio, values of 5.4701 ± 0.0013 and 5.4401 ± 0.0025 Å being reported for uranium oxides of O/U ratios 2.01 and 2.25 respectively). On the basis of a_0 values given by Belle and Lustman¹⁸) the uranium oxide product after reaction with graphite approximates to $UO_{2.01}$ or $UO_{2.02}$.

The ratios of moles of gas evolved to O/U ratio in excess of 2.00, and the X-ray analyses of the product, suggest that reduction of the higher oxide to $UO_{2.0}$ is occurring at temperatures to 1250°C . This conclusion is supported by metallographic examination of several of the compacts after reaction; two phases only (oxide and graphite) and no intermediate reactions product being observed. The measured gas quantities and compositions rule out the possibility that any carbide which may have been formed at high temperatures was subject to decarburisation on cooling.

4. Summary and Conclusions

Quantities of gas of the order of 8×10^{-4} mole/g graphite are evolved when graphite compacts, previously degassed at 200°C for 17 hours, are heated to 1250°C . The quantity of gas evolved increased with temperature to 1250°C and at 1250°C at least 75 % of the gas is evolved in the first 5 minutes of heating.

Reduction of $UO_{2.008}$, $UO_{2.014}$, $UO_{2.33}$ and U_3O_8 towards $UO_{2.0}$ occurs when compacts of the oxide and graphite are heated to 1250°C for periods up to 300 min. This is in agreement with thermodynamic data. Quantitative measu-

rements of the evolved gases are supported by X-ray and metallographic examination of the product which shows only UO_2 and unreacted graphite. Uranium carbide was not detected in the product. Generally, the rate of reduction falls off after 60 min reaction time.

The quantities of gas evolved for all uranium oxide/graphite compacts studied are approximately proportional to the oxygen content of the oxide in excess of the ratio $O/U = 2.00$. The measured CO_2/CO composition of the gases evolved from graphite and from reaction of the four uranium oxides with graphite approximate the composition determined by the equilibrium $CO_2 + C \rightleftharpoons 2CO$ at reaction temperature.

To ensure minimum reaction between uranium oxide and graphite the optimum composition of the oxide is $UO_{2.00}$. Reduction in surface area of the oxide and graphite, and also sintering of the oxide, should reduce the extent of reaction. The canning of stoichiometric uranium dioxide in impermeable graphite appears to have possible application in reactor fuel manufacture. However, the effect of irradiation on this system has not been investigated, and must be studied for a complete assessment of the potentialities of uranium oxide graphite fuels. Long term experiments with diffusion couples, supplemented by extensive metallographic and X-ray diffraction analyses, would give a more complete answer to the reduction of uranium oxides by graphite.

Acknowledgments

Acknowledgments are gratefully made to Mr. J. C. Taylor and Mr. B. L. Campbell, Analytical Group, Chemistry Section, for the X-ray and mass spectrometric analyses respectively.

References

- 1) U. Esch and A. Schneider, *Zeit. anorg. Chem.* **254** (1948) 527
- 2) H. A. Wilhelm, P. Chiotti, A. I. Snow and A. H. Daane, *J. Chem. Soc. Suppl.* **2** (1949) 318
- 3) M. W. Mallett, A. A. Gerds and H. R. Nelson, *J. Electro-Chem. Soc.* **99** (1952) 197

- 4) L. M. Litz, A. B. Garrett and F. C. Croxton, J. Am. Chem. Soc. **70** (1948) 718
- 5) USAEC Report (New York Operations Office, USA), NYO-2684 (1959)
- 6) J. J. Finley *et al.*, USAEC Report Oak Ridge Operations Office, USA, ORO-222 (1959)
- 7) N. Brett, D. Law and D. T. Livey, Harwell (UK) Report, AERE M/R-2574 (1958)
- 8) E. Barnes, W. Munro, J. Williams and P. Murray, Harwell (UK) Report, AERE M/R-1958 (1956)
- 9) H. C. Greenwood, J. Chem. Soc. **93** (1908) 1483
- 10) O. Heusler, Zeit. anorg. Chem. **154** (1926) 5353
- 11) B. Craven, M.Sc. Thesis, University of New South Wales (1959)
- 12) D. F. Sangster and J. Wright, Harwell (UK) Report, AERE C/R-583 (1951)
- 13) A. Glassner, Argonne (USA) Report, ANL-5107 (1953)
- 14) J. P. Coughlin, U.S. Bureau of Mines Bulletin 542 (1954)
- 15) O. H. Krikorian, University of California Radiation Laboratory Report, UCRL-2888 (1955)
- 16) A. R. Anderson, H. W. Davidson, R. Lind, D. R. Stranks, C. Tyzack and J. Wright, 2nd Geneva Conference (1958) 15/P/303
- 17) J. P. Redmond and P. L. Walker, Nature **186** (1960) 72
- 18) J. Belle and B. Lustman, Westinghouse Atomic Power Div. Report, WAPD-184 (1957)

NEW METALLOGRAPHIC TECHNIQUES FOR THE EXAMINATION OF URANIUM, URANIUM ALLOYS AND URANIUM DIOXIDE

J. F. R. AMBLER and G. F. SLATTERY

Fuel Element Development Laboratory, Springfields Works, UKAEA Development and Engineering Group, Salwick, Preston, Lancs., UK

Received 17 February 1961

An attack-polish reagent has been developed for the metallographic preparation of uranium alloys and uranium dioxide. The reagent consists of a slurry of hydrogen peroxide (30 wt %) and 5 % γ -alumina. Polishing is carried out on a polythene lap covered with terylene velvet. This method has many advantages over the standard electro-polishing techniques used for uranium and uranium alloys.

A new electrolytic etching technique described, for the study of the grain structure of uranium and uranium alloys using bright field illumination, provides a useful alternative to polarised light methods. The reagent is composed of ammonium persulphate/glycerol/water.

A new stain etch using hydrogen peroxide (30 wt %) has been developed for the general examination of grain size and distribution in uranium dioxide sintered compacts and is also ideal for studying duplex UO_2 and U_4O_9 phase structures. The etchant is a useful extension to the simple grain boundary etchants already available.

The results obtained by these new techniques are discussed, using specific metallographic structures as examples.

Un réactif de polissage-attaque a été mis au point permettant la préparation métallographique de l'uranium, de ses alliages et de l'oxyde UO_2 . Le réactif est une suspension d'alumine γ (5 %) dans de l'eau oxygénée H_2O_2 (30 % en poids). Le polissage est réalisé sur un disque de polythène recouvert d'un tissu en terylène. Cette méthode a de nombreux avantages sur les techniques de polissage électrolytique classique utilisées pour l'uranium et les alliages d'uranium.

Une nouvelle technique d'attaque électrolytique est décrite qui permet l'étude de la structure cristalline de l'uranium et de ses alliages en utilisant l'illumination en lumière blanche. Cette technique fournit une solution de rechange bien utile vis-à-vis des méthodes basées sur la lumière polarisée.

Une nouvelle attaque oxydante utilisant l'eau oxygénée à 30 % en poids a été mise au point pour déterminer la grosseur de grain et la répartition de la grosseur de grain, dans des agglomérés frittés de UO_2 . Cette méthode est aussi excellente pour étudier les structures mixtes de UO_2 et U_4O_9 . Le réactif élargit le domaine d'utilisation des réactifs attaquant les contours de grains dont on dispose déjà.

Les résultats obtenus avec ces nouvelles techniques sont discutés en prenant comme exemples des structures métallographiques typiques.

Es wurde eine Reagenz für die metallographische Präparation von Uran, Uranlegierungen und Uran-dioxyd entwickelt. Die Reagenz besteht aus Wasserstoff-Peroxyd (30 Gew %) und 5 % Aluminiumoxyd. Das Polieren wird mit einem Polythencap ausgeführt, der mit einem Terylensamt überzogen ist. Die Methode hat viele Vorteile gegenüber den electrolytischen Standardpoliertechniken, die für Uran und Uranlegierungen gebraucht werden.

Es wird ausserdem eine neue elektrolytische Ätz-methode beschrieben, die zum Studium der Kornstruktur von Uran und Uranlegierungen im Hellfeld angewendet wird, wobei eine brauchbare Alternative für die Anwendung der Untersuchungsmethode mit polarisiertem Licht besteht. Der Reagent ist aus Ammonium-Persulphat/Glyzerol/Wasser zusammengesetzt.

Ferner ist eine neue Möglichkeit der Farbätzung aufgefunden worden, die hauptsächlich zur Untersuchung der Korngrösse und -verteilung in gesintertem UO_2 angewendet werden kann. Es wird dabei 30 Gew % Wasserstoff-Peroxyd verwendet. Die Methode ist ideal zur Untersuchung von UO_2 und U_4O_9 -Phasenstrukturen. Diese Ätzmethode ist eine brauchbare Erweiterung der einfachen Korngrenzenätzung, wie sie im allgemeinen angewendet wird. Die durch diese neuen Techniken erhaltenen Ergebnisse werden diskutiert und Beispiele spezieller metallographischer Strukturen angeführt.

1. Introduction

New methods have recently been developed for the metallographic polishing and etching of uranium, uranium alloys and uranium dioxide.

The normal mechanical methods for the metallographic preparation of metals, finishing with diamond dust, are unsuitable for uranium since on subsequent examination under polarised light no grain structure is observed. The methods are also unsuitable for uranium dioxide since they produce a flowed surface layer, which on removal by etching reveals a network of fine scratches: it also fails to give a flat surface to the uranium dioxide specimen. Electrolytic polishing, although widely used for uranium¹⁾, is unsuitable for uranium alloys containing considerable quantities of secondary phase since it gives a heavily pitted surface. Sintered compacts of uranium dioxide are also difficult to polish electrolytically because of their low conductivity. This means that a high potential difference has to be used, leading to severe heating of the specimen. Electrolytic polishing also enlarges the uranium dioxide pore size. The work here reported has gone some way towards ameliorating these difficulties by defining an attack polishing procedure, equally applicable to uranium, uranium alloys and uranium dioxide.

After a polishing procedure had been established, attention was next turned to developing new etching techniques for these materials. For uranium and uranium alloys some substitute for polarised light examination was sought, because of its following disadvantages:

- (1) The macrograins break down on rotation of the microscope stage into a number of smaller grains, thus making grain size measurements very difficult.
- (2) The response to polarised light fails completely at higher magnifications, owing to partial depolarisation by a multi-component objective.

The present investigation resulted in the development of an electrolytic etch in an

oxidising reagent which permits grain size observation under bright field illumination.

The etching techniques available for uranium dioxide are perfectly satisfactory for revealing the grain boundaries. However, it was considered that a stain etch would reveal the general distribution of grain size more clearly and consequently such a stain etch was developed.

2. Attack Polishing of Uranium, Uranium Alloys and Uranium Dioxide

Previously, the authors electropolished uranium in a solution containing 1 volume orthophosphoric acid, 2 volumes acetic acid, 1 volume sulphuric acid and 1 volume water²⁾. The grain contrast under polarised light was improved by anodising in a solution containing 12 g chromic oxide, 200 ml orthophosphoric acid, and 50 ml water. These techniques were not fully satisfactory for the following reasons:

- (1) For complete surface examination, the current for electropolishing had to be adjusted according to the size of specimen. It was therefore difficult to standardise for routine polishing.
- (2) Electropolishing and anodising were unsatisfactory for more concentrated alloying additions due to surface pitting.
- (3) Anodising tended to pit the surface in uranium specimens. This was particularly troublesome with wire or thin strip specimens.
- (4) Before etching in the nitric/citric acids mixture to show secondary phases in uranium alloys, the anodic film had to be removed by re-polishing.

Attack-polishing provides an alternative technique and a reagent containing chromium trioxide, glacial acetic acid and water has been used with uranium³⁾. This reagent did not however work with uranium dioxide sintered compacts and a search was made for an attack polish reagent which would be suitable for uranium, uranium alloys and uranium dioxide.

Several oxidising reagents were tried since it was felt that the oxidation reaction could be controlled sufficiently to give a good polish. Hydrogen peroxide (30 wt %) was found to be the only suitable medium.

The uranium, uranium alloy and uranium dioxide specimens were mechanically polished on kerosene-impregnated silicon carbide papers. The uranium and uranium alloys were finished

with a 0.1 μ diamond paste. The specimens were then attack-polished in a slurry of hydrogen peroxide (30 wt %) containing 5 % γ -alumina, using a polythene lap covered with terylene (dacron) velvet. The polishing time varied between 10 and 15 min. The structures were free from pitting. The grain contrast of uranium and uranium alloys under polarised light was perfectly satisfactory but the contrast

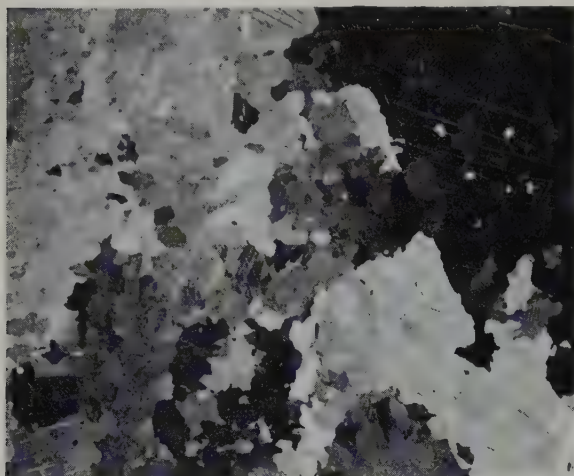


Fig. 1. Grain structure in cast pure uranium prepared by attack-polish reagent. Polarised light illumination. $\times 35$.

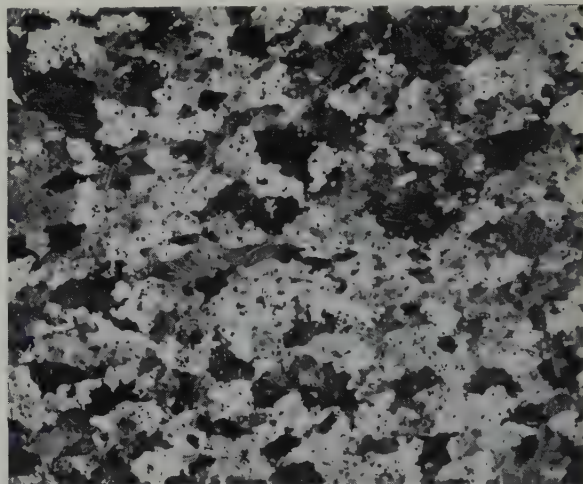


Fig. 2. Fine grained, beta-quenched uranium alloy. Attack-polished. Polarised light illumination. $\times 35$.

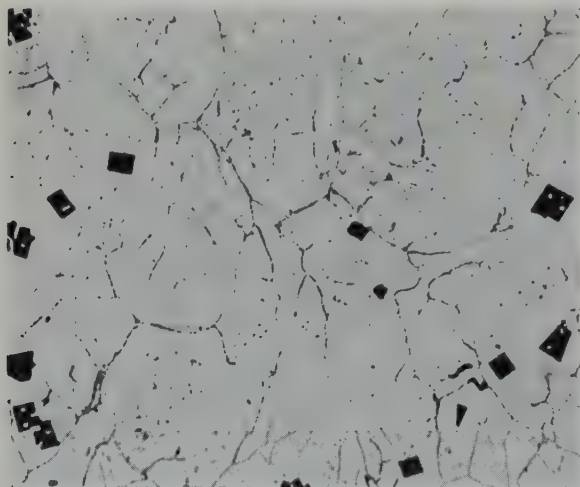


Fig. 3. Beta-quenched uranium alloy. Attack-polished and electrolytically etched in nitric/citric acid reagent to reveal the secondary intermetallic phases. $\times 350$.

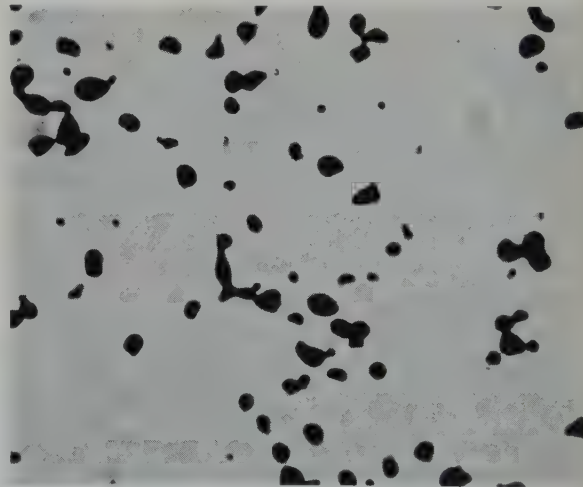


Fig. 4. UO_2 inclusions in uranium. Attack-polished. $\times 350$.

was improved even further by immersing the specimen in hydrogen peroxide for 5 min. The film formed by the hydrogen peroxide treatment could be subsequently removed by dipping in dilute sulphuric acid. The secondary inter-metallic phases in the uranium alloys were then etched in the conventional electrolytic nitric/citric acids reagent immediately after polarised light examination, since there was no anodic film to be removed.

The grain structure of cast uranium prepared by the attack-polish reagent is shown in fig. 1. The grain contrast was good and the sub-structure was clearly noticeable. Some of the macro-grains appeared to be composed entirely of sub-grains and the twin bands were easily visible. The structure of fine grained beta-quenched uranium alloy is shown in fig. 2. The inclusions could be seen at this low magnification. The grain contrast was equally as good as the corresponding electro-polished and anodised structure, whilst for fine detail, the structure was superior. After polarised light examination, the specimens were etched in nitric/citric acids to reveal the secondary intermetallic phases, fig. 3. This shows a typical intermetallic network and the stained UC inclusions are also clearly delineated. All non-metallic inclusions were retained in a perfectly flat condition by the attack polish. The uranium dioxide inclusions were revealed as dark grey rounded inclusions, fig. 4. The carbide inclusions were stained black by etching in dilute nitric acid for 5 sec, fig. 5 †. The duplex nature of some of these carbide inclusions was well demonstrated by this method of attack polishing.

An $U + \frac{1}{2}$ at % Cr alloy isothermally transformed at 450° C has a characteristic acicular type of structure. The attack-polish method gave good contrast with this structure whilst preserving the fine detail, fig. 6. A coarser, almost "feathery" structure was occasionally obtained at the centre of these specimens, fig. 7. The $U + 3.75$ at % Mo alloy gave excellent

grain contrast under polarised light, figs. 8 and 9. The as cast alloy had a fine acicular structure whilst the gamma annealed and slow cooled alloy had a coarse irregular structure. Etching in nitric/citric acids revealed a lamellar eutectoidal structure, fig. 10. The attack-polish was successful with U-V, U-Nb and U-Zr alloys up to about 5 at % alloying content. Above this concentration, the attack polish still gave excellent results but the response to polarised light fell away due to the increasing quantities of second phase.

The attack-polish produced a very flat surface free from scratches with sintered compacts of uranium dioxide. This was not so with diamond dust polishing where the surface was far from flat and although in the unetched condition it appeared to be scratch free, etching revealed a network of scratches. The porosity was also less than that observed after polishing with diamond dust, implying that the diamond paste was ripping out small quantities of oxide from the surface. Fig. 11 shows a micro-section of a high density sintered uranium dioxide compact. The porosity was typical of that found in sintered uranium dioxide compacts of high density. Fig. 12 is a high power photomicrograph of the typical ultrafine porosity present. X-ray powder examination has shown that the white phase is probably uranium nitride.

3. Mode of Operation of the Attack-Polish Reagent

The reaction involved in this polishing operation is primarily one of oxidation. The oxide film formed by the reaction is being removed continuously by the γ -alumina, thus exposing a fresh surface for further oxidation. The oxidation rate of uranium is high only on a freshly exposed surface; after the initial layer of oxide has formed the rate falls off quickly. This may not be so with a metal more reactive to continued oxidation. It is essential that the oxide build-up should not outpace its removal, otherwise it is impossible to polish by this method. Fortunately with uranium and uranium dioxide the oxidation rate is sufficiently low and

† The carbide in fig. 5 is designated UC (O.N), since it is likely to be a complex carbide, with carbon partially replaced by oxygen and nitrogen⁹).



Fig. 5. UC(O.N) inclusions in uranium. Attack-polished and etched in dilute HNO_3 . $\times 1500$.

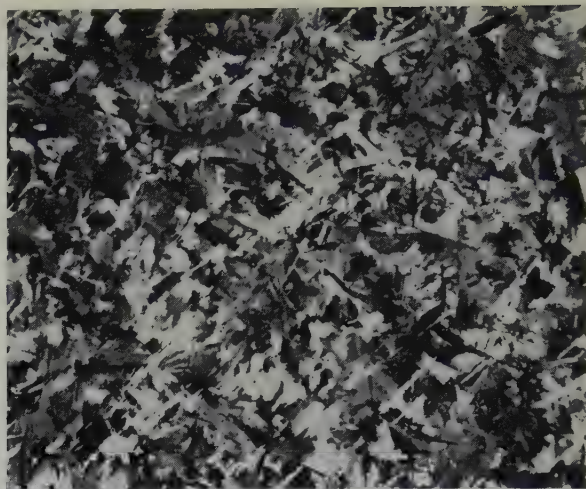


Fig. 6. U + $\frac{1}{2}$ at % Cr alloy isothermally transformed at 450°C and showing the characteristic acicular type structure. Attack-polished. Polarised light illumination. $\times 35$.

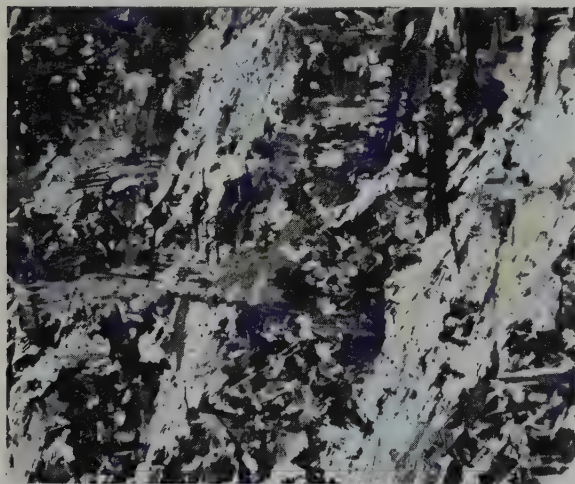


Fig. 7. As for fig. 6, showing the coarse feathery type of structure found at the centre of the specimen. $\times 35$

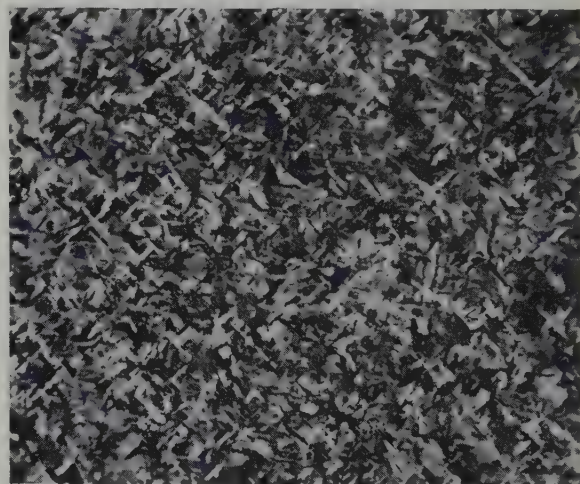


Fig. 8. U + 3.75 at % Mo alloy, as cast. Attack-polished. Polarised light illumination. $\times 100$

this cannot happen; it is thus almost impossible to overpolish them. This applies even allowing for different oxidation rates between grains of differing orientation.

4. Etching of Uranium for Bright Field Illumination

The conventional method of examining uranium is by polarised light since it is difficult

to etch the alpha-uranium structure. Three specific methods have been reported for the grain boundary etching of the alpha-uranium structure for examination under bright field illumination: (1) cathodic vacuum etching⁴); (2) chemical etching in a solution of 130 ml H_2SO_4 (concentrated), 50 ml H_2O_2 (30 wt %), 0.2 g Na_2SiF_6 and 60 ml H_2O ⁵); (3) the formation of epitaxial oxide layers by atmospheric oxida-

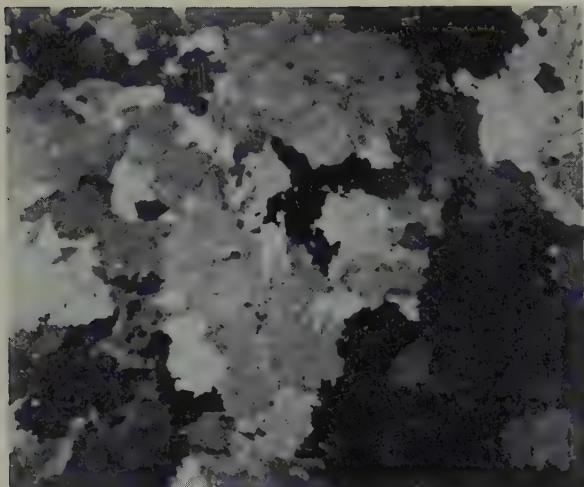


Fig. 9. U + 3.75 at % Mo alloy, gamma-annealed and slowly cooled. Attack-polished. Polarised light illumination. $\times 35$

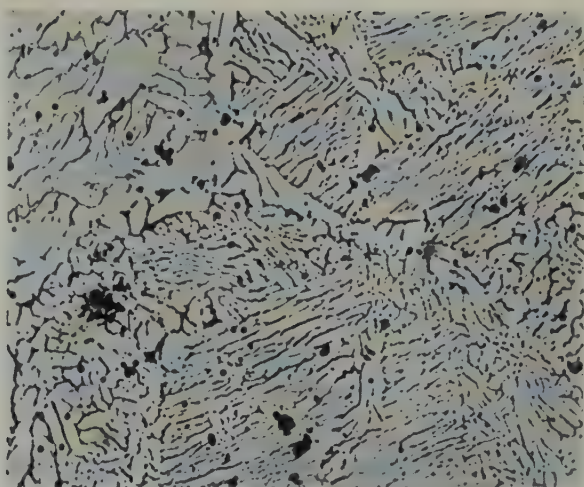


Fig. 10. As for fig. 9. Attack-polished and electrolytically etched in nitric/citric acids reagent to reveal the lamellar eutectoidal structure. $\times 350$

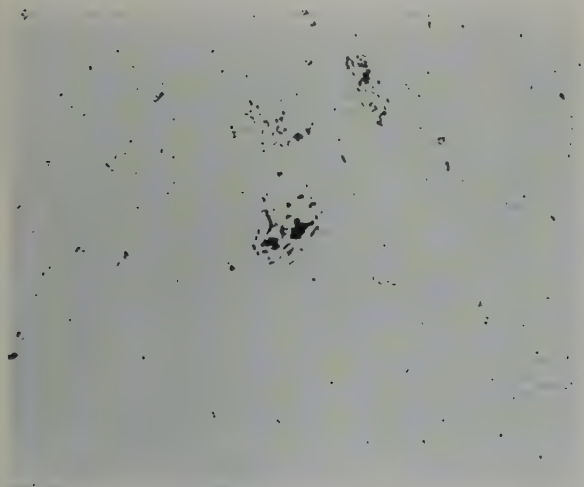


Fig. 11. High density sintered UO_2 compact, showing micro-porosity. Attack-polished. $\times 350$

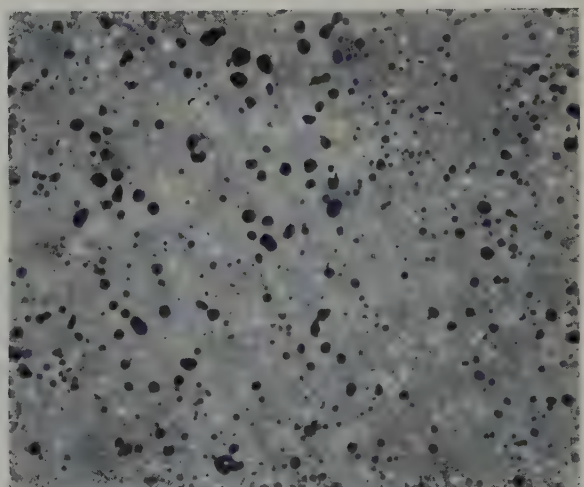


Fig. 12. As for fig. 11, showing the ultrafine porosity (black) and UN particles (white). Attack-polished. $\times 2100$

tion or anodic oxidation in a $\text{CH}_3\text{COOH}/\text{CrO}_3$ bath⁶). Chemical oxidation using a boiling saturated NaNO_3 solution and a combined anodic oxidation in a $\text{CrO}_3/\text{H}_3\text{PO}_4$ /alcohol bath, followed by chemical oxidation in a boiling saturated sodium pyrophosphate solution, have also proved successful⁷). The cathodic vacuum etch gives excellent results but the apparatus is rather elaborate. The chemical etchant can only be used within three minutes of adding

the sulphuric acid, and since the solution boils on mixing there could be a safety hazard associated with its use. The oxidation technique gives grain contrast and reveals the grain boundaries under bright field illumination. The results are excellent on large grained pure uranium and are particularly useful for showing grain boundary migration, sub-boundaries in polygonization, and twins. However, the authors have found that this technique is not so good

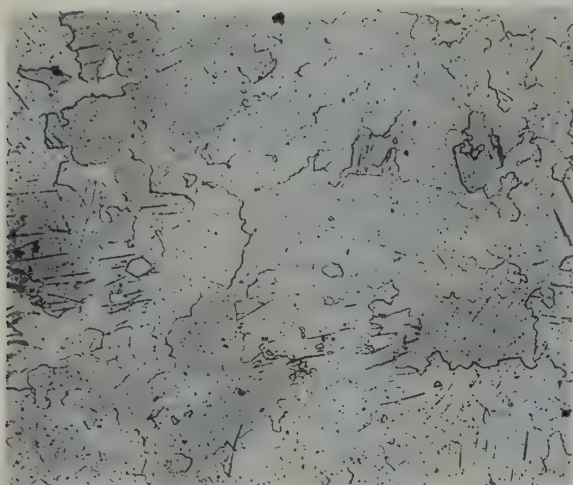


Fig. 13. Grain structure in cast pure uranium. Attack-polished and electrolytically etched in ammonium persulphate/glycerol/water reagent. $\times 50$



Fig. 14. As for fig. 13, showing the etched grain boundaries. Attack-polished and electrolytically etched in ammonium persulphate/glycerol/water reagent. Oblique illumination. $\times 1250$



Fig. 15. As for fig. 14, showing twin bands and a typical sub-grain. $\times 1250$

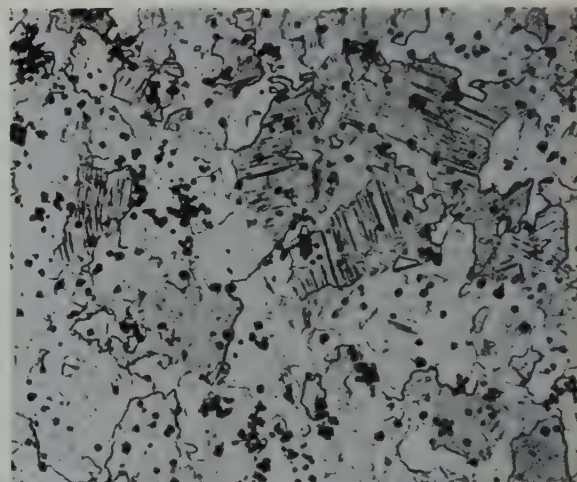


Fig. 16. Beta-quenched uranium alloy. Attack-polished and electrolytically etched in ammonium persulphate/glycerol/water reagent. The grains are stained because the short electropolish was deliberately omitted. $\times 100$

for fine grained uranium or for the structures found in uranium alloys.

Since chemical etching is more convenient than cathodic vacuum etching, it was decided to investigate further the potentialities of chemical etching. This approach failed to yield any new etchant and attention was turned to electrolytic etching. It was felt that electrolytic

etching in an oxidising reagent might yield promising results. Several reagents were tried without success until ammonium persulphate proved to be highly successful when used with glycerol and water. The etching solution contained 3 parts of a 10 % aqueous ammonium persulphate solution and 2 parts of glycerol. A stainless steel cathode was used and best

results were obtained with an open circuit voltage of between 8 and 10 volts. The etching time varied between 3 and 5 min and the solution was continuously agitated during etching. The specimen was then washed, dried and given a short electropolish in a standard bath containing sulphuric, acetic and phosphoric acids¹⁾ to remove any stain produced by electrolytic etching.

The etched structure of arc-melted uranium is shown in fig. 13. The characteristic irregular grain boundaries of the alpha uranium can be seen, although some of the grain boundaries are more clearly defined than others. This is probably due to the small orientation differences between some of the grains. Careful examination revealed the presence of sub-grain boundaries. Small pits were produced in the specimen surface but these were impossible to avoid. High power photomicrographs are shown in figs. 14 and 15. Fig. 14 shows etched grain boundaries whilst fig. 15 shows twin bands with a typical subgrain growing apparently from the twin bands.

A typical refined grain structure of beta-quenched uranium alloy, produced by etching in ammonium persulphate reagent, is shown in fig. 16. The short electro-polish recommended after etching was deliberately omitted to demonstrate the staining of some of the grains. Estimates of grain size obtained on etching agreed with those obtained by attack-polish using polarised light. The etch was also used successfully with the $U + \frac{1}{2}$ at % Cr alloy, fig. 17. This shows the characteristic equiaxed grain structure produced by isothermal transformation at 550° C in this alloy. The pitting in figs. 16 and 17 was due to the etching out of the non-metallic inclusions. There was no sign of the matrix type of fine pitting to be seen in fig. 13 for pure uranium and it is feasible that the inclusion attack protected the uranium matrix from pitting.

5. Stain Etching of Uranium Dioxide

There are several possible etchants for sintered uranium dioxide, e.g. nitric acid or hydrogen

peroxide/sulphuric acid mixture, but they are all grain boundary etchants. For grain size distribution of single phase UO_2 or U_4O_9 and general examination of duplex UO_2 and U_4O_9 phase structures, it was felt that a stain etch would be preferable. Several etching reagents were tried, but the only completely satisfactory reagent was found to be hydrogen peroxide (30 wt %).

The attack polished surface was ideally suited for either grain boundary etching or stain etching. The specimens were then stain-etched in hydrogen peroxide (30 wt %) for about 6 min. The time varied between specimens and the completion of etching was shown by a bluish colouration on the specimen surface. If the staining was uneven or the specimen overetched, then the surface film could be removed by dilute sulphuric acid. Care had to be taken when using both solutions since cross-contamination would have led to grain boundary etching of the uranium dioxide. Etching for too long a time gave a cracked surface film.

Fig. 18 shows a uniform single phase uranium dioxide structure revealed by stain etching. The surface was scratch free but this would not have been so if diamond dust, rather than attack polish, had been used. A duplex UO_2/U_4O_9 structure is shown in fig. 19. The U_4O_9 was present as needles precipitated within the UO_2 grains. Tuxworth and Evans⁸⁾ have shown that the U_4O_9 precipitates as platelets on planes parallel to the (111) planes of the parent UO_{2+x} phase. Single phase U_4O_9 is shown in fig. 20. Note the irregular size and shape of the U_4O_9 grains compared with those of UO_2 shown in fig. 18. This irregularity is characteristic of U_4O_9 .

The stain was produced by the interference phenomenon resulting from a thin hydrated oxide film on the surface of the uranium dioxide. This film varied in thickness with the orientation of the surface grains and as a result the grain structure was revealed.

6. Conclusions

The hydrogen peroxide attack-polish developed as a result of this work has many advant-

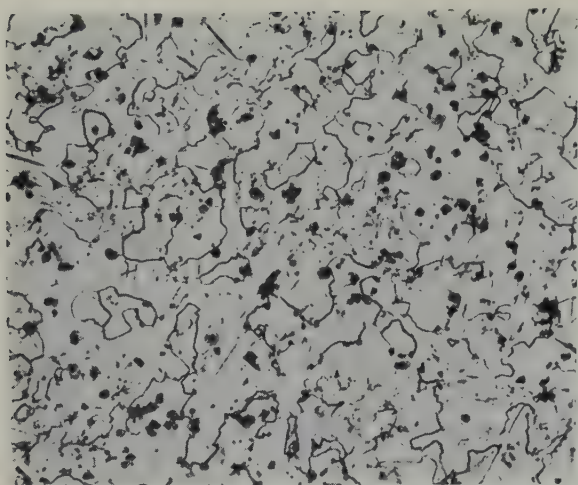


Fig. 17. $\text{U} + \frac{1}{2}$ at % Cr alloy isothermally transformed at 550°C . Attack-polished and electrolytically etched in ammonium/persulphate/glycerol/water.
 $\times 100$

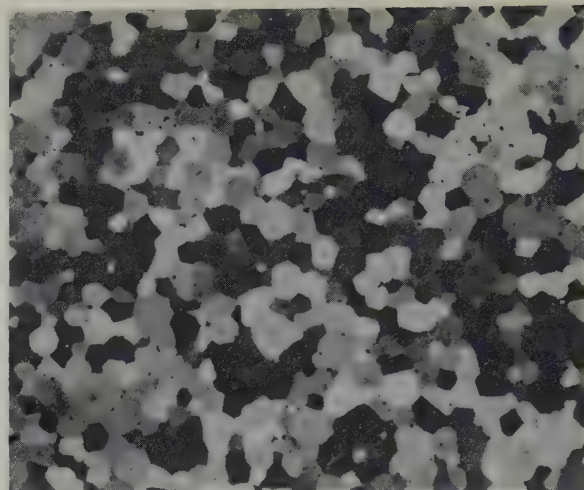


Fig. 18. High density sintered UO_2 . Attack-polished and stain etched in H_2O_2 (30 wt %). Bright field illumination. $\times 100$



Fig. 19. Duplex structure UO_2 and U_4O_9 (needles). Attack-polished and strain etched in H_2O_2 (30 wt %). Bright field illumination. $\times 500$



Fig. 20. Single phase U_4O_9 . Compare the structures shown in figs. 18 and 20. Attack-polished and stain-etched in H_2O_2 (30 wt %). Bright field illumination. $\times 100$

ages for the metallographic preparation of uranium, uranium alloys and uranium dioxide. For uranium and uranium alloys, these are:

- (1) The technique is simpler to control than electropolishing and it is practically impossible to overpolish the specimen. Polishing conditions are independent of specimen size variations. This makes it a versatile

method for routine examination of large numbers of samples, without any danger of deterioration in results.

- (2) The method can be used with all uranium alloys tried so far.
- (3) The need to anodise, to improve contrast under polarised light, is eliminated. For routine work, it is still preferable to increase

the grain contrast and this can be done by immersing the specimen in hydrogen peroxide.

- (4) There is no "polishing out" of inclusions as can happen during electropolishing.

For uranium dioxide, the advantages are:

- (1) A flat surface finish.
- (2) No enlargement of the pores in sintered compacts.
- (3) A scratch-free surface with no pitting.

A new electrolytic etch in a solution of ammonium persulphate, glycerol and water has been developed for the bright field examination of uranium. It has been used successfully to etch the grain boundaries in uranium and $U\% + \frac{1}{2} at\% Cr$ alloy.

The new stain etch developed for UO_2 , using 30 wt % hydrogen peroxide, is excellent for the general examination of grain size and distribution in sintered compacts. It is also ideal for revealing the duplex phase structures due to UO_2 and U_4O_9 .

Acknowledgments

The authors wish to thank Mr. J. H. Gittus, Research Manager, Fuel Element Development Laboratories, Springfield, for much useful comment on this paper, and Sir William Cook, Managing Director, and Dr. H. K. Hardy, Director, Development and Engineering Group, United Kingdom Atomic Energy Authority, for permission to publish this paper.

References

- 1) B. W. Mott and H. R. Haines, *J. Inst. Metals* **80** (1952) 621
- 2) M. D. Jepson, R. B. Kehoe, R. W. Nichols and G. Slattey, Second Geneva Conference, (1958) 15/P27
- 3) A. N. Holden, *Physical Metallurgy of Uranium* (Addison-Wesley Publishing Company, USA, 1958) p. 214
- 4) D. Armstrong, P. E. Madsen and E. C. Sykes, *J. Nucl. Mat.* **2** (1959) 127
- 5) W. N. Posey, *Metal Progress* **76** (1959) 101
- 6) A. Robillard, R. Boucher and P. Lacombe, *Métaux, Corrosion, Industries* **31** (1956) 433
- 7) H. Monti and J. Bloch, *Métaux, Corrosion, Industries* **31** (1956) 444
- 8) R. H. Tuxworth and W. Evans, *J. Nucl. Mat.* **1** (1959) 302
- 9) K. E. G. Meredith and M. B. Waldron, *J. Inst. Metals* **87** (1959-60) 311

GRAIN SHAPES IN QUENCHED URANIUM

B. R. BUTCHER, D. C. MINTY, K. E. G. MEREDITH and H. STRONG

UKAEA, Research Group, Metallurgy Division, Atomic Energy Research Establishment, Harwell,
Didcot, Berks., UK

Received 18 October 1960

Details are given of some experiments on the grain shapes and sizes produced in two grades of uranium, one with and one without small solute additions, after quenching from temperatures in the range of the β and γ phases. A tentative theory of the grain shapes produced by β -quenching these materials is put forward.

Deux nuances d'uranium, contenant ou non de petites quantités d'éléments d'addition en solution ont été examinées après trempe de β ou de γ , en ce qui concerne la forme et la taille des grains ainsi produits.

Une théorie est suggérée pour expliquer la forme des grains obtenus par trempe de β .

Es werden die Einzelheiten einiger Experimente angegeben, in welchen die Gestalt und Grösse der Körner von aus der β oder der γ -Phase abgeschreckten Uranproben untersucht wurden. Zwei Uransorten wurden verwendet, wobei die eine kleine Zusätze in gelöster Form enthielt, während die andere aus reinem Uran bestand. Es wird eine Theorie vorgeschlagen über die Gestalt der Körner in Materialien, die aus dem β -Zustand abgeschreckt wurden.

1. Introduction

The grain size of cast uranium is often reduced by quenching, the grain refinement being produced by one or more rapid phase changes. The method is very successful with impure metal, but with purer material small alloy additions have to be made before the reduction in grain size becomes marked¹). At Harwell a series of experiments has been started on the refining effect of small additions of various solutes. In the initial experiments, a subsidiary effect of the grain refining additions, previously noted by other workers, quickly became apparent. This was the effect of the solutes on the shape of the α grains after quenching from the β phase.

This paper gives some details of the preliminary observations on the grain shapes, and a tentative theory of grain shape is put forward.

2. Experimental Details

2.1. MATERIAL

Two grades of uranium were used; one had no deliberate alloy additions, and will be

referred to as *unadjusted* metal, while the other had added to it an extra few hundred parts per million of two solutes which occurred as impurities in the unadjusted metal, and will be referred to as *adjusted* metal. The adjusted metal was cast at the Springfield works into bars 1 metre long by 2.9 cm diameter, and the unadjusted metal was cast at Harwell, using Springfield billet uranium, into bars 33 cm long by 2.9 cm diameter. The impurity content, except for the two solutes, was similar in type and amount for both types of bar.

Samples 5 cm long were cut from the bars, since it was considered that heat treatments of this size would give results similar to those from full size bars which had been similarly treated. Records were kept of the position of the samples in the bars, but samples were picked randomly for heat treatment. No systematic effect of position was noted.

2.2. HEAT TREATMENT

Specimens were heated by dipping them into a salt bath containing a eutectic mixture of

potassium and lithium carbonates, which was controlled to $\pm 5^\circ\text{C}$. Quenching was effected either by transferring them to running water, or by plunging the specimens into still water and then agitating them. The water was at room temperature in both cases. The transfer time was 2.5 ± 0.5 seconds.

2.3. METALLOGRAPHY

The heat treated specimens were cut in half transversely, and then one half was cut longitudinally. Grinding was done in the orthodox manner, after which the specimens were either electropolished in a mixture of phosphoric acid, sulphuric acid, and water, or attack polished in a mixture of chromic acid, nitric acid, water, and γ alumina after a penultimate mechanical polish with diamond paste smeared on a felt lap.

The grain structure was examined under polarised light.

2.4. DETERMINATION OF COOLING RATES

The same type of specimens were used as described in § 2.1. At different radii on separate specimens a hole 3.2 mm in diameter was drilled to a depth of 2.5 cm. Pyrotenax thermocouples, 3.2 mm in diameter, were given at the tip a coat of soft solder on top of a similar coat of hard solder, to ensure good thermal contact, and inserted to the bottom of the hole. Quenching was carried out as detailed in § 2.2, and the signal from the thermocouple was fed to a Kelvin Hughes high speed recorder. The temperature from which the samples were quenched to record their cooling rate was 800°C .

2.5. GRAIN SIZE MEASUREMENT

In all quenched specimens, grain sizes and shapes were detected in the material near the surface of the bar which were different from those at the centre of the bar. This outer annulus near the surface is termed the *rim*, and the depth to which it persists, the *rim depth*. The material at the centre is referred to as the *core*.

This effect was most marked in β -quenched adjusted material where the grain size was

invariably smaller than that of unadjusted material similarly treated. Many of the grains in a band near the surface were disc shaped, i.e. they were roughly ellipsoidal with the major axes equal and parallel to the bar surface, and the minor axis radial. The core grains were equiaxed and tended to merge into the rim, so the rim depths could only be estimated to ± 0.5 mm.

Quenched unadjusted material showed rims containing long grains with their major axes normal to the bar surface, and the minor axes roughly equal and parallel to the bar surface. These were called columnar grains by analogy with grains found in some cast materials. When they were mixed with equiaxed grains the estimation of rim depths was difficult, and only accurate to ± 1.0 mm. The cores were large equiaxed grains.

Grain size measurements were made by the linear intercept method. Up to 100 grains were counted and the size found from the average of three counts. With disc-shaped and columnar grains both major and minor axes were measured.

The validity of these measurements was checked by subjecting nine random specimens from each batch of material to a standard treatment of 15 min. at 730°C followed by water quenching.

Measurements on these samples showed that rim depths were reproducible to ± 0.5 mm and grain sizes to within 10 % when below $500\ \mu$.

3. Results

3.1. COOLING RATES

Cooling rates were measured as the average rate of temperature fall from 795°C to 500°C . The results are shown in fig. 1.

3.2. GRAIN SHAPES

As detailed in § 2.5, rims of differently shaped grains were found in adjusted and unadjusted material after β -quenching. In some cases, with both materials, the periphery was occupied by a very thin rim of very small grains. The edges of the specimens were invariably rounded after

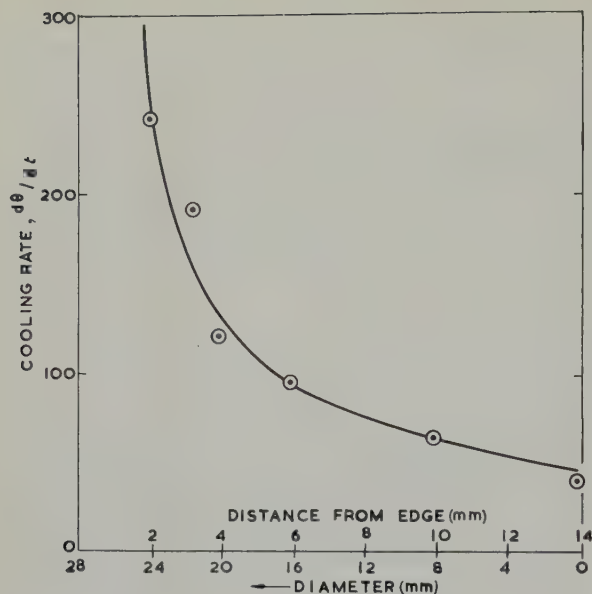


Fig. 1. Cooling rates ($^{\circ}\text{C}/\text{sec}$) versus diameter for water quenched bar.

polishing, and a critical examination to see if this effect was universal was not carried out. Typical examples of the rims of non-equiaxed grains are shown in figs. 2 and 3. In all cases the direction of these grains were influenced by the direction of heat extraction, so that at the

corners of the longitudinal sections, the major axes of the grains were at 45° to the axis of the bars.

A number of experiments to determine the effect of certain variables on the rim and core grain were performed.

3.2.1. Effect of soaking temperature

Samples were heated for 15 minutes at approximately 20° temperature intervals from 680 to 850°C , and then quenched. No systematic effect of quenching temperature was observed with unadjusted material, the columnar grains being up to 3 mm long by $\frac{1}{2}$ mm wide. The effect on the grain size of the adjusted material is shown in fig. 4. The length of the rim grains decreased with increasing temperature, while the width remained roughly constant, so that when quenched from above 800°C they were equiaxed. The core grain size also decreased with increasing quenching temperature, the effect being most marked from 680 to 720°C .

The effect of temperature on the rim depth can be seen in fig. 5. The rim depth reaches a maximum at approximately 750°C , and declines at higher temperatures. At these temperatures

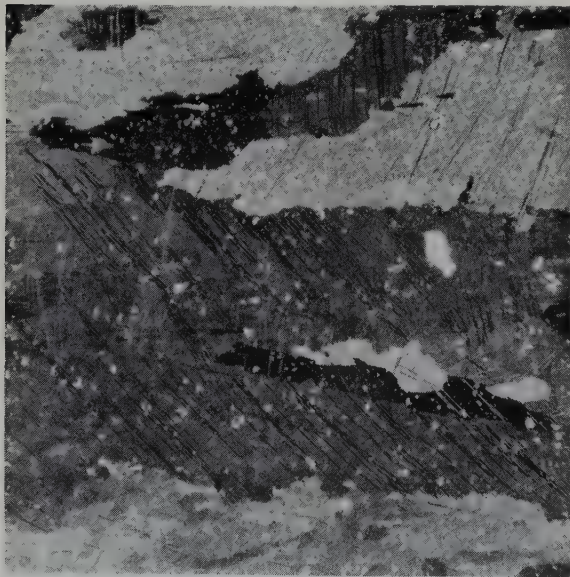


Fig. 2. Typical columnar grains in the rim of a quenched unadjusted specimen. Polarised light, $\times 55$. Specimen centre to the left, surface to the right.

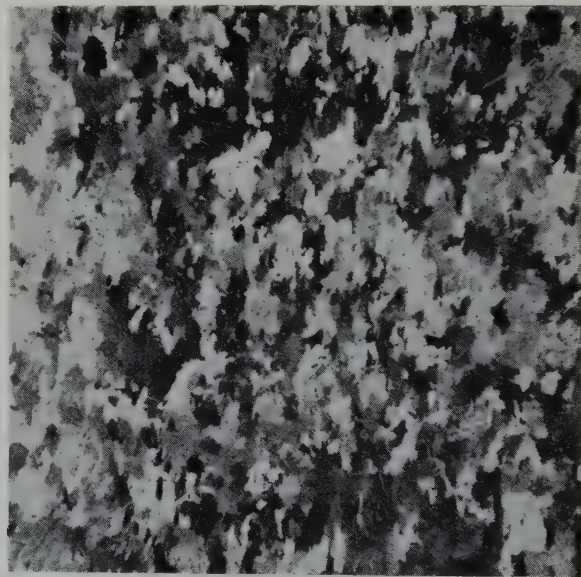


Fig. 3. Typical "disc" grains in the rim of a quenched adjusted specimen. Polarised light, $\times 55$. Specimen centre to the left, surface to the right.

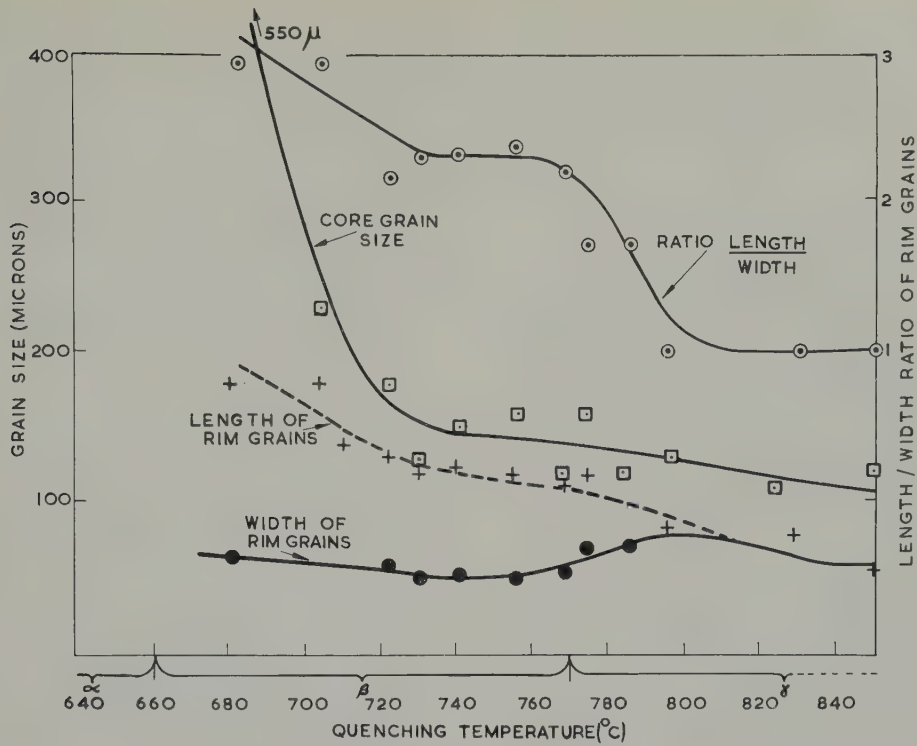


Fig. 4. The effect of quenching temperature on the grain size of adjusted material.

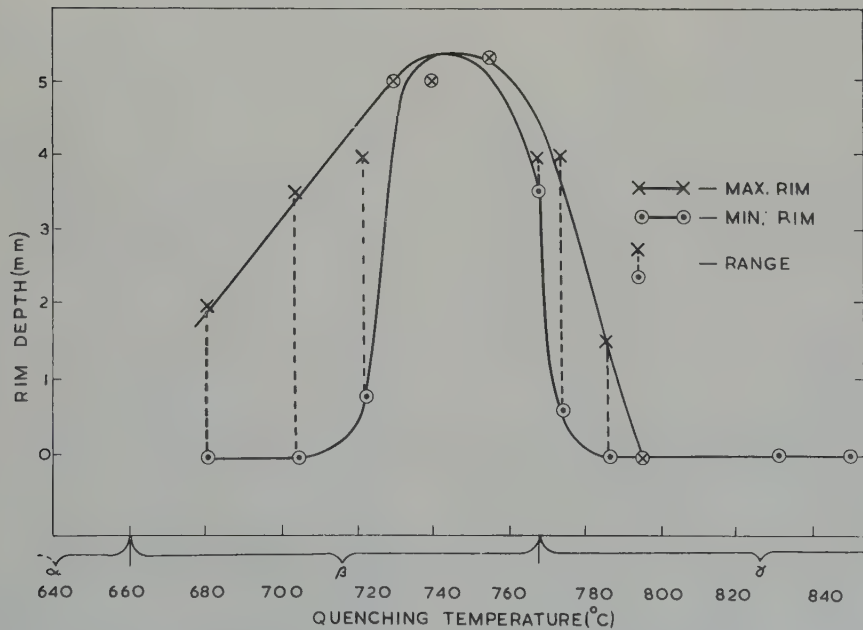


Fig. 5. The effect of quenching temperature on the rim depth of adjusted material.

there is still a rim effect, in that the rim grains are about half the size of those in the core (see fig. 4), but since they are more nearly equiaxed, it becomes increasingly difficult to distinguish the boundary between the rim and the core.

3.2.2. *Effect of soaking time*

These experiments were limited because the salt seriously attacked the specimens if they were held for over one hour at temperature. Increasing the soaking time from 3 to 60 minutes gave a tendency to increased refinement with the unadjusted material. With the adjusted material, increased times gave finer core grains, but coarser rim grains, and the rim grains became slightly more equiaxed.

3.2.3. *Effect of cooling rate*

Very little systematic work has been done. Quenching into still water, as opposed to running water, gave coarser structures, but the types of structure were the same. On the other hand, Williamson²⁾ has quenched small specimens 6 mm in diameter into mercury, and in both materials columnar grains resulted, this structure extending from the periphery to the centre of the specimens.

3.2.4. *Effect of repeated quenching*

Specimens of both materials were soaked for 15 min. at 730° C, and quenched, and thereafter quenched 9 times after soaking for 5 min. each time at 730° C. With the unadjusted material, the columnar structure was completely broken up, and a rim of fine equiaxed grains about 1 mm deep was formed. This gradually merged into a core of coarser grains. This effect has been noted before³⁾.

With the adjusted material, a deep rim of disc grains was formed, and both core and rim grains were coarser than would be expected from a single β -quench by a factor of 1.5 to 2.

4. Discussion

The outstanding conclusion arising from these experiments is that, on subjecting cast material to a single quench from the β range, a radical

change in the morphology of the α grains can be made by adding to the base material a small amount of solute. The effect is not so marked on quenching from the γ range, and multiple quenching can considerably affect the grain shapes. However, multiple quenches, because of their complexity, will not be considered. The relevant facts about a single β -quench emerging from this and other work are as follows:

a) The grain size of quenched adjusted uranium is much smaller than that of quenched unadjusted material.

b) For both materials a rim of limited depth exists, consisting of grains differently shaped from those in the core. In adjusted uranium the rim consists of disc-shaped grains, mixed with some which are equiaxed; in unadjusted uranium the rim grains are a mixture of columnar and equiaxed.

c) On quenching to various temperatures to allow isothermal transformation, the martensitic transformation takes place in material with a slight alloy content at a lower temperature than the same transformation in material without the alloy content⁴⁾.

d) The propagation of the transformation takes place by a band of mixed α and β moving through the material. This transformation band, postulated by Kehoe⁵⁾, has been demonstrated by Butcher and Baverstock⁶⁾. The width of this band is difficult to define. The leading edge can be postulated as passing through the boundaries of the growing α nuclei on the high temperature side of the band, but it will probably not be an isotherm, since different nuclei may become stable and grow at different temperatures. The trailing edge can similarly be envisaged as connecting the boundaries of the remanent β on the low temperature side of the band. Thus the band will be of slightly varying width at different points in any one material for constant temperature gradient and cooling rate, but will have some sort of average or typical width for the given conditions; this will be referred to as the band width.

e) The cooling rate, $d\theta/dt$, decreases rapidly with increasing distance from the perimeter up

to about 6 mm, and then decreases more slowly.

f) As $d\theta/dt$ decreases, the temperature of and growth rates are time and temperature transformation increases ⁷⁾.

An explanation of the change in morphology will be sought in the effect of a few hundred ppm of solute on the rate of nucleation, the rate of growth, and the transformation band width, together with the peculiar nature of the $\beta \rightarrow \alpha$ martensitic transformation of uranium, in which both nucleation and growth rates are time and temperature dependent.

The following assumptions will be made:

g) The transformation in both materials at the pertinent cooling rates is martensitic. This is a reasonable assumption from typical published TTT curves ⁴⁾.

h) There is a retarded growth direction in the α phase forming from the β phase. This again is reasonable, for the martensitic α forms as plates at room temperature in dilute alloys.

i) The width of the transformation band decreases as the temperature gradient $d\theta/dr$ (r =radius), at the transformation temperature, increases. This is almost self-evident for a constant cooling rate, but the kinetic effect of the cooling rate on the band width is unknown, i.e. the band width is an unknown function of $(d\theta/dr)/dt$. For a constant temperature gradient one might expect the band to be wider the greater the cooling rate. The width of the band may also be affected by the alloy content, as in general an alloy will transform over a broader temperature range than a pure metal on heating or cooling.

j) The linear rate of growth onto an α nucleus is greater in the preferred directions assumed in (h) than the rate of travel of the band, when the width of the band is less than or equal to one grain diameter. The rate of growth onto a nucleus in the direction of propagation of the band must be the same as the rate of travel of the band; a grain in which one of the preferred directions is perpendicular to the leading edge would be stopped from advancing beyond the leading edge because the temperature beyond the latter is too high for

growth to take place. If, however, the preferred directions were in a plane parallel to the leading edge, the growth could take place almost isothermally, so that the major axes of a grain in the latter case would be much greater than the major axes of a grain in the former.

k) The number of nuclei effective at the transformation temperature is higher in adjusted than in adjusted material, and the rate of nucleation decreases with increasing transformation temperature. The latter part of this assumption is common in nucleation theory. The first part can only be justified in that it is one possible explanation for the finer grain size in adjusted material.

Given these facts and assumptions, three situations can then be envisaged: the transformation band width is much less than the distance between nuclei; or the band width is of the same order as this distance, or it is much greater than this distance.

The transformation will, of course, be a continuous process moving from the periphery of the specimen to the centre. For simplicity, however, it will be imagined as taking place in steps, and the extreme edge, where very high cooling rates may lead to the formation of the very fine-grained thin rim, will not be considered. In the first case mentioned above, then, the periphery of the metal will cool rapidly until the transformation temperature apposite to that cooling rate is reached, whereupon the nuclei of α will grow as plates in various orientations. From (j), however, those plates oriented at 0 to 45° to the transformation band will be able to grow longer than those of other orientations, because the latter will be stopped by the leading edge of the band. As the band advances, however, the majority of crystals will advance with it, because of the scarcity of nuclei. If the rate of nucleation remained constant one might expect a roughly equiaxed structure, but as the band advances, the rate of cooling drops, the transformation temperature increases, and the number of effective nuclei decreases (assumption (k)). Thus a number of crystals will not be obstructed in their inward

growth by freshly developing nuclei, but will penetrate between them to become columnar grains. It is true that as the rate of nucleation decreases the band width increases, but so long as the ratio of band width to distance between nuclei remains much less than unity, this effect can occur.

In the second case, where the band width is of the same order as the distance between nuclei, at the start of transformation similar conditions will pertain as for the first case, and the plates oriented at 0 to 45° to the transformation band will grow longer than those

oriented at 45° to 90° to the band. As the band advances, however, the band width may still remain about the same as the distance between nuclei, both increasing roughly to the same extent. Fresh nuclei will be free to develop and obstruct the inward growth of the crystals, so that as the trailing edge of the band advances, growth onto crystals oriented at 0°–45° to the band will make them disc shaped, but make those oriented at 45°–90° to the band very roughly equiaxed.

In the third case, each nucleus will develop until the α plates touch, whereupon the inter-

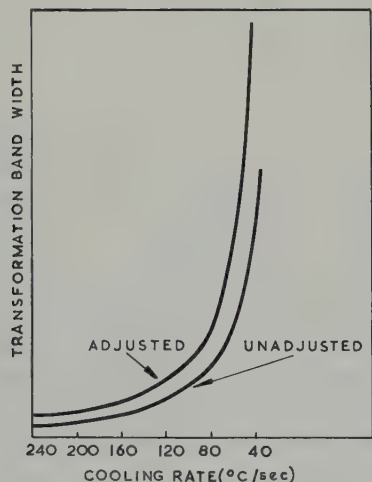


Fig. 6a. Transformation band width as a function of cooling rate for both materials.

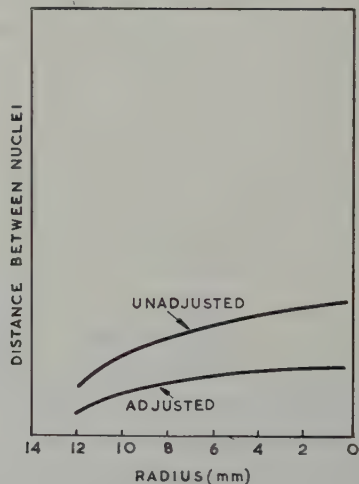


Fig. 7. Distance between effective nuclei as a function of radius for both materials.

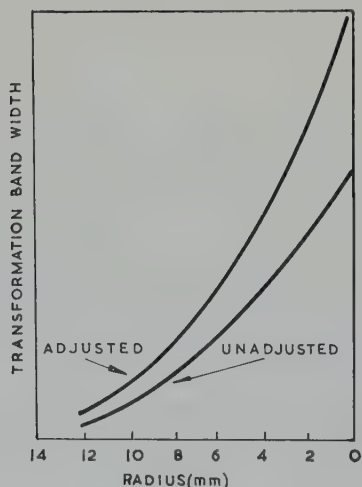


Fig. 6b. Transformation band width as a function of radius for both materials.

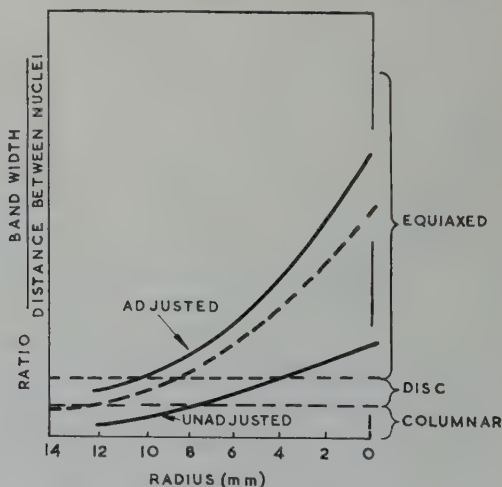


Fig. 8. Ratio of band width to distance between nuclei as a function of radius for both materials.

stices will be filled by growth in the non-preferred direction until an equiaxed structure is reached.

To explain the structures observed in adjusted and unadjusted material, more consideration must be given to the band width and distance between nuclei. If band width is considered as a function of cooling rate, nothing is known of this except that at infinite cooling rate the band width would be zero, and as the cooling rate tends to zero, the band width would tend to infinity, and therefore the function may tend to be hyperbolic if cooling rate is plotted on a linear scale. Moreover the curve for the adjusted material might lie above that for the unadjusted, since from (i) a broader band could be expected in the material with more alloy content (fig. 6a). When band width is plotted against radius, using fig. 1, the curves appear as in fig. 6b.

Again nothing is known about nucleation rates, but something about the distance between effective nuclei can be deduced from measurements on the specimens. For adjusted material, from fig. 4, in the β range this distance for the core grains will be two to four times that for the rim grains. Moreover the core grain size

does not vary greatly with radius, so the variation of distance between nuclei as a function of radius may be as shown in fig. 7. The core grains in the unadjusted material were two or three times bigger than those in the adjusted, so if the same type of curve is assumed for this material, it would be as shown in fig. 7. Thus the ratio of band width to distance between nuclei as a function of radius would be as shown in fig. 8 for each material. On this is superposed a band, about the ratio 1, in which it is supposed disc shaped grains can form. Below this band the grains would be columnar, and above, equiaxed. Thus, the adjusted material would have a rim of mixed disc-shaped and equiaxed grains, followed by a core of equiaxed grains. The unadjusted material would have a rim of columnar grains, which should be followed by an annulus of mixed equiaxed and disc shaped grains. In actuality it is followed by a confused structure, in which it is possible to distinguish a few disc shaped grains (fig. 9). Some support is, however, given to this hypothesis by fig. 10 which is a photomicrograph of the edge of an adjusted specimen which was treated appropriately to produce a typical β -quenched structure



Fig. 9. Rim/core boundary in unadjusted material. Polarised light. $\times 25$. Specimen centre to the left, surface to the right.

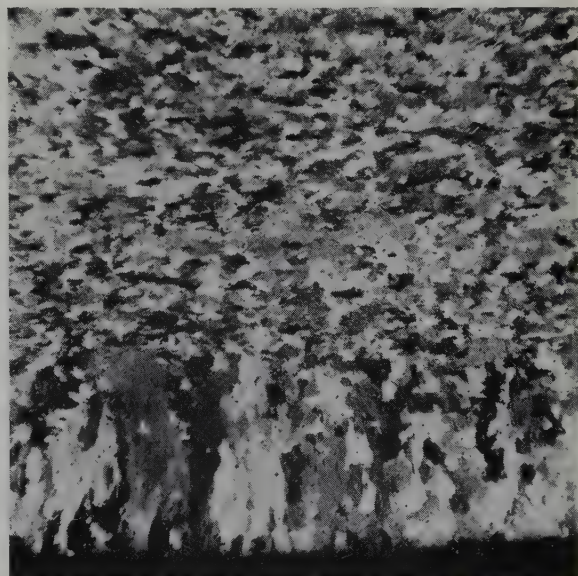


Fig. 10. Exceptional duplex rim in adjusted material. Polarised light. $\times 25$. Specimen centre to the left, surface to the right.

for ultrasonic measurements, but gave a unique result. The thin rim of small columnar grains is followed by a thick annulus of disc shaped grains, with a core of equiaxed grains. Although the reason for the behaviour of this specimen is not known, it is suggested that it could be due to the curve of fig. 8 being lowered to the dashed position.

5. Conclusions

It is not possible to come to a firm conclusion in this paper, since the theory developed is highly speculative and depends on a large number of assumptions. It is hoped, however, that the idea of transformation band width versus distance between nuclei as a criterion for grain shape will serve as a useful concept for anyone working in this field. Moreover it is hoped that the effect of certain solutes on the grain size may be interpreted by estimating their effect on the nucleation rate and the transformation band width.

Acknowledgements

The authors would like to thank Dr. H. M. Finniston for his encouragement, and Mr. M. Noakes who cast the unadjusted material and made heat treatment facilities available. In addition, they would like to thank the many colleagues who patiently listened to and criticised the authors' ideas.

References

- 1) e.g., G. Y. Sergeyev, V. V. Titova, Z. P. Nikolayeva, A. M. Kapteltrev and L. I. Kolobneva, Second Geneva Conference (1958) 15/P/2307
- 2) G. K. Williamson, private communication
- 3) E. E. Hayes, USAEC Report TID 7546 (1957)
- 4) M. D. Jepson, R. B. Kehoe, R. W. Nichols and G. F. Slattery, Second Geneva Conference (1958), 15/P/27
- 5) R. B. Kehoe, private communication
- 6) B. R. Butcher and D. Baverstock, *J. Nucl. Mat.* **3** (1961) 30
- 7) B. R. Butcher and D. C. Minty, UKAEA (Harwell) Report, AERE M/R 2462 (1958)

LETTERS TO THE EDITORS – LETTRES AUX REDACTEURS

THE RELATIONSHIP BETWEEN IRRADIATION GROWTH AND OTHER PROPERTIES OF ALPHA-URANIUM

J. J. STOBO and B. PAWELSKI

C. A. Parsons and Co. Ltd., Nuclear Research Centre, Newcastle upon Tyne 6, UK

Received 13 February 1961

Because of the irradiation growth phenomenon there is considerable interest in the measurement of preferred orientation in polycrystalline uranium. By X-ray techniques this is tedious because the high scattering power of uranium makes a large number of exposures necessary. Many properties of alpha-uranium are extremely anisotropic and it has therefore been of interest to see if an indirect measure of preferred orientation can be obtained by suitable property measurements.

The directions of interest in the growth phenomenon are the [100] which contracts and the [010] which expands. Correlations between the texture of worked uranium and the thermal expansion coefficient have been published ^{1,2,3}); these only give information about the change in orientation of [010] directions. Berlincourt's ⁴) data on resistivity indicate that this is a property which could be correlated with the [100] direction. Single crystal values of expansion coefficient and resistivity are:

Thus high resistivity in a particular direction indicates an excess of [100] directions over random while a low expansion coefficient indicates an excess of [010] directions. So, when the two measurements are made in the same direction on the same specimen, an estimate of the tendency to irradiation growth can be obtained.

References

¹) W. R. McDonnell, Du Pont (USA) Report, DP-258 (1957)
²) R. B. Russell, Nuclear Metals Inc. (USA) Report, NMI-TJ-9 (1957)
³) R. M. Mayfield, H. H. Chiswik and R. E. Machery, Argonne (USA) Report, ANL-5296 (1956)
⁴) T. G. Berlincourt, Phys. Rev. **114** (1959) 969
⁵) F. G. Foote, Proc. First Geneva Conference **9** (1955) 33

Direction	Expansion coefficient × 10 ⁻⁶ /°C (25°–125° C)	Resistivity μohm·cm (20° C)
[100]	21.7	42.2
[010]	– 1.5	27.3
[001]	23.2	28.0
Reference	⁵)	⁴)

THE EFFECT OF DISSOLVED OXYGEN ON THE TERMINAL SOLUBILITY OF HYDROGEN IN ALPHA ZIRCONIUM

A. BROWN

C. A. Parsons & Company Ltd., Nuclear Research Centre, Fossway, Newcastle upon Tyne 6, UK

and

D. HARDIE

Department of Metallurgy, University of Durham, King's College, Newcastle upon Tyne 1, UK

Received 16 March 1961

There has been considerable doubt about the effect which the presence of oxygen has upon the solubility of hydrogen in the hexagonal α zirconium. It is certain that the oxygen atom, because of its size, can only occupy the octahedral sites in the lattice and it seems that such occupation can prevent hydrogen from filling the neighbouring tetrahedral interstices. Martin and Rees ¹) suggest that as a result, three sites are blocked per oxygen atom in dilute solutions of oxygen in zirconium, whereas in a 50 at % alloy (which cannot in fact be obtained owing to the limited solubility of oxygen in zirconium) one site would be blocked per oxygen atom. Hall, Martin and Rees ²) have investigated the effect on the hydrogen absorption isotherms of oxygen present in solid solution in the zirconium and found that the volume of hydrogen absorbed decreased as the oxygen content increased, but the equilibrium pressure of hydrogen increased. However, they carried out their measurements at comparatively high pressures in the range 0.5 to 760 mm of mercury, and in fact determined the $\beta/(\beta+\delta)$ and $(\beta+\delta)/\delta$ phase boundaries. They were therefore dealing with a body-centred cubic structure instead of hexagonal close packing and their arguments concerning saturation solubility no longer strictly apply. Their work, which is in agreement with the later results of Edwards, Levesque and Cubi-

ciotti ³) merely indicates that the solubility of hydrogen in β zirconium is reduced by the presence of oxygen in solid solution.

Subsequent workers—Ells and McQuillan ⁴) and Gulbransen and Andrew ⁵)—have actually determined the terminal solubility of hydrogen in the α phase at temperatures respectively above and below the eutectoid, where equilibrium pressures are in the range 10^{-2} to 1 mm of mercury, but they made no systematic study of the effect which the presence of oxygen might have on this solubility. In fact it has been generally assumed that the original reasoning of Martin and Rees can be directly applied to the α solid solutions.

Work on the variation of solubility of hydrogen in both the α and β phases of zirconium when various alloying elements (including oxygen) are present has now definitely revealed that oxygen increases the terminal solubility in the α phase though it does reduce it in the β phase.

Using a high vacuum apparatus in which accurately measured amounts of hydrogen could be added to a reaction system containing zirconium and the equilibrium pressure determined by means of a Pirani type gauge, equilibrium pressure concentration isotherms have been plotted for zirconium containing 1200, 4200, 5600 ppm oxygen in the temperature

range 530–790° C. (The original zirconium contained the following impurities: Fe 275, C 100, O 1200, N 170, Al 150, Cr 30, Pb 40 ppm by weight, and Hf 1.9 wt %). The results are most readily assessed when plotted as the logarithm of the equilibrium pressure against reciprocal temperature for solutions of various hydrogen concentration. Since in pure zirconium the isothermal equilibrium pressure is invariant with composition in a two-phase region, the α and β fields on such a plot are generally separated by a single line. In the presence of oxygen however there is slight pressure variation with composition in the $(\alpha + \beta)$ field and this is then more truly represented by a band rather than a single line. The boundary shown in fig. 1 is in actual fact therefore the $\alpha/(\alpha + \beta)$ boundary and represents the terminal solubility of hydrogen in the α phase. The terminal solubility at any particular temperature is given by the intersection of an hydrogen isostere with this boundary. Although the pressure at the $\alpha/(\alpha + \beta)$ phase boundary for any particular temperature remains constant as the amount of oxygen present is increased, there is simultaneous movement of the isosteres in such a

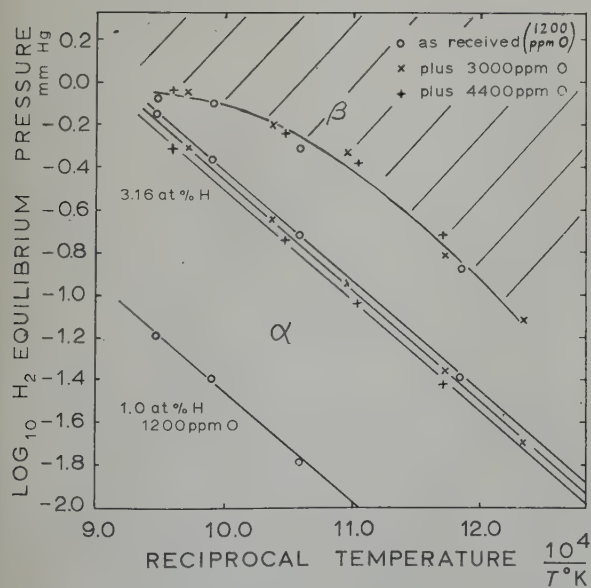


Fig. 1. The effect of oxygen content (ppm by weight) upon the equilibrium pressure-temperature relationships for solutions of hydrogen in α -zirconium.

way that the terminal solubility of hydrogen at any particular temperature in this region increases with the oxygen content of the zirconium. The heat of solution, as determined from the relationship $\Delta H = R \left(\frac{\partial \ln p}{\partial 1/T} \right)_c$ shows no significant variation and has a value of 23.7 ± 0.5 Kcals/g mole in all cases.

These results also seem to clarify interpretation of microstructures obtained in α zirconium after corrosion in high temperature



Fig. 2. Sample of zirconium — 1 wt % copper alloy after corrosion in steam at 1 atm. pressure at 600° C for 6 days, showing absence of hydride precipitation near the metal surface. (Photomicrograph provided by the Metallurgy Division, AERE, Harwell). $\times 400$



Fig. 3. Zirconium dilatometer specimen containing 112 ppm by weight of hydrogen, showing absence of hydride precipitation near the surface due to the increased solubility in this region resulting from the presence of oxygen in solution. $\times 70$

water or steam. Such structures frequently show a much greater quantity of precipitated hydride in the centre of the specimens compared with regions near the surface (fig. 2). This phenomenon can be explained without recourse to a hydrogen concentration gradient, since there is inevitably a higher oxygen concentration towards the surface and the decreased precipitation near the surface may simply be due to the increased solubility of hydrogen in the presence of dissolved oxygen. Such a result is also clearly demonstrated in the photomicrograph of a section from a dilatometric specimen, fig. 3. Due to prolonged heating in the dilatometer the specimen has absorbed some oxygen into the surface layers despite the vacuum of $<10^{-5}$ mm of mercury. As a result, on hydriding there is no precipitate apparent in the surface layers but there is copious precipitation in the rest of the specimen, due to the lower hydrogen solubility there. A similar effect has been observed in the contamination of titanium by water vapour ⁶).

Some preliminary investigations by means of

vacuum dilatometry at temperatures below the eutectoid indicate that the terminal solubility is also increased in this region and this is being examined further.

This work was carried out in the Department of Metallurgy, King's College, Newcastle upon Tyne, with financial and material support from the UKAEA, Atomic Energy Research Establishment, Harwell, to whom we are very grateful.

References

- ¹) S. L. H. Martin and A. L. G. Rees, *Trans. Faraday Soc.* **50** (1954) 343
- ²) M. N. A. Hall, S. L. H. Martin and A. L. G. Rees, *Trans. Faraday Soc.* **41** (1945) 306
- ³) R. K. Edwards, P. Levesque and D. Cubicciotti, *J. Amer. Chem. Soc.* **77** (1955) 1307
- ⁴) C. E. Ells and A. D. McQuillan, *J. Inst. Metals* **85** (1956-57) 89
- ⁵) E. A. Gulbransen, and K. F. Andrew, *Trans. Amer. Inst. Min. Metall. Engrs.* **203** (1955) 136
- ⁶) P. C. Hughes and I. R. Lamborn, *J. Inst. Metals* **80** (1960-61) 165

A PROPOS DE LA LETTRE DE A. MOORE ¹⁾ SUR L'AMELIORATION DES PROPRIETES MECANQUES DU BERYLLIUM COMMERCIAL PAR TRAITEMENTS THERMIQUES

P. BASTIEN et P. POINTU

Centre de Recherches de Physique des Métaux de l'Ecole Centrale des Arts et Manufactures, Paris

Reçu le 15 mars 1961

En faisant part de récents résultats obtenus dans l'étude des phénomènes de précipitation du Beryllium et leurs relations avec les propriétés mécaniques A. Moore suggérait un échange d'informations entre les différents chercheurs se préoccupant de ces questions. C'est pour répondre à ce vœu que nous exposerons ici rapidement certains des résultats obtenus.

A la suite des travaux en partie effectués dans les laboratoires du Dr. A. Kaufmann †, nous avons montré ²⁾ par mesures de résistivité, radiocristallographie et micrographie que, dans le métal commercial de réduction thermique, il se produit une précipitation d'impuretés, qui, par analyse à la microsonde électronique, s'avèrent être essentiellement des éléments de transition. Le précipité formé est cubique à faces centrées de paramètre $a = 6,07 \text{ \AA}$ et est solubilisé par chauffage entre 850 et 870° C. Il semble que ce soit ce même précipité que A. Moore a retrouvé dans son étude. Nous avons pu observer, de plus, qu'il existe une relation d'orientation entre le précipité et la matrice. Le plan (0001) de la matrice coïncide avec un plan (111) du précipité tandis qu'un plan (10 $\bar{1}$ 0) coïncide avec un plan (1 $\bar{1}$ 0). Nous attirons alors l'attention sur l'amélioration des propriétés mécaniques à chaud par un traitement de précipitation prolongé. Depuis, nous avons pu établir qu'un phénomène semblable de précipitation a lieu dans le métal commercial

de réduction électrolytique avec une température de solubilisation voisine de 790° C.

De très nombreux tests mécaniques ont mis en évidence les faits suivants ³⁾:

1. *Métal de réduction thermique fritté, filé*

Après recuit et refroidissement rapide, on note sur les courbes de traction un phénomène de Portevin–Le Chatelier. Ce phénomène est activé thermiquement. La contrainte et la déformation à l'arrêt du phénomène suivent la loi d'Arrhenius avec une énergie d'activation d'environ 40 kcal/mole. L'allongement en fonction de la température dépend d'une énergie d'activation de 40 kcal/mole également, ce qui apporte une confirmation indirecte de la liaison entre minimum de ductilité et vieillissement en cours de déformation. D'après l'aspect des courbes, il s'agit d'impuretés de *substitution*, probablement celles responsables du précipité cité, puisque des traitements thermiques entre 600 et 800° C font disparaître le phénomène de Portevin et relèvent la ductilité à chaud. Cependant, aussi longue que soit la durée du traitement, *la ductilité, bien que fortement améliorée, décroît entre 400 et 600° C pour le métal fritté, filé* contrairement à ce que trouvèrent Brown, Morrow et Martin ⁴⁾ pour le métal coulé, filé. Les très nombreux essais effectués nous permettent de considérer ce fait comme vérifié à l'échelle statistique.

† Nuclear Metals Inc. à Concord (Mass.) USA.

2. Métal de réduction électrolytique

Les mêmes phénomènes apparaissent, mais avec une amplitude plus faible. Entre des limites de température variables avec la vitesse de déformation, mais situées entre 380 et 500° C, on note une limite élastique supérieure et le phénomène de Portevin-Le Chatelier. Ceci se manifeste classiquement par un relèvement de la limite élastique entre 400 et 500° C. Les traitements de précipitation de longue durée relèvent l'allongement à la rupture de 13 à 20 % à 600°, c'est-à-dire que l'on retrouve la valeur du métal de réduction thermique surveillé. Un traitement de solubilisation fait disparaître la limite élastique supérieure en conservant le phénomène Portevin, mais un traitement à plus basse température (supérieure à 380°) fait, en général, réapparaître la limite élastique supérieure.

Des études métallographiques nous ont montré que les impuretés du béryllium commercial diffusent dès 200° C pour venir s'associer aux dislocations et défauts du réseau. Lorsque la température s'élève, on met en compétition l'évaporation thermique des atmosphères de Cottrell et la précipitation, ce qui explique les différents aspects de limite élastique supérieure et du phénomène de Portevin. Nous avons pu voir que, dès 500° C, les impuretés se réunissent au cours même de la déformation dans les bandes de déformation, ce qui peut amener une fracture intragranulaire. Comme A. Moore, nous avons observé le passage d'une fracture

intergranulaire à une fracture intragranulaire par traitement de surveillance. Nous pensons que c'est la présence dans les joints d'impuretés non précipitées qui amène à une fracture intergranulaire prématurée. C'est probablement en ces termes qu'il faut expliquer la différence d'allongement obtenue sur le métal coulé, filé et le métal fritté, filé. Un calcul approché donne sensiblement la même concentration en impuretés dans les atmosphères de Cottrell des deux nuances de métal commercial; ceci laisse supposer qu'après traitement de précipitation prolongé et refroidissement lent les mêmes quantités d'impuretés resteront non précipitées et fixées aux défauts et joints des grains. Nous pensons qu'on peut y voir l'explication de l'égalité des allongements après traitement de surveillance pour les deux nuances de métal fritté filé.

Ces travaux ont été effectués sous l'égide du Commissariat à l'Energie Atomique et plus particulièrement de Monsieur Salesse, chef du Département de Métallurgie.

Bibliographie

- 1) A. Moore, J. Mat. Nucl. 3 (1961) 113
- 2) P. Pointu, L. Espagno, P. Azou P. Bastien, C.R. Acad. Sci. (Paris) 250 (1960) 2365
- 3) Communication personnelle de Mr. Weisz (CEN Saclay)
- 4) A. Brown, F. Morrow et J. Martin, Nature 187 (1960) 494

BOOK REVIEWS

W. D. WILKINSON, *Extraction and Physical Metallurgy of Plutonium and its Alloys* (Interscience Publishers, New York, 1960) 314 pages. \$ 10.50.

Ce livre rassemble les communications présentées au symposium de San Francisco en février 1959, symposium organisé par le "Nuclear Metallurgy Committee" de l'AIME. Ce symposium rassemblait les spécialistes des Centres Nucléaires américains, anglais et français qui confrontaient les résultats obtenus depuis une quinzaine d'années. Cette confrontation était nécessaire en raison du secret qui a entouré, pour des raisons militaires, l'activité du plus grand laboratoire qui le premier a abordé durant la guerre les recherches sur le plutonium, celui de Los Alamos.

Après une introduction générale de l'éditeur, M. Wilkinson des laboratoires d'Argonne, ce livre est divisé en deux parties: la première constituant un tiers du livre rassemble six communications consacrées à la métallurgie extractive du plutonium; la seconde est réservée à huit communications montrant les divers aspects de la métallurgie physique du plutonium.

L'importance consacrée à la métallurgie extractive reflète les difficultés rencontrées dans les premières études américaines pour extraire le plutonium créé par la fission de l'uranium. Cette séparation nécessitait de connaître les propriétés chimiques de cet élément, inconnu jusque là sur la terre, afin de choisir la réaction de réduction la plus efficace pour obtenir une séparation quantitative du plutonium vis-à-vis non seulement de l'uranium mais aussi des autres produits de fission. Comme pour l'uranium, l'utilisation nucléaire du plutonium exige en effet une élimination aussi complète que possible des impuretés.

Parmi les méthodes de séparation des impuretés, les chercheurs de Los Alamos présentent leurs résultats sur l'extraction par solvant (tri-n-butyl phosphate dissous dans le kérosène) du Pu à partir des solutions d'acide nitrique. En ajustant convenablement les concentrations en acide nitrique et en nitrate d'aluminium, on obtient en un seul cycle d'extraction une bonne séparation de Cr, Ni, Cu, Fe et Ce. Il n'en est pas de même, pour Zr, Th et U pour les mêmes conditions opératoires. En outre, on compare les avantages et désavantages de diverses méthodes pour convertir les sels du Pu en métal et pour perdre le minimum

de métal au cours de cette conversion sous forme de scories. En général, il y a de grandes analogies entre l'extraction du Pu et de U: dans les deux cas, c'est la réduction d'un halogénure, fluorure (simple ou double) ou chlorure par Ca ou Mg. Pour Pu, les résultats américains, anglais et français sont d'accord sur le seul emploi du Ca. Un papier sur l'extraction des produits de fission du plutonium termine la première partie. Ce sont les méthodes pyro-métallurgiques qui sont généralement utilisées. Elles sont basées sur la solubilité différente dans l'état solide et l'état liquide des différents produits de fission. Ceux-ci peuvent être divisés en six groupes: gaz rares, alcalins et alcalino-terreux, terres rares, métaux nobles et réfractaires, métaux inertes et iode. Ce sont les méthodes de liquation et filtration qui permettent de séparer avec un rendement variable ces divers éléments. Ainsi Zr, Nb, Mo et La se concentrent préférentiellement dans les phases solides, tandis que les teneurs en Ru ne sont pas modifiées sensiblement par liquation.

Le titre de la deuxième partie, métallurgie physique, ne reflète pas exactement les sujets traités. Trois mémoires traitent des principes gouvernant la formation des alliages de Pu et la constitution des diagrammes d'équilibre, en particulier Pu-Ce et Pu-Zn. Deux mémoires sont consacrés à la métallographie du Pu et de ses alliages. Enfin deux papiers étudient la cinétique de transformation des trois premières variétés allotropiques α , β et γ du Pu et le comportement sous haute pression des alliages de Pu stabilisés en δ . L'intérêt pratique de cette dernière étude est évidente. Pu- δ étant la seule variété allotropique de structure cubique, la stabilisation de cette phase aux basses températures par des additions convenables telles que Al, Zn, In et Ce permettrait de réaliser des combustibles nucléaires à bases de Pu fissile ne présentant pas tous les désavantages des structures anisotropes analogues à celle de U- α et U- β .

Un dernier papier décrit quelques expériences sur la purification du Pu par fusion de zone. Ce procédé peut être intéressant pour disposer de métal très pur pour les études fondamentales sur la métallurgie physique du Pu, telles que l'étude des transformations entre les six variétés allotropiques du Pu. La fusion de zone peut aussi être considérée comme faisant partie de la pyrométallurgie des métaux nucléaires, c'est-à-dire des méthodes permettant de séparer les produits de fission de U ou Pu. Les chercheurs

de Los Alamos présentent quelques résultats sur la distribution des impuretés le long d'un barreau de Pu soumis à 10 passes de fusion de zone horizontale. Le but principal de l'étude est de vérifier si les taux de purification obtenus pour divers éléments correspondent bien aux valeurs des coefficients de partage déterminés à partir des liquidus et solidus des divers alliages binaires de Pu. En fait les impuretés Al, Co, Cr, Fe, Mn, Ni et Si se déplacent bien dans la direction prévue par les diagrammes d'équilibre des binaires correspondants mais la distribution de ces éléments en queue du barreau n'est pas conforme pour tous aux coefficients de partage des diagrammes d'équilibre. Il ne faut donc pas être trop optimiste pour cette méthode de purification et des progrès restent à faire pour éviter la contamination du barreau par les réfractaires.

Le livre est clairement présenté et largement illustré. On ne peut regretter qu'une chose, c'est l'absence de toute référence aux travaux soviétiques.

P. LACOMBE

H. G. VAN BUEREN, *Imperfections in Crystals* (North-Holland Publishing Company, Amsterdam, xviii + 676 pages. 1960. 110 sh.)

We can be grateful to the author for the perseverance which must have been needed to complete this wide-ranging book. Part I deals with the general properties of point defects and dislocations, part II with metals and part III with homopolar crystals. Most of the subjects one would expect to find are there—plasticity, diffusion, recovery and grain growth, optical properties of defects in ionic crystals and so forth—and some others. Three chapters (on the crystallography of dislocations, plasticity, diffusion and internal friction) are specifically devoted to crystals with the diamond structure. The chapter on internal friction in metals is the longest in the book (56 pp); an attempt is made to sort out its various sources. Readers specially interested in the properties of nuclear materials will find much in parts I and II on the production of defects by irradiation, their effect on physical properties and their annealing behaviour.

In his preface the author says that his aim is "(1) to give the reader a *bird's eye* view of the subject matter and to inform him about the research situation

such as it was at the end of 1958; and (2) to interest him in the variety of *theoretical ideas* that have been proposed in this field of study, which might prove stimulating". The book is thus not intended to be a substitute for monographs (where they exist) on the various topics. Indeed the author frequently refers the reader elsewhere for the derivation of results needed in the course of his argument. This is a pity when, as often, the missing derivation could have been sketched, in a dozen lines or so. As regards the second point, most of the concepts which the theorist uses as building-blocks are introduced, though there are some omissions, e.g. the so-called "chemical stress" on a dislocation in the presence of an excess or deficiency of vacancies. Some of them might have been presented more clearly. For example, anyone who meets the partial dislocation for the first time on p. 50 is unlikely to make much of fig. 6a, while fig. 6b will positively mislead him unless he realizes, with F. C. Frank, that a dislocation in the notation offsets the apparent misfit perpendicular to the slip-plane. Again, the dislocation pile-up is mentioned and figured several times, but nowhere is it presented as a definite configuration of dislocations with calculable properties.

As the book represents the state of things in 1958 some of its views may be a little out-of-date, at least temporarily; however, the references (and in part the text also) take note of some work published in 1959 and 1960. There are some errors due to misunderstanding on the part of the author. On p. 94, for example, it is stated that a free surface decreases the magnitude of the volume change produced by a point defect. This is the reverse of the conclusion reached in the work being reported. (The right hand side of eq. (35) must be multiplied by 3, and two lines above, "diminish" should read "increase".) The present reviewer did *not* say (p. 116) that the elastic interaction between point defects is always repulsive. The statement about the effect of alloying on stacking-fault energy on p. 165 seems to be wrong.

The beginner will probably do better to start with crisper accounts of the individual topics, but the reader who is already familiar with part of the subject will find, as the author intended, much stimulating matter concerning allied fields, and enough references to guide him to the sources.

J. D. ESHELBY

ABSTRACTS FROM VOL. 3 No. 3, TRANSLATED INTO RUSSIAN

ВЗАИМОДИФФУЗИЯ НИОБИЯ С ХРОМОМ, ЖЕЛЕЗОМ, НИКЕЛЕМ, МАРГАНЦЕМ И НЕРЖАВЕЮЩИМИ СТАЛЯМИ

Беркс Л. С. и Сибольд Р. Е.

Были приготовлены диффузионные пары при температуре около 1100°C из чистого ниобия и нержавеющей стали разных марок, а также из ниобия и каждого из примесных металлов: Cr, Fe, Ni и Mo. Используя электронный микроанализатор для исследования состава в диффузионном слое, были найдены стехиометрические составы для каждой пары элементов. При взаимодиффузии Nb-Cr всегда наблюдались фазы NbCr₂ и NbCr₇, а после длительного нагревания наблюдали кроме того фазу NbCr в твердом растворе с избытком ниобия. При взаимодиффузии в системе Nb-Fe наблюдалась промежуточная фаза NbFe₂ с избытком Nb в твердом растворе, причем существовали кроме того отдельные, богатые ниобием, соединения в железе на довольно большой глубине, в зависимости от присутствовавших в железе примесей. Диффузионные пары Nb-Ni часто плавилась уже при 1100°C, хотя эвтектический сплав, согласно литературным данным, должен

был бы плавиться при 1175°C. При температуре ниже 1095°C наблюдалась фаза NbNi в твердом растворе с избытком ниобия, причем фаза Nb₂Ni выделялась в решетке NbNi при охлаждении. При температуре выше 1095°C, вблизи точки плавления, происходит поточная диффузия приводящая к образованию зон длиной до 1400 мк, с фазой NbNi₃ которая выделяется в решетке NbNi при охлаждении.

Nb и Mo взаиморастворимы в любых пропорциях, причем коэффициент диффузии лежит в пределах от 3 до $7 \cdot 10^{-14}$ см²/сек.

Взаимодиффузия ниобия с нержавеющей сталью давала следующий состав главной зоны диффузии, в весовых процентах: Nb-40%, Fe-40%, Cr-8% и Ni-5%; предполагалось что в зоне существовала смесь из NbFe₂, NbCr₂ и Nb₂Ni. Небольшой слой у границы с ниобием предположительно состоял из смеси: NbFe₂, NbCr, Nb₂Ni.

ВЫСОКОТЕМПЕРАТУРНАЯ ДИФФУЗИЯ В СИСТЕМАХ:

Nb-Pt, Nb-Se, Nb-Zn, Nb-Co, Ni-Ta и Fe-Mo

Сибольд Р. Е. и Беркс Л. С.

При помощи электронного микроанализатора определялся состав и развитие фаз в биметаллических диффузионных системах при 1100°C. Было определено 18 фаз в шести бинарных системах: Nb-Pt, Nb-Se, Nb-Zn, Nb-Co, Ni-Ta, Fe-Mo. Во всех случаях фазы имели стехиометрический состав и выражались простыми целочисленными отношениями. Системы Nb-Se и Nb-Zn аналогичны в образовании фаз, в том смысле что в системе Nb-Se наблюдаются фазы: NbSe, Nb₂Se₃, NbSe₂, тогда как в системе Nb-Zn имеются фазы: NbZn, Nb₂Zn₃, NbZn₂, NbZn₃. Взаимодиффузия ниобия и платины с образованием Nb₃Pt, NbPt, NbPt₂, NbPt₃, по-видимому исключает возможность длительного

применения платиновых термопар в контакте с ниобием, при 1100°C.

Единственные фазы образующиеся при взаимодиффузии ниобия и кобальта, неизвестны в литературе и имеют состав Nb₃Co₂, NbCo₄. Эта система показала кроме того существование довольно широкой области содержащей 5 вес. % ниобия в кобальте, в соответствии с границей растворимости видимой на фазовых диаграммах.

Взаимодиффузия ниобия с танталом образует зоны с сильным растрескиванием и грануляцией. Зоны состоят из фаз: TaNi₃, TaNi₂, TaNi, Ta₃Ni₂, причем чистый тантал выделяется при охлаждении в решетке TaNi₂, начиная с 1100°C. В системе Fe-Mo наблюдалась только одна фаза Mo₂Fe₃.

САМОДИФФУЗИЯ ИОНОВ КИСЛОРОДА В ДВУОКИСИ УРАНА

Аускери А. Б. и Белл Ж.

Самодиффузия кислорода в стехиометрической и нестехиометрической двуокиси урана была измерена посредством реакции изотопического обмена между порошком двуокиси урана, с нормальным содержанием кислорода O^{18} и углекислым газом обогащенным кислородом O^{18} .

Для стехиометрического урана диффузия кислорода может быть представлена в виде уравнения

$$D = 1,2 \times 10^3 \exp(-65.300/RT)$$

между 550 и 780°C.

Для нестехиометрического урана скорости диффузии повышаются а энергия активации понижается более чем на половину.

Предполагается что ионы кислорода представляются носителями тока диффузии в промежуточном положении. Следовательно, имеет место щелевая диффузия.

ДЕЙСТВИЕ ИЗЛУЧЕНИЙ НА ТАНТАЛОВЫЙ ЭЛЕКТРОД НАМАЗАННЫЙ ОКИСЬЮ ТАНТАЛА

Фитс Ф. С. и Найт В.

Изследовано действие лучей гамма и электронов на электроды Ta_2O_5/Ta . Результаты сравниваются с полученными ранее с лучами У.Ф. и рентгеновскими. Измеренные фототоки пропорциональны интенсивности облучения в слабой дозе.

Для более сильных доз степень возрастания

фототока уменьшается. Заметное увеличение толщины окиси после облучения измерено не было.

Электролитические конденсаторы из листового тантала были признаны пригодными для обычных быстрых измерений фототока.

МИКРОАНАЛИЗ ЭЛЕКТРОННЫМ ЛУЧОМ НЕКОТОРЫХ СПЛАВОВ ПЛУТОНИЙ-ЖЕЛЕЗО

В. Д. Скотт

Простой способ, заключающийся в предварительном покрытии образца тонким слоем пластика, позволяет изучать плутоний в микроаналитическом электронно-лучевом приборе обычного коммерческого типа, не внося в него никаких изменений, и без необходимости помещения прибора в перчаточную камеру.

Не было обнаружено никакого загрязнения прибора радиоактивностью.

Представлены и обсуждаются полученные таким путем результаты изучения микрораспределения элементов в ряде сплавов плутоний-железо.

ЭЛЕКТРОЛИТИЧЕСКИЕ МОНОКРИСТАЛЛЫ ДВУОКИСИ УРАНА

Робинс Р. Г.

Отдельные монокристаллы двуокиси урана были получены при электролизе хлористого урана в расплавах хлоридов щелочных металлов, при напряжениях меньших кажущегося потенциала разложения для реакции: $UO_2Cl_2 \rightarrow UO_2 + Cl_2$ и при малой плотности катодного тока. Электролиз проводился с платиновым катодом и

угольным анодом. Кристаллы двуокиси урана вырастали на катоде размером до 3-х мм в поперечнике и массой около 50 мг. Наблюдались также второстепенные реакции, в результате которых на катоде образовывались кристаллы приблизительного состава: UO_2 , U_4O_9 , U_3O_8 .

ХАРАКТЕРИСТИКИ BeO ПРИ СПЕКАНИИ

Е. А. Ейткен

Описано влияние различных параметров на характеристики при спекании окиси бериллия. Было обнаружено, что наличие паров воды в атмосфере спекания задерживает уплотнение брикетов из окиси бериллия. Спеканность можно улучшить за счет предварительной сушки брикетов при 900°C на воздухе и спекания их в сухой атмосфере. Влияние паров воды на скорость спекания в значительной степени уничтожается при добавлении 1/4 мол. % MgO к брикету из BeO.

Порошок окиси бериллия, прокаленный при 1250°C вместо 900°C, спекается с меньшей скоростью, но, по-видимому, можно достичь таких же конечных плотностей за счет более длительного времени спекания или более высоких температур.

Наличие 1/4 мол. % $AlO_{1,5}$, $CrO_{1,5}$, MgO и NiO повышает конечную плотность брикетов из BeO по сравнению с брикетами без добавки. Особенно эффективными в повышении плотности являются MgO и Al_2O_3 .

САМОДИФФУЗИЯ ИОНА УРАНА В UO_2

А. Б. Оскерн, Дж. Белл

Методом уменьшения поверхностной активности был определен коэффициент диффузии урана (U^{+4}) в UO_2 стехиометрического состава.

Диффузию урана в температурном интервале 1450°–1785°C можно представить уравнением $D = 4,3 \times 10^{-4} \exp(-88000/RT)$.

КИНЕТИКА ФАЗОВЫХ ПЕРЕХОДОВ В СПЛАВЕ ЦИРКОНИЙ — УРАН — ВОДОРОД

Бокрос Ж. С.

Изучалась кинетика эвтектоидного перехода в сплаве уран-цирконий-водород (атомный состав 0,03 : 1 : 1). Во время перехода, при закаливании, через эвтектоидную ступень, твердая β -фаза находящаяся в равновесии при 600°C, быстро переходит в метастабильную α' -фазу при температуре свыше 450°C. Кроме того происходит с большой скоростью разрушение α' -фазы при температуре свыше 450°C; начинаясь

менее чем через 10 секунд, это разрушение становится тотальным приблизительно через 30 минут. Ниже 450°C разложение α' -фазы совершается гораздо более медленно.

Обратный переход α -фазы циркония и гидрида циркония в β -фазу при 600°C совершается с большой скоростью; переход начинается менее чем через 10 секунд и оказывается наполовину законченным уже через 100 секунд.

ИЗУЧЕНИЕ РАЗУПОРЯДОЧЕНИЯ ПОД ОБЛУЧЕНИЕМ U_2Mo -ФАЗЫ

Блох Ж. Дула Ж. Блэн Ж.

Мы подвергли облучению сплавы урана-молибдена, состава U_2Mo которые обладали упорядоченной квадратичной структурой.

Были произведены 2 серии облучений, одна в реакторе ЕЛ2 в интервале температур от 20 до 65°C и другая в реакторе „Мелюзина” при температуре жидкого азота.

Кристаллографический анализ показал что

переход от квадратичной структуры γ' -фазы к кубической структуре γ -фазы происходит постепенно с ростом дозы облучения. Наконец было определено что роль столкновений является подавляющей при разупорядочении этого сплава и что их число равняется приблизительно 300.000 на один распад.

ИЗМЕРЕНИЕ ТЕПЛОПРОВОДНОСТИ СТЕРЖНЕЙ ИЗ ОКИСИ УРАНА В МЕТАЛЛИЧЕСКОЙ
ОБОЛОЧКЕ ВО ВРЕМЯ ОБЛУЧЕНИЯ

И. Коэн, Б. Ластман, Дж. Д. Айхенберг

Одной из слабых сторон, использования холоднопрессованной и спеченной UO_2 для топливных элементов реактора был недостаток необходимых данных о факторах, влияющих на термическое поведение окисных топливных элементов. Завершен ряд опытов внутри реактора, целью которых было измерение „эффективной” теплопроводности UO_2 как функции радиа-

льного зазора между горючим и оболочкой, атмосферы газа, заполняющей зазор, и температуры в центре горючего. Эксперименты показывают большую чувствительность теплопроводности элемента к величине начального зазора в сборке в результате барьера теплового сопротивления в промежутке между горючим и оболочкой.

ПИСЬМА В РЕДАКЦИЮ

ОПЫТ ПО ВЫЯСНЕНИЮ РОЛИ ТОЧЕЧНЫХ ДЕФЕКТОВ ПРИ ОБРАЗОВАНИИ α -УРАНА
ПОД ОБЛУЧЕНИЕМ

Томпсон М. В.